Single Atom Delivery into a Bottle Beam Trap Using an Optical Conveyor Belt and Quantum Coherent Gain in a Matterwave Transistor

by

Brad A. Dinardo

B.S., Physics and Mathematics, Juniata College, 2011

M.S., Physics, University of Colorado, Boulder, 2014

A thesis submitted to the

Faculty of the Graduate School of the

University of Colorado in partial fulfillment

of the requirements for the degree of

Doctor of Philosophy

Department of Physics

2018

This thesis entitled:
Single Atom Delivery into a Bottle Beam Trap Using an Optical Conveyor Belt and Quantum Coherent Gain in a Matterwave Transistor
written by Brad A. Dinardo
has been approved for the Department of Physics

_____

Prof. Dana Z. Anderson

_____

Prof. Murray Holland

Date _____

The final copy of this thesis has been examined by the signatories, and we find that both the content and the form meet acceptable presentation standards of scholarly work in the above mentioned discipline.

Dinardo, Brad A. (Ph.D., Physics)

Single Atom Delivery into a Bottle Beam Trap Using an Optical Conveyor Belt and Quantum Coherent Gain in a Matterwave Transistor

Thesis directed by Prof. Dana Z. Anderson

The work of this dissertation falls into two broad categories. In the first part, I describe loading a single atom from a reservoir into a blue-detuned crossed vortex bottle beam trap using a dynamic 1D optical lattice. The lattice beams are frequency chirped using acousto-optic modulators, which causes the lattice to move along its axial direction and behave like an optical conveyor belt. A stationary lattice is initially loaded with approximately 6000 atoms from a reservoir, and the conveyor belt transports them 1.1 mm from the reservoir to a bottle beam trap, where a single atom is loaded via light-assisted collisions. Photon counting data confirm that an atom can be delivered and loaded into the bottle beam trap 13.1 % of the time.

In part II, I describe a theory and experiment in the field of atomtronics that displays a coherent gain mechanism for a triple-well matterwave transistor oscillator. I start with a well-established semi-classical description of an atomtronic transistor but model the system using a many-body formalism. The quantum model predicts interesting physics when the atoms flowing through the transistor have sufficiently low enough temperatures such that the motional state of a dipole oscillating BEC, placed in the transistor itself, couples atom transitions between high lying transistor energy eigenstates. In this regime, the coupling gives rise to a new gain mechanism that increases the flux of matterwaves flowing out of the transistor system, compared to when the coupling is absent. Our experiments suggest that the gain mechanism is coherent and increases the spread of matterwave energy that flows out of the transistor.

Dedication

To my parents, Karen and Joe Dinardo, whose unconditional love and support throughout my life made me the person that I am today.

Acknowledgements

There are so many people that I must thank for helping me throughout my academic career. First, I thank my advisor, Dana Z. Anderson, for his constant support, advice, and help throughout my time here at JILA. Dana has made me a better scientist and person and I will forever be grateful for his absolute dedication to my graduate career. Second, I must absolutely thank Leslie Czaia for her enormous help throughout my time at JILA. Leslie assisted with so many crucial aspects of my experiments behind the scenes, and saved me weeks (or months) with her expertise. Moreover, I will forever be indebted to the graduate students of the Anderson lab. An old saying goes "If you want to go fast, go alone. If you want to go far, go together." With that I must thank my fellow graduate students: Kai Hudek, Seth Caliga, Cameron Straatsma, Carrier Weidner, and Curtis Rao. Without you, I would never have made it through this wonderful, yet challenging experience.

I also need to thank former Anderson Lab post docs Hoon Yu and Marko Zgonik. I must also credit the JILA machine and instrument shop, as they did so many incredible things behind the scenes to help me with my research. For that I thank Hans Green, Blaine Horner, Tracy Keep, and Kim Hagen. I cannot tell you how many times I went to the JILA electronic shop with a fried circuit and was given great advice on how to fix the problem. Thus, I must thank Terry Brown, Carl Sauer, and James Fung-A-Fat. Additionally, I need to extend a very big thanks to the University of Wisconsin, Madison neutral atom quantum computing team, including Mark Saffman, Marty Lichtman, and Michal Piotrowicz. I also extend a great thanks to Evan Salim and Steve Hughes from ColdQuanta as well as Sterling McBride and Joey Michalchuk from SRI Sarnoff for their help. I was also very fortunate to have very memorable professors here at CU Boulder. I thank

Chris Greene, K.T. Mahanthappa, Shanta de Alwis, Oliver DeWolfe, James Thompson, and Victor Gurarie for very memorable classes.

I would never be here without the incredibly talented professors from Juniata College. I thank Jamie White, Jim Borgardt, Norm Siems, Mary Atchley, Mark Pearson, Ben Sunderland, Henry Escuadro, John Bukowski, Catherine Stenson, Kim Roth, Jerry Kruse, and Paul Schettler. I remember on my very first day at Juniata College meeting Dr. Siems in his office. He told me "When you think you've worked hard, just work a little harder." I never forgot that advice and I credit it to helping me get through college and my graduate studies. Additionally, I must thank some of the great teachers I had growing up in Altoona, PA: From Logan Elementary, I thank Bill Killian and Randy Bickel. From D.S. Keith Jr. High School, I thank John Banyas, Stephen Lightner and Frank Swalga. Finally, from Altoona Area High School, I had the great pleasure of learning from Joe Falger, Eric Stoudnour, Jim Krug, Mike Ergler, David Borst, Roger Menard, Marie Suter, and E. Preston Rice.

Finally, I want to thank my parents, Karen and Joe Dinardo as well as my brother Derek. Without them, I would never be here. For as long as I remember, they encouraged me to pursue my passions and did whatever they could to support me through life. Thank you all.

Contents

Chapter

Figures

Figure

Chapter 1

Part I: Introduction and Motivation

The work of this dissertation falls into two broad categories: transporting and loading single neutral cesium atoms into optical bottle beam traps in order to facilitate a continuously operating quantum computer and developing a purely quantum thermodynamic model and experiment for a matterwave transistor oscillator that demonstrates the existence of a matterwave gain mechanism. The former is part of a five year collaboration between institutions working on the Atomic Qubit Array (AQuA) project, which itself is part of the IARPA Multi-Qubit Coherence Operations (MQCO) program. The latter is in the field of atomtronics and aims to demonstrate the existence of a matterwave gain mechanism in an atomtronic transistor oscillator for the eventual use in ultracold atomic experiments. This chapter briefly summarizes both research areas as well as introduces motivation for each subject. The fundamental and basic theoretical methods that are essential to understanding both experiments, as well as the ultra high vacuum systems necessary to perform the work, are described in part I of this dissertation.

1.1 AQuA Project Summary: Neutral Atom Quantum Computing

Part II[1] of this dissertation describes work occurring within the field of neutral atom quantum computing. First proposed by Richard Feynman at Caltech in 1959 [6], quantum computing is a general, all-encompassing term that describes storing information in a two-state quantum system in order to perform algorithms analogous to how classical computers perform algorithms using

[1] The fundamental and basic theoretical methods that are essential to understanding both experiments as well as the ultra high vacuum systems necessary to perform the work are described in part I of this dissertation.

binary transistor states, or bits. The two-state quantum system, called a qubit, could be the spin of an atomic ground state, a ground state and Rydberg state atom pair, electronic states of an ion, a Josephson junction, or a SQUID to name a few examples. Irrespective of the type of qubit, the ambition of quantum computing is to perform algorithms exponentially faster than classical computers. A major milestone in the field was achieved in 1995, when quantum computing was first demonstrated by using a single trapped ion to serve as a qubit to perform quantum logic [7]. Since then, multi-qubit quantum logic gate operations have been performed experimentally with multiple trapped ions [8, 9, 10], numerous superconductors [11, 12, 13], collections of photonic qubits [14, 15], and neutral Rydberg atom pairs [2, 16, 1, 17, 18]. Just like a classical computer, the number of qubits in a quantum computer directly influences its productivity. Most recently, using superconducting qubits, IBM has steadily increased their commercially available quantum computer from 2 qubits in 2016, to 16 qubits in 2017, and finally to using a 20 qubit register in 2018. It is clear that the current state-of-the-art in quantum computing has progressed to the point where it is necessary to increase the number of qubits. Large scale quantum computers that would compute with tens to hundreds of qubits would exceed the capabilities of classical computers by being able to solve integer factorization, such as using Shor's algorithm [19], or inverting functions by using Grover's algorithm [20], faster than any classical computer. While experiments with trapped ions [21, 22, 23] and superconducting qubits [24, 25] have already succeeded in realizing high fidelity many-qubit quantum gates, using an array of *neutral atom* qubits also remains an attractive and viable solution to scaling a qubit register to an arbitrarily large amount.

1.1.1 Scaling a Neutral Atom Quantum Computer to Many Qubits

The Atomic Qubit Array-49 (AQuA) project aims at developing and demonstrating a continuously operating atomic qubit array of 49 individual qubits. The qubit array concept, shown in figure 1.1, features a 2D array of neutral atom qubits all with equal separation between each neighboring qubit. The AQuA-49 project operates with qubit gates based on exciting neutral atoms to Rydberg states. Using neutral atoms, one can theoretically scale the amount of qubits N to as high

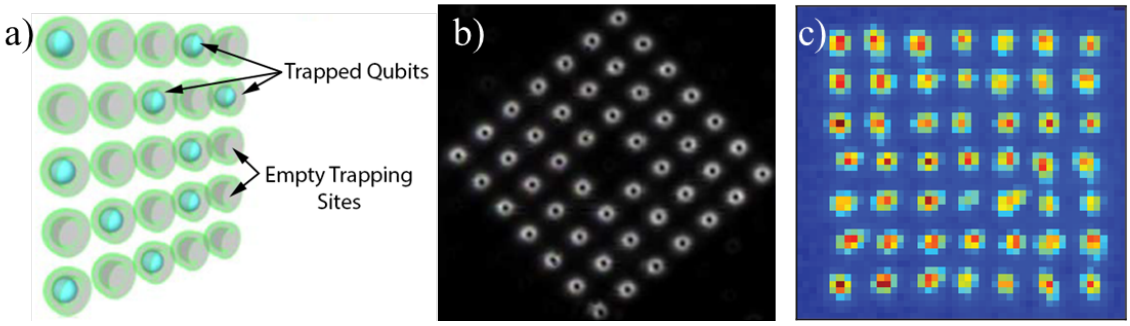

Figure 1.1: a) Concept of the neutral atom qubit array. Single qubits are located in individual optical traps, each separated by distance d. b) 8x8 site qubit array made with individual optical traps where each is capable of confining a single atom. c) Fluorescence image of single atoms occupying each optical trap of the array. These images are taken from references 1 and 2.

as one desires with very minimal crosstalk between the remaining $N-1$ qubits. This is because neutral atoms differ from ions with respect to their state dependent interaction properties. This is evident in figure 1.2, which shows the two particle interaction strength as a function of separation distance r for two ions, two neutral ground state rubidium atoms, and two rubidium atoms excited to Rydberg states.

First, a pair of ions separated by a distance r interact predominantly with the $1/r$ Coulomb potential. Because the Coulomb potential only decreases with a single power of r, it remains strongly interacting, even at long distances, which are great attributes for qubits. The drawback is the Coulomb interaction is always on, making it difficult to create an arbitrarily large register of ion qubits. Next, the interaction between two ground state neutral atoms is dominated by the $1/r^6$ van der Waals potential at short distances and by the $1/r^3$ magnetic dipole-dipole interaction at large distances[2] . With a separation of 10 μm, this $1/r^6$ ground state interaction is very weak at approximately $U/\hbar \approx 10^{-5}$ Hz in frequency units. However, at this same separation, two *Rydberg* state atoms have a very strong r^{-3} electric dipole-dipole interaction of approximately 10^7 Hz. This result gives the core principle of operation of the neutral atom qubit array: selectively turning on the Rydberg interaction (by exciting an atom to such a state) allows one to selectively increase an atom-atom interaction by 12 orders of magnitude [1]. The ability to control the interaction

[2] Here, long distances refers to any atom separation $r \approx 30$nm.

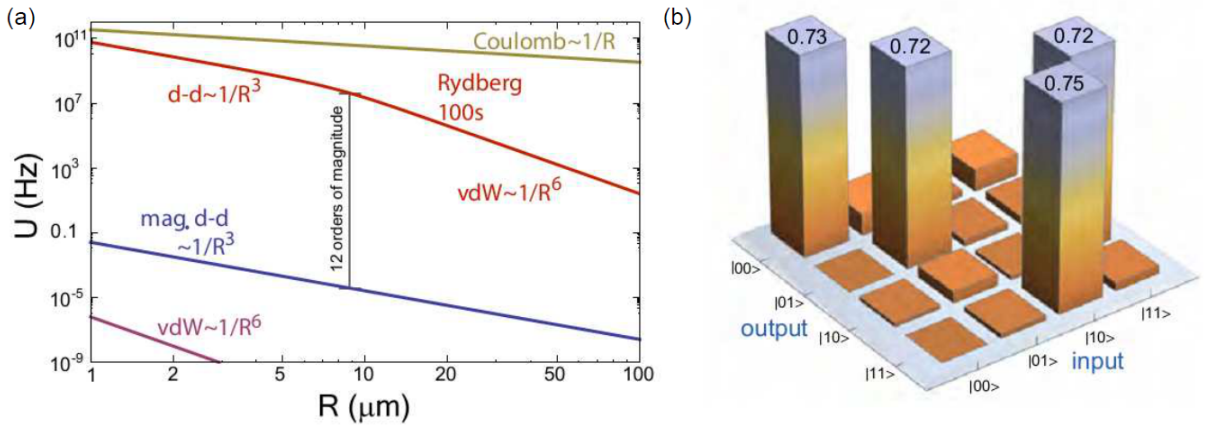

Figure 1.2: a) Two-body interaction strength for two ions (due to the Coulomb interaction), two ground state rubidium atoms (due to the van der Waals and magnetic dipole-dipole interaction), and two Rydberg states excited to the 100s level. b) CNOT truth table obtained with two Rydberg state Rb atoms excited to $n = 97$ with a separation of 10 μm. Images are taken from [1] [2]

strength by a factor of 10^{12} over a wide spatial range appears to be unique to the Rydberg system and makes an array of Rydberg-mediated quantum gates a viable solution to a many-qubit quantum computer. In fact, recently, a controlled-NOT (CNOT) gate has been demonstrated between two Rydberg state qubits [2] and it's measured truth table is shown in figure 1.2.

1.1.2 Drawback of a Neutral Atom Qubit Array: Atom Loss

A drawback of using neutral atom qubits, as opposed to ion qubits and superconducting qubits, is that neutral atoms must be held in optical traps enclosed inside ultra high vacuum chambers. This results in unavoidable atom losses due to finite lifetimes on all of the neutral atom qubits trapped in the array shown in figure 1.1. Atom loss poses a serious problem since finite trapping lifetimes endangers the ability of using an array of neutral atom qubits to perform arbitrarily long quantum algorithms. The solution to this problem, which is the subject of part II of this dissertation, is to reload any array traps that lose a qubit (due to background gas collisions) with a new, pre-cooled atom from some distant cold atom reservoir. Providing or transporting a pre-cooled atom from some reservoir has been accomplished in past experiments [26, 27, 28, 29, 30, 31]. However, common to each of these experiments is that they take place in large vacuum systems

where optical isolation and stray field isolation throughout the chamber occurs easier than in a very compact vacuum cell (such as the vacuum cell used in this dissertation). Moreoever, these experiments all involve loading single atoms into a physically visible object (such as a cavity) as opposed to an infrared optical trap, whose location cannot be assumed *a priori*.

1.1.3 Solution to Atom Loss: Transporting Atoms to Reload Distant Unoccupied Array Optical Traps

Site selective atom reloading of the qubit array can be accomplished by using a dynamic, one-dimensional optical lattice (also called an optical conveyor belt) to deliver a single atom to an unoccupied array site [32]. The concept of such an atom reloading scheme is shown in figure 1.3. Moreover, the atom transport system must be scalable such that it is capable of addressing and delivering to an array of sites and not just a single site. Accordingly, the atom transport system must be "steerable" in that it could deliver an atom to one site and then be repositioned and deliver an atom to another array site. Finally, the qubit array in the AQuA-49 project is located in a miniaturized and portable vacuum chamber which makes optical isolation an intricate problem: Any stray light from the atom transportation lasers can destroy the qubit array coherence and will disrupt any ongoing quantum computations. Thus, to transport atoms from a reservoir to an empty qubit array site without disrupting any occupied array sites, the issue of optical isolation presents a compelling, but otherwise difficult problem.

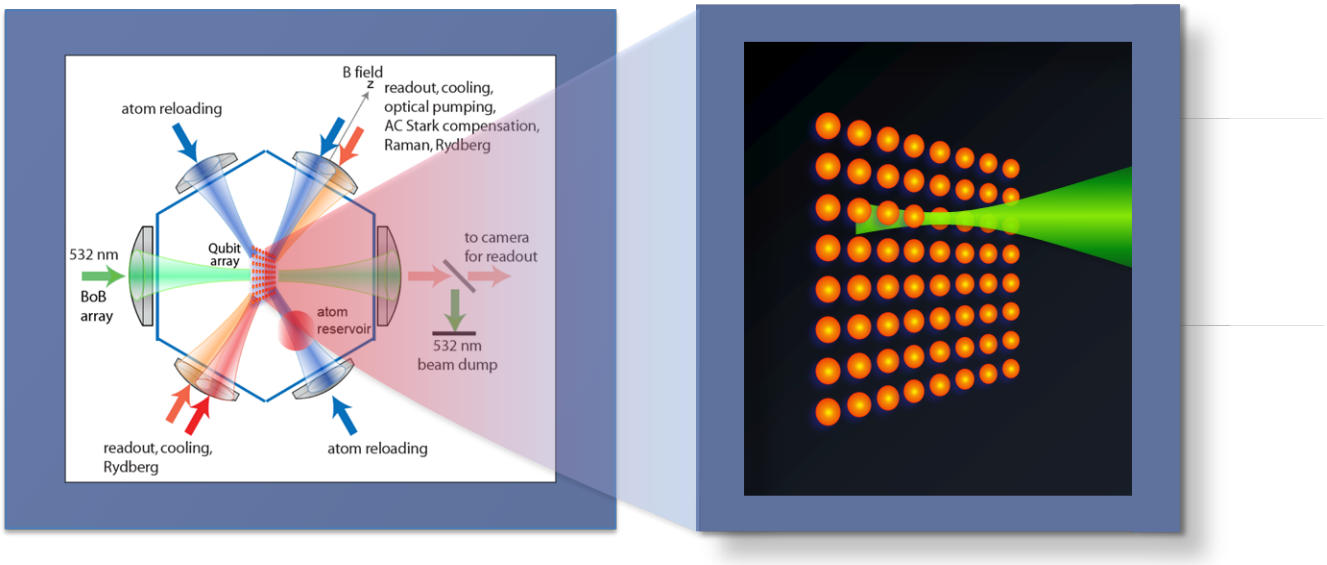

Figure 1.3: Dissertation Part II: Concept of reloading an empty qubit array site with a new atom from some distant cold atom reservoir. A single atom can be delivered using a dynamic one-dimensional optical lattice without running into adjacent array sites.

1.2 Ultracold Matterwave Transistor Oscillator

Part III of this dissertation involves a drastically different theory and ongoing experiment in the field of atomtronics that introduces a new gain mechanism for a matterwave transistor oscillator. We start with a well-established, *semiclassical* description and experiment [33][5][34] of an atomtronic transistor and model the system with a purely quantum mechanical formalism. This quantum model differs from the semiclassical results only when the atoms flowing through the transistor have sufficiently low enough temperatures. In this "low temperature regime", the motional state of a dipole oscillating BEC, placed in the transistor itself, couples atom transitions between high lying transistor energy eigenstates as an atom current flows through the transistor. In this case, the transistor oscillator displays interesting physics that was not observed in the semiclassical theory or experiments, namely the presence of coherent gain mechanism that broadens the range of atom energy (and hence momentum) that may flow through the transistor.

1.2.1 Atomtronics: Ultracold Atomic Circuits

Atomtronics [35][36] is an emerging field of ultracold atomic physics that focuses on quantum circuits that operate as atom analogues to electrical circuits, where an atom current takes the place of an electron current and the chemical potential takes the place of a voltage. In their design, atomtronic circuits are drastically different from their electronic circuit counterparts, as they involve manipulating ensembles of ultracold atoms to flow through a variety of potential energy landscapes, such as

- Optical potentials produced from laser beams (in particular, the experiments in [37][38])
- Harmonic magnetic potentials created with atom chips (as demonstrated in references [39][40][41][42][43])
- A hybrid combination of optical and magnetic potentials, such as the transistor potential used throughout chapters 7 and 8 of this dissertation.

At the heart of all atomtronic circuits is a Bose-Einstein condensate (BEC) [44], which supplies a source of coherent, ultracold atoms that are controlled to flow throughout a network of quantum potentials. Some recently demonstrated atomtronic circuits of note include BECs flowing throughout double-well [33] and triple-well potentials [5], as well as BECs flowing through 1D optical lattices [45][46][47] and optical ring lattices [48][49][50]. Irrespective of the circuit potential geometry, the objective of atomtronics remains the same: manipulate a current of ultracold atoms in some tailored potential in order to study fundamental physics or to create purely quantum mechanical technologies [51].

Accompanied with such high aspirations of atomtronics comes a difficult, innate challenge ingrained in the field: such ultracold atom circuits are inherently a many-bodied, open quantum system, since atoms and BECs interact and dissipate as they flow throughout the circuit from some source to a sink or drain. While this immensely complicates the theoretical description of atomtronic circuits, complete descriptions are usually simplified by invoking various approximations, such as

- Neglecting dissipation and treating the atomtronic circuit as a closed system (as demonstrated in references [52][53][54][55])
- Reducing the many-bodied system from a very large number to a three or four-body problem
- Ignoring the BEC mean-field interaction effects (as described in reference [34]).

Despite the the necessity of using approximations *just* to solve for *something*, atomtronics has made unwavering progress in ultracold atom technologies such as realizing quantum simulators [56][57][58][59], improving precision measurements [60][61], creating an atomtronic analogue to a SQUID (called an AQUID, or atomtronic quantum interference device [62][63]), and realizing the first-ever atom battery [33]. Moreover, if used in conjunction with well-established matterwave interferometry experiments, atomtronics can help enhance inertial sensing and gravimetry sensitivities by up to 10 orders of magnitude as compared to their light wave interferometry counterparts [64]. Finally, atomtronics can conceive new types of quantum technologies by combining various

atomtronic circuit elements into an integrated ultracold atom circuit. One such integrated ultracold circuit, which is the subject of part III of this dissertation, is a matterwave transistor oscillator.

1.2.2 Analogue between Electronic and Matterwave Transistors

Fundamental to many technological developments since its demonstration by Bardeen, Shockley, and Brattain at Bell Labs in 1948, the transistor is a three-terminal semiconductor electronic device that uses an applied voltage or current on one terminal to amplify or switch electrical signals on another terminal [65]. An *atomtronic* transistor would behave similarly to its semiconductor counterpart by switching or amplifying atom, or matterwave, currents rather than electrical currents. Moreover, in place of three electrical terminals (commonly known as the source, gate, and drain terminals) found on semiconductor transistors, an atomtronic transistor features three quantum potential energy wells that are capable of confining ultracold atoms. In similar form and function to the semiconductor transistor, these three potential energy wells, which are labeled the source-well, gate-well, and the drain-well, together behave as an atomtronic transistor source (to source an ultracold atom ensemble to flow through the system) a gate (confining an additional ultracold ensemble to provide a gain mechanism), and a drain (which functions as the output port of the transistor).

1.2.3 Emergence of a Gain Mechanism for a Matterwave Transistor

Most importantly, for such source-gate-drain system to be called an atomtronic transistor, it *must* display a gain mechanism for a matterwave or atom current. In this atomtronic transistor oscillator, gain occurs due to the emergence of a new atom-BEC interaction that occurs when atom currents collide with a dipole oscillating BEC confined to the transistor gate-well. This new interaction, which specifically arises due to the motional state of an oscillating gate-well BEC coupling high lying gate-well energy eigenstates, is very similar to the Rabi model interaction between two-level atoms and a photon field. The interaction serves to increase the atom current flowing through the transistor by ultimately amplifying the matterwave probability amplitude in

the transistor drain-well. This manifests itself in an increase of the atom flux Φ, or atoms per unit time flowing into the drain-well, as well as broadening the range of energies (and momenta) carried by the atom current flowing through the potential (figure 1.4).

1.3 Dissertation Outline

The remainder of this dissertation is organized in the following way: Chapter 2 provides some fundamentals and the basic theory for the methods that are essential to understanding the work contained within this dissertation. The concepts of laser cooling, optical trapping, magnetic trapping, evaporation, and Bose-Einstein condensation as they pertain to the experiments in this dissertation are summarized. Chapter 3 describes in detail the ultra high vacuum systems and the atom chip system that together, provide the experimental bedrock for this thesis. Next, we present single atom transport experiments to reload optical traps for quantum computing (as motivated in section 1.1.3): In chapter 4, we describe an atom transport system for loading a single atom from a reservoir into a blue-detuned crossed vortex bottle beam trap using a dynamic 1D lattice. Chapter 5, details scaling the atom transport and reloading system to deterministically load any arbitrary site of an array of bottle beam traps. Chapter 6 concludes the atom transport and reloading work and gives an outlook for the field. Finally, we present the atomtronic transistor oscillator theory and experiments (as motived in section 1.2): Chapter 7 details a model for the matterwave transistor oscillator and explicitly derives the many-bodied Hamiltonian for the system, showing the emergence of a gain mechanism. Chapter 8 describes the ongoing experimental efforts and results with the matterwave transistor oscillator and presents data suggesting the presence of a coherent gain mechanism as well as coherence in the ultracold current flowing through the system. Chapter 9 concludes by looking ahead at the future of the atomtronic transistor experiments as well as providing interesting applications for such a matterwave transistor device.

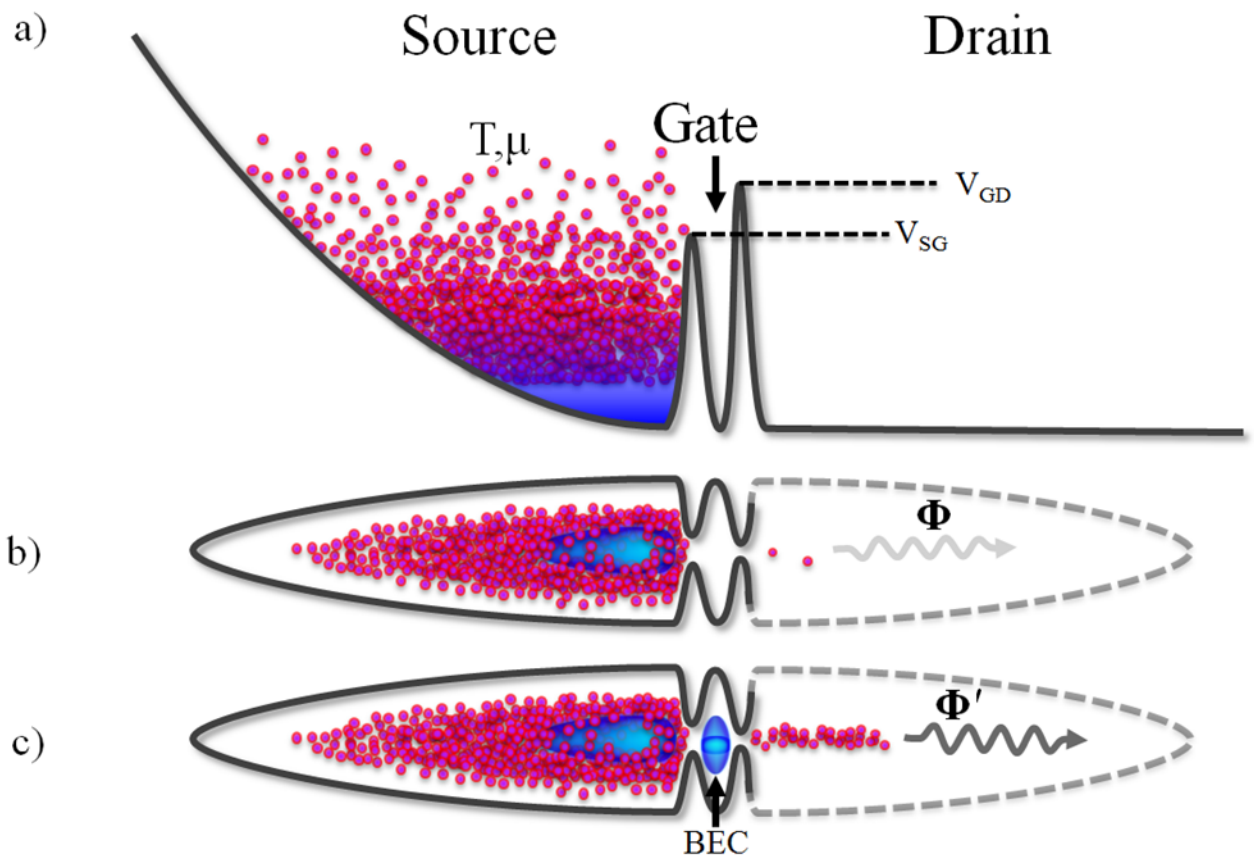

Figure 1.4: Dissertation Part III: Setup and principle of operation of the matterwave transistor oscillator. a) A 1D potential energy diagram of the triple well matterwave transistor where an ensemble of atoms at chemical potential μ and temperature T occupy the source well. The source well and drain wells are separated by the gate well, which is created with two repulsive Gaussian barriers called the Source-Gate (SG) and Gate-Drain (GD) barriers, which have heights V_{SG} and V_{GD}, respectively. Images b) and c) convey the principle of operation of the transistor, showing that a greater matterwave flux Φ' flows through the gate when a dipole oscillating BEC occupies the gate well, compared to the matterwave flux Φ when a BEC is absent from the gate.

Chapter 2

Laser Cooling and Trapping ^{133}Cs and ^{87}Rb Atoms

The work and experiments covered in this dissertation involves manipulating and imaging cold and ultracold atoms. For the AQuA-49 single atom reloading experiment, we must be able to cool ^{133}Cs atoms to a temperature of approximately 15 μK and confine them in optical dipole traps. For the atomtronics transistor oscillator experiments, we must be able to trap even colder atoms of ^{87}Rb in magnetic potentials and rapidly condense them to a Bose-Einstein condensate with a temperature of about 50 nK. Remarkably, the atoms used in our experiments begin at a considerably higher temperature of 300 K, meaning the atoms for our experiment must be cooled by as much as twelve orders of magnitude. Thus, producing any type of successful results relies on our ability to efficiently cool and trap atoms in a compact vacuum apparatus. Therefore, a brief overview on the fundamental principles involved in our laser cooling and trapping techniques used throughout both experiments is given. This chapter is outlined as follows:

Starting from the Hamiltonian of a two-level atom interacting with a laser field (section 2.1.1) we quickly arrive at forces that give rise to optical dipole trapping (2.1.2), magneto-optical trapping (2.1.3), and polarization gradient cooling (2.2.1); all of which are absolutely essential to the experiments in this dissertation and can cool an initially room temperature ensemble of 10^9 atoms to about $10 - 20$ μK in about one second. We then show how these pre-cooled atoms are subsequently trapped in magnetic potentials (2.4.1) that are produced on an atom chip, which allows further cooling with forced radio-frequency evaporation (2.5.1) to produce a Bose-Einstein condensate (2.6) with a temperature as low as 50 nK.

2.1 Atom-Photon Interactions

2.1.1 Hamiltonian and Energy Shift

Consider a two-level atom with a ground state $|g\rangle$ and an excited state $|e\rangle$, with energies E_g and E_e, respectively. By placing the atom in an oscillating electric field $\mathbf{E}$ produced by a laser beam with frequency ω, the atoms will gain an induced electric dipole moment $\hat{\mathbf{d}}$. In such a configuration, the atom experiences an energy shift [66, 67] given by the interaction Hamiltonian

$$H' = -\hat{\mathbf{d}} \cdot \mathbf{E}. \tag{2.1}$$

Because H' is a perturbation to the energy of the atom, the associated change in the atom's ground state energy E_g is given by standard perturbation theory [68, 69, 70] as

$$\begin{aligned} \Delta E_g &= \sum_{e \neq g} \frac{|\langle e| H' |g\rangle|^2}{E_e - E_g} \\ &= \langle g| \hat{\mathbf{d}} \cdot \mathbf{E} |e\rangle \underbrace{\frac{1}{E_e - E_g + \hbar\omega}}_{\text{absorption}} \langle e| \hat{\mathbf{d}} \cdot \mathbf{E} |g\rangle + \langle g| \hat{\mathbf{d}} \cdot \mathbf{E} |e\rangle \underbrace{\frac{1}{E_e - E_g - \hbar\omega}}_{\text{emission}} \langle e| \hat{\mathbf{d}} \cdot \mathbf{E} |g\rangle \end{aligned} \tag{2.2}$$

where the first term is the energy shift due to the atom absorbing a photon of energy $\hbar\omega$ from the laser and the second term represents the energy change due to the atom emitting a photon of energy $\hbar\omega$. In both the single atom loading and transistor oscillator experiments described in this dissertation, the cooling laser frequency ω is very close to resonance. That is $E_e - E_g \approx \hbar\omega$. Thus, the absorption contribution to the ground state energy shift (equation 2.2) is negligible compared to the emission contribution. Using this approximation, the ground state energy shift for an atom in the laser field can be approximated as

$$\Delta E_g \approx \langle g| \hat{\mathbf{d}} \cdot \mathbf{E} |e\rangle \frac{1}{E_e - E_g - \hbar\omega} \langle e| \hat{\mathbf{d}} \cdot \mathbf{E} |g\rangle = \frac{|\langle g| \hat{\mathbf{d}} \cdot \mathbf{E} |e\rangle|^2}{E_e - E_g - \hbar\omega} = \frac{|\langle g| \hat{\mathbf{d}} \cdot \hat{\boldsymbol{\epsilon}} |e\rangle|^2}{E_e - E_g - \hbar\omega} E^2 \tag{2.3}$$

where $\hat{\boldsymbol{\epsilon}}$ is a unit vector indicating the direction of the electric field with magnitude E produced by the laser.

The ground state energy shift (equation 2.3) can also be examined using classical electrodynamics. Using that the induced dipole moment is proportional to the electric field by means of the

atom polarizability [67], the shift to the ground state energy of the atom in the laser beam can also be expressed as

$$\begin{aligned}\Delta E_g &= -\hat{\mathbf{d}} \int d\mathbf{E} = -\alpha(\omega) \int \mathbf{E} \cdot d\mathbf{E} \\ &= -\frac{1}{2}\alpha(\omega) E^2\end{aligned} \tag{2.4}$$

where the relation $\hat{\mathbf{d}} = \alpha(\omega)\mathbf{E}$ was used with the atomic polarizability $\alpha(\omega)$ defined as a function of the frequency ω of the laser electric field $\mathbf{E}$. By equating equations 2.3 and 2.4, one finds that the atomic polarizability for a two-level atom in the laser electric field is

$$\alpha(\omega) \approx \frac{|\langle g| \hat{\mathbf{d}} \cdot \hat{\boldsymbol{\epsilon}} |e\rangle|^2}{E_e - E_g - \hbar\omega}. \tag{2.5}$$

Before continuing on, a correction factor *must* be applied to the atomic polarizability result of equation 2.5. In its current state, the result of equation 2.5 intrinsically assumes an infinite lifetime[1] for an atom in the excited state $|e\rangle$. This, of course, is false since an excited state decays exponentially with time constant $\tau = 1/\Gamma_e$, where Γ_e is the linewidth of the transition $|e\rangle \to |g\rangle$. The polarizability in equation 2.5 can be corrected to reflect this finite lifetime by including the *complex* energy shift of $i\hbar\Gamma_e/2$ due to transitions to the ground state[2] . That is $E_e \to E_e - i\hbar\Gamma_e/2 = \Delta E_e$. Applying this energy shift in equation 2.5, the atomic polarizability becomes

$$\alpha(\omega) = \frac{|\langle g| \hat{\mathbf{d}} \cdot \hat{\boldsymbol{\epsilon}} |e\rangle|^2}{E_e - i\hbar\Gamma_e/2 - E_g - \hbar\omega} = \frac{|\langle g| \hat{\mathbf{d}} \cdot \hat{\boldsymbol{\epsilon}} |e\rangle|^2}{\hbar(\delta^2 + \Gamma_e^2/4)} \left(\delta + i\frac{\Gamma_e}{2}\right) \tag{2.6}$$

where we have introduced the laser detuning $\delta = \omega_e - \omega_g - \omega$ with $\omega_e = E_e/\hbar$ and $\omega_g = E_g/\hbar$ being the energy eigenvalues of the $|e\rangle$ and $|g\rangle$ states as expressed in frequency units.

This argument is also extended to the ground state $|g\rangle$ where in a very general case, the

[1] The infinite lifetime arises because the energy E_e of the excited state $|e\rangle$ is purely real. Thus, the probability of finding the atom in the excited state is a stationary state and will never decay, since

$$|\Psi|^2 = |A|^2 \exp\left[i\frac{E_e}{\hbar}t\right] \exp\left[-i\frac{E_e}{\hbar}t\right] = |A|^2 = \text{ constant.}$$

[2] By including the imaginary energy shift $-i\hbar\Gamma_e/2$ to the excited state energy, the probability amplitude correctly reflects a decay with time constant $\tau = 1/\Gamma_e$ due to the finite lifetime $1/\Gamma_e$ of the excited state:

$$|\Psi|^2 = |A|^2 \exp\left[i\left(\frac{E_e + i\hbar\Gamma_e/2}{\hbar}\right)t\right] \exp\left[-i\left(\frac{E_e - i\hbar\Gamma_e/2}{\hbar}\right)t\right] = |A|^2 e^{-\Gamma_e t}.$$

ground state energy shift ΔE_g in a laser beam is also written as a complex quantity [68]:

$$\Delta E_g = V_g - i\hbar\Gamma_g/2. \tag{2.7}$$

The real component V_g represents the energy shift of the atom ground state due to the laser electric field $\mathbf{E}$ and the imaginary component $-i\hbar\Gamma_g$ accounts for the finite lifetime $\tau = 1/\Gamma_g$ of $|g\rangle$ due to transitions $|g\rangle \rightarrow |e\rangle$ that are induced by the atom absorbing the laser radiation field. We can then insert equation 2.6 into equation 2.4 and equate the result to equation 2.7 to formulate an expression representing the ground state energy shift of an atom due to a laser field:

$$\begin{aligned} V_g - i\hbar\Gamma_g/2 &= -\frac{1}{2}\alpha(\omega)E^2 \\ &= -\frac{1}{2}\frac{|\langle g|\hat{\mathbf{d}}\cdot\hat{\boldsymbol{\epsilon}}|e\rangle|^2}{\hbar(\delta^2+\Gamma_e^2/4)}\left(\delta + i\frac{\Gamma_e}{2}\right)E^2 \\ &= -\frac{\hbar}{2}\frac{\Omega^2}{\delta^2+\Gamma_e^2/4}\left(\delta + i\frac{\Gamma_e}{2}\right) \end{aligned} \tag{2.8}$$

where we have introduced the Rabi frequency $\Omega = |\langle g|\hat{\mathbf{d}}\cdot\mathbf{E}|e\rangle|/\hbar$, which is merely the magnitude of the original perturbation $H' = -\mathbf{d}\cdot\mathbf{E}$ (equation 2.1) expressed in frequency units [71]. Equation 2.8 is a very important result for the laser cooling and trapping used throughout this dissertation: By equating the purely real components, equation 2.8 gives the atom energy shift due to scattering photons from the laser electric field and directly leads to the optical dipole force that is used to trap and repel atoms. Additionally, by equating the purely imaginary components of equation 2.8, one arrives at the atom energy shift due to absorbing photons from the laser field and leads immediately to the radiation force, which permits the cooling of atoms in an optical molasses and leads to more effective cooling by means of a magneto-optical trap.

2.1.2 Optical Dipole Force

By equating the purely real components of both sides of equation 2.8, we arrive at an expression for the effective potential V_g:

$$V_g = -\frac{\hbar\delta}{2}\frac{\Omega^2}{\delta^2+\Gamma_e^2/4}. \tag{2.9}$$

This effective potential V_g is called the optical dipole potential [72] and while not obvious in this form, V_g permits atom trapping at the maxima of an intense laser beam. To see this, some simple algebra is used to rewrite equation 2.9 in a form that is more enlightening to the experimentalist:

$$\begin{aligned} V_g = -\frac{\hbar\delta}{2}\frac{\Omega^2}{\delta^2+\Gamma_e^2/4} &= -\frac{\hbar}{2}\frac{\delta}{\delta^2+\Gamma_e^2/4}\frac{|\langle g|\hat{\mathbf{d}}\cdot\hat{\boldsymbol{\epsilon}}|e\rangle|^2}{\hbar^2}E^2 \\ &= -\frac{3}{2}\frac{\pi c^2}{\omega_0^3}\left(\frac{\delta}{\delta^2+\Gamma_e^2/4}\right)\epsilon_0 c E^2\left(\frac{|\langle g|\hat{\mathbf{d}}\cdot\hat{\boldsymbol{\epsilon}}|e\rangle|^2}{3\hbar c^3\pi\epsilon_0}\omega_0^3\right) \end{aligned} \tag{2.10}$$

where c is the velocity of light, $\omega_0 = \omega_e - \omega_g$, and ϵ_0 is the permittivity of free space. Some identities can be used to further simplify this result. We first use that the intensity $I(x)$ of an electromagnetic wave with amplitude E can be expressed as $I = c\epsilon_0 E^2$ [67]. Additionally, we use that linewidth of the excited state $|e\rangle$ can be alternatively expressed as $\Gamma_e = \omega_0^3|\langle g|\hat{\mathbf{d}}\cdot\hat{\boldsymbol{\epsilon}}|e\rangle|^2/3\hbar c^3\pi\epsilon_0$ [72]. Finally, the lasers used for dipole trapping in the experiments described in this dissertation (section 4.5.1 and 8.2.1) are detuned far[3] from resonance and hence we can state that $\delta^2 >> \Gamma_e^2$. Using these identities and the approximation $\delta^2 >> \Gamma_e^2$, we can write that the optical dipole potential imparted onto an atom by a far-detuned laser beam is

$$V_{dip} \approx -\frac{3}{2}\frac{\pi c^2}{\omega_0^3}\left(\frac{\Gamma_e}{\delta}\right)I(x). \tag{2.11}$$

Equation 2.11 shows that the optical dipole potential can be attractive (and trap atoms) or repulsive (and repel atoms) depending on the sign of the laser detuning (figure 2.1). It immediately follows that if the laser features a spatially varying intensity ($\nabla I(x) \neq 0$), then the atom will experience an attractive or repulsive force (depending on the sign of the laser detuning δ) directed towards or away from the laser intensity maximum given as

$$\mathbf{F}_{dip} = \frac{3}{2}\frac{\pi c^2}{\omega_0^3}\left(\frac{\Gamma_e}{\delta}\right)\nabla I(x). \tag{2.12}$$

The result $\mathbf{F}_{dip}$ of equation 2.12 is called the optical dipole force and is a very useful tool to trap (or repel) neutral atoms that have been previously cooled to milliKelvin temperatures or lower

[3] As described in chapters 4 and 5, we use a 1064 nm and 760 nm laser for dipole trapping and repelling of ^{133}Cs and ^{87}Rb atoms, respectively. That corresponds to detunings of order 10^{12} Hz for ^{133}Cs and 10^9 Hz for ^{87}Rb. For both types of atoms, the linewidths are of order 10^6 Hz, thus validating $\delta^2 >> \Gamma_e^2$.

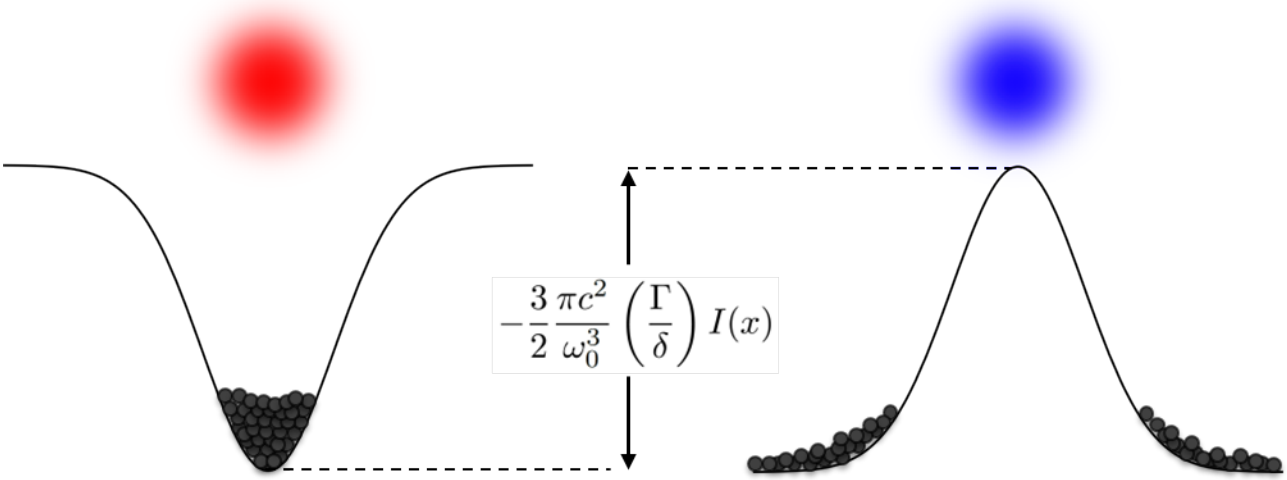

Figure 2.1: Optical Dipole Potential: Illustration showing how a laser beam red-detuned ($\delta < 0$) or blue-detuned ($\delta > 0$) from resonance can trap or repel atoms, respectively. For both cases, the function drawn is the potential energy curve V_{dip} as a result of the real component of the atom-photon interaction $-\hat{\mathbf{d}} \cdot \mathbf{E}$. For the red-detuned laser beam, the V_{dip} is a potential energy well and can trap sufficient cooled atoms, while for the blue-detuned case, V_{dip} is a potential energy barrier which can repel atoms. Both read and blue-detuned optical dipole potentials are relied on heavily throughout this dissertation.

[73]. The experimental consequences of equation 2.12 are frequently used throughout both experiments presented in this dissertation, most notably facilitating the optical trapping and transport of single neutral ^{133}Cs atoms (section 4.4 and 4.5) and for constructing and preparing atoms in the matterwave transistor oscillator potential (section 8.2 and 8.3).

2.1.3 Radiation Force

Returning to equation 2.8, if we instead equate the purely imaginary components, we immediately arrive at an expression for Γ_g, or the rate that atoms absorb a photon from the laser beam:

$$\Gamma_g = \frac{\Gamma_e}{2}\frac{\Omega^2}{\delta^2 + \Gamma_e^2/4} \tag{2.13}$$

where again, δ is the detuning of the laser beam from resonance. Now, for simplicity, consider a two-level atom placed in a one-dimensional light field produced by a single pair of counter propagating laser beams along the $\hat{x}$ direction (figure 2.2a). Since the atom receives $\hbar k$ momentum after absorbing a photon from the beam, the rate of change of momentum, or force, due to absorbing a quanta of light *from each laser beam* is then

$$\mathbf{F}_{rad} = \hbar\mathbf{k}\Gamma_g = \hbar\mathbf{k}\frac{\Gamma_e}{2}\frac{\Omega^2}{\delta^2 + \Gamma_e^2/4} \tag{2.14}$$

which is called the radiation force. Equation 2.14 is only valid when the atom in the laser field is at rest. In actual experiments in the lab, atoms are always moving with some non-zero velocity. An atom moving along the $+\hat{x}$ direction with velocity $\mathbf{v}$ will observe[4] the frequency of each laser beam (with wavenumber $\mathbf{k}$) to be Doppler shifted [74] by an amount $\mathbf{k}\cdot\mathbf{v}$ [75]. Thus, the radiation force[5] on an atom moving at velocity $\mathbf{v}$ due to a pair of counter-propagating laser beams is

$$\mathbf{F}_{rad} = \mathbf{F}_{-\hat{x}} + \mathbf{F}_{+\hat{x}} = \hbar\mathbf{k}\frac{\Gamma_e}{2}\left[\frac{\Omega^2}{(\delta + kv)^2 + \Gamma_e^2/4} - \frac{\Omega^2}{(\delta - kv)^2 + \Gamma_e^2/4}\right]. \tag{2.15}$$

For a red-detuned laser beam ($\delta > 0$), equation 2.15 imparts a velocity dependent, frictional force on the atoms [76] with the dependence on δ shown in figure 2.2b.

[4] This Doppler shift of the laser beams is observed by the atom in it's rest frame.
[5] The subscripts $\pm\hat{x}$ denote the force from each laser beam propagating in the $\pm\hat{x}$ direction.

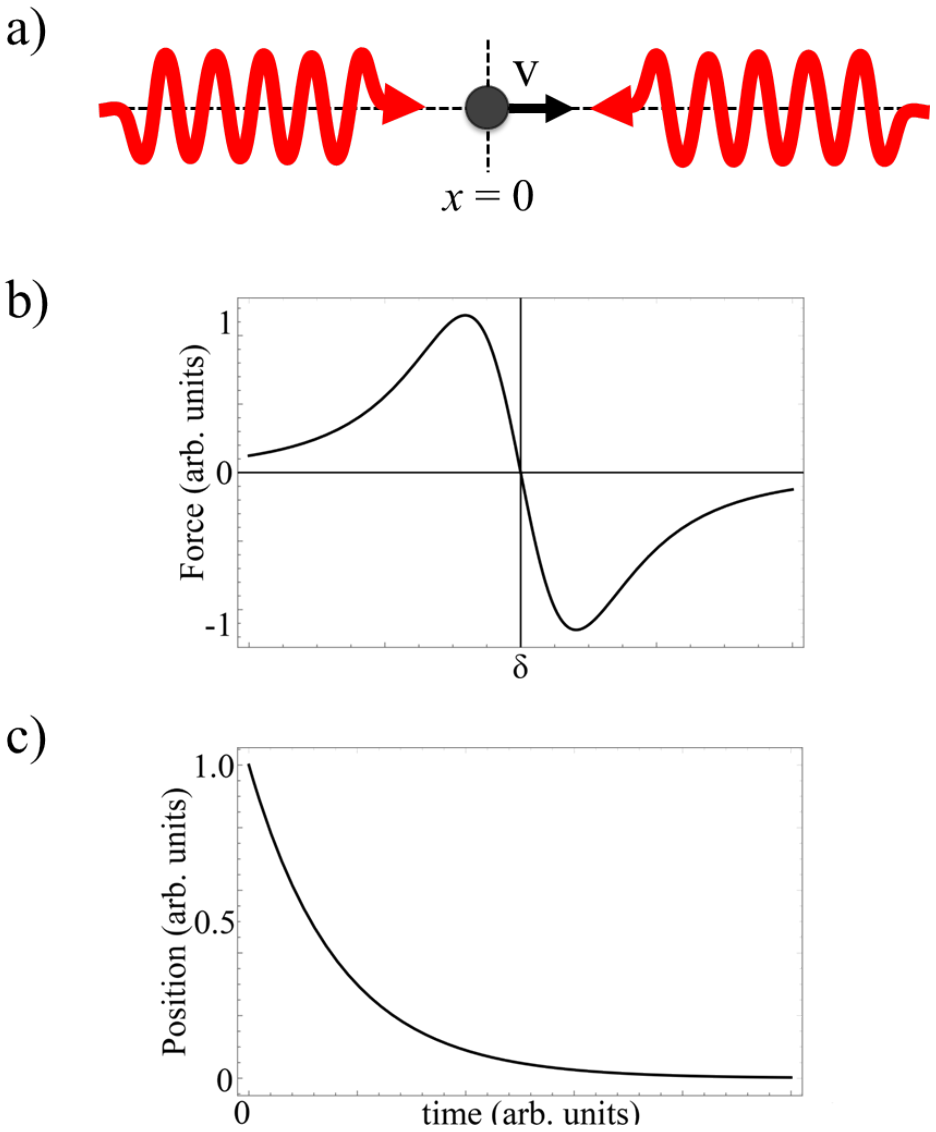

Figure 2.2: a) 1D configuration for optical molasses featuring two counter-propagating laser beams of equal intensity overlapping a the atom. b) Plot showing the radiation force $\mathbf{F}_{rad}$ from equation 2.15 that is imparted on an atom moving with velocity v in the $+\hat{x}$ from a pair of laser beams detuned from resonance by δ. The plot shows the maximum frictional force imparted to the atom occurs at a frequency detuning to the red ($\delta > 0$) of the atomic resonance. c) Solution to the equation of motion for an atom subjected to the radiation force from a pair of counter-propagating lasers when placed in an inhomogeneous magnetic field (equation 2.17) as described in section 2.1.4.

Physically, the radiation force occurs due to the Doppler effect: the atom absorbs (and scatters) more photons from the laser that propagates *against* the atom's motion because this light, if red-detuned in the lab frame by some amount δ, is subsequently blue-shifted in the atom frame back onto (or near) resonance with the $|g\rangle \leftrightarrow |e\rangle$ transition. Consequently, the atoms absorb far *less* light from the other laser beam (which propagates in the same direction of the atom) since in the atom frame this laser is Doppler shifted out of resonance. By red-detuning the lasers to the optimal δ (figure 2.2b), the radiation pressure from the laser light imparts a maximum frictional force, or optical molasses, that removes kinetic energy from the atoms, cooling them in the process. This method of laser cooling is called Doppler cooling, since it relies on the Doppler effect to systematically remove energy from atoms that move against a counter-propagating laser beam.

While the radiation force given in equation 2.15 has the capabilities of cooling atoms to a few hundred microKelvin, atom trapping with it is unstable as the radiation force $\mathbf{F}_{rad}$ is divergence-less.[6] Because $\nabla \cdot \mathbf{F}_{rad} = 0$, the radiation force cannot possibly be center-seeking at all points in space and consequently fails as a stable means to trap atoms [77]. The force given in equation 2.15 can be made stable by introducing a positionally dependent magnetic force *in addition* to the radiation force by placing the entire atom-radiation field system into an inhomogeneous magnetic field (figure 2.3a).

2.1.4 Magneto-Optical Trapping of Atoms

Consider a one-dimensional case where an atom is placed into a magnetic quadrupole field generated by anti-Helmholtz coils (figure 2.3a). The magnetic field $\mathbf{B}$ varies linearly along the $\hat{\mathbf{x}}$ direction with a gradient of magnitude $B' = \partial B/\partial x$. Due to the Zeeman effect [78], when the atom

[6] Because the electric field intensity (encapsulated in the Rabi frequency Ω) from the laser beam is Gaussian, the radiation force can be described more generally in cylindrical coordinates as

$$\mathbf{F}_{rad} \propto \frac{\hat{\mathbf{z}}}{z^2} e^{-r^2/z^2} + \hat{\mathbf{r}} \frac{r}{z^3} e^{-r^2/z^2}$$

and taking the divergence yields

$$\nabla \cdot \mathbf{F}_{rad} = \frac{1}{r}\frac{\partial}{\partial r}\frac{r}{z^3} e^{-r^2/z^2} + \frac{\partial}{\partial z}\frac{1}{z^2} e^{-r^2/z^2} = 0.$$

is located at position x in the magnetic field $\mathbf{B}$, the atomic energy levels change according to

$$\Delta E = g\mu_b m B' x \tag{2.16}$$

where g is the Lande g factor, μ_b is the Bohr magneton, and m is the magnetic quantum number of the atom. The important result of equation 2.16 is that magnetic field establishes a positionally dependent energy shift for the atom. Combining this with the discussion in section 2.1.3, given an atom moving with velocity $\mathbf{v}$ in an inhomogeneous magnetic field, the atomic transition $|g\rangle \rightarrow |e\rangle$ experiences an effective Doppler shift (in frequency units) of $\Delta\nu_{\text{dop}} = \pm kv$ as well as an additional Zeeman shift (in frequency units) of $\Delta\nu_{\text{zee}} = g\mu_b x B'/\hbar$. Therefore, when inserting values for the total detuning δ for the radiation force $\mathbf{F}_{rad}$ given in equation 2.15, one must consider the effects of both the Doppler shift of the laser light and the Zeeman shift of the atomic transition. In this case, the total radiation force on an atom becomes

$$\begin{aligned}\mathbf{F}_{rad} &= \hbar\mathbf{k}\frac{\Gamma_e}{2}\left[\frac{\Omega^2}{\left(\delta + kv + \frac{g\mu_b B'}{\hbar}x\right)^2 + \frac{\Gamma_e^2}{4}} - \frac{\Omega^2}{\left(\delta - kv - \frac{g\mu_b B'}{\hbar}x\right)^2 + \frac{\Gamma_e^2}{4}}\right] \\ &= -2\hbar\mathbf{k}\Gamma_e\left(\frac{\Omega^2\delta}{\left(\delta^2 + \frac{\Gamma_e}{4}\right)^2}\right)\left(kv + \frac{g\mu_b B'}{\hbar}x\right).\end{aligned} \tag{2.17}$$

With the result of equation 2.17, the radiation force $\mathbf{F}_{\text{rad}}$ is now proportional to *both* the velocity and position of the atom. In this instance, the divergence of $\mathbf{F}_{\text{rad}}$ is non-zero and in cases where $k^2 >> g\mu_b B'/\hbar$ (which is common in our cold atom experiments) the motion of an atom subjected this force is that of an overdamped harmonic oscillator (figure 2.2c). Thus, the radiation force in equation 2.17 permits the trapping of atoms in the minimum of the magnetic quadrupole field.

In order to ensure that atoms remain trapped, the radiation force must *always* be directed towards the B-field minimum (located at $x = 0$). This can occur by giving the counterpropagating lasers orthogonal, circular polarizations σ_+ and σ_- (figure 2.2a). The physics behind this trapping scheme is illustrated in figure 2.3b and is explained as follows: The atom in the $+\hat{x}$ region of the magnetic field will absorb the greatest amount of light from the σ_- beam due to the magnetic field Zeeman shifting the $m = -1$ magnetic sublevel much closer to resonance with the σ_- laser while

subsequently shifting the $m = +1$ magnetic sublevel further out of resonance with the σ_+ laser. Thus, when the atom is in the $+\hat{x}$ region, it experiences a net force *opposing* its motion. The opposite effect occurs when the atom is in the $-\hat{x}$ region of the magnetic field, as the atom absorbs a greater amount of the σ_+ laser and experiences a net force directed in the $+\hat{x}$ direction. Thus, the total net force is *always* directed towards the origin $x = 0$. This atom trapping configuration is called a magneto-optical trap (MOT) [79] and with it, we can cool atoms to the Doppler temperature limit, which corresponds to a temperature of 145.57 μK for ^{87}Rb and 125 μK for ^{133}Cs. The MOT is a ubiquitous tool in cold atom science and serves as the starting point for both experiments presented in this dissertation.

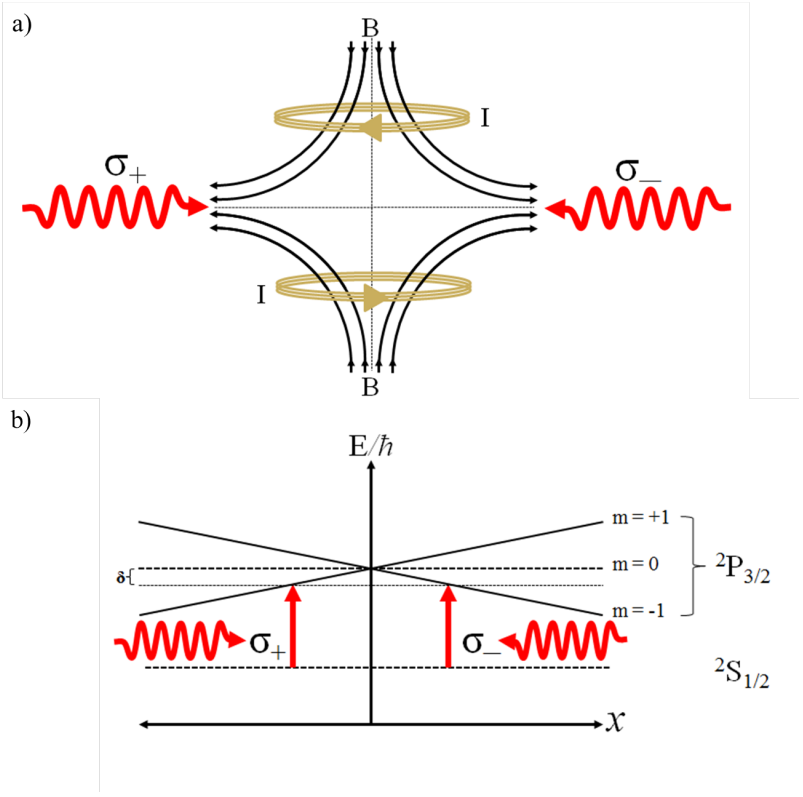

Figure 2.3: a) Schematic showing the setup of a 1D MOT. Current running in opposite directions through a pair of coils produces an anti-Helmholtz field with an approximate linear gradient B'. A pair of counter-propagating lasers with orthogonal, circular polarization overlaps the zero point of the B-field. b) Energy level diagram showing how the spatially varying B-field Zeeman shifts the $m = \mp 1$ sublevel closer to resonance with the $\sigma_\mp$ laser when in the $\pm\hat{x}$ region of the B-field. Thus, the atom is always experiencing a net force directed towards the zero point of the B-field.

2.1.5 Sub Doppler Cooling with σ_+/σ_- Polarization Gradients

Using the laser cooling methods described in section 2.1.4, we can create a MOT of approximately 10^9 ^{133}Cs or ^{87}Rb atoms but only cool them to their respective Doppler temperature limits of 125 μK and 145.57 μK [80]. These temperatures are too hot to achieve any of the experimental goals of this dissertation. In order to further cool our atoms to between 10-20 μK, we continuously remove more kinetic energy from the atoms by utilizing polarization gradient cooling (PGC) [81].

To understand the key physics of PGC that leads to cooler temperatures than the Doppler limit, we must abandon the simple two-level atom model and consider that real atoms have multiple ground states. As a simple example, consider an atom with a triplet ground state ($J_g = 1$) coupled to a quintuplet excited state ($J_e = 2$) in a region with no external magnetic field[7] . Since the cooling lasers are red-detuned from resonance, atoms absorb more light from the laser beam they are propagating *against* (as described in section 2.1.3). Thus, in the one-dimensional setup with no external magnetic field (figure 2.4a), an atom moving with positive velocity $v > 0$ absorbs considerably more light from the σ_- laser than the σ_+ laser.

As a result, there is a considerably greater population of atoms optically pumped to the $|m = -2\rangle$ magnetic sublevel than the $|m = +2\rangle$ sublevel (figure 2.4b), creating an unbalanced radiation pressure and subsequently a net frictional force directed in the propagation direction of the σ_- laser. The opposite effect occurs when the atoms move with negative velocity $v < 0$ (figure 2.4c). Therefore, the σ_-/σ_+ polarization gradient creates a net damping force that would (theoretically) continue until the atoms absorb both σ_- and σ_+ beams with equal efficiency. This additional damping mechanism is capable of removing energy well below the Doppler limit because the actual atom cooling in σ_-/σ_+ PGC is a direct result of a population imbalance of magnetic sublevels and not *purely* from a Doppler shift [83] (such as cooling in section 2.1.3). The lowest obtainable temperature is limited by the recoil energy atoms gain when emitting a photon during the cooling process. This temperature limit, called the recoil limit, corresponds to $T = 198$ nK and $T = 180$ nK for ^{133}Cs and ^{87}Rb atoms, respectively [84].

[7] It should be noted that this method of PGC is suppressed when atoms are in an external magnetic field [82].

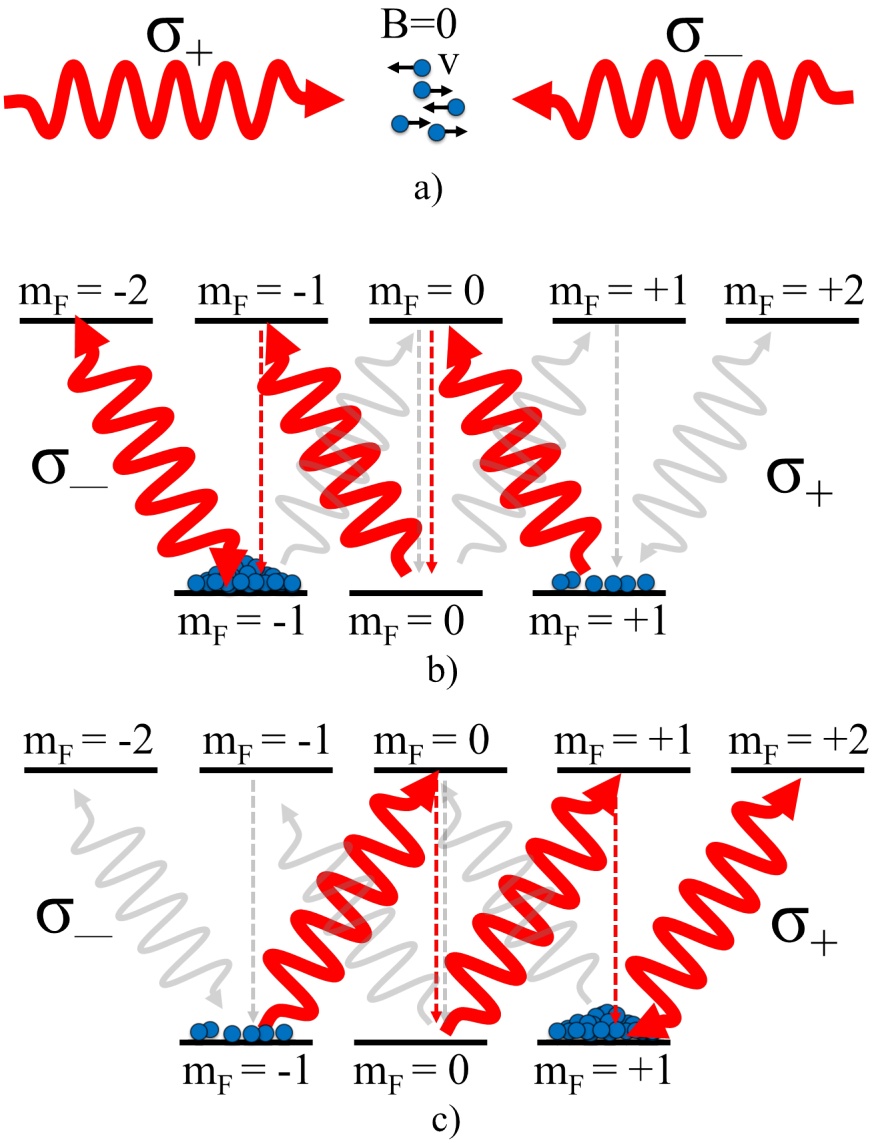

Figure 2.4: a) Digram showing the 1D σ_-/σ_+ PGC mechanism setup. b) Atoms moving against the σ_- laser feature a greater probability of absorbing the σ_- beam and are preferentially pumped to the $m = -2$ Zeeman sublevel over the $m = +2$ sublevel (this population imbalance of optical pumping is illustrated by thick, red lines for the dominant absorption path and dim grey lines for the less common absorption path). c) The reverse outcome occurs when atoms move against the σ_+ laser beam. The population imbalance of the Zeeman sublevels creates an unbalanced radiation pressure and subsequently establishes a net frictional force directed *against* the atom's motion.

2.2 Cooling Further to Degeneracy

The laser cooling and trapping methods outlined in section 2.1 are used in this dissertation to cool ensembles of both ^{133}Cs and ^{87}Rb to about 10-20 μK (see sections 4.3.3 and 8.2.2). This temperature is sufficiently cold enough for the IARPA single atom transport and loading experiments but is still too warm by orders of magnitude for the ultracold matterwave transistor. In that experiment, ensembles of ^{87}Rb atoms must be cooled to approximately 50 nK, which is beyond the capabilities of the laser cooling methods outlined in this dissertation. Furthermore, the phase space density of the atoms must be high enough such that the ^{87}Rb atoms transition into a Bose-Einstein condensate (BEC). In order to reach BEC, pre-cooled atoms (by means of PGC described above) are confined to a harmonic magnetic potential produced on an atom chip[8] and then cooled to degeneracy by performing forced radio-frequency (RF) evaporative cooling. The remaining sections of chapter 2 outline the basis for understanding the final stages of producing ultracold ^{87}Rb atoms on an atom chip for the matterwave transistor oscillator experiments (chapters 7 and 8).

2.2.1 Magnetic Trapping Interaction

Consider a neutral atom placed in a magnetic field. The potential[9] energy between the atom's magnetic moment $\hat{\boldsymbol{\mu}}$ and the external magnetic field $\mathbf{B}$ is given by the Zeeman effect as

$$U = -\hat{\boldsymbol{\mu}} \cdot \mathbf{B} = m_f g_F \mu_B B \tag{2.18}$$

where m_f is the z-component of the atomic angular momentum (or magnetic quantum number), g_F is the Landé-g factor, and μ_B is the Bohr magneton[10] . If the magnetic field is spatially varying, then the atom experiences a force given by the gradient of equation 2.18:

$$F = -\nabla U = \nabla(\hat{\boldsymbol{\mu}} \cdot \mathbf{B}) = -m_f g_f \mu_B \nabla B \tag{2.19}$$

[8] Specifics of the atom chip used for the experiments in this dissertation is covered in-depth in section 3.3

[9] While this interaction is very weak, magnetically trapping atoms provides a very efficient method to compress and manipulate previously cooled atoms into a Bose-Einstein condensate [85].

[10] Where the Bohr magneton is $\mu_B = e\hbar/2m_e$ where e and m_e are the charge and mass of the electron.

The magnetic force can be attractive (thus strong-field seeking) or repulsive (weak-field seeking) depending on the sign of $m_f g_F$. This is very important for carrying out magnetic trapping experiments as all magnetic fields are divergenceless ($\nabla \cdot \mathbf{B} = 0$), which means they do not feature a local maximum. This renders strong-field seeking magnetic potentials useless as a means to magnetically trap neutral atoms. Thus, the potential in equation 2.18 *must* be made to be a repulsive, weak-field seeking potential. We can satisfy this requirement experimentally (section 8.2.2) by optically pumping the atoms into a magnetic sublevel where $m_f g_F < 0$. With $U = -\hat{\boldsymbol{\mu}} \cdot \mathbf{B} < 0$ fulfilled, atoms can now be magnetically trapped but *only* if the external magnetic field $\mathbf{B}$ features a local minimum. Magnetic fields featuring such localized minima suitable for atom trapping in the transistor oscillator experiments (as well as how the fields are experimentally created with an atom chip) are detailed in sections 3.3.1 and 3.3.2.

2.2.2 Radio Frequency Evaporation

Using the methods of section 2.1.5 and 2.2.1, an ensemble of atoms at a temperature of approximately 10-20 μK can be prepared in a harmonic magnetic trap. To further cool the atoms such that their phase space density is high enough to form a BEC, we use a process called radio frequency (RF) evaporation to continuously remove the warmest atoms from the magnetic trap, leaving only the "coldest of the cold" to remain in the magnetic potential. Consider an ensemble of ^{87}Rb atoms optically pumped to a magnetic trapping sublevel, such as $|F = 3, m_F = 2\rangle$ (figure 2.5). To lower the temperature of this trapped atom ensemble, RF radiation with frequency ω_{RF} irradiates the atoms. Since the energy difference between adjacent Zeeman sublevels in the magnetic potential is approximately[11] $\Delta E = g_F \mu_B B$, RF photons that are tuned to the frequency

$$\omega_{RF} = g_F \mu_B B / \hbar \tag{2.20}$$

induce RF spin flips where atoms undergo multi-photon transitions from the $|m_F = +2\rangle$ trapped state to the $|m_F = -2\rangle$ anti-trapped state and are subsequently scattered from the trap (figure

[11] This relation only holds for cases where the magnetic field strengths are small. An analysis of RF evaporative cooling in large magnetic fields is covered in reference 21.

2.5a). Consequetly, by sweeping the RF frequency $\omega_{\rm RF}$ from infinity down to some arbitrary $\omega_{\rm flip}$, atoms with energy above $\hbar\omega_{\rm flip}$ will be pumped from the $|m_F = +2\rangle \rightarrow |m_F = -2\rangle$ magnetic sublevel and subsequently expelled from the trap (figure 2.5a). This process permits *selectively* removing warmer atoms above a certain energy in the magnetic potential *without* changing the tightness of the trap, allowing for efficient rethermalization. The expelled atoms carry away energy, leaving the atom ensemble at a reduced temperature. By continuously ramping $\omega_{\rm RF}$ lower and lower, forced RF evaporation can maintain a high cooling rate by regularly removing the hottest atoms in the trap as long as the RF sweeping speed is slow enough to allow the remaining cooler atoms time[12] to rethermalize. RF evaporation and rethermalization is repeated until the atom phase space density is high enough for a BEC. Shown in section 8.2.4, we use RF evaporation to cool 20 μK atoms to energies 10-20 kHz above the trap bottom, which then condense into a 50 nK BEC.

[12] The phenomenon of runaway evaporation, which is the maximum efficiency of RF evaporative cooling, occurs when the time per collision, $\tau_{\rm col}$, *decreases* as the atom ensemble cools. Runaway evaporation emerges when the trap tightness and RF sweeping rate are such that $\tau_{\rm trap}/\tau_{\rm th} \gtrapprox 100$ where $\tau_{\rm trap}$ is the $1/e$ lifetime of the magnetic trap.

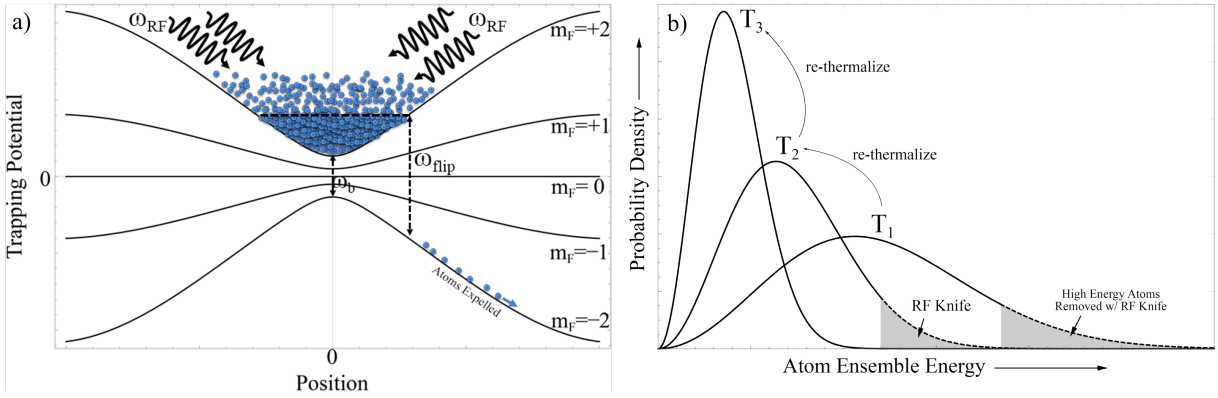

Figure 2.5: a) Illustration of the RF evaporation process. An ensemble of atoms is initially pumped to the $|m_F = +2\rangle$ trapping state and confined in a magnetic potential. The RF photon frequency is the swept from infinity down to $\omega_{\rm flip}$. All atoms with energy above the energy corresponding to the $\omega_{\rm flip}$ RF photons (pictured above the thick dotted line) undergo spin flips and are pumped to the $|m_F = -2\rangle$ anti-trapping state and expelled from the trap. By continuing the RF sweep down to just above the trap bottom ω_b, only the coldest of the cold atoms will remain in the trap and can undergo transition into a Bose-Einstein condensate. b) Illustration showing how each RF knife sweep removes the outer tails of the Maxwell-Boltzmann distribution of the trapped atom ensemble. By continuously cutting out the hottest atoms while allowing rethermalization time, the RF evaporation process leaves a large enough density of atoms at low temperature to result in a high enough phase space density for Bose-Einstein condensation to occur.

2.2.3 Reaching Bose-Einstein Condensation

For the experiments in this dissertation, RF evaporation is the final stage to condensing atoms into a BEC. For the transition from a gas to a BEC to occur during evaporation, the de Broglie wavelength

$$\lambda = \frac{h}{p} = \frac{h}{\sqrt{3mkT}}. \tag{2.21}$$

of each atom with momentum p and temperature T must become larger than the inter-atomic spacing of the gas. That is, the phase space density, PSD must be greater than unity

$$\text{PSD} \equiv \lambda^3 n \geq 1 \tag{2.22}$$

where n is the number of atoms per unit volume. Equation 2.21 reveals that as the gas is cooled, the de Broglie wavelength of each atom increases, eventually reaching a critical temperature T_c whereby the de Broglie waves of each atom begin to overlap. By cooling the gas even further to the ultracold regime ($T << T_c$), the de Broglie wavelength of each atom becomes so large that all of the atom de Broglie waves completely overlap, rendering each atom of the gas indistinguishable (figure 2.6). At this temperature, nearly the entire gas has condensed into a BEC that must be treated quantum mechanically and is described *en masse* according to the Bose-Einstein[13] distribution.

[13] For temperatures where the de Broglie wavelengths of each atom are much smaller than the inter-atomic spacing d between each atom, the particles are *distinguishable* from each other and hence the gas behaves classically and is described with Maxwell-Boltzmann statistics.

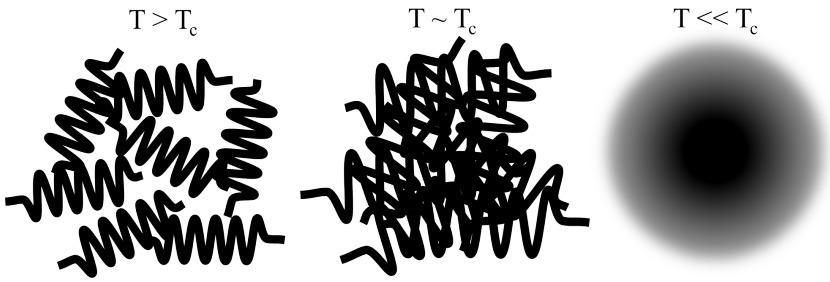

Figure 2.6: Illustration depicting the overlap of de Broglie waves as atoms are cooled from above the critical temperature T_c to well below it. As $T << T_c$, the de Broglie waves overlap so much that all atoms are completely indistinguishable from one another.

In order to gain a fundamental understanding of the onset of a BEC from trapped ultracold atoms (with respect to the transistor oscillator experiment) we examine the phase transition with the constraint that the atoms are not interacting with each other. After an RF evaporation and rethermalization sequence (section 2.2.2), consider an ensemble of atoms in a state of thermal equilibrium at temperature T and chemical potential μ in a magnetic potential. The average occupancy $\overline{n}$ of a state with energy ϵ is described by the Bose-Einstein distribution:

$$\overline{n}(\epsilon) = \frac{1}{e^{(\epsilon-\mu)/kT} - 1}. \tag{2.23}$$

Moreover, in the transistor oscillator experiment described in chapters 7 and 8 of this dissertation, the cold atom gas is confined to an anisotropic harmonic oscillator potential given as

$$V(x, y, z) = \frac{1}{2} m \left(\omega_x^2 x^2 + \omega_y^2 y^2 + \omega_z^2 z^2\right) \tag{2.24}$$

where m is the mass of each atom and the ω_i represents the atom oscillation frequencies along the $i = \hat{x}, \hat{y}, \hat{z}$ axis of the potential. The corresponding energy levels of the anisotropic potential are

$$\epsilon(n_x, n_y, n_z) = \underbrace{\left(n_x + \frac{1}{2}\right)\hbar\omega_x}_{\epsilon_x} + \underbrace{\left(n_y + \frac{1}{2}\right)\hbar\omega_y}_{\epsilon_y} + \underbrace{\left(n_z + \frac{1}{2}\right)\hbar\omega_z}_{\epsilon_z} \tag{2.25}$$

where n_x, n_y and n_z are integers. Each atom thus has an energy ϵ_x, ϵ_y and ϵ_z due to oscillation along the respective axis. The energy of this system (equation 2.25) is plotted in figure 2.7 and the number of available energy states of this system when the atom has total energy $\epsilon = \epsilon_x + \epsilon_y + \epsilon_z$ is readily given by the integral[14]

$$\eta(\epsilon) = \frac{1}{\hbar^3\omega_x\omega_y\omega_z} \int_0^{\epsilon} d\epsilon_x \int_0^{\epsilon-\epsilon_x} d\epsilon_y \int_0^{\epsilon-\epsilon_x-\epsilon_y} d\epsilon_z = \frac{\epsilon^3}{6\hbar^3\omega_x\omega_y\omega_z}. \tag{2.26}$$

It immediately follows that the density of states, or the number of available energy states between ϵ and $\epsilon + d\epsilon$ is

$$g(\epsilon) = \frac{d\eta(\epsilon)}{d\epsilon} = \frac{\epsilon^2}{2\hbar^3\omega_x\omega_y\omega_z}. \tag{2.27}$$

[14] The integral $\eta(\epsilon)$, and hence the number of available energy states in the anisotropic potential, is merely the volume of first octant of figure 3 bounded by the plane $\epsilon = \epsilon_x + \epsilon_y + \epsilon_z$.

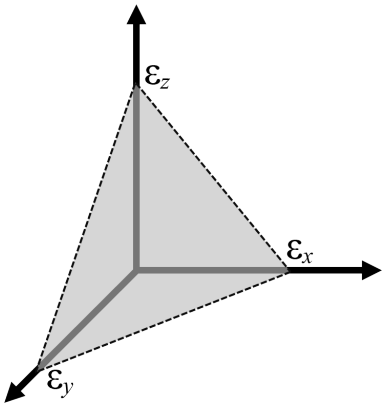

Figure 2.7: Plot in "energy space" showing the energy of an atom in the anisotropic harmonic oscillator as a function of occupying the n_x, n_y, and n_z energy levels. Note that for an atom occupying some arbitrary energy state $\epsilon(n_x, n_y, n_z)$, the total atom energy is a plane $\epsilon = \epsilon_x + \epsilon_y + \epsilon_z$.

Knowing the density of states (equation 2.27), as well as the Bose-Einstein distribution (equation 2.23), one can readily determine the experimental conditions on atom temperature T and trapped atom number N where all atoms of the gas are in an excited state (meaning the ensemble temperature is exactly at criticality T_c). For this simplified case of a non-interacting gas, the number of particles in the excited state N_{ex} reaches a maximum when the chemical potential $\mu = 0$. That is

$$\begin{aligned} N_{\text{ex}}(\mu = 0, T_c) &= \int_0^\infty g(\epsilon)\overline{n}(\epsilon)d\epsilon \\ &= \frac{1}{2\hbar\omega_x\omega_y\omega_z}\int_0^\infty \frac{\epsilon^2}{e^{\epsilon/kT_c} - 1}d\epsilon \\ &= \frac{k^3T_c^3}{2\hbar\omega_x\omega_y\omega_z}\Gamma(3)\zeta(3) \end{aligned} \tag{2.28}$$

where $\Gamma(n)$ and $\zeta(n)$ are the Gamma and Riemann zeta functions, respectively. Rearranging equation 2.28 and solving for T_c gives the critical temperature

$$T_c = \hbar k N^{1/3}\left[\frac{\omega_x\omega_y\omega_z}{\Gamma(3)\zeta(3)}\right]^{1/3} \approx 0.94\hbar\overline{\omega}N^{1/3} \tag{2.29}$$

where for $T > T_c$ all atoms in the gas are in an excited state. It immediately follows that if the atom ensemble is cooled lower than T_c, atoms begin to abruptly occupy the anisotropic harmonic potential ground state, which is the onset of Bose-Einstein condensation. By cooling the atom temperature $T << T_c$, one achieves a macroscopic occupation of the harmonic oscillator ground state and can produce a pure BEC.

2.3 Collisions Between Pairs of Low Energy Atoms in a BEC

While section 2.2.3 gives a very good description of the key characteristics of the BEC, it does not address any interactions or collisions between atoms in the ultracold ensemble. In the theory and experimental progress of the ultracold transistor oscillator (chapter 7 and 8), interactions between low energy, ultracold atoms are not only omnipresent, but they drive the matterwave gain mechanism and *must* be accounted for. Specifically, the interactions that we must address are binary elastic scattering events between pairs of atoms with very small total energy. By small, we mean that the scattering process is dominated by the s-wave contribution to the wavefunction[15] . For s-wave scattering of indentical bosons, the scattering cross section is $\sigma = 8\pi a^2$ where a is the scattering length given in the Born approximation [70] as

$$a = \frac{m_r}{2\pi\hbar^2} \int e^{i(\mathbf{k}'-\mathbf{k})\cdot\mathbf{r}} V(\mathbf{r}) d^3\mathbf{r} \tag{2.30}$$

where m_r is the reduced mass of the two atoms, $V(\mathbf{r})$ is the effective two-body interaction and where $\mathbf{k}$ and $\mathbf{k}'$ are the wave vectors of the atom before scattering and after scattering, respectively. Because the interactions here are due to s-wave scattering, the momentum transfer $\hbar\mathbf{k}' - \hbar\mathbf{k}$ due to the scattering process is approximately zero. Thus, equation 2.30 can be approximated as

$$a = \frac{m_r}{2\pi\hbar^2} \int V(\mathbf{r}) e^{i(\mathbf{k}'-\mathbf{k})\cdot\mathbf{r}} d^3\mathbf{r} \approx \frac{m}{4\pi\hbar^2} \int V(\mathbf{r}) d^3\mathbf{r}. \tag{2.31}$$

The effective two-body interaction $V(\mathbf{r}, \mathbf{r}')$ between identical atoms at points $\mathbf{r}'$ and $\mathbf{r}$ in equation 2.31 is treated as a discrete contact interaction

$$V(\mathbf{r}', \mathbf{r}) = g\delta(\mathbf{r}' - \mathbf{r}) \tag{2.32}$$

where g denotes the energy of the interaction (defined shortly) and $\delta(\mathbf{r}' - \mathbf{r})$ is the Dirac delta function.

[15] That is, we only consider components of each atom's wavefunction with orbital angular momentum $l = 0$. As a result, the total scattering cross section σ drastically simplifies to

$$\sigma = \frac{4\pi}{k^2} \sum_{l=0}^{\infty} (2l+1) \sin^2 \delta_l \rightarrow \frac{4\pi}{k^2} \sin^2 \delta_0$$

where δ_l is the phase shift experienced by the $l = 0$ partial wave due to the scattering event.

Inserting equation 2.32 into equation 2.31, one arrives at the scattering length between two atoms in the BEC as

$$a \approx g\frac{m}{4\pi\hbar^2}\int \delta(\mathbf{r}' - \mathbf{r})d^3\mathbf{r} = g\frac{m}{4\pi\hbar^2}. \tag{2.33}$$

Using the result of equation 2.33, we can write the very important result that the effective interaction between two colliding atoms at low energy in the BEC is constant and is given by

$$g = \frac{4\pi\hbar^2 a}{m}. \tag{2.34}$$

Equation 2.34 is essential to the transistor oscillator theory and its implications will be used frequently throughout the remainder of chapter 2 as well as chapters 7 and 8 of this dissertation.

2.3.1 BEC Many-Bodied Hamiltonian and Gross-Pitaevskii Equation

Given that there are N interacting atoms in the BEC, the BEC is described with a many-bodied Hamiltonian

$$H = \sum_{i=1}^{N}\left[-\frac{\hbar^2}{2m}\nabla_i^2 + V(\mathbf{r}_i)\right] + g\sum_{i<j}\delta\left(\mathbf{r}_i - \mathbf{r}_j\right). \tag{2.35}$$

Using this many-bodied Hamiltonian in the Schrödinger equation yields the Gross-Pitaevskii equation [86]:

$$\left[-\frac{\hbar^2}{2m}\nabla^2 + V(\mathbf{r}) + g|\psi(\mathbf{r})|^2\right]\psi(\mathbf{r}) = \mu\psi(\mathbf{r}) \tag{2.36}$$

where the eigenvalue $\mu = \partial E/\partial N$ is the BEC chemical potential and $\psi(\mathbf{r})$ is the total wavefunction for a system of N indistinguishable bosons making up the BEC, which is given as

$$\psi(\mathbf{r}) = \psi_1(\mathbf{r}_1)\psi_2(\mathbf{r}_2)...\psi_N(\mathbf{r}_N) \tag{2.37}$$

where $\mathbf{r}_i$ refers to the position of the ith boson in the BEC. The Gross-Pitaevskii equation is a form of the Schrödinger equation that consists of a linear contribution from the external potential $V(\mathbf{r})$ confining the atoms and a non-linear contribution $g|\psi(\mathbf{r})|^2$ modeling the averaged, or mean field, interaction with all of the other atoms in the BEC. An important approximation can be

made to equation 2.36 when the kinetic energy of the atoms is much less than the mean-field[16] . In such cases, the kinetic energy operators $-\hbar^2\nabla_i^2/2m$ are ignored, which reduces the Gross-Pitaevskii equation to the much simpler

$$\left[V(\mathbf{r}) + g|\psi(\mathbf{r})|^2\right]\psi(\mathbf{r}) = \mu\psi(\mathbf{r}). \tag{2.38}$$

This result is called the Thomas-Fermi approximation and equation 2.38 has the solution

$$|\psi(\mathbf{r})|^2 = \frac{\mu - V(\mathbf{r})}{g}. \tag{2.39}$$

Equation 2.39 is very important as it gives the atom density profile of a BEC. It states that in the Thomas-Fermi approximation, atoms condensed into a BEC fill the external trapping potential $V(\mathbf{r})$ uniformly up to the condensate chemical potential μ [87].

2.3.2 BEC Characteristics in the Thomas-Fermi Approximation

In the transistor oscillator theory and experiments described in chapters 7 and 8 this thesis, the external trapping potential is harmonic along the $\hat{x}$, $\hat{y}$, and $\hat{z}$ axes. From equation 2.39, the atomic density n of the BEC is an inverted parabola (figure 2.8). In the transistor oscillator experiments (chapter 8) observing this characteristic inverted parabola profile for the atom density establishes that the atoms have reached Bose-Einstein condensation. The radius R (in position space) of the BEC, or Thomas-Fermi radius, is defined as the distance from the center of the condensate to the position $\mathbf{r}$ that satisfies $\mu = V(\mathbf{r})$. Atoms located within this radius are Bose-condensed while atoms outside the radius remain as thermal atoms. For a harmonic potential $V(r) = m\omega^2 r^2/2$, the Thomas-Fermi radius, R is readily calculated as

$$R = \sqrt{\frac{2\mu}{m\omega}}. \tag{2.40}$$

[16] At equilibrium, the mean-field pseudopotential and the external potential are both proportional to R^2, while the kinetic energy is proportional to $1/R^2$. Additionally, the mean-field increases linearly with atom number N. Thus for atom numbers of $N > 10^4$ (which is very common in the ultracold atom experiments performed in chapters 7 and 8 of this dissertation) we can accurately state that the kinetic energy of atoms in the BEC is indeed negligible compared to V and g.

The number of atoms in the condensate can be found by inserting the harmonic potential into the solution to the Gross-Pitaevskii equation (equation 2.39) giving

$$\begin{aligned} |\psi(\mathbf{r})|^2 &= \frac{m\mu}{4\pi\hbar^2 a}\left(1 - \frac{1}{2}\frac{m\omega^2 r^2}{\mu}\right) \\ &= \frac{m\mu}{4\pi\hbar^2 a}\left(1 - \frac{r^2}{R^2}\right). \end{aligned} \tag{2.41}$$

Integration over the radial coordinate from the origin to the Thomas-Fermi radius R gives the total atom number in the BEC as a function of the chemical potential μ:

$$\begin{aligned} N = \int |\psi(\mathbf{r})|^2 d\mathbf{r} &= \frac{m\mu}{4\pi\hbar^2 a}\int_0^R \left(1 - \frac{r^2}{R^2}\right) 4\pi r^2 dr \\ &= \frac{m\mu}{4\pi\hbar^2 a}\frac{8\pi}{15}R^3 \\ &= \frac{8\pi}{15}\left(\frac{2\mu}{m\omega^2}\right)^{3/2}\frac{\mu}{g} \end{aligned} \tag{2.42}$$

where in the final line of equation 2.42, the definitions of the Thomas-Fermi radius (equation 2.40) and the scattering length (equation 2.33) are used. Rearranging this result and solving for μ yields the Thomas-Fermi approximation for the BEC chemical potential:

$$\mu = \frac{\hbar\omega}{2}\left(\frac{15Na}{a'}\right)^{2/5} \tag{2.43}$$

where $a' = \sqrt{\hbar/m\omega}$. Equation 2.43 is used throughout the remainder of this dissertation when referring to the BEC chemical potential.

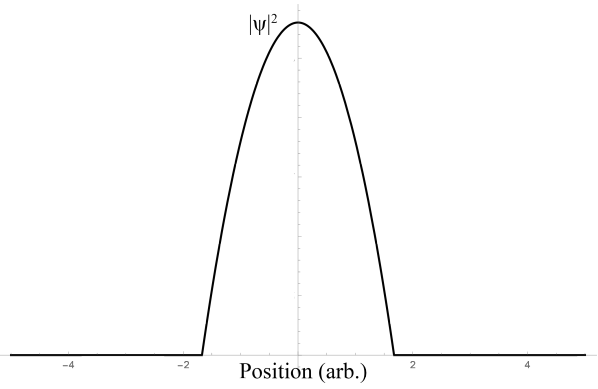

Figure 2.8: Density profile (and solution to the Gross-Pitaevskii equation) of the BEC in the Thomas-Fermi approximation when confined to a harmonic potential.

Chapter 3

Compact Ultra High Vacuum Systems for the Optical Conveyor Belt and Transistor Oscillator Experiments

The single atom transport and reloading experiments (chapter 4 and chapter 5) as well as the matterwave transistor oscillator experiments (chapter 8) are conducted in an ultra-high vacuum (UHV) environment, which corresponds to pressures below 10^{-10} Torr. While such laboratory environments have been available to scientists since the 1970s, the UHV systems custom designed specifically for the experiments in this dissertation are unique in that each can produce an UHV environment suitable for MOTs and BECs, all the while remaining small enough to carry on a commercial airplane. As an added bonus, the vacuum chamber for the atom transport experiments has the interesting design of containing no metal[1] nuts, bolts, or screws and is completely held together with optical and anodic bonds.

The goal of this chapter is to describe the structure and layout of two UHV systems constructed particularly for the work in this dissertation: one for the optical conveyor belt experiments (section 3.1) and the other for the transistor oscillator experiment (section 3.2). In both sections, we show how the UHV design assists in completing the scientific goals of each experiment. Components that play pivotal roles in achieving experimental results, such as the 2D and 3D MOT chambers, the Hex Cell (section 3.1.2, specific the atom transport system), and the atom chip (section 3.3, specific to the transistor oscillator system) are further described in detail and are referred to many times in subsequent chapters.

[1] This design constraint was implemented in order to eliminate any and all unwanted magnetic fields that would introduce noise into the Rydberg atom qubit gate operations performed by the UW Madison team (see section 1.2)

3.1 Atomic Qubit Array Cell

The first set of experiments in this dissertation, the transport and delivery of single atoms into optical bottle beam traps (chapters 4 and 5), is conducted in the Atomic Qubit Array (AQuA) Cell, and is shown in figure 3.1. This system is designed to provide a small footprint, portable, UHV environment with 6 windows of optical access in order to permit:

- Single atom transport and reloading into vacant optical bottle beam sites of the qubit array with an optical conveyor belt during simultaneously occurring qubit logic gate operations.
- Providing a continuous source of pre-cooled cesium atoms in an adjacent chamber for use in the atom transport and reloading procedure.
- Isolation between the atom production and dispenser region (a region of higher pressure) and the MOT, bottle beam, and atom transport regions (regions of UHV pressures).
- Multiple ion pumps assigned to different chambers of the vacuum system in order to permit differential pumping [88] between higher and lower pressure regions
- Apertures between each adjacent chamber such that atoms can be deterministically transported from the lower 2D and 3D MOT chambers into the hex cell using a movable optical molasses.

In order to achieve the above listed performances, the AQuA cell design was based off of a double MOT vacuum configuration [89] featuring a ^{133}Cs source region, a 2D MOT region, a 3D MOT region, and a hexagonal chamber featuring six windows with anti-reflection (AR) coating on both ambient and vacuum faces. The AQuA cell was fabricated at the Sarnoff Corporation where the entire vacuum system was constructed with no metal nuts, bolts, or screws and is entirely held together by over 50 optical contact bonds [90][91] and anodic bonds [92][93][94]. Even the ion pumps themselves are anodically bonded to the cell. Using a much larger vacuum pump in conjunction with a bakeout process, the AQuA cell was pumped down to UHV pressures at ColdQuanta. Details of the principle components of the AQuA cell are described briefly in the following sections.

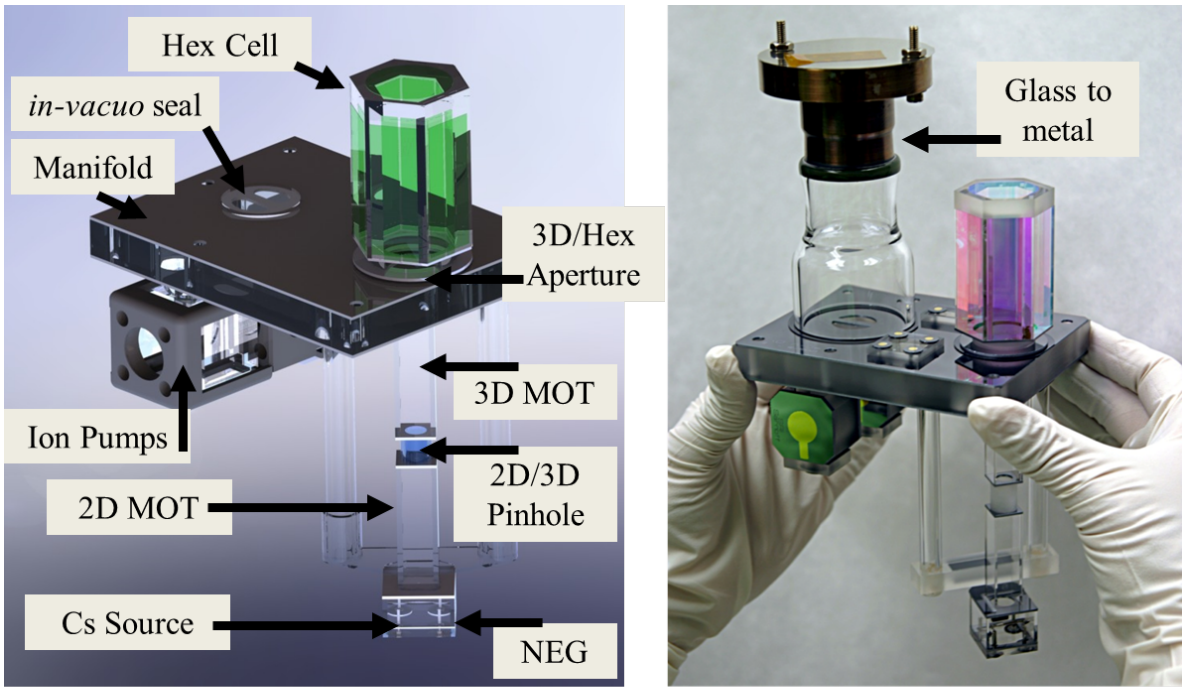

Figure 3.1: a) Schematic of the AQuA cell vacuum chamber, showing the locations of the three main regions of the device: the Cs source and 2D MOT region, the 3D MOT region, and the Hex cell. The location of the pinhole that isolates the 2D and 3D MOT chambers is shown. Additionally, the positions of the ion pumps and non-evaporable getters are also shown. The cell manifold serves as a mechanical foundation for the AQuA cell. The manifold is a 1 cm thick, machined Pyrex block that is polished on all faces. Channels are machined throughout the interior of the manifold to connect the 3D MOT chamber to the Hex cell and also to connect each ion pump to its respective pumping load. The long lever-arm aspect of the 2D and 3D MOT chamber leaves the cell very susceptible to vibrations. Therefore, two Pyrex support rods are fixed to the bottom of the 2D MOT chamber and are connected to the AQuA cell manifold. b) The AQuA cell prior to vacuum processing and bakeout being held with hands for scale. The glass to metal is used to connect the cell to a bakeout station. The final vacuum seal is completed by anodically bonding a Pyrex window *in-vacuo* (while still connected to the bakeout station) onto the cell manifold. The glass to metal is completely removed after pumping the AQuA cell down to UHV.

3.1.1 Cesium Source Chamber, 2D and 3D MOT Chambers

Shown in figure 3.2a, at the very bottom of the AQuA cell is the cesium source, which contains an SAES alkali metal cesium dispenser (figure 3.2b) that evaporates a nearly pure gas of ^{133}Cs into the 2D MOT chamber when the dispenser is heated above a critical temperature. The dispenser temperature is held constant by running an electrical current of 3.5 A through it at all times during the experiments. Additionally, a SAES non-evaporable getter (NEG) is also included inside the cesium source region for improved vacuum quality. Current is supplied to the dispenser and NEG via electrical feedthroughs connected to conductive silicon pads located on the bottom, ambient side of the source chamber (figure 3.2a and d).

Anodically bonded directly above the cesium source is the 2D MOT chamber, which is a 1 cm x 1 cm x 4.5 cm Pyrex vacuum chamber designed to support a 2D+ MOT from the background ^{133}Cs gas produced in the source. Because this chamber is filled with warm, cesium vapor, the pressure in this chamber is higher than UHV at approximately 10-100 nanotorr. The 2D MOT chamber is capped with a 500 μm thick silicon wafer that features a 750 μm diameter pinhole drilled in the center. As described in section 4.3.1, a 2D+ MOT loaded from this background vapor provides a transversely cooled beam of atoms that can be vertically transported to the 3D MOT (and also Hex cell) chamber by passing through the 2D-3D pinhole (figure 3.2c). Also separating the 2D and 3D MOT chambers is a Pyrex cylinder, which is bonded to the 2D MOT pinhole and contains an additional getter for improved vacuum quality. Anodically bonded to the top of this cylinder is the 3D MOT chamber, which has the same dimensions as the 2D MOT chamber and is also made of Pyrex. In order to have MOT lifetimes of 10-20 seconds, the 3D chamber must be kept at a lower pressure of approximately 0.1 nanotorr, which is orders of magnitude lower than the adjacent connecting 2D chamber pressure. Sufficient isolation between the high and low pressure MOT chambers is provided by the 2D-3D pinhole, as the 0.024 mL/sec conductance of the pinhole is negligible compared to the 0.4 L/sec pumping rate of the ion pumps (described in section 3.1.2). Because of the very low background pressure of 0.1 nanotorr in the 3D chamber, a 3D MOT cannot

be loaded from a background gas. Instead, a stream of pre-cooled 2D+ MOT atoms are pushed through the 2D-3D pinhole and into the 3D MOT chamber, where they are used to source the 3D MOT. This design of using a 2D MOT to directly source a 3D MOT in an entirely separate vacuum chamber is called a double-MOT cell and it improves the 3D MOT lifetime by decoupling the atom lifetime (which is set by the 3D chamber vapor pressure) from the MOT load time (which is set by the 2D chamber vapor pressure) [89]. Similar to the 2D MOT chamber, the 3D chamber is also capped with a silicon disc but features a larger pinhole with a 3.18 mm diameter. This pinhole is larger so that the 3D MOT itself can be transported vertically into the Hex cell (figure 6.1), located above the 3D MOT chamber. This entire source-2D-3D MOT vacuum ensemble is then anodically bonded to the AQuA cell manifold. Finally, we note that the magnetic fields that are required to make the 2D+ and 3D MOTs are produced with permanent magnets that are mounted on 3D printed braces that firmly mate to the outside of the MOT chambers (figure 3.2d).

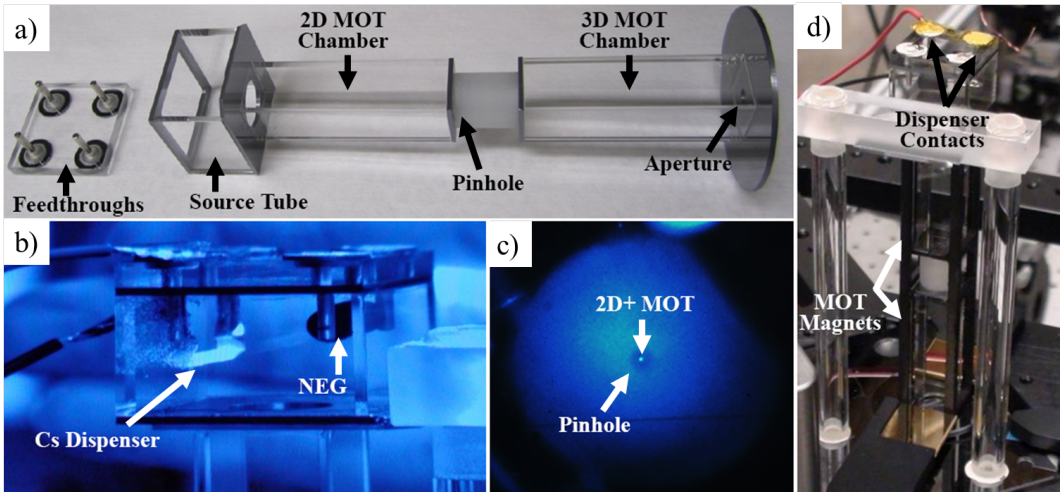

Figure 3.2: a) Anodically bonded source tube, 2D MOT, and 3D MOT chambers. The bottom of the source tube, which contains the conductive feedthroughs, is not yet anodically bonded to the chamber. b) Close up view of the AQuA Cell source tube showing the glowing Cs dispenser and the non-evaporable getter. The dispenser is glowing due to running 3.5 A through it in order to expel a cesium gas via thermal emission. c) View looking up vertically through the bottom of the source tube through the 2D MOT chamber where the bright dot in the center is fluorescence from a 2D+ MOT that centered on the 2D-3D pinhole. d) 2D and 3D MOT chamber with the permanent MOT magnets attached. The silver contacts that connect to the Cs dispenser are also shown.

3.1.2 Hex Cell

Located above the 3D MOT chamber is the most visually prominent feature of the AQuA cell: the six sided Hex Cell chamber (figure 3.3), which provides an UHV environment of less than 0.1 nanotorr with six faces of optical access and serves as the location for a majority of the single atom transport and reloading experiments as well as the qubit array and bottle beam trapping sites. The Hex cell walls are AR coated on all inside and outside faces for the 532, 780, 852, 1038, and 1064 nm wavelength lasers used in the qubit logic gate (from UW Madison) and single atom reloading experiments. The Hex cell is optically contact bonded to the top of the Pyrex manifold (figure 3.1) and is pumped by its own individual ion pump, separate from the 2D-3D ion pump. At the base of the Hex cell exists an elliptically shaped aperture that is aligned with the 2D-3D pinhole to allow the 2D+ MOT atoms to be transported directly into the Hex cell, bypassing the 3D chamber entirely, such that a small 3D MOT can be created in the Hex cell to serve as a cold atom reservoir for the single atom transport and reloading experiments (figure 4.7).

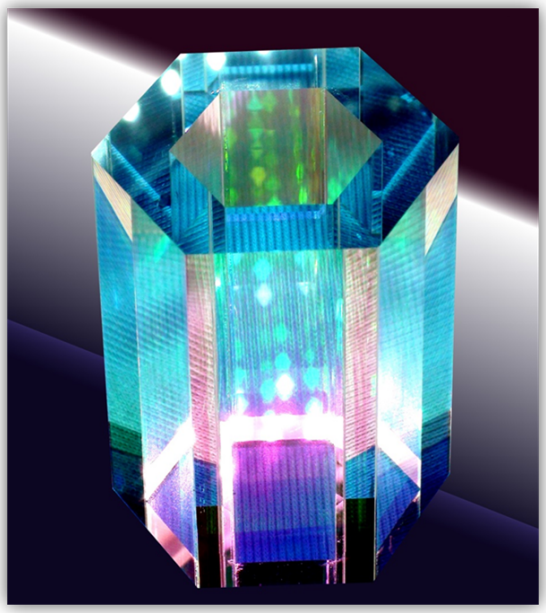

Figure 3.3: AQuA Hex cell, which serves as the location for the single atom transport and reloading experiments, as well as the location of the qubit array.

3.1.3 Anodically Bonded Ion Pumps

The AQuA cell features two 0.4 L/sec ion pumps that are constructed by anodically bonding each component together rather than using large nuts, bolts, screws, or epoxies. A schematic of the ion pumps is shown in figure 3.4a. The body of each ion pump is a machined Pyrex block that features two drilled out bore holes that are oriented at right angles to each other: one positioned horizontally and the other vertically. The principle components built around this Pyrex block are:

- The anode is formed by attaching a titanium cylinder to the inside of the Pyrex block that runs along the vertically oriented bore hole. A conductive rod is placed inside the horizontally oriented hole and is welded to the titanium cylinder. This rod extends all the way to the very left-most side of the ion pump which is capped with metalized conductive silicon. Electrical contact between the silicon and the rod is made with a metal spring which forms the anode feedthrough.

- The cathode is formed by capping the top and bottom of the pump with metalized conductive silicon. A small Pyrex ring is anodically bonded to each cathode. Placed in between this Pyrex ring and the cathode is a titanium disc that is slightly bowed, giving the disc spring-like properties and forming the cathode feedthrough.

- Connectivity between the anode and cathode is provided by the spring force present in the titanium disc. Due to its slight radius of curvature, the disc is constantly pushing on both the cathode and the titanium cylinder, which maintains constant electrical connectivity.

- Two neodymium magnets are mounted on the top and bottom cathodes to produce the magnetic field required for the ion pump to function. A custom Mu Metal box placed over the ion pumps provides magnetic shielding.

This entire ion pump apparatus is then anodically bonded directly to the Pyrex manifold foundation of the AQuA cell. The 1 cm thick Pyrex manifold features channels machined throughout its interior to connect the ion pumps to their respective vacuum load.

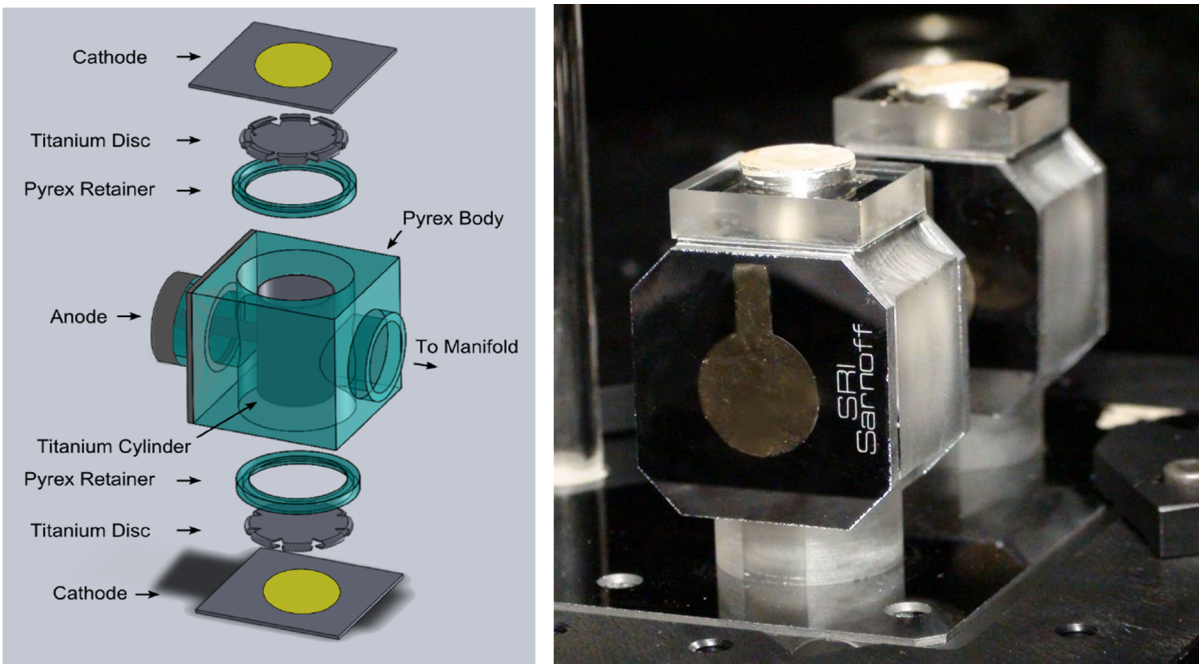

Figure 3.4: Left: Schematic showing the construction of the AQuA cell ion pumps. The body is made from a machined Pyrex block with tubular bore holes running horizontally and vertically through the Pyrex. A titanium cylinder is placed in the center. A metal rod is welded to the titanium cylinder and is connected to the silicon anode by a spring. The spring pushes on both the the rod and the andode and forms the anode feedthrough. The cathode is formed in a similar manner by using a bowed titanium disc to act as a spring to ensure a constant connection between the titanium cylinder and metalized silicon. The titanium disc forms the cathode feedthrough and forms an electrical connection between the anode and cathode. The opening on the right side of the Pyrex body is then anodically bonded to the AQuA cell manifold. Right: Completed AQuA cell ion pumps. Note that the ion pumps in this image are rotated 90 degrees from the given schematic. The metalized silicon forming the anode and cathode is clearly visible. The bottom of the pump is then anodically bonded to the AQuA cell manifold.

3.2 Atomtronics Double MOT Vacuum Cell

The UHV system, called the "atomtronics cell," used for the ultracold transistor oscillator experiments is also a double-MOT cell, although it is a different design. An image of the UHV cell and its principle components is shown in figure 3.5. The fundamental source-2D-3D chamber design described in section 3.1.1 for the AQuA cell is also used for the atomtronics cell.

- Similar to the AQuA cell system, the ^{87}Rb source for this cell is also an SAES alkali metal dispenser located at the base of the 2D MOT chamber. An NEG is included adjacent to the dispenser to improve vacuum quality.

- The 2D and 3D MOT chambers, made with Pyrex walls with dimensions of 2 cm x 2 cm x 4 cm, are larger than those of the AQuA cell. The ambient and vacuum side walls of the 3D MOT chamber are AR coated for 780 nm laser light.

- A major difference between the AQuA cell and the atomtronics cell is that an atom chip (section 3.3) is anodically bonded to the top of the 3D chamber and forms the upper surface of the cell. The atom chip, which described in section 3.3, is a major component in producing BECs with the atomtronics cell.

- Unlike the AQuA cell, the base of the 2D and 3D MOT chambers are attached to ConFlat flanges via glass-to-metal anodic bonds. The atomtronics cell is then held together by bolting each MOT chamber onto a spherical cube.

- Isolation between the 2D and 3D MOT chambers is provided by a 750 μm pinhole, which is drilled into a silicon wafer placed at the top of the 2D MOT chamber (see figure 3.5). The pinhole permits differential pumping between the 2D and 3D chambers, resulting in a background pressure 0.1 nanotorr in the 3D chamber.

- An Agilent 2 L/sec ion pump is also bolted to the spherical cube to maintain UHV.

When bolting each chamber or ion pump onto the spherical cube, a copper gasket is placed between the base of the ConFlat and the spherical cube. A vacuum seal is established when knife edges, found at the base of the ConFlat, as well as on the spherical cube, are tightly pressed into the copper gaskets, creating a knife-edge seal. The atomtronics cell was initially pumped down to UHV by bolting the entire vacuum cell to a much larger vacuum station via a copper pinch off tube and following a standard bakeout procedure at approximately 300°C. Following bakeout, the atomtronics cell was separated from the bakeout station by "pinching" the pinch off tube with a set of hydraulic jaws. After removal, the system is soft baked for 5-7 days at 120°C to remove any water moisture that erroneously entered the cell during pinch-off.

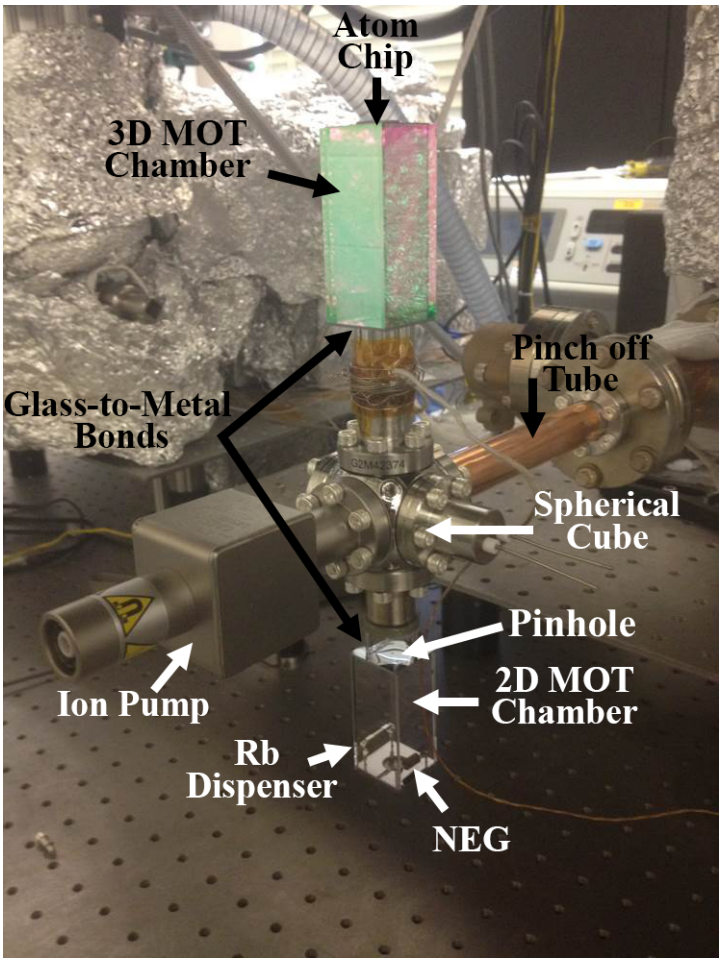

Figure 3.5: Image of the atomtronics vacuum cell. The cell is still attached to the bakeout station via the copper pinch off tube and has not yet been pinched-off.

3.3 Atom Chip: Making Magnetic Traps for Ultra Cold Atoms

The top surface of the atomtronic cell 3D chamber is an atom chip [95, 96, 97] (figure 3.6a). Found on both the ambient and vacuum sides of the chip are small gold wires, ranging in width from 100-500 μm (figure 3.6b). Running electrical currents through various atom chip wires produces the magnetic fields necessary to setup a harmonic magnetic potential in order to perform magnetic trapping, evaporative cooling, and ultimately Bose-Einstein condensation of an ensemble of ^{87}Rb atoms. The atom chip is also used to form the harmonic magnetic potential for the matterwave transistor oscillator (figure 1.4). A 2 mm wide Pyrex window built into the center of the chip (figure 3.6b) allows for optical access of atoms trapped in the magnetic potentials as well as *in-situ* imaging of the BEC confined to a magnetic potential (section 8.3.1). In this final section of chapter 3, we give a brief overview of the magnetostatics of the atom chip relevant to the transistor oscillator theory and experiments covered in chapters 7 and 8.

3.3.1 Producing 3D Harmonic Magnetic Potentials

While there many wires on the atom chip, to form harmonic potentials for the transistor oscillator experiment, we only need to consider a small set of wires positioned at the centrally located chip window, specifically:

- A single pair of parallel oriented "guide-wires." The guide-wires are shown in figure 3.6b as the set of parallel running wires extending over the atom chip window.
- Two pairs of parallel oriented "H-wires." The H-wires can also be found in figure 3.6b as the yellow colored wires running along the outer edge of the chip window and oriented perpendicular to the guide-wires.

Consider running a current I_x through one of the chip guide-wires. Compared to the size of the atoms as well as the dimensions of a BEC[2] , the guide-wire is considered to be infinitely long.

[2] In the transistor oscillator experiments, typical BEC dimensions are 50-100 μm in the longitudinal direction.

From Ampere's law [98], the current I_x running through the guide-wire produces a magnetic field (called the "guide-wire field") given by

$$\mathbf{B} = \frac{\mu_0}{2\pi}\frac{I_x}{r}\hat{\boldsymbol{\phi}} \tag{3.1}$$

with corresponding field gradient $\mathbf{B}'$ and curvature $\mathbf{B}''$ of

$$\begin{aligned} \mathbf{B}' &= -\frac{\mu_0}{2\pi}\frac{I_x}{r^2}\hat{\boldsymbol{\phi}} \\ \mathbf{B}'' &= \frac{\mu_0}{\pi}\frac{I_x}{r^3}\hat{\boldsymbol{\phi}} \end{aligned} \tag{3.2}$$

where μ_0 is the permeability of free space and r is the distance from the wire (figure 3.6c). To produce a local minimum in this field (to permit magnetic trapping), we apply a bias field in the $\hat{\mathbf{y}}$ direction with strength $\beta_y\hat{\mathbf{y}}$ (figure 3.6d). As shown in figure 3.6e, the vector summation of the y-bias field with the guide-wire field (equation 3.1) creates a quadrupole field by canceling the guide-wire field below the wire at a depth d given by

$$d = \frac{\mu_0}{2\pi}\frac{I_x}{\beta_y}. \tag{3.3}$$

Since the magnetic field features symmetry along the axis of the guide-wire (in and out of the page with figure 3.6e), a local minimum exists a distance d below the entire length of the guide-wire. This forms a hollow, tube-like region of zero magnetic field surrounded by high magnetic field, which permits loose confinement along the direction of the guide-wire (i.e. the longitudinal direction) and strong confinement perpendicular to the guide-wire (i.e. the radial direction). While the guide-wire magnetic field, gradient, and curvature features symmetry in $\hat{\mathbf{r}}, \hat{\boldsymbol{\phi}}, \hat{\mathbf{z}}$ cylindrical coordinates, it is useful for the transistor oscillator experiment to express all fields and their derivatives in rectilinear coordinates[3] . Accordingly, the total guide-wire magnetic field from equation 3.1 (with the y-bias field included) in rectilinear coordinates is

$$\mathbf{B} = \frac{\mu_0 I_x}{2\pi}\left[\left(\frac{z}{y^2+z^2} - \beta_y\right)\hat{\mathbf{y}} + \frac{y}{y^2+z^2}\hat{\mathbf{z}}\right]. \tag{3.4}$$

[3] When performing the actual experimental work in the lab, we will be applying many additional bias fields purely in the $\hat{x}$, $\hat{y}$, and $\hat{z}$ directions (section 5.2), making rectilinear units easier to visualize in the lab.

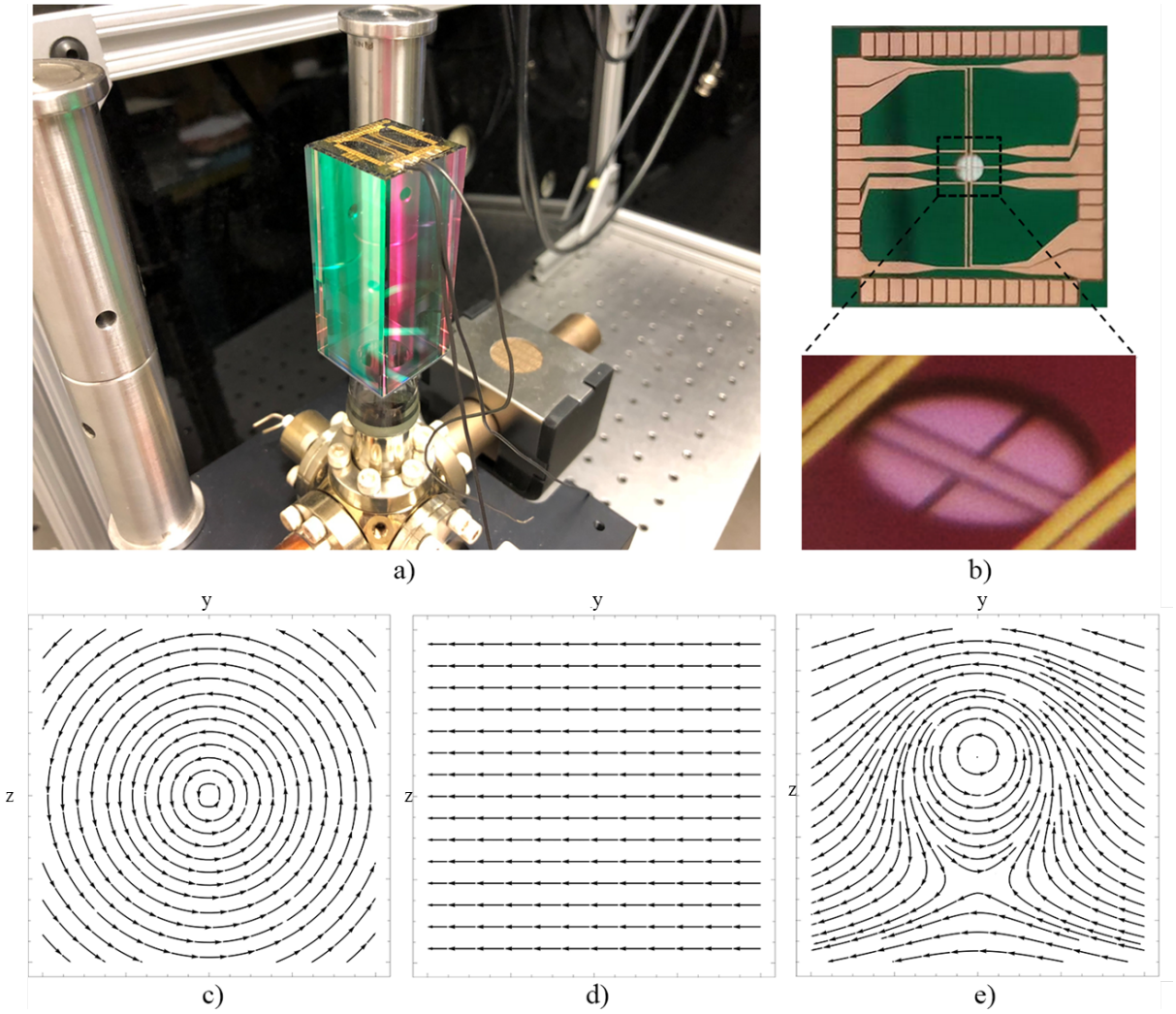

Figure 3.6: a) Vacuum cell with atom chip serving as the top of the cell. b) Underside of the atom chip that is inside the vacuum. The guide wires are shown at the center of the chip. c) 2D cross section of the magnetic field lines produced by running current through one guide wire. d) Uniform bias field oriented purely in the y-direction. e) Summation of the guide wire field and the y-bias field. The result gives a magnetic quadrupole field featuring a local minimum a distance d below the chip guide wire. This plot is a 2D cross-section that is symmetric in and out of the page and thus the field minimum runs below the entire length of the wire, giving a region where magnetic trapping of atoms is permitted.

By choosing to orient the guide-wire along the $\hat{\mathbf{x}}$ axis, the local minima of the quadrupole field is found by simply taking the limit of equation 3.4 as $y \to 0$ and $z \to d$. In this limit, we find approximations for the guide-wire fields:

$$B_y \approx \frac{\mu_0 I_x}{2\pi} \frac{1}{z^2} - \beta_y \tag{3.5a}$$

$$B_z \approx \frac{\mu_0 I_x}{2\pi} \left(\frac{y}{y^2 + d^2} \right). \tag{3.5b}$$

With equations 3.5a and 3.5b, one of the requirements for magnetic trapping is satisfied: a localized minimum for a magnetic field has been produced. In the lab, however, the quadrupole fields from equations 3.5a and 3.5b produced by the atom chip are *very* problematic for atom trapping and reaching BEC. Plotting the fields B_y and B_z (figure 3.7), we immediately observe that a cusp exists at the zero of both fields. This cusp not only perturbs the harmonic potential, but it also results in atom losses [99] due to heating[4] via Majorana spin flips [100]. The cusp in fields B_y and B_z can be removed by adding another bias field $\beta_x \hat{\mathbf{x}}$, along the direction of the guide-wire (figure 3.7). With the addition of this *x-bias field*, the total field of the guide-wire is approximately

$$\mathbf{B} = \beta_x \hat{\mathbf{x}} + \left(\frac{\mu_0 I_x}{2\pi} \frac{1}{z^2} - \beta_y \right) \hat{\mathbf{y}} + \left(\frac{\mu_0 I_x}{2\pi} \frac{y}{y^2 + d^2} \right) \hat{\mathbf{z}}. \tag{3.6}$$

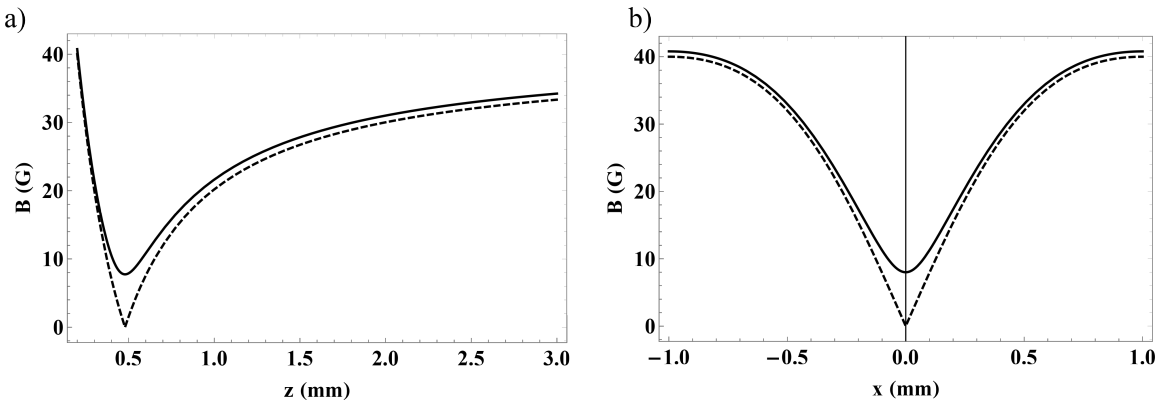

Figure 3.7: Plots of the guide-wire magnetic field in the $\hat{z}$ and $\hat{x}$ directions. The solid and dashed lines represent the magnetic fields with and without the additional x-bias field.

[4] The cusp in the magnetic field creates a discontinuity where the atoms cannot adiabatically follow the field. At the zero crossing, the field gradient is undefined, which can induce spin flips [100] (called Majorana spin flips) into a strong-field seeking state (that is $m_f g_F > 0$) where the atom can no longer be trapped [99].

Using the magnetic field from equation 3.6, we can form a magnetic potential that can confine atoms along the radial direction but cannot trap atoms along the longitudinal direction, since $\nabla_x \mathbf{B} = 0$. In order to confine atoms along the $\hat{x}$, or longitudinal direction, we run a current I_H through a pair of "H-wires" centered about the atom chip window (figure 3.8a) that run perpendicular to the guide wire (figure 3.6b). The H-wires are fabricated to be a rectangular wire with a width w. They are wider than the guide-wires because they carry a considerably higher current load. Each pair of H-wires and its conjugate pair placed symmetrically on the opposite side of the chip window is separated by distance l. Therefore, running a current I_H through the H-wire pair produces a magnetic field given by Ampere's law as

$$\mathbf{B}_H = \frac{\mu_0 I_H}{2\pi w}\left[\ln\left(1+\frac{w}{x+l/2}\right) - \ln\left(1+\frac{w}{x-l/2}\right)\right]\hat{\mathbf{x}}. \tag{3.7}$$

By combining the magnetic fields from the guide-wire (equation 3.6) and the H-wire (equation 3.7), the total field forms a 3D harmonic magnetic potential capable of trapping atoms in a local field minimum. This configuration is called an Ioffe-Pritchard trap and is shown in figure 3.8c).

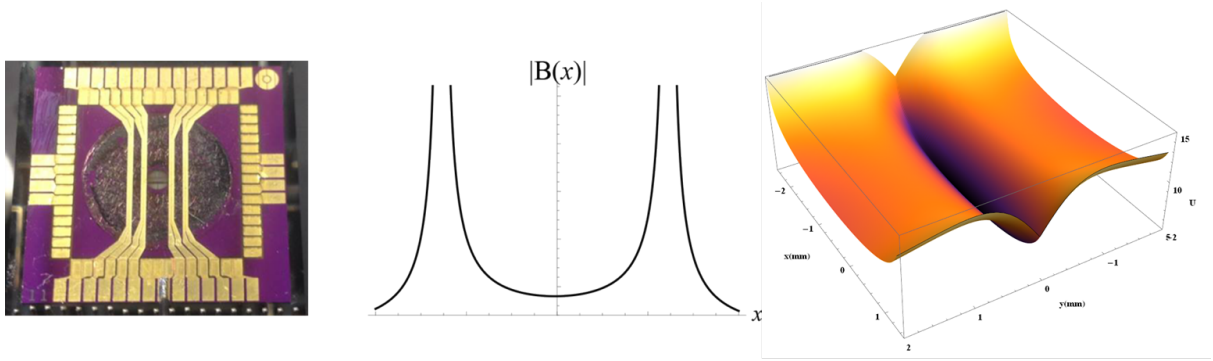

a) b) c)

Figure 3.8: a) Top view of the ambient side of the atom chip. The vertically running pairs of wires are the H-wires and are centered about the chip window. b) Plot of the H-wire magnetic field $\mathbf{B}_H$ (equation 3.7) produced by running current of equal direction and magnitude through two pairs of H-wires centered about the chip window. c) Combined magnetic potential forming an Ioffe-Pritchard trap from the guide-wire field (equation 3.6) and the H-wire field (equation 3.7)

3.3.2 Double Guide Wire IP Trap

The magnetic fields used to radially confine ultracold atoms (equation 3.6) was formed by running current I_x through a single guide-wire. This places the magnetic trap a distance d (equation 3.3) *below* the wire, which blocks optical access. In order to gain optical access to ultracold atoms trapped in the magnetic potential, we must move the trap out from under the guide wire. This can be accomplished by adiabatically ramping up an oppositely flowing current through the *second* guide-wire (running parallel to the first, separated by distance l; figure 3.6b) from 0 to $-I_x$. Under this new set of conditions, the magnetic field (and hence the potential) is shifted directly under the chip window, forming what is called the "split guide-wire trap." This is readily shown by applying Ampere's law to the case of running currents of equal magnitude I_x but with opposite directions through both guide wires separated by distance l (figure 3.6b). The resulting magnetic field is

$$\mathbf{B} = \frac{\mu_0 I_x}{2\pi}\left[\left(\frac{z}{(y+l/2)^2+z^2} - \frac{z}{(y-l/2)^2+z^2}\right)\hat{\mathbf{y}} + \left(\frac{y+l/2}{(y+l/2)^2+z^2} + \frac{y-l/2}{(y-l/2)^2+z^2}\right)\hat{\mathbf{z}}\right] \tag{3.8}$$

and is plotted in figure 3.9a.

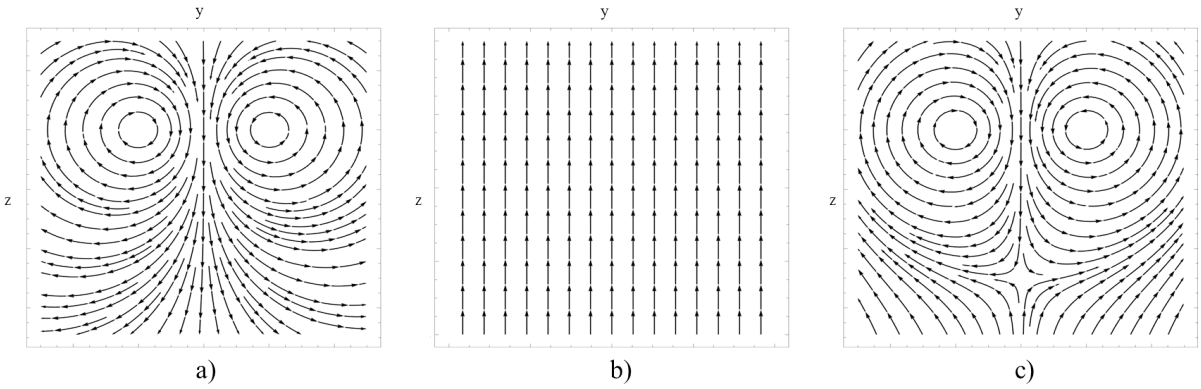

Figure 3.9: a) 2D cross section of the magnetic field produced by running currents I_x and $-I_x$ through the pair of guide-wires separated by distance l (equation 3.8). b) Uniform bias field oriented purely in the z-direction. c) Summation of the split guide-wire field (equation 3.8) and the z-bias field. The result gives a magnetic quadrupole field featuring a local minimum a distance $\mathcal{D}$ below the center of the atom chip window. This plot is a 2D cross-section that is symmetric in and out of the page and thus the field minimum runs below the entire chip window, giving a region where both magnetic trapping of atoms and optical access is permitted.

Similar to the single guide-wire trap, a local minimum in equation 3.8 can be formed by applying a bias field, this time oriented in the $\hat{z}$ direction with magnitude β_z (figure 3.9b). By adding the bias field to equation 3.8, a quadrupole field oriented along the x-axis is formed at a depth $\mathcal{D}$ below the chip window where

$$\mathcal{D} = \sqrt{\frac{\mu_0}{2\pi}\frac{I_x l}{\beta_z} - \frac{l^2}{4}}. \tag{3.9}$$

Physically, the quantity $\mathcal{D}$ represents the z value where the z-bias field, β_z, cancels the $\hat{\mathbf{z}}$ component of the split-guide wire field (equation 3.8) along the entire line $y = 0$ (figure 3.9c). As in the single-guide wire case, Majorana spin flipping is avoided by transforming the quadrupole trap into an Ioffe-Pritchard trap by adding an x-bias field β_x along the direction of the split guide-wires. Therefore, the total field that gives rise to the split guide-wire Ioffe-Pritchard trap is

$$\begin{aligned}\mathbf{B} = \frac{\mu_0 I_x}{2\pi}&\left[\frac{z}{(y+l/2)^2+z^2} - \frac{z}{(y-l/2)^2+z^2}\right]\hat{\mathbf{y}} \\ &+ \left[\frac{\mu_0 I_x}{2\pi}\left(\frac{y+l/2}{(y+l/2)^2+z^2} + \frac{y-l/2}{(y-l/2)^2+z^2}\right) + \beta_z\right]\hat{\mathbf{z}} + \beta_x\hat{\mathbf{x}}.\end{aligned} \tag{3.10}$$

The local minima of the total magnetic field that forms the split guide-wire Ioffe-Pritchard trap is found by taking the limit of equation 3.10 as $y \to 0$ and $z \to d$, giving

$$B_x = \beta_x \tag{3.11a}$$

$$B_y = \frac{\mu_0 I_x}{2\pi}\left[\frac{\mathcal{D}}{(y+l/2)^2+\mathcal{D}^2} - \frac{\mathcal{D}}{(y-l/2)^2+\mathcal{D}^2}\right] \tag{3.11b}$$

$$B_z = \frac{\mu_0 I_x}{2\pi}\left[\frac{l}{l^2/4+z^2}\right] - \beta_z. \tag{3.11c}$$

From equations 3.11b and 3.11c, the magnitude of the total[5] field at the location $z = \mathcal{D}$ is

$$\begin{aligned}|B| &= \sqrt{B_x^2 + B_y^2} \\ &= \left(\left[\frac{\mu_0 I_x}{2\pi}\left(\frac{\mathcal{D}}{(y+l/2)^2+\mathcal{D}^2} - \frac{\mathcal{D}}{(y-l/2)^2+\mathcal{D}^2}\right)\right]^2 + \beta_x^2\right)^{1/2}.\end{aligned} \tag{3.12}$$

While this expression gives the total B-field located a distance $\mathcal{D}$ under the chip window, from an experimentalist point of view, it is more useful to also only consider the field at small y values,

[5] Recall from equation 3.9 and the sentence that follows it, that B_z vanishes when $z = \mathcal{D}$. Therefore, equation 3.11a is not used in the magnitude of the total field at the location $z = \mathcal{D}$.

since after all, atoms are localized to $y \approx 0$ when trapped in the field minimum. Therefore, the field is expanded in a Maclaurin series

$$|B| = \beta_x + \frac{8\pi^2}{\mu_0^2 I_x^2}\frac{\mathcal{D}^2}{l^2}\frac{\beta_z^4}{\beta_x}y^2 + \mathcal{O}(4). \tag{3.13}$$

The trapping forces on an atom in this spatially varying magnetic field are readily calculated by evaluating the first and second spatial derivatives of equation 3.13, giving corresponding field gradient B' and curvature B'' of

$$|B'| = \frac{16\pi^2}{\mu_0^2 I_x^2}\frac{\mathcal{D}^2}{l^2}\frac{\beta_z^4}{\beta_x}y \tag{3.14a}$$

$$|B''| = \frac{8\pi}{\mu_0 I_x l}\frac{\beta_z^3}{\beta_x} \tag{3.14b}$$

where the definition of $\mathcal{D}$ given in equation 3.9 is used in solving $|B''|$. Using equations 3.14a and 3.14b, we immediately arrive at the radial trapping force imparted onto atoms in the split guide wire trap:

$$\mathbf{F}_{\text{rad}} = -\nabla\left(\hat{\boldsymbol{\mu}}\cdot\mathbf{B}\right) \approx -\mu_b B' = -\frac{16\mu_b\pi^2}{\mu_0^2 I_x^2}\frac{\mathcal{D}^2}{l^2}\frac{\beta_z^4}{\beta_x}y \tag{3.15}$$

which features a trapping frequency in the radial direction of

$$\omega_{\text{rad}} = \sqrt{\frac{\mu}{m}B''} = \sqrt{\frac{8\pi}{\mu_0 I_x}\frac{\mu}{ml}\frac{\beta_z^3}{\beta_x}}. \tag{3.16}$$

The trapping potential along the longitudinal direction is still provided by the same H-wire field given in equation 3.7. Thus the trapping force and corresponding trapping frequencies in the longitudinal direction are found by evaluating the first and second spatial derivatives of equation 3.7 and are

$$\mathbf{F}_{\text{long}} = -\nabla_x\left(\hat{\boldsymbol{\mu}}\cdot\mathbf{B}_H\right) = -\frac{4\mu_0 I_H}{\pi w}\left(\frac{x}{l^2 - 4x^2}\right) \tag{3.17}$$

$$\omega_H = \sqrt{\frac{\mu}{m}B_H''} \approx \sqrt{\frac{\mu\mu_0}{\pi w}\frac{2I_H}{ml}}. \tag{3.18}$$

3.4 Conclusion to Part I

With the laser cooling and trapping theory outlined in chapter 2 and the vacuum cells and atom chip systems outlined in chapter 3, we have all of the universal tools and methods required

to perform the atom transport and atom transistor experiments. Any additional methods that are specific to either experiment are described within their respective chapters.

Chapter 4

Part II: Individual Atom Delivery of Neutral Cs Atoms into Bottle Beam Traps Using a Dynamic 1D Optical Lattice

4.1 Motivation for Single Atom Delivery into Bottle Beam Traps

Advances in neutral atom quantum computing have led to the recent development and demonstration of a 49 element atomic qubit array, where quantum information is stored in the ground states of neutral cesium atoms and two-qubit gates implemented with Rydberg states [101, 102, 1, 103, 104, 105]. The qubit array is comprised of a 7x7 grid of individual optical bottle beam (BoB) traps (figure 4.1a) whereby each BoB confines exactly one cesium atom. The ambitious goal of the IARPA AQuA-49 project, as described in section 1.1, is to use such a qubit array, located inside an UHV chamber, to perform quantum logic gates involving multiple qubits for an arbitrarily long length of time (figure 4.1b). Due to collisions with thermal background atoms in the surrounding vacuum chamber (figure 4.1c), trap lifetimes of qubits are on the order of $\tau = 100$ sec, [3, 1, 103, 105, 106, 107] and thus an array of $N = 49$ cesium qubits will lose one qubit every $\tau/N \approx 2.0$ seconds, on average. Even with extreme high vacuum of 10^{-4} nanotorr, trapped atom lifetimes would be about 1 day. [108] For a quantum computer to run arbitrarily long algorithms, atom loss would be an issue. Therefore, to sustain a functional neutral atom qubit array for an indefinite period of time, a new atom must be reloaded into the vacant BoB array site in a timely manner. Past work has made advances in loading single atoms into BoB traps by overlapping the BoB with a magneto-optical trap (MOT)[109, 110]. This solution will certainly reload the newly vacant BoB site but will also disturb other loaded, neighboring sites due to collisions with other

MOT atoms. A more suitable solution involves reloading a lost atom by delivering a new atom from a distant cold atom reservoir by means of a movable, dynamic 1D lattice (figure 4.1d) similar to the atom transport experiments covered in references [111, 112, 113]. The latter solution is the subject of this chapter, which covers our work in solving the problem of atom reloading and describes experiments that demonstrate transporting and subsequent loading of a single neutral cesium atom into a distant, unoccupied optical BoB trap.

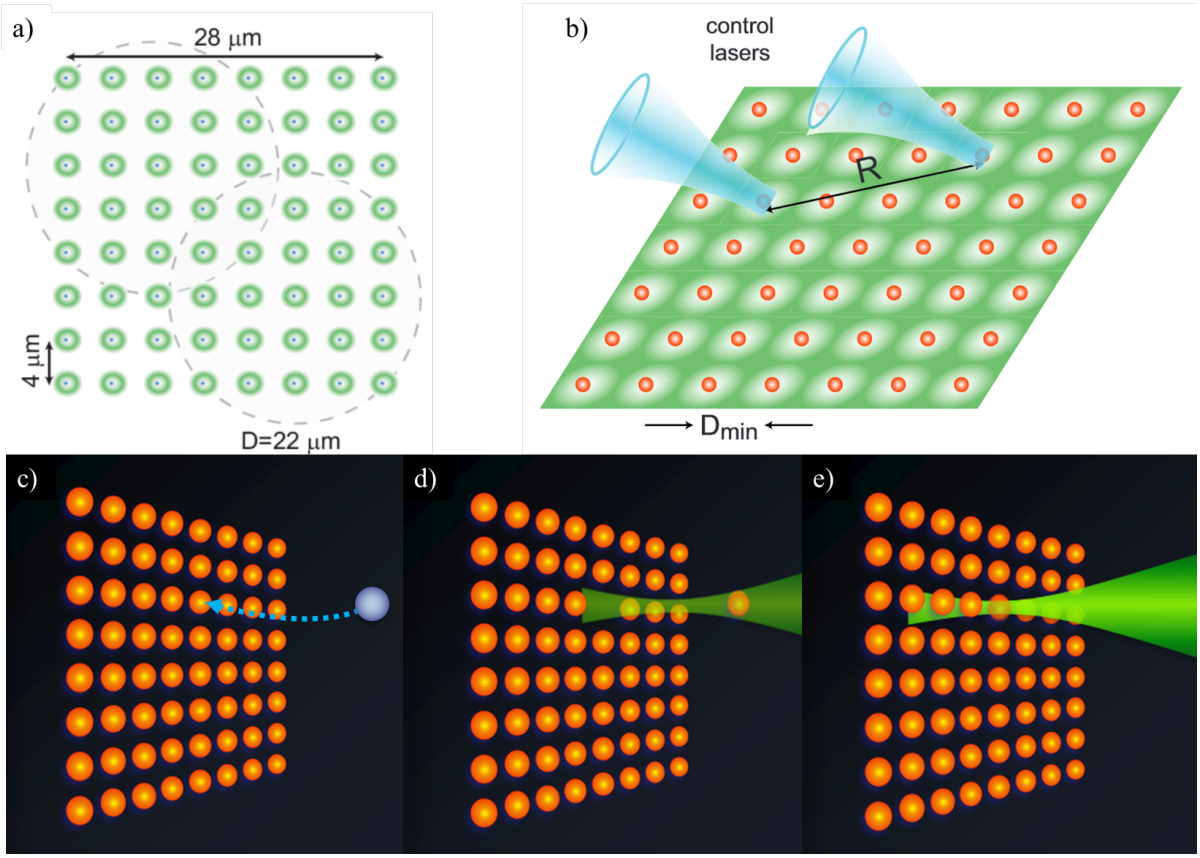

Figure 4.1: (Color online) a) Schematic of a qubit array constructed with a 2D grid of equally spaced optical bottle beam traps. b) Concept of using pairs of entangled Rydberg state atoms to perform quantum logic gates and operations involving multiple qubits simultaneously. c) A stray background gas atom collides with a trapped qubit and expels it from the BoB trap. d) A new pre-cooled cesium atom is transported with an optical conveyor belt to the empty BoB site. e) Exactly one atom at most is then transferred into the BoB trap, reloading the empty site and keeping the array fully occupied.

The experiment functions by initially loading a few thousand atoms into a red-detuned 1D optical lattice from a background cold atom reservoir. Precise frequency control over the lattice beams allows us to move the lattice back-and-forth along its axial direction, making it function as an "optical conveyor belt." With this setup, we demonstrate transporting the small atom ensemble approximately 1.1 mm to an empty optical BoB trap followed by transferring exactly one atom at most into the BoB trap. An added challenge for this experiment arises due to the lack of an *a-priori* physical reference point for the BoB trap. The remainder of this chapter is organized as follows: Section 4.2 describes the laser system and beam layout for the 852 nm cooling, repump, and probe lasers, as well as the 780 nm bottle beam laser system and the 1064 nm optical conveyor belt lasers. The layout of each beam with respect to each other in the AQuA Hex cell is also provided. Section 4.3 details the laser cooling processes to produce a reservoir of sufficiently cold atoms in the Hex cell for use in the transport and reloading experiments. Section 4.4 describes generating and implementing the optical conveyor belt. Section 4.5 outlines the crossed vortex BoB trap as well as the system for detecting single atoms confined to such an optical potential. Finally, section 4.6 demonstrates the single atom delivery into a BoB trap using the optical conveyor belt.

4.2 Laser System and Beam Layout

The single atom transport and reloading experiment requires the use of three sets of lasers with various detunings from the ^{133}Cs D2 line ($\lambda = 852.347$ nm, $\nu = 351.725$ THz) :

- Three 852 nm lasers that are on resonance with the ^{133}Cs D2 line.
- One 780 nm laser for BoB traps that is blue-detuned from resonance.
- One 1064 nm laser for atom transport that is red-detuned from resonance.

The 852 nm resonant laser light was produced using Vescent Photonics D2-100-DBR-852 distributed Bragg reflector (DBR) diode lasers. The transport and reloading experiment requires three individual DBRs: one to provide cooling light, one to provide repump light, and one to act as a probe

laser to perform absorption imaging. In addition, a New Focus VAMP TA-7616 tapered amplifier (TA) was used to amplify the light emitted from the cooling DBR from 70 mW to 500 mW of total usable laser power. Blue detuned light at 780 nm, used to form optical bottle beam traps and bottle beam arrays, is produced with a Sanyo DL 7140-201 S laser diode and is amplified by a Toptica BoosTA Pro to 3 W of laser power. Finally, the red detuned 1064 nm laser that is used for optical dipole trapping is a 30 W, IPG Photonics YLR-30-1064-LP-SF laser. A block diagram of the 852 nm, 780 nm, and 1064 nm laser systems are shown in figure 4.2 and figure 4.3.

4.2.1 Layout of 852 nm Cooling, Repump, and Probe Lasers

The 852 nm cooling, repump, and probe laser setup as well as each laser's corresponding atomic transition used within the ^{133}Cs D2 manifold is shown in figure 4.2 and described here. The frequency locking scheme for the cooling laser[1] involves picking off 5 mW of the cooling light from the main beam and blue shifting it by 145 MHz with an acousto-optic modulator (AOM). This blue-shifted light was then sent into a Vescent Photonics saturated absorption spectroscopy (SAS) module and locked to the $|F = 4\rangle \rightarrow |F' = 5\rangle$ D2 cycling transition. Using this locking scheme, realize that the main cooling light that was *not* picked off is subsequently left *red-detuned* from the cycling transition by 145 MHz. This red-detuned light was then used to seed the New Focus TA, which then outputs 500 mW of laser light. The output of the TA supplies cooling light for both the 2D and 3D MOTs. Acousto-optic modulators are used to shift the frequency of the 2D and 3D MOT light such that the 2D beam is detuned $-2.9\Gamma \approx 95$ MHz and the 3D beam is detuned $-2.3\Gamma \approx 76$ MHz from the $|F = 4\rangle \rightarrow |F' = 5\rangle$ cycling transition. It is important to note that with respect to the 3D MOT cooling light path, the AOMs are setup in the cat's eye, double pass configuration [114], which allows one to shift the 3D MOT frequency without imparting any spatial deflections to the beam. After passing through the AOMs, a total of 100 mW of 2D MOT light and 60 mW of 3D MOT light is then coupled into a polarization maintaining fiber.

[1] It should be noted that since the lasers are DBR lasers, they are extremely sensitive to back-reflected light. Thus, the cooling and repump laser outputs initially pass through two optical isolators providing 60 dB of isolation.

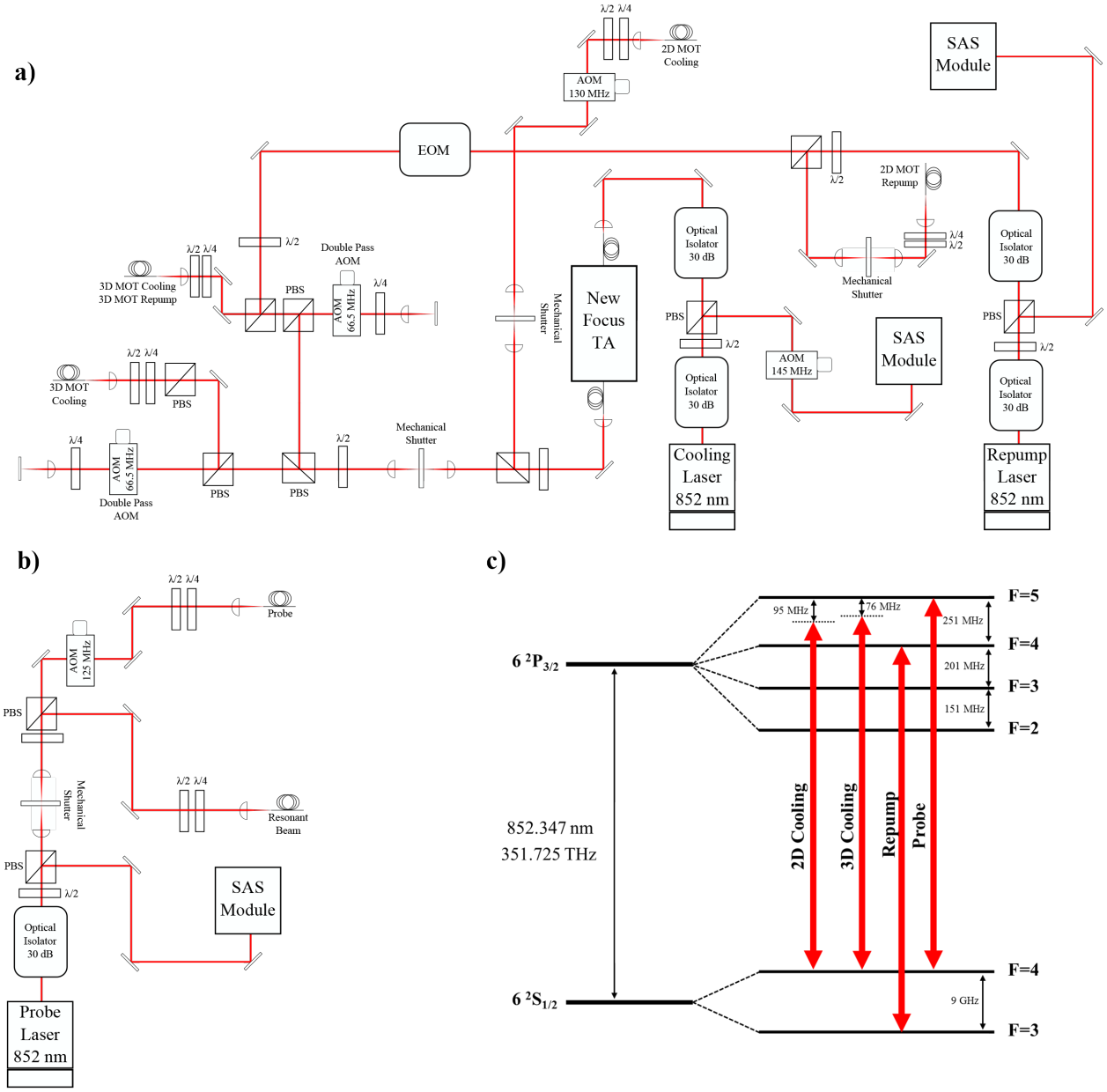

Figure 4.2: (Color online) a) Setup for the 852 nm cooling and repump lasers. b) Setup for the 852 nm probe lasers. In both schematics, mechanical shutters are used to turn on and off the laser beams. Additionally, all fibers are 852 nm, polarization maintaining fibers. c) Laser locking scheme for the Cs D2 transitions used in the single atom transport and loading work.

In order to keep atoms contained within the cycling transition, the repump laser is locked resonant to the $|F = 3\rangle \rightarrow |F' = 4\rangle$ transition (figure 4.2c). Repumping light is then split such that it can be supplied to both 2D and 3D MOT setups. Variable attenuation of the 3D repumping light is provided by the combination of an electo-optic modulator (EOM) and a polarizing beam splitter (PBS) on the input and output of the EOM. As seen in the laser schematic shown in figure 4.2a, the 2D MOT repumping light is coupled into its own polarization maintaining optical fiber while the 3D MOT repump light first spatially overlaps the 3D cooling light and is coupled into the 3D MOT polarization maintaining fiber[2] . This arrangement results in 10 mW of 2D repump and 5 mW of 3D repump light coupled into the respective fibers. Finally, the probe laser, which is used for absorption imaging (described in chapter 4.2), is locked to the $|F = 4\rangle \rightarrow |F' = 3\rangle / |F' = 5\rangle$ crossover transition. The probe light is blue shifted onto resonance with the $|F = 4\rangle \rightarrow |F' = 5\rangle$ cycling transition by using an AOM driven at 125.5 MHz. Additionally, a small amount of probe light is picked off from the main beam line to act as a resonant beam[3] .

4.2.2 1064 nm Transport Lasers

The setup for the 1064 nm atom transport laser and the 780 nm bottle beam laser is shown in figure 4.3.

The red-detuned, 1064 nm fiber laser supplies 30 W of laser power that is split with a PBS to send 18 W to a vertical dipole trap setup[4] and 12 W to form the optical conveyor belt. After the PBS, a 2:1 telescope de-magnifies the beam waist from 3 mm to the desired waist of 1.5 mm. The light is then equally split with another PBS, where each beam subsequently passes through a double pass AOM setup. Each AOM is driven by its own individual Agilent 33250 80 MHz arbitrary waveform generator (AWG) that shifts the frequency of one beam by $\Delta\nu_1 = 2 \times 78 = 156$ MHz

[2] Note that while the 3D MOT cooling and 3D repumping light are coupled into the same polarization maintaining fiber, the repump light polarization is oriented perpendicular to the polarization maintaining axis.

[3] While not actually used in the single atom transport and loading experiment, the resonant beam is a very useful tool for the experimentalist as it can be overlapped with other non-resonant beams (such as the 780 nm and 1064 nm light used in the experiment) and used as a nifty alignment tool.

[4] During the development of this experiment, work involving vertical transportation of atoms from a MOT to the optical BoB traps was implemented in a moving molasses MOT. While this is not the subject of this chapter, it opens some interesting extensions to the atom transport work and thus is discussed further in appendix A.

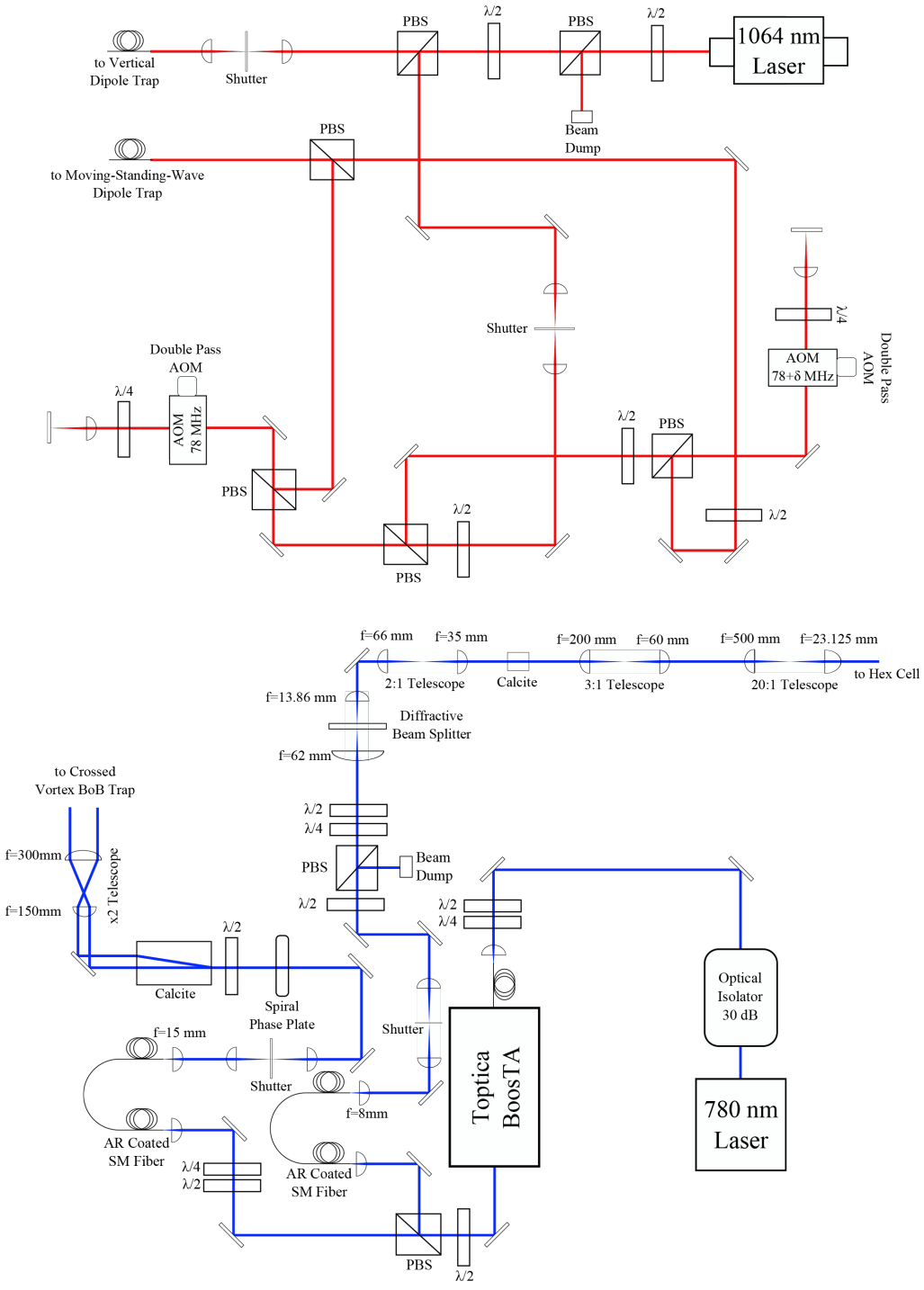

Figure 4.3: (Color online) a) Setup of the 1064 nm atom transport laser system. b) Schematic of the 780 nm blue-detuned bottle beam laser system.

and the other by a *variable* amount of $\Delta\nu_2 = 2 \times (78 + \delta) = 156 + 2\delta$ MHz, where the amount δ is tunable. To minimize phase jitter between the two beams, both AWGs are frequency locked and phase synchronized via their internal 10 MHz clocks. The frequency shifted light emerging from the double pass AOMs is then combined and spatially overlapped at a final PBS. This setup produces two co-propagating 1064 nm beams with *orthogonal* linear polarizations with a mutual frequency detuning of $\Delta\nu = 2\delta$. The pair of beams is then sent to the AQuA cell (section 4.2.4) to form the optical conveyor belt for atom transport and delivery (section 4.4.1).

4.2.3 780 nm Bottle Beam Lasers

Shown in figure 4.3b, for the blue detuned, 780 nm laser, 30 mW of light is sent directly to seed the Toptica BoosTA, which outputs a total of 3 W of light. Output from the TA splits at a PBS where it is either sent to a crossed vortex bottle beam setup or the Gaussian beam array bottle beam setup (used in chapter 5). For both paths, the light is first spatially filtered by passing through an anti-reflection coated, single mode fiber and then propagated through a system of beam shaping lenses to set the correct beam waist of $w_0 = 0.8$ mm for the crossed vortex BoB setup and $w_0 = 1.2$ mm for the BoB array setup.

4.2.3.1 Crossed Vortex BoB Setup

The objective of the crossed vortex BoB setup is to generate two co-propagating Laguerre-Gaussian (LG01) beams with equal intensity and orthogonal polarizations. Shown in figure 4.4, the LG01 beams are created by propagating a TEM00 mode, Gaussian laser beam with initial beam waist of 0.8 mm, through an RPC Photonics spiral phase plate (SPP). The SPP imparts an azimuthal dependent phase delay of the form $e^{\pm il\phi}$ on the incident TEM00 mode by slowing the phase of the Gaussian beam as a function of it's azimuthal angle, where l is an integer called the topological charge[5] of the outgoing LG mode.

[5] Here, l indicates how many times the phase of the beam is shifted by 2π for every full azimuthal rotation of the TEM00 beam mode. The $\pm$ sign of the topological charge indicates the sign of the helicity of the outgoing LG beam.

For every complete 2π rotation of the azimuthal angle ϕ of the TEM00 mode, the total phase delay $\Delta\phi$ imparted on the light with wavelength λ passing through the SPP is

$$\Delta\phi = 2\pi l = \frac{2\pi}{\lambda}(n-1)\,d \tag{4.1}$$

where d and n are the thickness and refractive index of the SPP, respectively [115]. As a result of the phase delay, the SPP transforms the laser electric field from a Gaussian mode into a Laguerre-Gaussian mode $LG_{p,l}$ described by

$$\begin{aligned} E(r,\phi,z) =& \sqrt{\frac{2p!}{\pi\,(p+|l|)!}}\frac{1}{w(z)}\left(\frac{r\sqrt{2}}{w(z)}\right)^{|l|}\exp\left(-\frac{r^2}{w^2(z)}\right)L_p^{|l|}\left(\frac{2r^2}{w^2(z)}\right)\exp\left(-ik\frac{r^2}{2R(z)}\right) \\ &\times e^{-il\phi}e^{-ikz}\exp\left[i(|l|+2p)\tan^{-1}\left(\frac{z}{z_R}\right)\right] \end{aligned} \tag{4.2}$$

where p is the radial index, l is the topological charge, $L_p^l(x)$ are the associated Laguerre polynomials, and $R(z)$ is the radius of curvature of the beam, given as $R(z) = z + z_R^2/z$. The phase profile of the SPP used in this experiment is shown in figure 4.4a and it was carefully manufactured to impart a topological charge of exactly $l = +1$ on the incoming TEM00 mode of $\lambda = 780$ nm light, which transforms it into an LG01 mode beam in the far-field (figure 4.4b) with intensity profile

$$\begin{aligned} I(r,z) &= \frac{2P}{\pi w_0^2}\left(\frac{2r^2}{w^2(z)}\right)\exp\left(-\frac{2r^2}{w^2(z)}\right)\left[L_0^1\left(\frac{2r^2}{w^2(z)}\right)\right]^2 \\ &= \frac{4P}{\pi w_0^2}\left(\frac{r^2}{w^2(z)}\right)\exp\left(-\frac{2r^2}{w^2(z)}\right) \end{aligned} \tag{4.3}$$

where P is the total laser power in the LG01 mode [116]. The LG01 beam is then split into two co-propagating beams separated by 2.5 mm with equal intensity and orthogonal polarizations by passing the beam through a calcite beam displacer. Upon exit from the calcite, the two LG01 beams pass through a 2x telescope designed to increase both the beam separation to 5 mm and the beam waist to 1.61 mm. This configuration of two co-propagating "vortex" LG01 beams with orthogonal polarization is then sent to the AQuA Hex cell (section 4.2.4), where tightly overlapping them forms a crossed vortex BoB trap (section 4.5.2, figure 4.19).

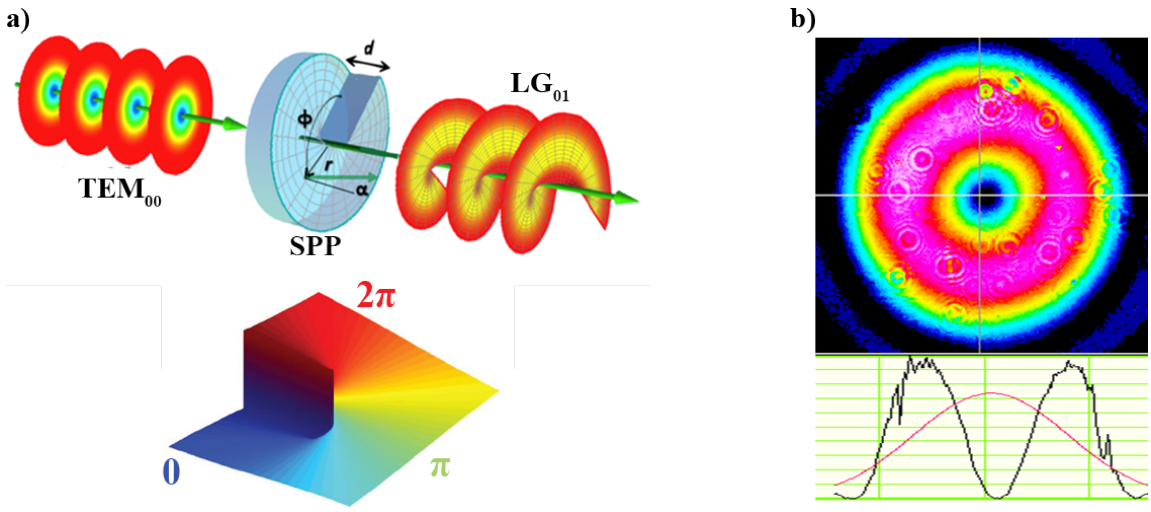

Figure 4.4: (Color online) a) Drawing illustrating a SPP transforming a TEM00 mode Gaussian laser beam into an LG01 mode Laguerre-Gaussian beam. The phase profile of the SPP used in this work, showing how one full azimuthal rotation retards the TEM00 phase by 2π, is shown below. b) The LG01 mode created in this experiment by sending the TEM00 mode through the SPP.

4.2.3.2 Gaussian Array BoB Setup

Returning to the 780 nm laser system shown in figure 4.3b, blue-detuned light can also be directed to the Gaussian beam array setup to create an array of bottle beam traps. After emerging from the AR coated, single-mode fiber, the beam is focused through a Holo/Or MS-248-X-Y-A diffractive beam splitter which diffracts a single TEM00 mode beam into a 2x2 array of identical Gaussian beams, all with with parallel linear polarizations (figure 4.5a). A set of telescopes and additional calcite beam displacers serves to de-magnify the array to the desired dimensions while increasing the number of beams in the array. First, a 66:35 telescope images the 2x2 array through a calcite beam displacer cut to a thickness of 353 μm which replicates the 2x2 array into an array of 8 identical Gaussian beams separated from their nearest neighbor by 353 μm (figure 4.5b). Since the calcite is a birefringent material, the 4 replicated Gaussian beams have an *orthogonal* polarization to the 4 original beams. Additionally, in order to have equal spacing of each array beam (from their nearest neighbor), the fast axis of the calcite must be rotated by 45 degrees with respect to the diffractive beam splitter.

After passing through the calcite, the array of 8 Gaussian beams is further de-magnified by a 200:60 telescope and then demagnified again with a 500:23.125 telescope (figure 4.5c) and imaged into the center of the AQuA Hex cell (section 4.2.4) for use in the experiments. At the focus of the 0.4 NA, 23.125 mm lens, each Gaussian beam has a focused beam waist of $w_0 = 2.21$ μm and is separated from its nearest neighboring beam by a distance $d = 4.95$ μm. The aspect ratio[6] s, which is defined as the ratio of the focused beam spacing to focused beam waist, is $s = d/w = 2.23$. After passing through all of the optics required to produce the array, the total optical power remaining in the array is 750 mW, which gives a uniform distribution of 47 mW per beam in the array. As described in section 5.1.1, the optical intensity profile of the array at the focus of the 23.125 mm lens (figure 4.5c) creates a two BoB traps.

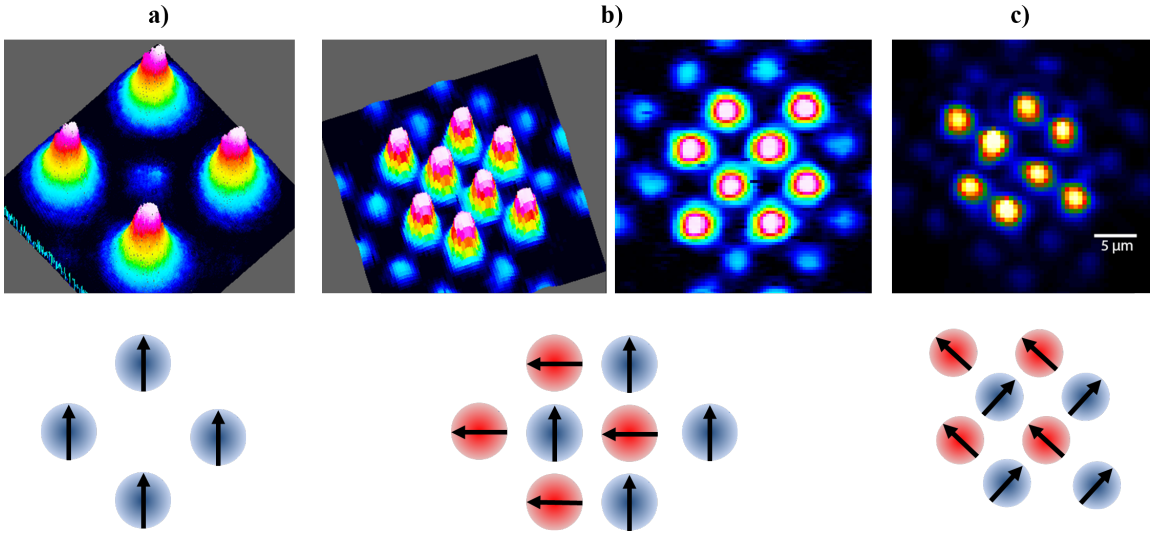

Figure 4.5: (Color online) This set of images shows the formation of the Gaussian beam array at various locations of the optical setup. a) Intensity plot and the direction of linear polarization of the 4 identical Gaussian beams taken after a single Gaussian beam passes through the diffractive beam splitter. b) Intensity and polarization diagrams for the array after the 4 identical Gaussians pass through the calcite and are focused by the 200:60 demagnifying telescope. c) Image showing the array after focusing with the 500:23.125 demagnifying telescope. As shown in section 4.9, this intensity profile in c) is what is focused into the Hex cell to make an array of bottle beam traps.

[6] While not explained until section 4.9, the section devoted to atom trapping in the array, it should be noted that the aspect ratio $s = d/w$ is not merely some spurious detail but rather is a very critical parameter for actually trapping atoms in the Gaussian beam array.

4.2.4 Layout of Laser Beams in the AQuA Hex Cell

The 852 nm cooling and MOT lasers from section 4.2.1 as well as the 1064 nm and 780 nm transport and BoB lasers from section 4.2.2 and 4.2.3 all converge at the center of the AQuA Hex cell. Figure 4.6 shows the placement of each beam inside the vacuum chamber. The BoB traps are formed at the focus of the 780 nm BoB lasers and are offset from the 1064 nm atom transport lasers (functioning as an optical conveyor belt) by an angle of $\Theta = 60°$. Additionally, the cooling lasers that form a 3D MOT intersect at an angle of $\Theta = 60°$ (as opposed to the traditional 90° angle from most MOT setups).

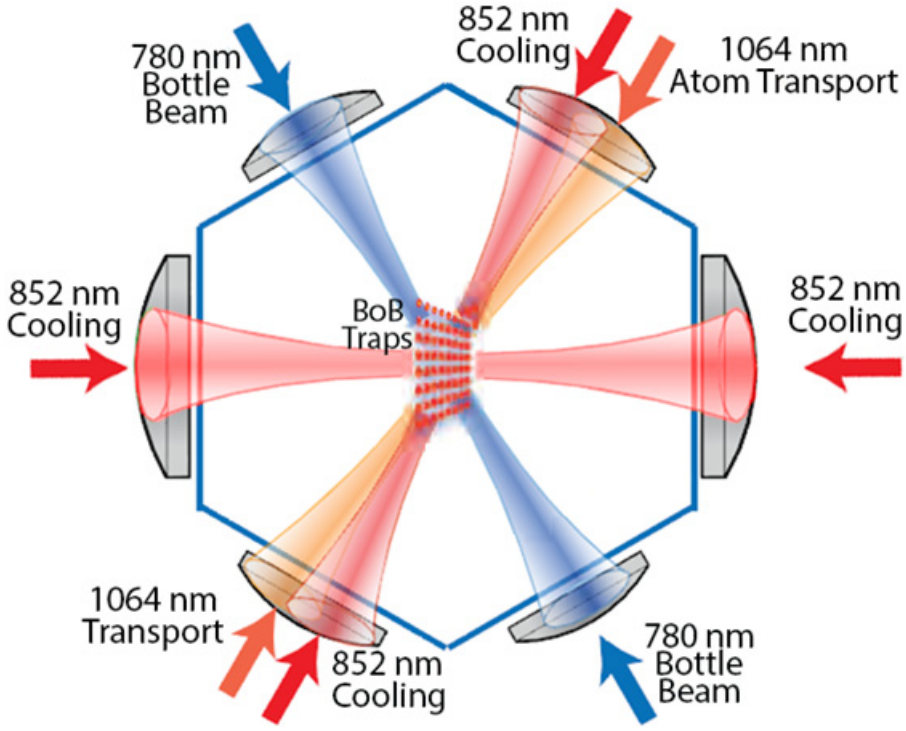

Figure 4.6: (Color online) Transport, loading, and imaging lasers entering the vacuum cell. The 780 nm beams generate the BoB trap at the center of the cell, while 1064 nm lasers are used to generate the dynamic 1D optical lattice for atom transport. Finally, laser cooling, optical molasses, and fluorescence imaging are performed with the 852 nm beams.

4.3 Producing a Reservoir of Cold Atoms

A 3D magneto-optical trap [117][118][119][120] of cesium atoms located in the AQuA Hex cell provides a continuous reservoir of cold atoms for the experiment. As described in section 3.1, atoms that source the 3D MOT are initially trapped and cooled in a 2D+ MOT located in a chamber below the Hex cell and then sent upwards into the 3D MOT chamber via a "push beam." Here, the experimental process of creating such a cold atom reservoir in the AQuA cell is described.

4.3.1 2D+ MOT

Shown in figure 4.7, the 2D+ MOT is created by overlapping two pairs of retroreflecting 50 mW, cylindrically shaped beams with orthogonal σ_+/σ_- circular polarizations in the lower, 2D MOT chamber. Both beams consist of a combination of 2D cooling and repump light that enters the system through individual fibers, is collimated with an $f = 50$ mm aspherical lens, and is spatially overlapped[7] at a polarizing beam splitter (PBS). A telescope made from a pair of cylindrical lenses then enlarges the beam and gives it an elliptical profile with a beam waist of $w = 0.5$ mm along the semi-minor axis and a waist of $w = 1.0$ mm along the semi-major axis. Using a PBS, the light is then split into two beams with equal intensity. A pair of $\lambda/4$ waveplates for each beam controls the circular polarization such that all beams overlap at an angle of 90° at the center of the 2D chamber (inset 1 of figure 4.7b) with orthogonal σ_+/σ_- circular polarizations.

Additionally, four permanent magnets located outside the 2D chamber creates a 2D quadrupole field with gradient 15 G/cm. A 2D+ MOT is then created by red-detuning the 2D cooling light by $\delta = 2.9\Gamma$. The resulting MOT force provides strong confinement of atoms in the $\hat{x}$ and $\hat{y}$ directions but no confinement in the $\hat{z}$ direction. A vertically oriented push beam overlaps the 2D MOT along the loose $\hat{z}$ axis (inset 2 of figure 4.7b) and provides a momentum kick to transfer cooled atoms up through the 2D and 3D pinholes to provide a flux of approximately 10^9 cooled atoms per second into the AQuA Hex cell to subsequently source a 3D MOT.

[7] Prior to overlapping the cooling and repump, approximately 3 mW of cooling light is picked off and sent vertically through the cell to function as the push beam.

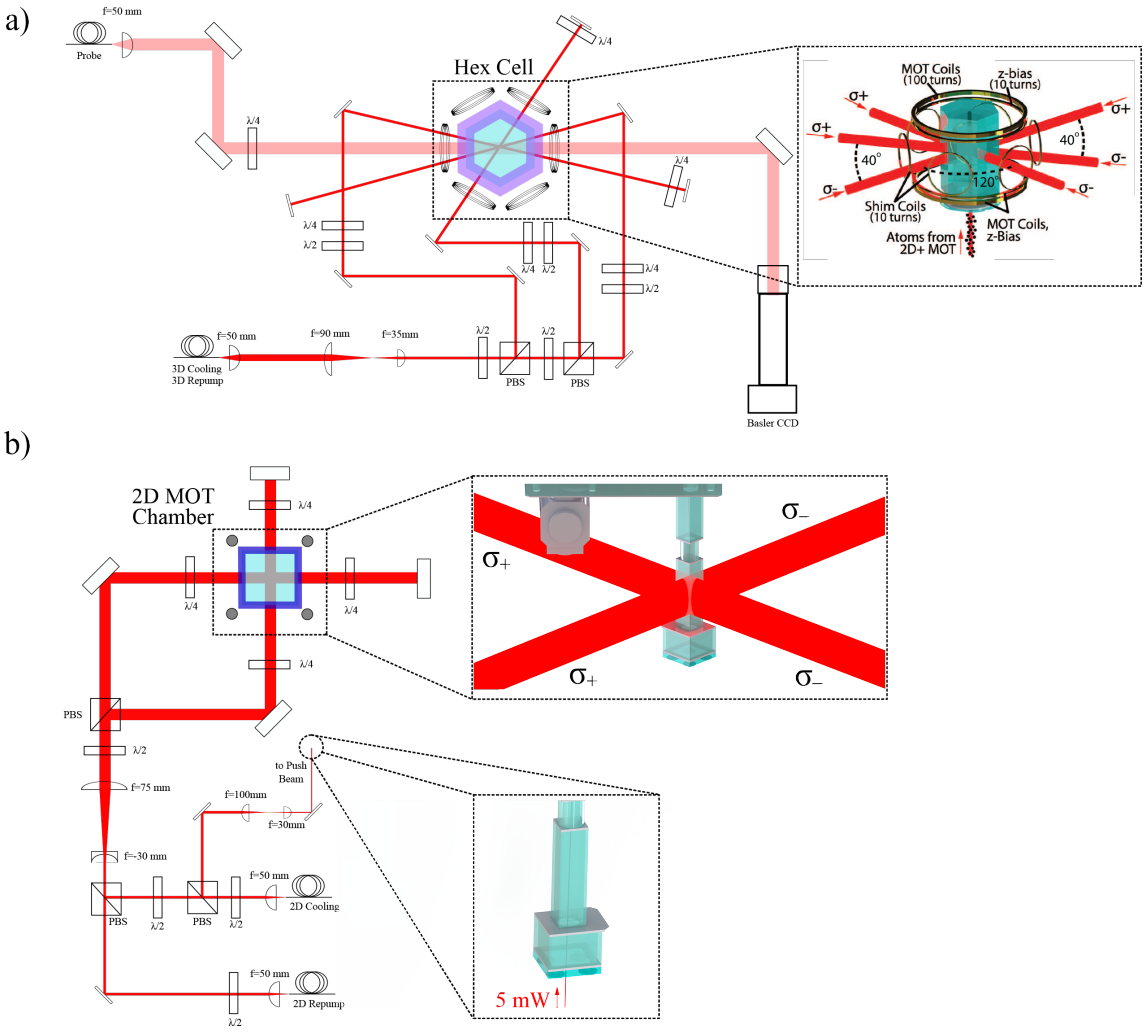

Figure 4.7: (Color online) a) Optical setup to form a 3D MOT in the AQuA Hex cell. The inset shows the orientation of the 6 3D cooling beams, the vertically oriented push beam, MOT coils, and shim coils. A weak probe beam intersects the MOT location and is focused onto a Basler CCD for absorption imaging. b) Optical setup to form a 2D+ MOT in the AQuA 2D chamber. Inset 1 shows the orientation of the 4 cooling beams. Inset 2 shows the location of the vertically oriented push beam. The push beam enters at the base of the 2D chamber and propagates vertically through the entire AQuA cell, exiting through the top surface of the Hex cell. Since it overlaps the 2D MOT, it "pushes" atoms into the Hex cell that are used to seed the 3D MOT.

4.3.2 3D MOT

Figure 4.7a diagrams the 3D MOT setup. The 3D MOT is created by retroreflecting three pairs of $\lambda = 852$ nm laser beams that are red-detuned $\delta = -2.9\Gamma$ from the $|F = 4\rangle \rightarrow |F' = 5\rangle$ cycling transition and overlapped with repumping light resonant with the $|F = 3\rangle \rightarrow |F' = 4\rangle$ transition at the center of the AQuA Hex cell. Both cooling and repump beams enter the system through the same fiber. A total of 30 mW of 3D cooling light and 5 mW of 3D repump light is collimated from the fiber launcher by using an $f = 50$ mm aspherical lens. Immediately after collimation, a 90:35 telescope demagnifies the beams to a collimated beam waist of $w_0 = 1.5$ mm. A series of polarizing beam splitters then separates the laser light into three beams of equal intensity. Lastly, before entering the AQuA Hex cell, each beam passes through a $\lambda/2$ waveplate followed by a $\lambda/4$ waveplate combination to give the MOT beams a σ_+ (or σ_-) circular polarization. The optics of the 3D MOT setup are completed by retroreflecting each beam to spatially overlap itself inside the Hex cell. An additional $\lambda/4$ waveplate located in front of each retroreflecting mirror ensures the circular polarization of the retroreflected light is orthogonal to the initial light beam. Thus, shown in the inset of figure 4.7a, each pair of 3D MOT beams has the σ_+/σ_- circular polarization necessary for cooling (as described in figure 2.2a).

The final orientation of the 3D MOT beams as they appear in the actual experiment in the lab is shown in the inset of figure 4.7a. It is important to note that the three pairs of σ_+/σ_- MOT beams do not actually overlap at 90° angles along three orthogonal directions (which is the "modus operandi" for most MOT setups). Rather, two pairs of σ_+/σ_- MOT beams oriented on the same vertically oriented plane intersect in an "X" shape which crosses at an angle of $\theta_{1,2} = 40°$. The third pair of σ_+/σ_- beams intersects the "X" pair at an angle of $\theta_3 = 120°$ (see inset of figure 4.7a). While this optical setup differs from the conventional MOT setup of three pairs of orthogonal beams, 3D atom confinement is still achieved (although it is weaker than the conventional setup) since *components* of each beam are projected along the orthogonal $\hat{x}, \hat{y}$, and $\hat{z}$ directions.

With the laser setup completed, a pair of coils, where each is made with 100 turns of 20

gauge wire, is oriented along the $\hat{\mathbf{z}}$ direction of the AQuA Hex cell (inset of figure 4.7a). Running 1 A of current through the coils when the coil pair is oriented in the anti-Helmholtz configuration generates a positionally dependent magnetic field $\mathbf{B}(x)$ with gradient magnitude of $|B'| = 16$ G/cm. A flux of atoms is sent into the AQuA Hex cell from the 2D+ MOT formed in a chamber below the Hex cell and sources the 3D MOT [121]. Using this described 2D+/3D double MOT setup, a 3D MOT of approximately 10^7 atoms is created within 1 second of loading time (figure 4.8). This small 3D MOT functions as the reservoir of pre-cooled ^{133}Cs atoms for use in the atom transport and loading experiments described in sections 4.4, 4.5 and 4.6.

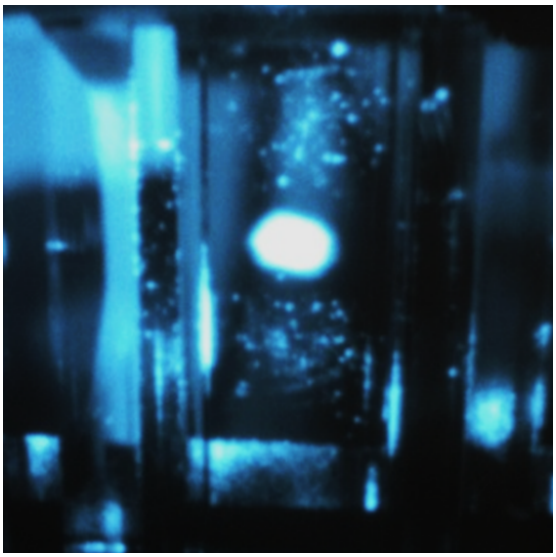

Figure 4.8: (Color online) Fluorescence image of A 3D MOT of approximately 10^7 cesium atoms and a diameter of 3 mm created in the AQuA Hex cell. The atoms that source the 3D MOT are initially cooled in a 2D+ MOT located in a chamber below the Hex cell. The 2D+ MOT atoms are subsequently pushed up into the Hex cell by use of a push beam.

After loading the 3D MOT, the cooling beams were further detuned to -20Γ which serves to act as an effective compressed MOT (CMOT) stage, since only atoms at the most intense region of the MOT beams will consistently absorb the laser light [3]. After the CMOT stage, time-of-flight absorption imaging (described in reference [122]) was performed to measure the temperature of the atoms to be $T_x = 80.1$ μK and $T_y = 67.7$ μK along the $\hat{x}$ and $\hat{y}$ directions, respectively, giving an average 3D MOT temperature of $T = 73.9$ μK (figure 4.9).

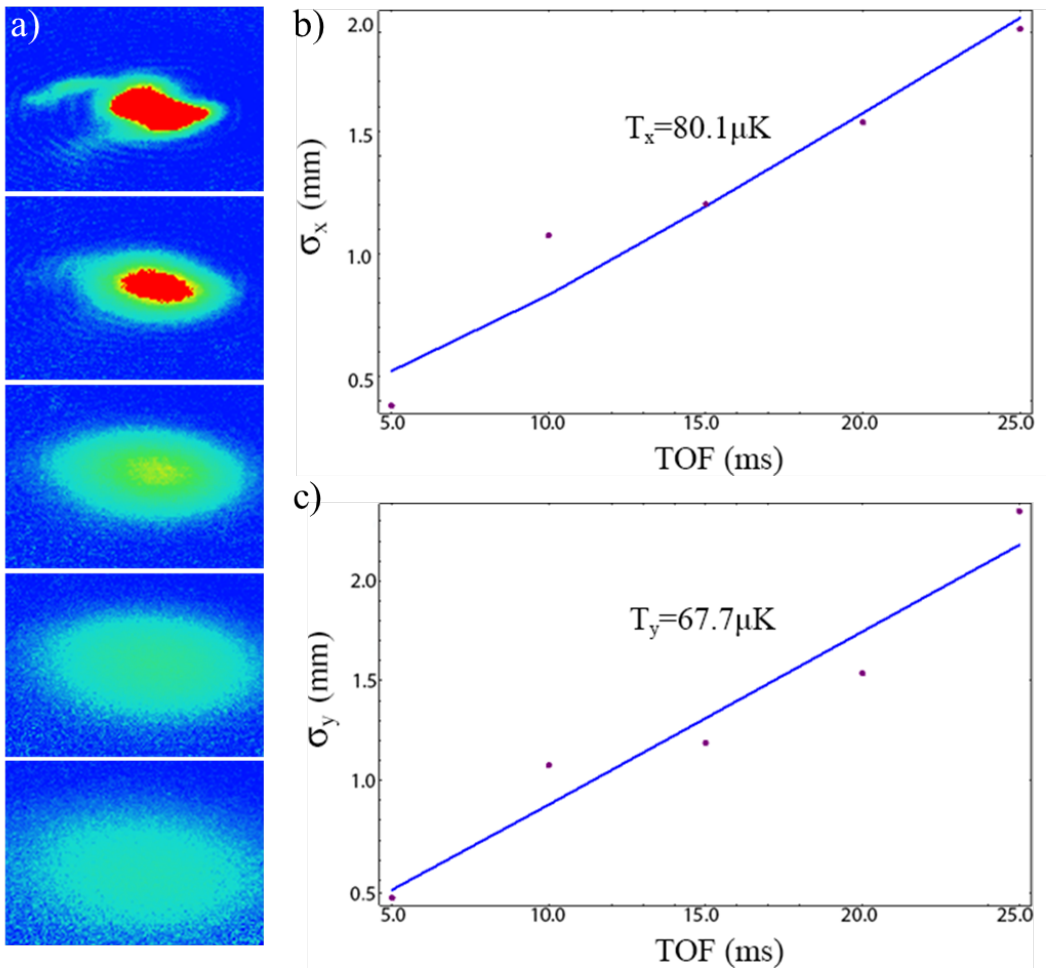

Figure 4.9: (Color online) a) Time-of-flight (TOF) absorption images of the 3D MOT after performing a CMOT stage. From top to bottom the TOF expansion times are 5 ms, 10 ms, 15 ms, 20 ms and 25 ms. b) and c) show the expansion of the Gaussian width $\sigma_x(t)$ and $\sigma_y(t)$ of the 3D MOT as a function of time. The TOF expansion data corresponds to atom temperatures of $T_x = 80.1$ μK and $T_y = 67.7$ μK along the $\hat{x}$ and $\hat{y}$ directions, respectively, giving an average temperature of 73.9 μK.

4.3.3 Polarization Gradient Cooling

In order to obtain maximum single atom loading probability and transport efficiency in the BoB trap and optical conveyor belt, we implement a polarization gradient cooling (PGC) stage after forming the 3D MOT to decrease the MOT temperature and increase the MOT atom density [123, 124, 125]. To perform PGC, the MOT coils are switched off while shim coils are turned on in order to eliminate or reduce stray magnetic fields to milligauss levels at the center of the Hex cell such that effective PGC can be applied to the atoms. During PGC, the 3D MOT lasers are left on but detuned -50 MHz or approximately -9.6Γ. After 10 ms of PGC, time-of-flight absorption imaging was performed to measure the temperature and density of the 3D MOT atoms to be approximately $T = 22.9$ μK and 10^{10} atoms/cm^3, respectively (figure 4.10). Polarization gradient cooling leaves the atoms with an energy that is a factor of about 100 smaller than the crossed vortex bottle beam trapping potential and a factor of about 25 smaller than the Gaussian beam array bottle beam trapping potentials. Most importantly, as discussed in sections 4.5.5 and 4.6.1, the high atom density remaining after PGC permits the average number of atoms that can be loaded into the crossed vortex BoB traps to be of order unity.

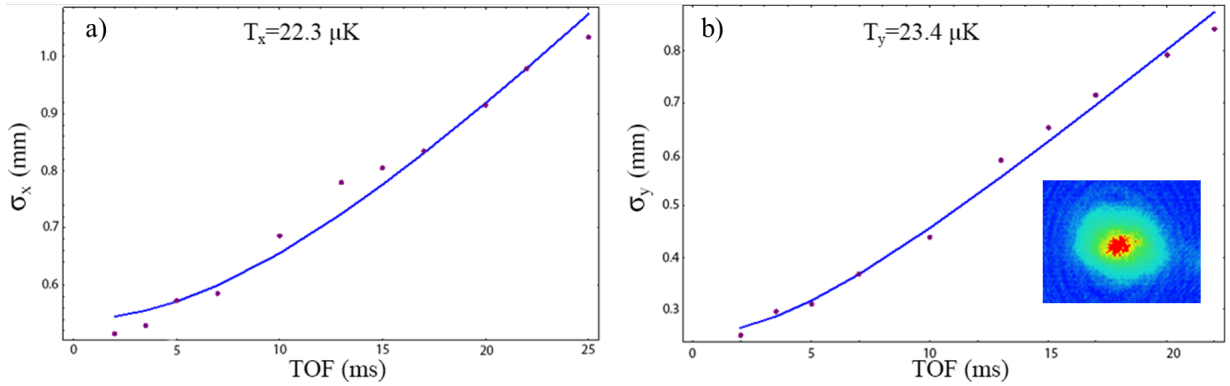

Figure 4.10: (Color online) a) and b) show Gaussian width σ_x and σ_y time of flight expansions of the 3D MOT atom cloud after performing 10 ms of polarization gradient cooling. Expansion of the atom cloud along the $\hat{x}$ and $\hat{y}$ directions gives respective temperature measurements $T_x = 22.3$ μK and $T_y = 23.4$ μK and average atom cloud temperature of 22.9 μK. The inset of b) shows an absorption image of a cesium 3D MOT with atom density of 10^{10} atoms/cm^3.

4.3.4 3D MOT and PGC Pagoda Coil System

Before concluding this section on generating a sufficiently cold ^{133}Cs atom reservoir, it is imperative to briefly outline the coil system for generating the larger magnetic quadrupole field necessary for the 3D MOT and the considerably smaller shim fields needed for PGC. We required the coil system to be capable of providing shim coils for all six AQuA Hex cell windows in order to produce bias fields along the optical axis of all cooling beams.

Moreover, the system must also provide shim coils for the $\hat{z}$ direction as well as providing a set of anti-Helmholtz coils for producing the 3D MOT magnetic fields. Most importantly, the mounting scheme must fully permit optical access to all windows of the AQuA Hex cell. With the assistance from professor Mark Saffman and Marty Lichtman from the University of Wisconsin, Madison, we were able to meet all of the above described design constraints by constructing a "pagoda" style coil mount[8] (figure 4.11a).

The pagoda coil mount is 3D printed from ABS plastic and features a heat deflection temperature of 98° C at 0.46 MPa and 88° C at 1.8 MPa. A recessed lip is found on all six vertical faces as well as the top and bottom faces of the pagoda mount in order to wrap the shim and 3D MOT coils. Once each coil was wrapped on its respective face of the pagoda mount, each coil was permanently fastened to the mount using Araldite epoxy. The finished coil system was then mounted over the Hex cell (figure 4.11b). When fixed around the Hex cell, there exists 5 mm of clearance between the outer surface of the Hex cell windows and the inner surface of the pagoda mount. The finished product (figure 4.11c) features 3 pairs of x-y shim coils for magnetic bias fields oriented normal to the Hex cell windows with gradients of 0.624 G/A, 0.639 G/A, and 1.54 G/A. The 1.54 G/A shim is higher to help cancel residual fields from the 0.624 G/A and 0.639 G/A shims (figure 4.11d). The shim coils oriented in the vertical direction create a magnetic bias field in the $\hat{z}$ direction with a gradient of 1.73 G/A. Finally, the set of anti-Helmholtz coils used to create the 3D MOT magnetic quadrupole field has a magnetic field gradient of 16 G/A.

[8] The "pagoda" mount aptly gets its name due to its slight resemblance of the religious pagoda structures found in eastern as well as southern Asia.

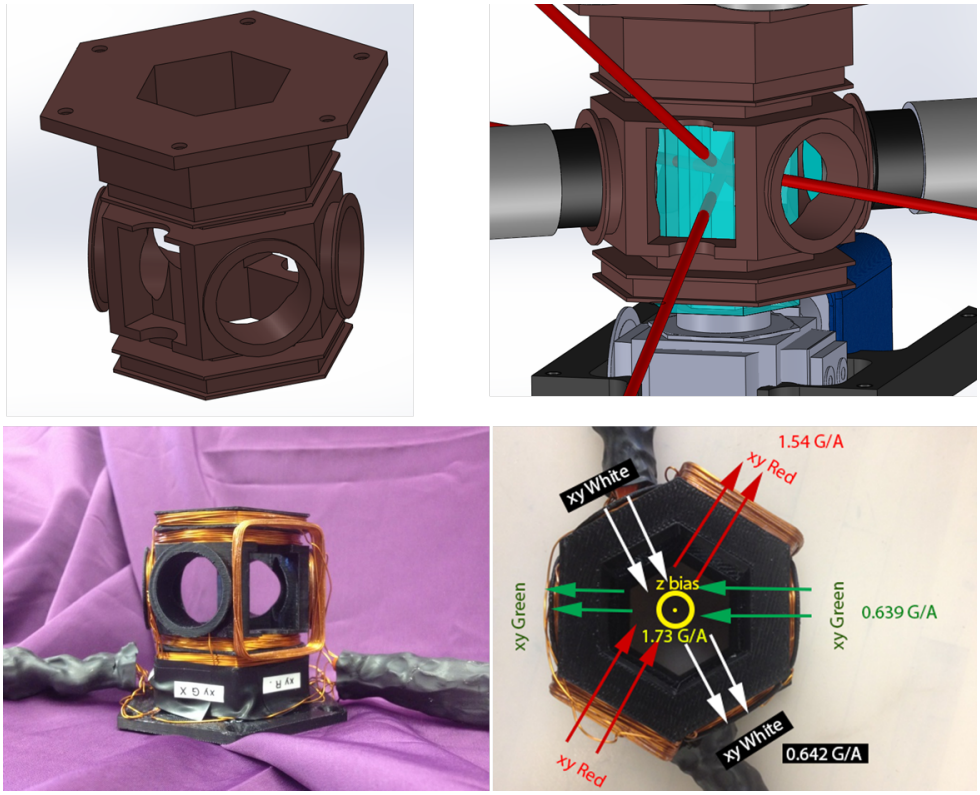

Figure 4.11: (Color online) Pagoda coil mount: a) 3D rendering of the pagoda coil mount. b) Rendering showing the pagoda mount position with respect to the Hex cell, the 3D MOT beams, as well as any high numerical aperture lenses. Note that optical access of all Hex cell windows is still permitted. c) Photograph of the pagoda coil system. d) Plot showing the direction of the magnetic field gradients from the 3 pairs of x/y shim coils as well as the z-bias coils.

4.4 Atom Transport System: Optical Conveyor Belt

4.4.1 1D Dynamic Lattice Potential

Atoms are transported from the 3D MOT to a single crossed vortex BoB trap by utiliing an optical conveyor belt. The optical conveyor belt is a 1D optical lattice potential that can move atoms back and forth along the axial direction of the lattice [126, 127, 128, 129]. Our optical conveyor belt is created inside the AQuA Hex cell by overlapping two $P = 5$ W, $\lambda = 1064$ nm, counter-propagating Gaussian laser beams with frequencies ω_1 and ω_2 and equal intensities of $I = 3.75 \times 10^8$ mW/cm^2 (figure 4.12). The resulting standing wave potential is [126, 128]

$$U(r, z, t) = U_0 \frac{w_0^2}{w(z)^2} \exp\left(-\frac{2r^2}{w(z)^2}\right) \cos^2(\pi \Delta\omega t - kz) \tag{4.4}$$

where w_0 is the laser beam waist size, $w(z)$ is the Gaussian beam waist, $k = 2\pi/\lambda$ is the wavenumber, and $\Delta\omega = \omega_1 - \omega_2$ is the detuning between the two 1064 nm beams.

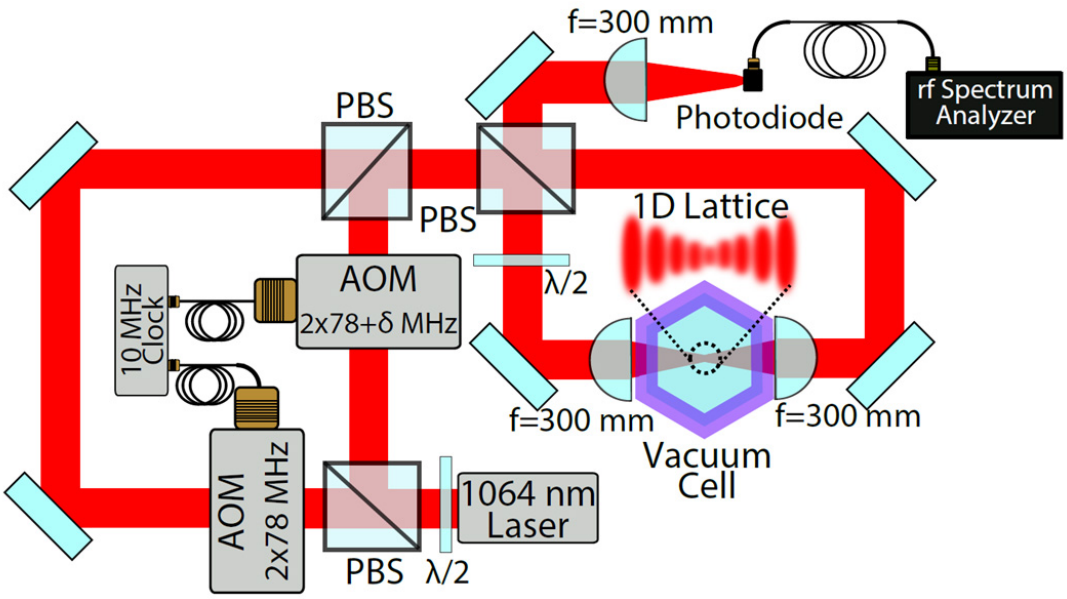

Figure 4.12: (Color online) Schematic of the optics and RF electronics used to create and transport the optical conveyor belt. An RF spectrum analyzer measures the velocity of the conveyor belt by measuring $\Delta\omega$ of the lattice beams.

The quantity U_0 is the maximum dipole potential and is defined as [72]

$$U_0 = \frac{\hbar\Gamma}{2}\frac{P}{\pi w_0^2 I_0}\frac{\Gamma}{\Delta}, \tag{4.5}$$

where $\hbar = 1.05 \times 10^{-34}$ J·s is the reduced Planck's constant, P and I_0 are the total laser power and saturation intensity at the atoms, $\Delta = 70$ THz is the detuning between the 1064 nm beam and the cesium D2 transition frequency, and $\Gamma = 2\pi \times 5.22$ MHz is the natural linewidth of the cesium D2 transition. In the atom transport experiments, both $\lambda = 1064$ nm lasers have an equal power of $P = 5$ and intensity of $I = 3.75 \times 10^8 \mathrm{mW/cm^2}$. From equation 4.6, focusing the beams to a waist of $w_0 = 30\mu$m at the center of the Hex cell produces a 1D lattice with with a maximum trapping depth of $U_0/k_B = -1.88$ mK. where $k_B = 1.38 \times 10^{-23}$ J/K is the Boltzmann constant. The axial and radial harmonic oscillation frequencies Ω_z and Ω_{rad} of atoms trapped at the focus of the 1D lattice are

$$\Omega_{\mathrm{z}} = 2\pi\sqrt{\frac{2U_0}{m\lambda^2}} = 2\pi \times 454 \text{ kHz} \tag{4.6}$$

$$\Omega_{\mathrm{rad}} = \sqrt{\frac{4U_0}{mw_0^2}} = 2\pi \times 3.6 \text{ kHz} \tag{4.7}$$

where the numerical values are computed using the values for U_0 and w_0 listed above.

The velocity v of the lattice potential $U(r, z, t)$ along the axial direction of the lattice is controlled by changing the lattice beam detuning $\Delta\omega$. The velocity[9] of the 1D lattice as a function of laser detuning is

$$v = \frac{\lambda\Delta\omega}{4\pi}. \tag{4.8}$$

The value of $\Delta\omega$, and hence v is set by passing each lattice beam through an acousto-optic modulator (AOM) initially driven at 78 MHz in a double-pass configuration (full schematic shown in figure 4.3 and concisely summarized in figure 7.8). The double-pass geometry allows for changes in laser frequency while avoiding changes in beam pointing, which is critical for maintaining the lattice

[9] To understand why detuning the lattice beams induces motion of the lattice, realize that there exists a reference frame moving along the axial direction of the lattice at a velocity v where both lattice beams are Doppler shifted to the same frequency, that is $\Delta\omega = 0$ in *this* frame. From the lab frame of reference, this is consistent with the lattice propagating along the axial direction with the same velocity v. Consequently, atoms that are trapped in this 1D lattice potential $U(r, z, t)$ are also translated with the same velocity v.

beam overlap throughout the experiment. To minimize phase jitter in the lattice, both AOMs are driven with independent RF drivers that are frequency locked and phase synchronized via the RF drivers' internal 10 MHz clocks.

4.4.2 Properly Accelerating the Dynamic 1D Lattice

It is important to note that in our atom transport experiments, the lattice detuning $\Delta\omega$, and hence conveyor belt velocity v, cannot just be "snapped" on instantaneously, as the resulting acceleration will heat the atoms out of the lattice. Rather, motion of the lattice is achieved by adiabatically frequency chirping one lattice beam by $\Delta\omega$. Frequency chirping the beams at an adiabatic rate is important since the total potential experienced by atoms trapped in the optical conveyor belt becomes a *tilted* lattice potential. In the atom reference frame, the complete optical conveyor belt potential along the direction of the lattice acceleration becomes

$$\begin{aligned} U_{\text{tot}}(r=0,z,t) &= U_0 \frac{w_0^2}{w(z)^2}\cos^2(kz) + maz \\ &\approx U_0 \cos^2(kz) + maz \end{aligned} \tag{4.9}$$

where a is the acceleration of the atoms. Shown in figure 4.13, the total potential is tilted upward or downward when the respective conveyor belt acceleration is positive or negative. During any atom transport sequence, as long as the 1D lattice potential is greater than the maz contributions from atom accelerations, then atoms will remain trapped in the optical conveyor belt. To solve for the maximum permitted acceleration in the tilted, moving potential, the local minimum of equation 4.9 as a function of acceleration a is computed by equating the spatial derivative of U_{tot} to zero:

$$\frac{dU}{dz} = -2U_0 k\cos(kz)\sin(kz) + ma = 0 \tag{4.10}$$

and solving for a

$$a = 2U_0\frac{k}{m}\cos(kz)\sin(kz). \tag{4.11}$$

Since the maximum value of $\cos(kz)\sin(kz) = 0.5$, it immediately follows that the maximum of equation 4.11, and hence maximum optical conveyor belt acceleration $a_{\max}$, is

$$a_{\max} = U_0 \frac{k}{m} \approx 5 \times 10^5 \text{ m/s}^2 \tag{4.12}$$

where the numerical value is computed using the values for U_0, k, and m listed in section 4.4.1. With the result in equation 4.12, we have an absolute speed limit for how fast we can transport the atoms with the optical conveyor belt. However, this does not tell us *how* to accelerate the atoms. During transport, a minimal amount of heating will occur when frequency chirping one of the lattice beams in a fashion that minimizes the rate of change of acceleration of the atoms.

Using equation 4.8, the velocity of the optical conveyor belt as a function of the mutual lattice beam detuning is

$$v = \frac{c}{2} \frac{\Delta\omega}{\Omega_z} \tag{4.13}$$

where $\omega = 2\pi c/\lambda$ is the initial, un-shifted frequency of the $\lambda = 1064$ nm transport laser. It immediately follows that the time rate of change of acceleration of the optical conveyor belt is

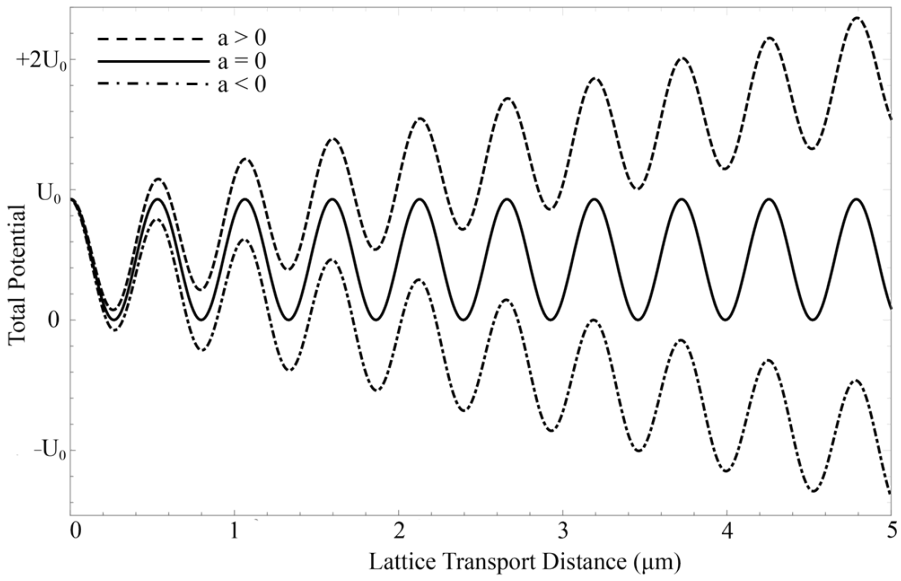

Figure 4.13: (Color online) Plot showing the Moving Standing Wave Potential for positive acceleration ($a > 0$), negative acceleration ($a < 0$), and no acceleration ($a = 0$).

expressed as

$$\frac{da}{dt} = \frac{d^2v}{dt^2} = \left(\frac{1}{\Omega_z} \frac{d^2\Delta\omega}{dt^2} - \frac{1}{\Omega_z^2} \frac{d\Delta\omega}{dt} + \frac{\Delta\omega}{\Omega_z^3} \right). \tag{4.14}$$

In our experiments, the lattice chirping $\Delta\omega$ will be a linear ramp. Thus, the $d^2\Delta\omega/dt^2$ term vanishes. Additionally, as shown in upcoming section 4.4.3, the lattice axial trap frequency $\Omega_z \gg \Delta\omega$, and thus we can approximate that $\Delta\omega/\Omega_z^3 \approx 0$. Using these approximations, the magnitude of the time rate of change of the conveyor belt acceleration is

$$\left| \frac{da}{dt} \right| = \frac{1}{\Omega_z^2} \left| \frac{d\Delta\omega}{dt} \right|. \tag{4.15}$$

In order to minimize this function, the lattice chirping must satisfy

$$\Omega_z^2 \gg \frac{d\Delta\omega}{dt}. \tag{4.16}$$

Equation 4.16 can be used to define a dimensionless adiabatic chirping parameter

$$\xi = \frac{\Omega_z^2}{d\Delta\omega/dt} \tag{4.17}$$

whereby $\xi \ll 1$ must be satisfied to transport atoms with minimal heating imparted from changes in acceleration of the optical conveyor belt. In our experiments, the desired adiabaticity parameter is $\xi \approx 10^{-3}$. Figure 4.14 displays a plot of the adiabaticity parameter ξ as a function of the frequency acceleration $d\Delta/dt$ and shows that $\xi = 10^{-3}$ is possible for $d\Delta\omega/dt \approx 2 \times 10^8$ Hz/sec, which corresponds to a frequency chirp of 500 kHz over 5 ms. Thus, any slower acceleration will always satisfy the desired ξ parameter. With proper acceleration schemes understood, we now demonstrate transporting atoms with the optical conveyor belt.

4.4.3 Demonstration of Atom Transport with an Optical Conveyor Belt

Approximately 6,000 atoms are loaded into the conveyor belt by overlapping the 1D lattice and the 3D MOT for 530 ms [130]. After loading the lattice, the MOT is turned off, leaving behind a reservoir of cold atoms in the lattice. To transport atoms using this optical conveyor belt, one lattice beam is linearly frequency chirped by 200 kHz over 5 ms. Because the AOMs are

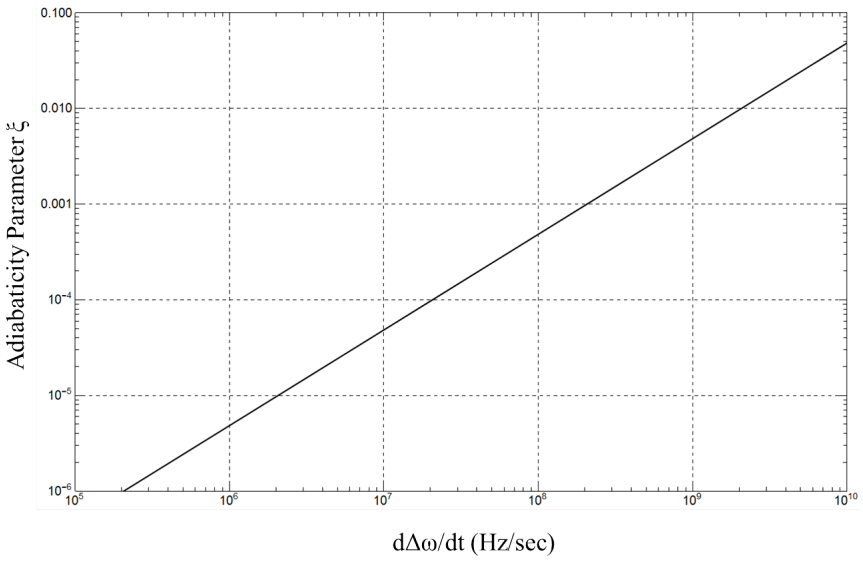

Figure 4.14: (Color online) Plot of the adiabatic parameter ξ as a function of the lattice chirping parameters $d\Delta\omega/dt$.

in the double pass configuration, this causes a lattice beam detuning of 400 kHz. With 400 kHz detuning, the optical conveyor belt accelerates to a maximum velocity of 212 mm/s. After this acceleration, the lattice beam is linearly chirped down -400 kHz over 5 ms to give zero detuning for the lattice. This process displaces any loaded atoms by 0.53 mm in 10 ms. The atoms are transported back to their original starting location by repeating the process in reverse. The entire procedure transports the atoms a total distance of 1.1 mm in 20 ms. A composite time-lapse image of this entire transport process is shown in figure 4.15.

As the optical conveyor belt motion abruptly starts and stops, large forces are imparted to atoms trapped in the 1D lattice. Consequently, cold atoms in the conveyor belt can be heated and even ejected from the lattice. As described in section 4.4.2 and equation 4.16, minimizing this heating effect is achieved by chirping the moving lattice at a much lower rate than the square of the lattice axial oscillation frequency. For motion of our optical conveyor belt the inequality holds as $\Omega_z^2 \sim 10^{12}$ s^{-2} and $d\Delta\omega/dt \sim 10^8$ s^{-2}. Additionally, we found that this transport process preserves approximately 87 percent of the atoms trapped in the optical conveyor belt. This atom survival probability is approximately equal to the atom survival in the stationary lattice over the same time

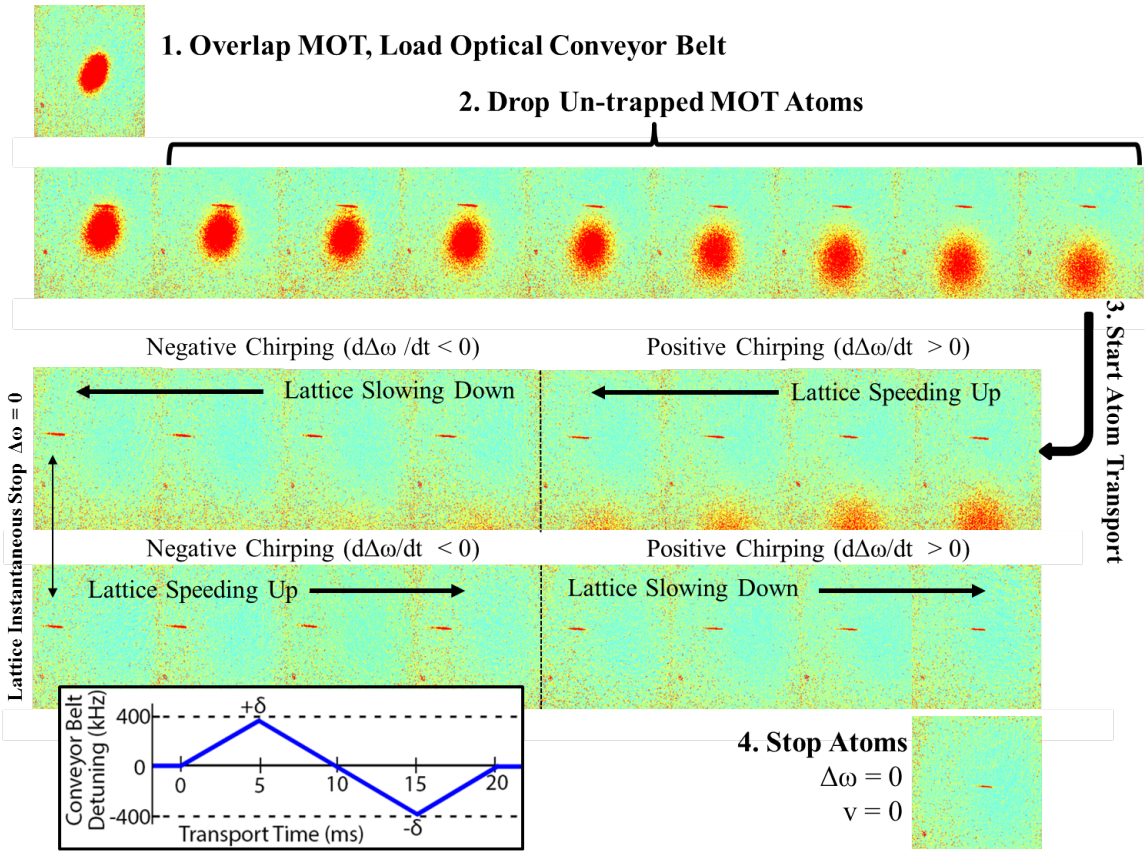

Figure 4.15: Absorption images showing the sequence of transporting cold atoms with an optical conveyor belt: 1) Atoms are loaded into the conveyor belt by overlapping the 1D lattice and the 3D MOT. 2) The MOT is turned off, leaving behind a reservoir of cold atoms in the lattice. 3) The frequency of one lattice beam is linearly frequency chirped and the optical conveyor belt accelerates to a maximum velocity. After this acceleration, the frequency of this lattice beam is linearly chirped again but with the opposite sign in order to slow the atoms down to a halt. The atoms are transported back to their original starting location by repeating the process in reverse. 4) Atoms are then held in place at the desired, final location. The inset shows a plot displaying the relative detuning $\Delta\omega$ of the lattice beams as a function of time during the conveyor belt transport process.

period (figure 4.16). Because the process of transferring a single atom from the conveyor belt and loading it into a BoB trap relies heavily on the atom density in the lattice, we chose to use the 400 kHz frequency chirping, as it permitted the farthest and fastest transport with the highest remaining atom density after transport. Also shown in figure 4.16, we tested transporting atoms at a much faster velocity and greater transport distances by using higher frequency chirps and longer transportation times. While we achieved greater transport distances of up to 5.32 mm, the more intense accelerations resulted in the atom survival rate rapidly declining to below 50 percent. More importantly, for these more intense accelerations, the remaining atom density after transport drops far below the remaining atom density of the stationary lattice over the same time durations, showing that heating due to these greater accelerations is outweighing the natural heating rate of the lattice.

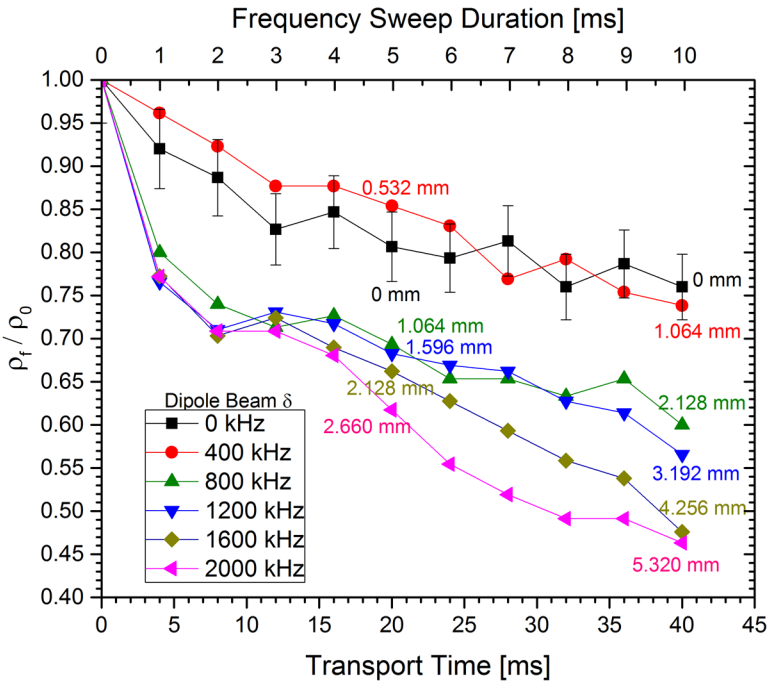

Figure 4.16: Change in atom density (atoms/cm^3) in the moving standing wave dipole trap after transport. The final density ρ_f is compared to the initial atom density ρ_0 for various AOM detunings and frequency sweep times for the moving standing wave dipole trap. The numbers written inside the plot show the transportation distance for each set of parameters. Note the black points indicate atom survival in the stationary lattice.

4.4.4 Laser Beam Overlap and Alignment Considerations

Successful atom transport with the optical conveyor belt depends critically on the degree of overlap between the two 1064 nm lattice beams and their relative polarization. The amplitude of the beat note $\Delta\omega$ of the 1D lattice beams is a maximum when the beams are entirely overlapped with parallel polarization. [131] Moreover, the line width of the beat note is used to quantify the phase jitter, and hence the axial position fluctuations of the conveyor belt. [131, 132, 133] The beat note is measured by focusing the overlapped 1D lattice beams onto a photodetector that is connected to an RF spectrum analyzer (Fig. 4.12). The lattice beams are focused using a lens with the same focal length used to focus the lattice in the vacuum cell.

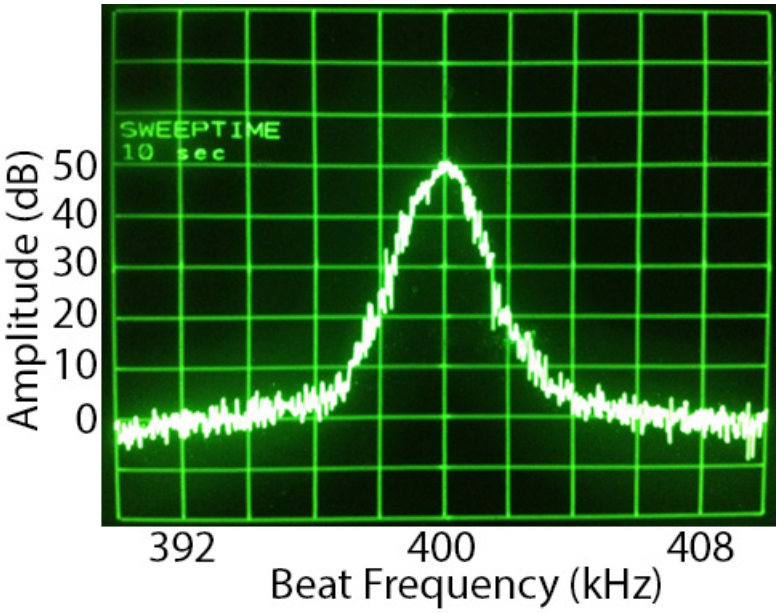

Figure 4.17: (Color online) Beat note spectrum measured by overlapping the two 1064 nm optical conveyor belt laser beams. The frequency spectrum peaks at 400 kHz and has a full-width at half-max of 1.33 kHz as measured at the -3dB point. This signal is used to quantify the lattice beam overlap, relative polarization, and phase jitter.

Additionally, to avoid beam distortions on the 780 nm BoB when passing through the 7.3 mm thick cell windows, the front face of the 0.4 NA lens must be aligned normal to the cell walls. [134] Otherwise, the BoB will never completely close in the axial direction, giving atoms an opportunistic

path to escape the trap. In order to have precise control over the position of the 0.4 NA lens, the lens is mounted with a compact lens positioner that provides adjustments along the x, y, and z axes in addition to control over θ_x and θ_y.

To deliver and load an atom into the BoB trap, the foci of the 780 nm and 1064 nm beams must overlap. As shown in Fig. 4.6, the optical axis of the 1064 nm conveyor belt and 780 nm BoB lie on the same plane but are at a 60 degree angle with respect to each other. To overlap their foci, an 852 nm resonant beam is sent backwards though the photon collecting fiber shown in Fig. 4.19 and is focused through the BoB trap. After transporting atoms to the BoB site, the conveyor belt is held in place while the resonant beam is snapped on. The resonant beam causes any trapped atoms in its path to be ejected from the conveyor belt. Performing absorption imaging provides visual proof of atoms ejecting from the trap and approximates the degree of overlap between the conveyor belt and BoB trap. Course adjustments of the conveyor belt position were made until only atoms at the focus of the conveyor belt were observed to be ejected. Fine alignment of the conveyor belt position was made by turning on the 3D MOT lasers after transporting atoms to the BoB site and counting the photons emitted from the atoms while still held in the lattice using the methods from section 4.5.3. Micron-scale adjustments of the conveyor belt position were made to optimize the fluorescence signal. With the photon counting signal at a maximum, there exists adequate overlap between the foci of the BoB trap, photon detection optics, and conveyor belt lasers. However, this degree of overlap contains the largest source of error for this technique, due to the lack of a distinct, physical reference point for the microscopic BoB trap.

With the optical conveyor belt system and the atom transport process described, we now introduce the optical bottle beam traps that we will deliver a single transported atom into.

4.5 Trapping Single Atoms in a Crossed Vortex Bottle Beam Trap

4.5.1 Overview of Optical Bottle Beams

An optical bottle beam (BoB) is an electric field distribution that features a region of low optical intensity completely surrounded by high optical intensity. Various BoB intensity profiles taken from the PhD thesis of Siyuan Zhang[10] are shown in figure 4.18. In this dissertation, the laser light used to form the BoB intensity profiles has wavelength $\lambda = 780$ nm and is blue-detuned from resonance. From equations 2.11 and 2.12, by using blue-detuned light, the regions of the BoB with high intensity produce a repulsive potential, forcing the atoms to seek regions of low optical intensity. Thus, atoms can become trapped in the central, dark region of the BoB. While a red-detuned dipole trap is considerably easier to implement for trapping atoms, the upside of the blue-detuned BoB trapping scheme is that it is very useful for confining single cesium atoms for use in quantum computing (which is the intended application of this work). Atoms in the dark, blue-detuned traps subsequently scatter less photons than if they were trapped in a red-detuned dipole trap of comparable depth. Since the qubit decoherence time is proportional to the photon scattering rate of the trapped qubit, trapping in blue-detuned BoBs can result in coherence times 300 times longer than those observed in red-detuned dipole traps with similar trapping depths [135].

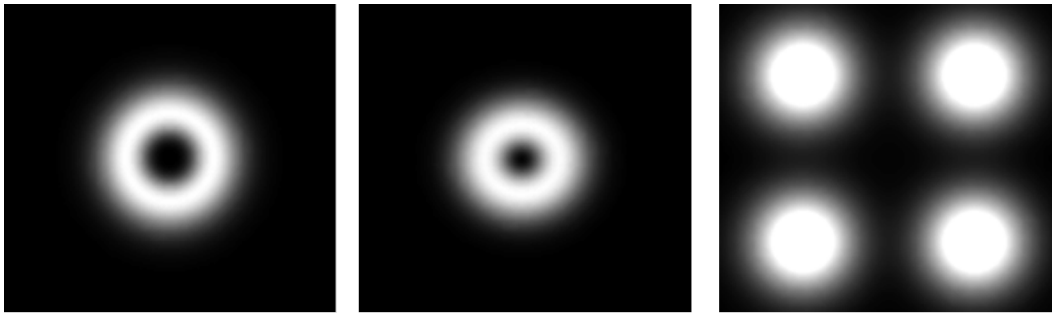

Figure 4.18: (Color online) Various Bottle Beam Intensity Profiles: a) Gaussian interference BoB made from the destructive interference of two TEM00 Gaussian modes with different waists. b) Crossed Vortex BoB made from a Laguerre-Gaussian LG01 mode. c) Gaussian Beam Array BoB made from four TEM00 Gaussian modes.

[10] From Mark Saffman's group at the University of Wisconsin, Madison.

4.5.2 Generating a Crossed Vortex Bottle Beam Trap

The intensity profiles of the BoBs shown in figure 4.18a,b would generate radial confinement (along $\hat{x}$ and $\hat{y}$) but not axial confinement along the direction of beam propagation ($\hat{z}$, i.e. in and out of the page). To provide confinement along the axial direction, additional blue-detuned light must close the ends of the BoB (or "cap" the bottle beam). A BoB trapping potential is formed for the experiment in this dissertation by using a high numerical aperture (0.4 NA) lens to tightly cross two co-propagating Laguerre-Gaussian LG01 beams with orthogonal linear polarizations at a tight focus. Because the LG01 beams are sometimes called "vortex beams" this optical configuration gives the trap the appropriate name of "Crossed Vortex Bottle Beam Trap."

The complete, detailed schematic for generating the co-propagating pair of orthogonally polarized LG01 beams with identical beam waists of $w = 1.61$ mm and separated by distance $d = 5$ mm is shown back in section 4.2.2, figure 4.3b. With the LG01 beams created, figure 4.19 shows how we form the BoB trap by using a high quality, diffraction limited 0.4 NA lens with focal length $f = 23.125$ mm to tightly focus and overlap the LG01 beams at the center of the AQuA Hex cell. As the beams are focused with the lens, they are rotated by

$$\theta = \tan^{-1}\left(\frac{d}{2f}\right) = 6.17^{\circ}. \tag{4.18}$$

Because the rotation is small ($\theta < 10^{\circ}$) the changes in polarization to each LG01 beam can be neglected. The resulting crossed vortex intensity profile I_{CV} is also shown in figure 4.19 and is given as the sum of both linearly polarized LG01 beams:

$$I_{\mathrm{CV}}(r,z) = I_{l,p}\left(r_+, z_+\right) + I_{l,p}\left(r_-, z_-\right) = I_{1,0}\left(r_+, z_+\right) + I_{1,0}\left(r_-, z_-\right) \tag{4.19}$$

where the intensity of each LG beam, $I_{l,p}(r,z)$ is defined in equation 4.3. For the intensities in equation 4.19, the radial coordinates $r_\pm$ are defined [102] as

$$r_\pm = \sqrt{y^2 + (x\cos\theta \pm z\sin\theta)^2} \tag{4.20}$$

and the axial coordinates $z_\pm$ are

$$z_\pm = z\cos\theta \mp x\sin\theta. \tag{4.21}$$

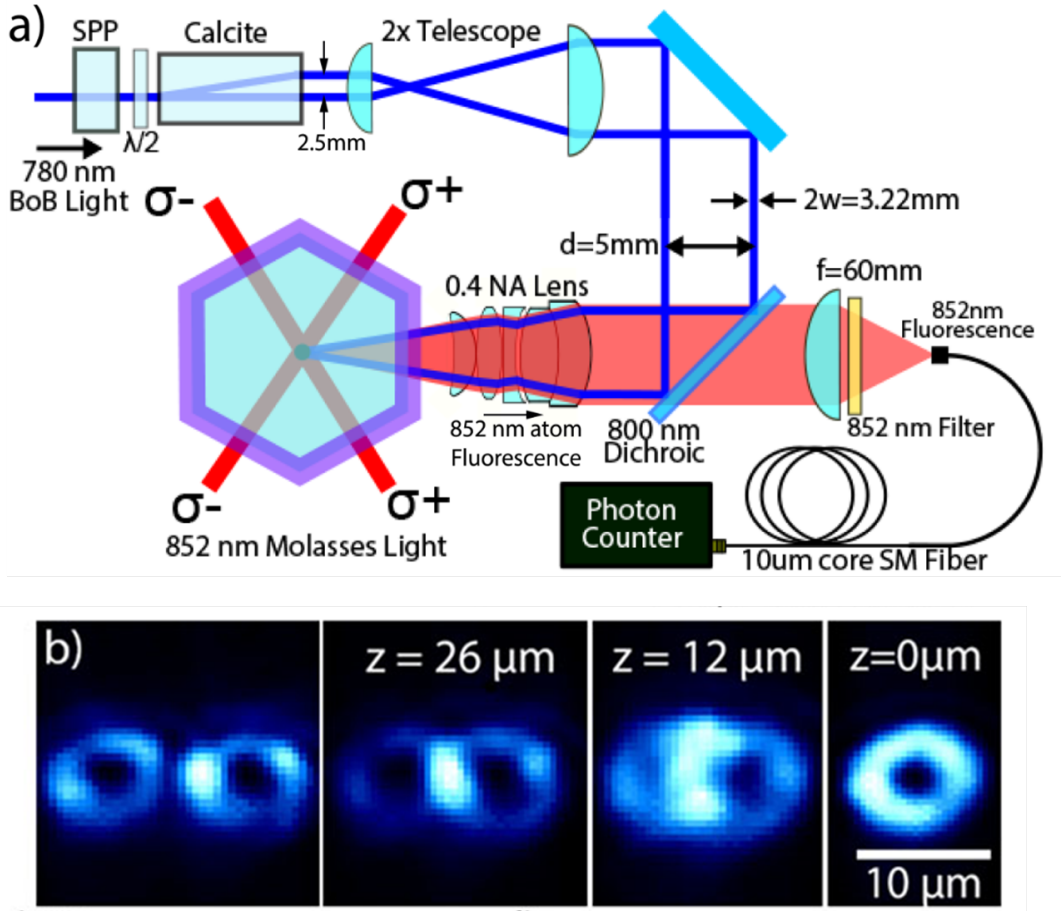

Figure 4.19: (Color online) Top: Optical setup for generating and imaging the crossed vortex bottle beam trap. The added optical molasses light is used for fluorescence imaging on an atom trapped in the BoB. A fraction of atom fluorescence is collected with the 0.4 NA lens and propagated into a counter to perform photon counting statistics. Bottom: Intensity profile at of the crossed vortex BoB trap forming as the two LG01 mode lasers are focused at the focal plane of the 0.4 NA lens. Images a), b), c), and d) show the trap at axial lengths $z = 34$ μm, $z = 26$ μm, $z = 12$ μm, and $z = 0$, respectively from the focus of the 0.4 NA lens.

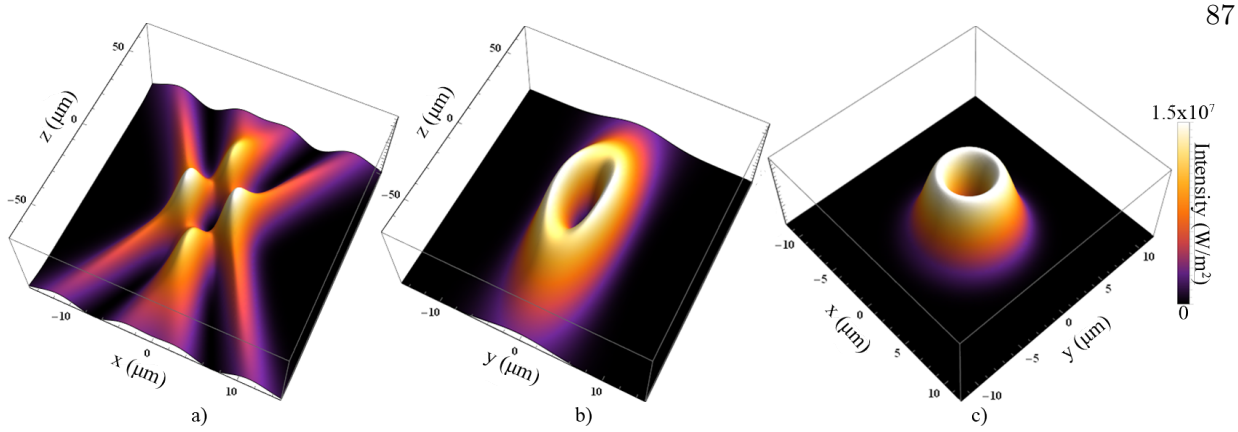

Figure 4.20: (Color online) Crossed Vortex Bottle Beam trapping potentials along the xz, yz, and xy planes at the focus of the 0.4 NA lens.

where the $\pm$ subscripts refer to the π_+ and π_- linearly polarized LG01 beams, respectively. The total optical trapping potential of the crossed vortex BoB trap is then numerically calculated by inserting equation 4.19 into equation 2.11. The calculated trapping profiles along the orthogonal xz, yz, and xy planes at the focus of the crossed vortex BoB are plotted in figure 4.20. With respect to the parameters of this experiment, at the focus of the 0.4 NA, $f = 23.125$mm lens, the crossed vortex BoB trap has a width of 5.5 μm in the radial direction and an axial length of 52 μm. Using 300 mW of 780 nm light produces a calculated BoB trap depth of $U/k_B = 1.65$ mK, with harmonic oscillation trap frequencies of $\Omega_{\text{rad}} = 2\pi \times 51$ kHz in the radial direction and $\Omega_{\text{z}} = 2\pi \times 5.3$ kHz in the axial direction (figure4.21).

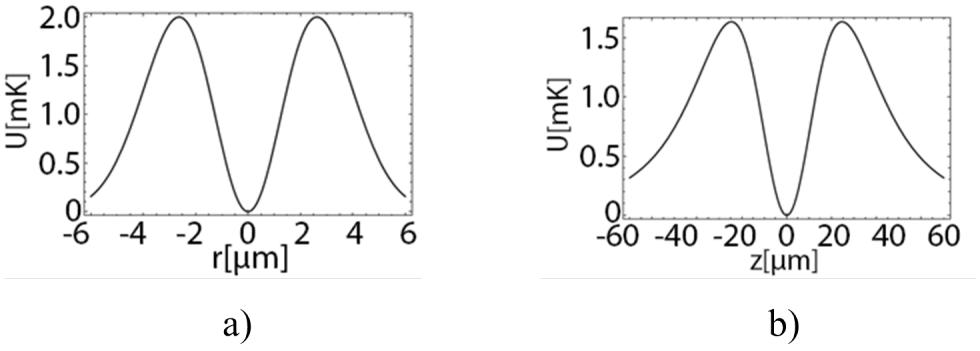

Figure 4.21: Numerically calculated a) radial and b) longitudinal trap depths produced by the crossed vortex BoB.

Finally, in order to get an intuitive understanding of how the final size of the crossed vortex BoB affects the trapping depth, the equations for the trapping potential can be vastly simplified by choosing to perform a Taylor series expansion of the intensity (equation 4.19) about the origin. Such expansion of the trap depth about $(x = 0, y = 0, z = 0)$ gives [102]

$$U(x) \approx -\frac{2\alpha P \cos^2\theta}{\pi\epsilon_0 c w^4} x^2 \tag{4.22a}$$

$$U(y) \approx -\frac{2\alpha P}{\pi\epsilon_0 c w^4} y^2 \tag{4.22b}$$

$$U(z) \approx -\frac{2\alpha P \sin^2\theta}{\pi\epsilon_0 c w^4} z^2. \tag{4.22c}$$

Equations 4.22a, 4.22b, and 4.22c convey a very important result that the crossed vortex BoB trap potential scales as w^{-4}, meaning (for the experimentalist) that meticulous care must be made when focusing the LG01 beams though the thick Hex cell walls to ensure that as little distortions as possible occur such that the final beam waist of $w_0 = 5.5$ μm is correct.

4.5.3 Detecting a Loaded Single Atom

Fluorescence imaging is used to detect the presence of a single atom loaded into the crossed vortex BoB trap. When a single atom is loaded, a 3D optical molasses is applied to the trapped atom by turning on the 3D MOT lasers and detuning them -30 MHz. Repump light is also turned on. Additionally, the MOT coils are turned off and shim coils are used to eliminate any residual magnetic fields. This induces atom fluorescence while continuously cooling the trapped single atom. As shown in figure 4.19, the fluorescence is collected and collimated with the same 0.4 NA, f=23.125 mm lens used to focus the BoB trap. Photons collected from the trapped atom are separated from the 780 nm trapping light by an 800 nm short-pass dichroic mirror (also shown on figure 4.19). The collimated fluorescence is then focused by an f=60 mm achromatic doublet lens into a 10 μm core diameter single mode optical fiber that is coupled into a single photon counting module (SPCM). The 10 μm fiber functions as a pinhole for spatial filtering of the fluorescence. Since the optical magnification from the BoB trap to the pinhole is 2.6, a window 3.85 μm in diameter is thus selected at the BoB trap focus. Two 852 nm laser line filters are used to eliminate stray 780 nm BoB light.

The SPCM works alongside an avalanche photodiode to count individual photons emitted from the trapped atom over an arbitrary time interval. When exposed to optical molasses, the trapped atom scatters on the order of 10^5 photons over a 50 ms interrogation time. Since the fluorescence collecting lens has an effective focal length of 23.125 mm and an aperture of 18 mm, the collection angle is $\Omega/4\pi = 4.67\%$. Total transmission of the photon collecting optics is approximately 50% and the quantum efficiency of the SPCM at 852 nm is 54%. Thus, the maximum photon collection efficiency is approximately 1.1%. Additionally, noise of approximately 100 counts/sec of 780 nm light and approximately 25 dark counts/sec is recorded using the photon counter.

4.5.4 Loading a Bottle Beam Trap from a Background MOT

To verify that our BoB is capable of trapping a single atom, we first attempted to load the BoB trap directly from a 3D MOT. The MOT was loaded for 1 second followed by PGC (as described in section 4.3.3) for 10 ms. During the final 5 ms of PGC, the BoB is snapped on in 300 μs and overlaps the central and most dense region of the 3D MOT. If multiple atoms are initially loaded into the BoB trap, a useful process between pairs of atoms called light assisted collisions[11] will reduce the trap occupation to zero or one atom [136]. After loading the BoB trap and allowing time for light assisted collisions, all MOT lasers are turned off for 20 ms to let any untrapped atoms fall away due to gravity. After this fall time, the MOT beams are turned back on and fluorescence imaging on the trapped single atom is performed (described in section 4.4.3). A histogram of the photon counting data recorded by the SPCM is shown in figure 4.22.

The photon counting statistics for 1002 independent atom loading attempts show two Poisson distributions corresponding to either 0 or 1 atom confined in the BoB trap after any given loading trial. When 0 atoms are present in the BoB trap, a mean of $n_{bg} = 125$ background photons are counted over 50 ms (figure 4.22). This signal arises from stray 852 nm molasses light and 780 nm

[11] As atoms confined in the BoB approach each other in the presence of the MOT laser light, there exists a critical inter-atomic separation where the laser light excites a long-range, attractive dipole-dipole interaction between pairs of atoms, which results in the atom pair gaining considerable kinetic energy leading to collisions that expel *both* atoms from the BoB trap. Consequently, if an even number of atoms occupy the BoB trap, they will all pair-collide until no atoms remain in the trap, whereas an odd number of atoms will pair-collide until only one atom remains in the trap.

trapping light being collected by the detection optics. During trials when one atom is loaded in the BoB trap, the number of photons detected over 50 ms increases to a mean of $n_1 = 215$ counts (Fig. 4.22) due to the added fluorescence from the atom trapped in the BoB. Photon counting statistics show that a single atom is loaded into the BoB trap in 45.2% of all loading trials. The near complete absence of multi-atom loading events is due to light assisted collisions and the collisional blockade effect. [136, 137, 138]

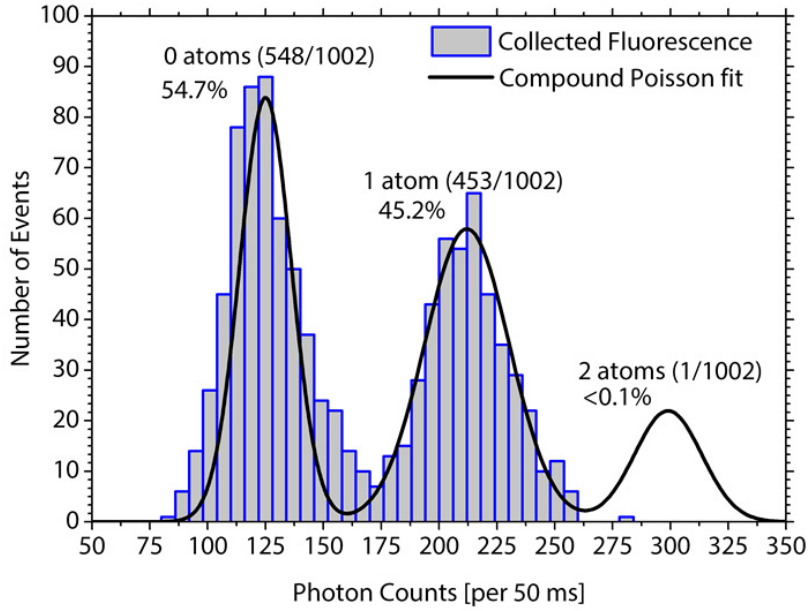

Figure 4.22: (Color online) Histogram of photon counting data recorded during fluorescence imaging of the BoB trap. Two Poisson distributions are present with means of 125 counts and 215 counts, corresponding to 0 or 1 atom present in the BoB trap, respectively. The histogram is fitted with a compound Poisson distribution over atom and photon number.

The photon counting data is fitted to a compound Poisson fit

$$\mathcal{P}(n) = A \sum_{k=0}^{2} \frac{N^k e^{-N}}{k!} \frac{1}{\sqrt{2\pi\left(n_{bg} + kn_1\right)}} \exp\left[-\frac{\left(n - \left(n_{bg} + kn_1\right)\right)^2}{2\left(n_{bg} + kn_1\right)}\right] \tag{4.23}$$

For random loading following a Poisson distribution

$$P(k) = \frac{N^k e^{-N}}{k!} \tag{4.24}$$

the probability of loading a single atom (assuming that on average we load one atom) has an upper bound of $P(1) = e^{-1} = 0.368$. Thus, following random loading, $P(1) \leq 0.368$. However,

from figure 4.22, a single atom is loaded 45.2% of all loading trials, corresponding to a variance of $(\Delta N)^2 = 0.452N$ which is *smaller* than the variance of the Poisson distribution, $(\Delta N)^2 = 0.368N$, which shows that the atom loading is sub-Poissonian in nature.

4.6 Demonstration of Single Atom Delivery and Loading into a Crossed Vortex Bottle Beam Trap

This section chronicles the experimental results of delivering and loading a single atom into a crossed vortex BoB trap. A discussion on applying the results to qubit array systems (as discussed in section 1.3) as well as motivating scaling the experiment to address an array of BoB traps (as discussed in chapter 5) is included.

4.6.1 Atom Transport and Reloading Operation

Each run of the experiment begins with using the 3D MOT system described in section 4.3.2 to create a reservoir of 10^6 atoms at $T \approx 75$ μK within 1 second. During the last 480 ms of the 3D MOT loading time, the 1064 nm optical conveyor belt lasers with no mutual detuning ($\Delta\omega = 0$) are un-shuttered and overlap the MOT. Approximately 5000 to 6000 of the 3D MOT atoms are loaded into the stationary 1D lattice. Polarization gradient cooling, as described in section 4.3.3 is applied throughout the final 10 ms of the conveyor belt loading time, cooling the loaded atoms to $T \approx 25$ μK and increasing the atom density to $\rho \approx 10^{10}$ atoms/cm^3.

It is essential to mention that the probability of loading a single atom into the BoB trap is directly proportional to the atom density trapped in the optical conveyor belt. With the BoB approximated as an ellipsoid, an upper bound for the BoB trap volume is

$$V = \frac{4}{3}\pi r_{rad}^2 r_z \tag{4.25}$$

where r_{rad} is the radius along the radial direction and r_z is the axial radius. Fig. 4.19 shows that $r_{rad} = 2.75$ μm and $r_z = 26$ μm, which gives a total BoB trapping volume of approximately 8.23×10^{-10}cm^3. After the entire atom transport sequence (Fig. 4.15), approximately 3,000 atoms

remain in the conveyor belt and the atom density is approximately 1.4×10^9 atoms/cm^3. Thus, an upper bound to the expected number of atoms that can be overlapped with the BoB trap is $\langle N \rangle = V_{\text{BoB}} \times \rho$ [139] which corresponds to overlapping an average of 1 atom per trial. Therefore, maintaining an atom density of 10^9 atoms/cm^3 in the conveyor belt after transport is crucial.

After loading the optimal atom density into the optical conveyor belt, atoms are transported 1.1 mm to the BoB trap site by following the frequency chirping sequence outlined in section 4.4.3 where one lattice beam is linearly frequency chirped by 400 kHz over a 5 ms time interval and accelerated to a maximum velocity of 212 mm/s. The lattice beam is then linearly chirped down -400 kHz over another 5 ms period to instantaneously stop the conveyor belt before repeating the chirping sequence in reverse to bring the atoms back to the starting point. This series of lattice beam frequency chirps first transports atoms a distance of 0.530 mm along the axial direction followed by an additional 0.530 mm in the reverse direction for a total transport distance of 1.1 mm in 20 ms. Time-of-flight temperature measurements performed on the transported atoms show that atom temperatures rise to 70 μK after transport in the conveyor belt. Ballistic expansion in the radial direction of the conveyor belt was chosen for time-of-flight temperature measurements since it expands faster and therefore shows greater temperature dependence than in the axial direction [140]. To load a single atom in the BoB trap from the conveyor belt and also to successfully image the loaded atom, the transported atom temperature should optimally be a factor of 50 colder than the BoB trap depth [106]. To cool the transported atoms to such an optimal temperature, an additional 10 ms of PGC is applied to the atoms immediately after transport while still held in the 1D optical lattice. The intense light shift imparted by the lattice (equation 2.11) detunes the atoms an additional -8Γ, giving a total detuning of -14.6Γ. When applying PGC after transport the atoms have an average temperature of 15 μK as compared to a temperature of 70 μK when no extra PGC is applied (figure 4.23).

During the final 5 ms of the additional PGC, the BoB trap is snapped on and overlaps the focus of the optical conveyor belt. This permits an atom to load from the transported 1D lattice into the BoB trap. After loading, the optical conveyor belt is turned off while still holding the BoB

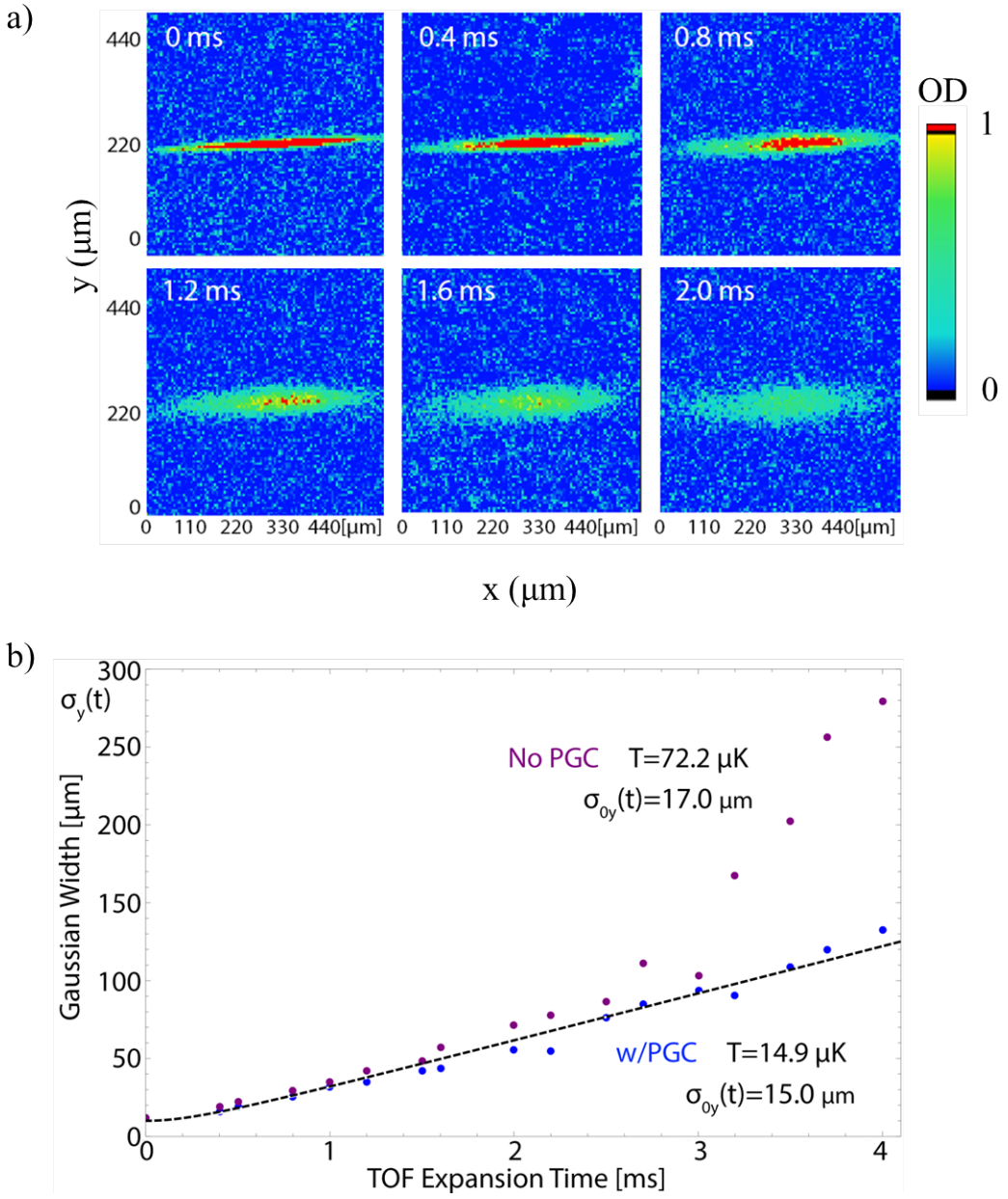

Figure 4.23: (Color online) a) Density profiles of ^{133}Cs atoms at different time-of-flight (TOF) expansion times after horizontal transport with the optical conveyor belt. b): Graph showing the size of the atom clouds at different TOF expansion times when extra PGC is applied (blue dots) compared to no PGC (purple dots). The TOF expansion data shown here corresponds to an atom cloud temperature of 14.9 μK when PGC is applied to the transported atoms. Without the extra PGC, the transported atom temperature is considerably higher at 72.2 μK.

trap to allow all untrapped atoms to fall away. At this point in the experiment, the BoB is loaded with either zero or one atom. A complete synopsis of the timing scheme for single atom loading via an optical conveyor belt is presented in figure 4.24.

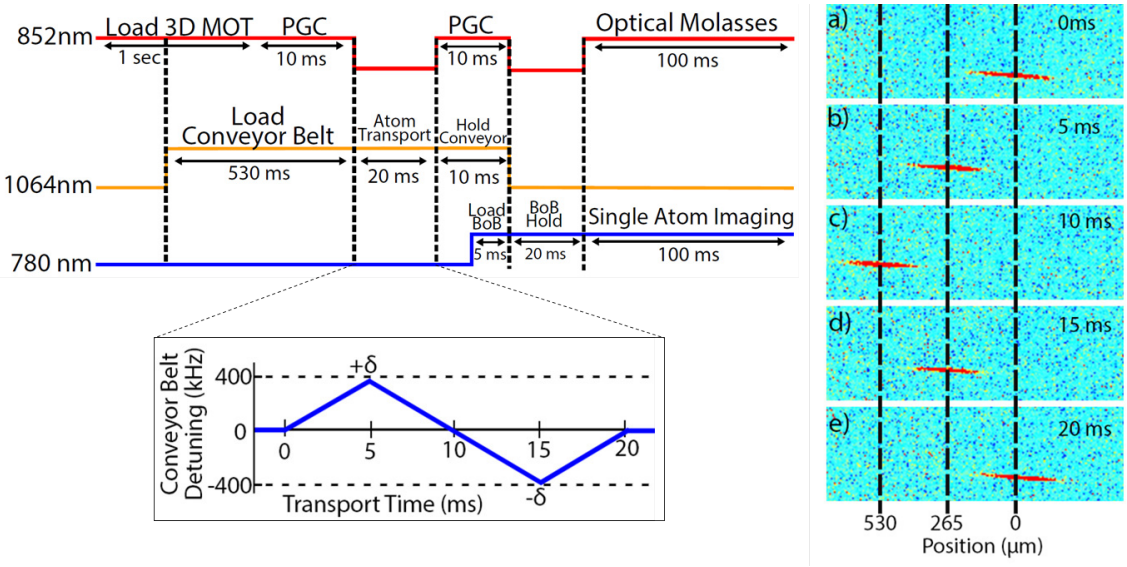

Figure 4.24: (Color online) Summary of the Atom Transport and Loading Experiment: Left: Timing scheme for different stages of the atom transport and delivery process involving the 780 nm BoB lasers, 852 nm MOT lasers, and the 1064 nm conveyor belt lasers. A graph shows the mutual detuning $\Delta\omega$ between the 1D lattice beams as a function of time during the conveyor belt transport process. Right: Absorption images showing atoms transported 1.1 mm with the optical conveyor belt at various times during travel. Images a), b), c), d), e) show the loaded conveyor belt at 0, 5, 10, 15, and 20 ms, respectively. Furthermore, images a) and e) show the conveyor belt at the initial and final transport locations. Images b) and d) show the conveyor belt when it reaches the maximum velocity of 212 mm/s. Image c) shows the conveyor belt at the turn around point. Approximately 3,000 atoms remain in the conveyor belt after transport.

Fluorescence imaging, as described in sections 4.5.3 and 4.5.4, is performed on the BoB trap for 100 ms to observe if zero or a single atom is successfully delivered and loaded into the trap. A histogram of the photon counting data is shown in figure 4.25. During fluorescence imaging, an average of 300 photons are detected when no atom is present in the BoB trap. When an atom is loaded into the BoB trap, the average number of counted photons increases to 570 counts. The photon counting statistics for 843 atom delivery and loading attempts confirm that an atom can be delivered and loaded into the BoB trap 13.1% of the time, with no multi-atom loading events ever recorded.

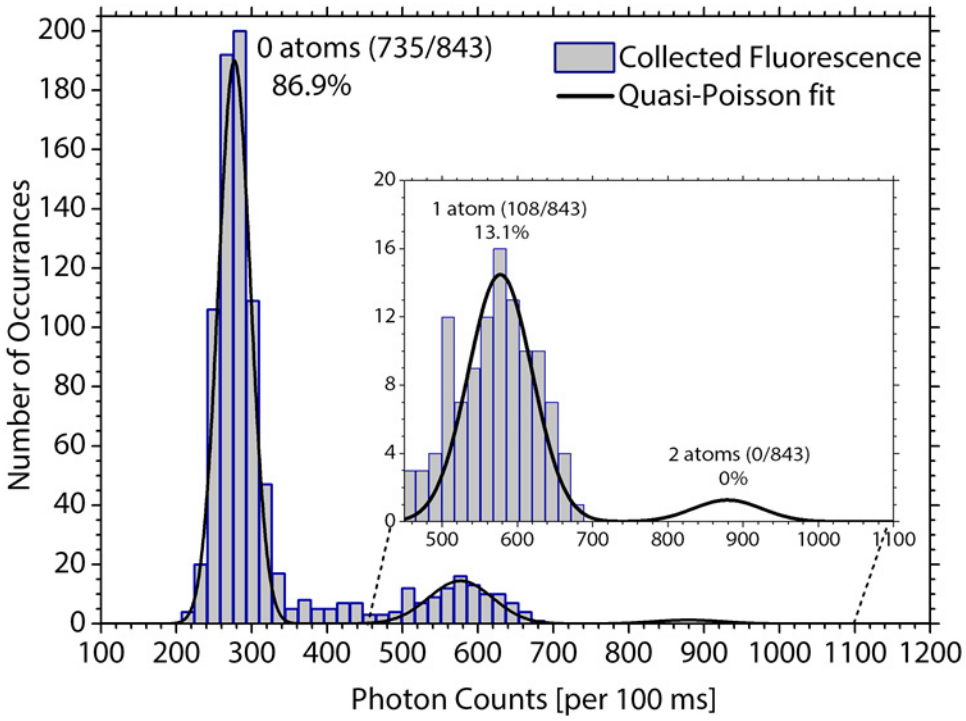

Figure 4.25: (Color online) Histogram of photon counting data recorded during fluorescence imaging of the BoB trap after delivering the atom via an optical conveyor belt. Two Poisson distributions are present with means of 300 counts and 570 counts. The peaks correspond to loading 0 or 1 atom, respectively, in the BoB trap with the optical conveyor belt. The histogram shows that a single atom is delivered into the BoB trap 13.1% of the time. The histogram data is fitted to a compound Poisson distribution over atom and photon number.

4.6.2 Further Discussion for Continuous, Uninterrupted Loading

This technique provides a method for correcting atom loss errors for single atom BoB traps used in neutral atom quantum computing systems. In order to provide an optimal vacuum environment for trapped qubits and qubit gate operations, the 3D MOT that supplies the source of cold atoms for atom reloading should be located in a separate vacuum chamber positioned adjacent to the chamber that houses the BoB traps. This also permits the 3D MOT to be on continuously, as the MOT footprint will not disturb any previously trapped atoms. Using an uninterrupted 3D MOT, the presented technique for single atom delivery and loading takes a total of 680 ms, as the procedure (fig. 4.24) involves loading the conveyor belt (530 ms), transporting and loading the atom into a BoB trap (50 ms), and then finally imaging to verify the presence or absence of a single atom (100 ms). The total time for delivering and loading an atom can be reduced to a little as 55 ms total, as far-off resonance dipole traps, and hence the optical conveyor belt, can be loaded in as little as 10 ms, depending on the trap detuning, intensity, and the vacuum background pressure,[130] while single atom signals can be observed using fluorescence imaging with exposure times as little as 5-10 ms [1, 141]. Additionally, the BoB hold time discussed in both section 4.6.1 and figure 4.24 can be decreased to 10 ms. Even shorter hold times are possible but at the expense of introducing fluorescence noise from untrapped atoms that may be collected during imaging.

With a 13.1% probability of successful single atom delivery and loading, 33 loading trials will need to run in order to have single atom loading with 99% confidence. Working in the lower limit of a 55 ms loading time, the procedure will require 1.82 seconds to reload an atom if all 33 trials are needed, which is within the necessary interval of time of 2 seconds to keep a 49 element qubit array continuously occupied (discussed in sections 1.2 and 1.3). Additionally, with a 13.1% probability of successful atom reloading, 50 loading trials are required to reload an atom with 99.9% confidence, which requires 2.75 seconds if all trials are needed, which is slightly greater than the necessary time to reload a site.

Finally, the single atom loading efficiency of this technique may be improved by incorporating

methods that suppress the inherit stochastic characteristics present with using red-detuned, light-assisted collisions to prepare a single atom in the BoB trap. One such method uses a feed-back mechanism to rapidly prepare a 3D MOT with a single atom,[142] while another method uses additional blue-detuned lasers, rather than MOT lasers, to induce repulsive light-assisted collisions to prepare single atoms in dipole traps [143, 144, 145, 137]. These methods have the capabilities to prepare single atoms directly from a MOT within 20-200 ms with average efficiencies ranging from 80% to 90%. If implemented after atoms are delivered to the BoB trap via transport as discussed in section 4.4, they may increase the single atom loading efficiency.

4.6.3 Demands to Upscale Transport and Loading System

We have shown a method to transport and load a blue-detuned BoB trap with a single atom by using a dynamic 1D optical lattice. The transporting lattice, called an optical conveyor belt, is initially loaded with a few thousand atoms. Using the optical conveyor belt, atoms are transported a distance of 1.1 mm to a crossed vortex BoB trap. After transport, a single atom is then loaded into the BoB trap via light assisted collisions. Photon counting data confirms that an atom can be delivered and loaded into the bottle beam trap 13.1% of the time. Implementing this work to reload a functional qubit array[3, 1, 103, 105, 106, 107] requires deterministically loading any arbitrary site of an array of BoB traps. An additional pair of acousto-optic modulators for each of the 1D lattice beams can reposition the optical conveyor belt to permit loading of any BoB array site at an arbitrary location [146, 147]. Modifications were made to the atom transport and loading apparatus in order to "steer" the optical conveyor belt with the eventual goal of loading any site of an arbitrarily large array of bottle beam traps such as those shown in figure 1.1. By "steering" the optical conveyor belt, we mean giving the atom transport system the capabilities of delivering an atom to one BoB trap and the repositioning the conveyor belt and delivering an atom to another array BoB trap. Scaling up the atom delivery system to accommodate an array of BoB traps is described in detail in chapter 5.

Chapter 5

Steering the Optical Convyeor Belt: Addressing an Array of Bottle Beam Traps

In order to transport and load atoms into an *array* of *multiple* BoB traps, the optical conveyor belt must be "steerable." As mentioned in section 4.6.3, the conveyor belt can be transported not only along its axial direction, but also along the $\hat{x}$ and $\hat{y}$ directions by utilizing an additional pair of acousto-optic modulators for each lattice beam. This allows one to reposition the optical conveyor belt to permit loading of a BoB trap at an arbitrary (x, y, z) location. To properly demonstrate a steerable optical conveyor belt, an array of BoB traps, rather than one single trap, must be made.

5.1 Ineffectiveness of an Array of Crossed Vortex BoB Traps

The process of making an array of crossed vortex BoB traps involves taking a pair of LG01 beams and using a diffractive optic element (DOE) to replicate or "copy" the beams into an array of LG01 beams on a conjugate plane of the image plane of the final 0.4 NA lens used to focus the BoBs into the Hex cell (figure 5.1). While this setup concept is relatively simple to construct, it creates extensive problems with the resulting array of crossed vortex BoBs. The calcite beam displacer and DOE result in the tightly crossing BoBs at the image plane having the *same* polarization, rather than orthogonal polarizations. As a result, considerable phase dependent interference effects commonly arise, making it very difficult to implement as a qubit array capable of performing sensitive quantum computations. Accordingly, the geometry of the BoB array was modified[1] from

[1] Our collaborators at UW-Madison, who actually perform the quantum algorithms with the qubit array, firmly insisted on making this change. Since our work at CU-Boulder was to be able to reload the UW-Madison array, we naturally changed our geometry as well.

an array of crossed vortex BoBs to a "Gaussian Beam Array" (GBA), that subsequently forms an array of BoB traps. This final chapter for the atom transport and reloading project shows the GBA system (5.1), the steerable conveyor belt (5.2), and the corresponding atom transport results (5.3).

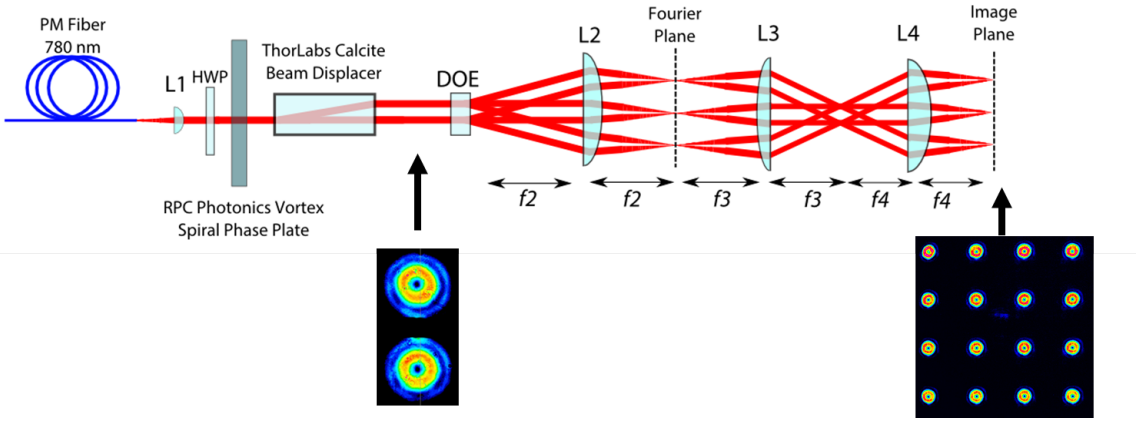

Figure 5.1: (Color online) Bottle Beam Array Concept: A combination of a calcite beam displacer and a diffractive beam splitter is used to form and array of crossed vortex BoB traps. However, polarization fluctuations between interfering tightly overlapping LG01 beams at the focal plane of the 0.4 NA lens render this concept useless for quantum computation purposes.

5.2 Atom Trapping in a Gaussian Beam Array of BoBs

5.2.1 Gaussian Beam Array (GBA)

The optical system for creating the Gaussian beam array (GBA) with two BoB trapping sites is shown formally in figure 4.3b and summarized in figure 5.2a. A Toptica BoosTA Pro sends 3W of 780 nm light into a polarization maintaining, anti-reflection coated, fiber with 65% coupling efficiency. After emerging from the fiber, the Gaussian beam is collimated and sent through a polarizing beam splitter (PBS). This PBS serves to keep the polarization of the outgoing beam constant by mapping minor polarization drifts from the TA and fiber into minor power drifts in the beam. This single Gaussian beam is then focused through a Holo/Or MS-248-X-Y-A diffractive beam splitter (DBS), which diffracts the single beam into a 2x2 array of identical Gaussian beams which are all collimated with a $f = 13.86$ mm aspherical lens. A 66:35 telescope then images the 2x2 array pattern through a 353 μm thick calcite crystal to replicate the 2x2 array into an

arrangement of 8 identical Gaussian beams separated from their nearest neighbor by $d = 353$ μm. In order to have equal spacing of each of the 8 array beams, the fast axis of the calcite is rotated by 45° with respect to the diffractive beam splitter axis. After passing through the calcite, the array of 8 Gaussian beams is demagnified by a 200:60 telescope and then further demagnified and imaged through the AQuA Hex cell walls (figure 4.6) with a 500:23.125 telescope[2] . At the focus of the 23.125 mm lens, each Gaussian beam has a focused beam waist of $w_0 = 2.21$ μm and is separated from its nearest neighboring beam by a distance $d = 4.95$ μm. The aspect ratio s, which is defined as the ratio of the focused beam spacing to focused beam waist is $s = d/w = 2.23$. After passing through all of the optics required to produce the array, the total optical power remaining in the array is 750 mW, which gives a uniform distribution of 47 mW per beam in the array setup. An image showing the optical intensity of the GBA as it is swept through the focus of the 200:60 telescope is shown in figure 5.2b. As this 8 beam array is focused, there exists two regions of low optical intensity surrounded by high optical intensity (similar to the figure 4.18c) that creates two distinct BoB traps capable of confining atoms (figure 5.2b).

5.2.2 Analysis of Trapping Potential of Gaussian Beam Array

To understand how the array of Gaussian beams in figure 5.2b creates two BoB traps, let us examine the array at the plane of the array focus. Specifically, we examine one the two identical dark regions of minimum light intensity surrounded by four intense Gaussian beams that is outlined clearly in figure 5.3. Each of the four Gaussian beams in this arrangement has intensity [148]

$$I(r) = I_0 e^{-2r^2/w_0^2} \tag{5.1}$$

where w_0 is the focused beam waist and I_0 is the maximum intensity that occurs at $r = 0$. As shown in figure 4.5b, each of the four beams has a polarization that is orthogonal to its nearest neighboring beam. It immediately follows that the total optical intensity exactly in-between two

[2] This $f = 23.125$ mm lens is the same 0.4 NA, high quality lens used to focus the crossed vortex BoB traps in section 4.5.2.

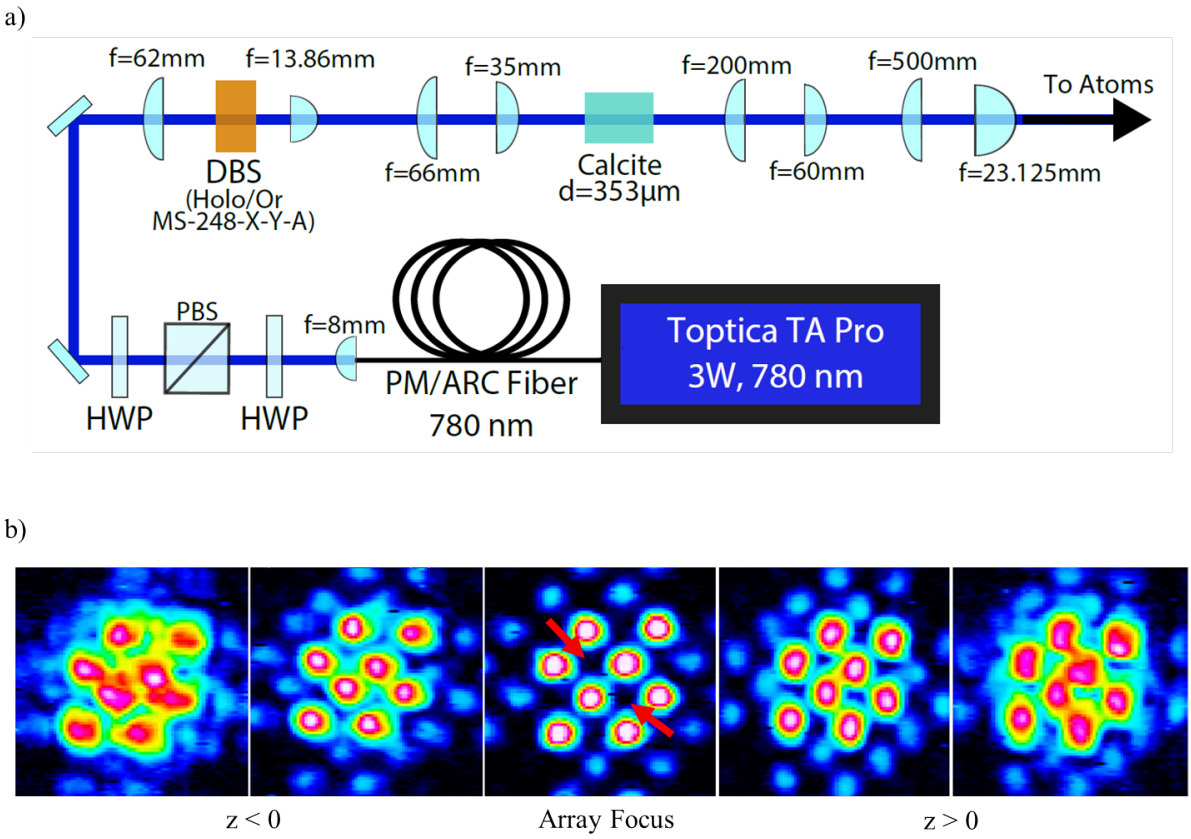

Figure 5.2: (Color online) Top: Optical setup to generate a GBA that produces two bottle beam trapping sites. Bottom: Intensity images of the GBA as one sweeps through the focus of the array. As one moves away from the focus in the positive and negative axial direction, each Gaussian beam in the array rapidly diverges and interferes to cap off the bottle beam trap and produce a barrier in the z-direction. This permits the intensity pattern to function as a 3D trapping potential. The locations of the focus of the two BoB traps are indicated with a red arrow.

nearest-neighboring beams, which corresponds to an array saddle point I_{sp}, is

$$\begin{aligned} I_{sp} &= I(d/2) + I(d/2) \\ &= I_0 e^{-2(d/2)^2/w_0^2} + I_0 e^{-2(d/2)^2/w_0^2} \\ &= 2I_0 e^{-d^2/2w_0^2} \end{aligned} \tag{5.2}$$

where d is the separation between neighboring Gaussian beams. The lowest optical intensity in

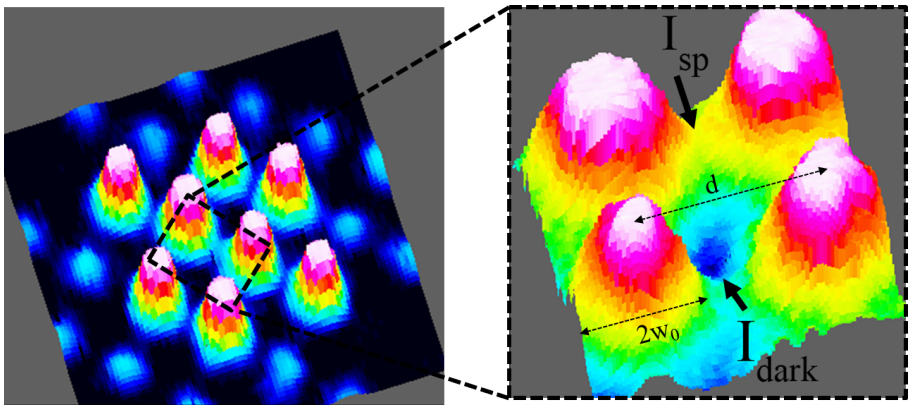

Figure 5.3: (Color online) Optical intensity image showing a central, dark region of minimum light intensity surrounded by four intense Gaussian beams. Each beam has an equal waist of w_0 and is separated from it's nearest neighboring beam by distance d. Adding the intensities of all four beams creates bright saddle points with intensity I_{sp} that surrounds the central, dark region with intensity I_{dark}. Because the laser light used to create this pattern is blue-detuned from resonance, the gradient in optical intensity $I_{sp} - I_{\text{dark}}$ creates a potential energy well that can confine atoms in the central, dark region.

the central, dark region I_D, occurs at a distance $r = d/\sqrt{2}$ from the middle of each focused beam, and is equal to the sum of intensities from all four Gaussian beams at this central point $r = d/\sqrt{2}$:

$$\begin{aligned} I_D &= 2 \times \left[I(d/\sqrt{2}) + I(d/\sqrt{2}) + 2\sqrt{I(d/\sqrt{2})I(d/\sqrt{2})}\cos\phi \right] \\ &= 2 \times \left[I_0 e^{-2((d/\sqrt{2})^2/w_0^2)} + I_0 e^{-2((d/\sqrt{2})^2/w_0^2)} + 2\sqrt{I_0 e^{-2((d/\sqrt{2})^2/w_0^2)} I_0 e^{-2((d/\sqrt{2})^2/w_0^2)}} \right] \\ &= 2 \times \left[I_0 e^{-d^2/w_0^2} + I_0 e^{-d^2/w_0^2} + 2I_0 e^{-d^2/w_0^2} \right] \\ &= 8I_0 e^{-d^2/w_0^2}. \end{aligned} \tag{5.3}$$

Comparing equations 5.2 and 5.3, there exists a non-zero, optical intensity gradient between the bright saddlepoints I_{sp} and the dark central region I_D. Since the laser light used to create these

intensity profiles is blue-detuned from resonance, equations 2.11 and 2.12 state that a potential energy well is created that permits 2D atom confinement at the dark regions; that is the four beams together form a single 2D BoB trap. Furthermore, from equation 2.11, the total trapping depth is proportional to the difference of bright optical intensity (equation 5.2) and dark optical intensity (equation 5.3)

$$\begin{aligned} I_{\text{trap}} &= I_S - I_D \\ &= 2I_0 e^{-d^2/2w_0^2} - 8I_0 e^{-d^2/w_0^2} \\ &= 2I_0 e^{-d^2/2w_0^2}\left(1 - 4e^{-d^2/2w_0^2}\right) \\ &= 2I_0 e^{-s^2/2}\left(1 - 4e^{-s^2/2}\right) \end{aligned} \tag{5.4}$$

where we use the definition $s = d/w_0$, which was defined in section 5.2.1 as the aspect ratio of the array.

It is useful to the experimentalist to express the results of equation 5.4 in terms of the average optical intensity of the entire 2D trap (shown in the inset of figure 5.3). Since each BoB trap is constructed from four Gaussian beams separated by distance d, the average optical intensity is

$$\bar{I} \approx \frac{P}{d^2} = \frac{\pi w_0^2 I_0}{2d^2} = \frac{\pi I_0}{2s^2} \tag{5.5}$$

where P is the total power of all four Gaussian beams combined.

Thus, we can use equation 5.5 to express I_0 in terms of the average intensity [106] with

$$I_0 \approx \frac{2s^2}{\pi}\bar{I}. \tag{5.6}$$

Inserting equation 5.6 into equation 5.4 gives the total 2D trapping intensity as

$$I_{\text{trap}} = 4\frac{s^2}{\pi}\bar{I}e^{-s^2/2}\left(1 - 4e^{-s^2/2}\right). \tag{5.7}$$

By plotting equation 5.7 (figure 5.4), it is immediately evident that the largest intensity difference, and hence the deepest BoB trap, will occur when the set of four focused Gaussian beams has an aspect ratio of $s = d/w = 2.2$. This is a very important result, as it dictates what lenses and (more importantly) what calcite thicknesses to use when forming the GBA in the Hex cell, as shown figure 5.2a.

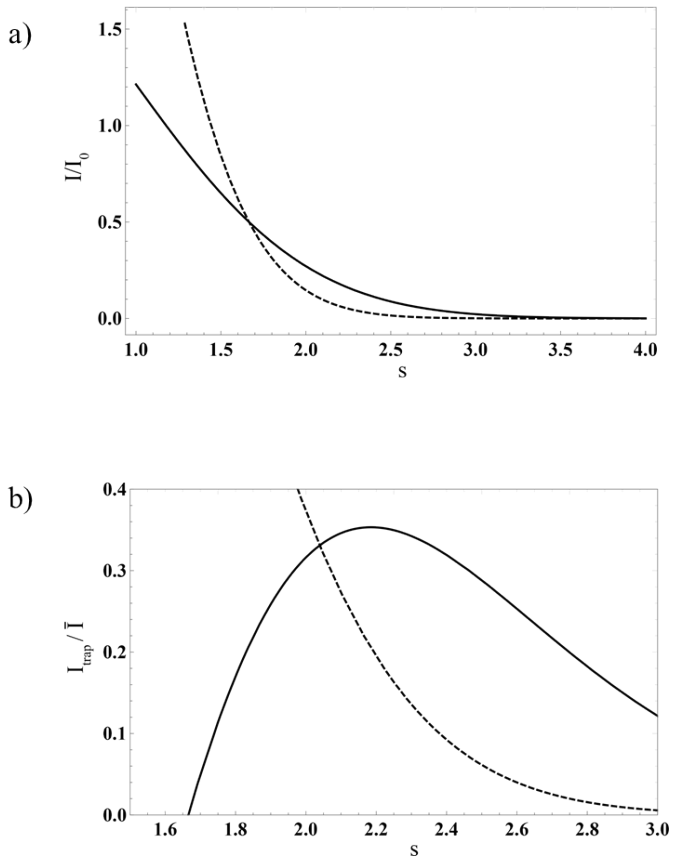

Figure 5.4: (Color online) a) Plots of the normalized intensity of the bright saddle points I_{sp}/I_0 (solid line) and the central dark region I_{dark}/I_0 (dashed line) as a function of the array aspect ratio s. b) Plot of the normalized trapping intensity $I_{\text{trap}}/\bar{I} = (I_{sp} - I_{\text{dark}})/\bar{I}$ (solid line) between the bright saddle-point and the central dark region of one trapping site in the GBA as a function of the aspect ratio s. The dashed line shows the intensity of the dark, central region that is present at the same aspect ratio s, thus indicating the non-zero bias to the trap bottom present in the setup. From this plot, it is determined that the deepest trapping depth occurs at $s = d/w_0 = 2.2$.

The total optical intensity in equation 5.7 results in 2D atom confinement in the radial direction but provides no confinement in the loose, axial direction of the array. In order for the array BoBs to trap atoms in three dimensions, a repulsive optical potential in the *axial* direction must also be formed. Similar to how tightly overlapping two LG01 beams "caps" off the crossed vortex BoB trap with high light intensity (section 4.5.2), the overlap of the Gaussian beams as they rapidly diverge when propagating out of the GBA focus (figure 5.2b) "caps" the array BoBs with high optical intensity and provides a repulsive potential barrier to give axial confinement in addition to radial confinement.

5.2.3 Atom Trapping in the Focused Array

When finally focusing the array into the AQuA Hex cell to its desired size (using with the $f = 23.125$ mm lens), the GBA has focused beam waists of $w_0 = 2.21$ μm and beam separations of $d = 4.95$ μm (figure 5.5). This configuration gives a final aspect ratio of

$$s = \frac{d}{w} = 2.23 \tag{5.8}$$

which is very close to optimal aspect ratio of $s = 2.20$. Note that the focal plane of the array is carefully aligned to overlap with the focus of the optical conveyor belt (figure 4.6). As explained in section 4.5.2, scrupulous care must be taken when focusing the GBA though the thick Hex cell walls to ensure that as little distortions as possible occur to the array beams such that the aspect ratio $s = 2.23$ is preserved. Inspection of figure 5.5 shows that this focused GBA pattern contains two low intensity dark regions that are each surrounded by four bright saddle points, thus forming two 3D BoB traps.

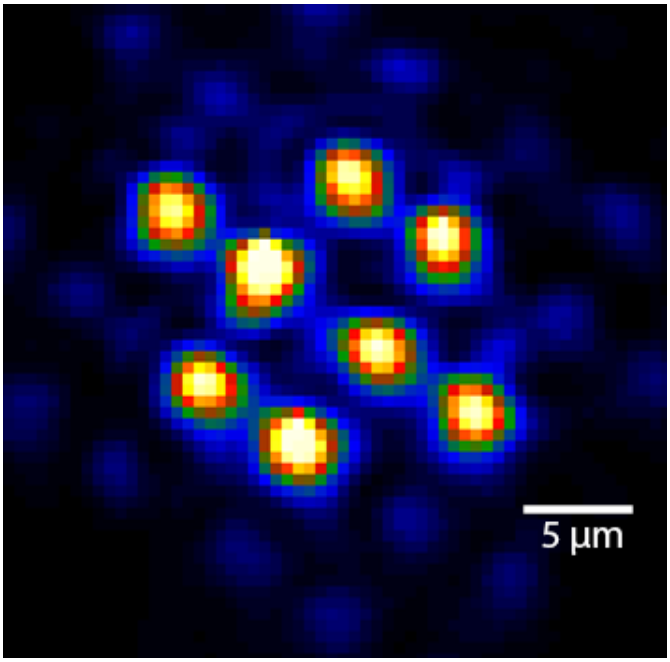

Figure 5.5: (Color online) Intensity image of the Gaussian beam array at the focus of the 0.4 NA $f = 23.125$ mm lens. Each beam in the array has a beam waist of $w_0 = 2.21$ μm and is separated from its nearest neighbor by $d = 4.95$ μm. This gives an aspect ratio of $s = d/w = 2.23$.

To get an explicit calculation for the trap depth as a function of the atom position in each BoB, we add the intensities [102] from each diagonally opposite pairs of Gaussian beams:

$$\begin{aligned} I(x,y,z) = \frac{c\epsilon_0}{2}\left[|E(x-d/2,y-d/2,z)+E(x+d/2,y+d/2,z)|^2\right] \\ + \frac{c\epsilon_0}{2}\left[|E(x+d/2,y-d/2,z)+E(x-d/2,y+d/2,z)|^2\right] \end{aligned} \tag{5.9}$$

where c is the velocity of light, ϵ_0 is permittivity of free space, and $E(x,y,z)$ is the electric field of a Gaussian laser beam given as

$$E(x,y,z) = E_0\left(\frac{w_0}{w(z)}\right)\exp\left[-\left(\frac{x^2+y^2}{w^2(z)}\right)\right]. \tag{5.10}$$

We plug equation 5.9 into equation 2.11 to numerically calculate a dipole trapping depth of 547 μK along the radial (x,y) directions and a trap depth of 578 μK along the axial z direction when the total optical power in the entire array is 750 mW. The corresponding trapping frequencies are $\Omega_{\text{rad}} = 2\pi \times 8.35$ kHz along the radial direction and $\Omega_z = 2\pi \times 2.58$ kHz along the axial direction. The radial and axial trapping potentials for each BoB trap in the array are plotted in figure 5.6.

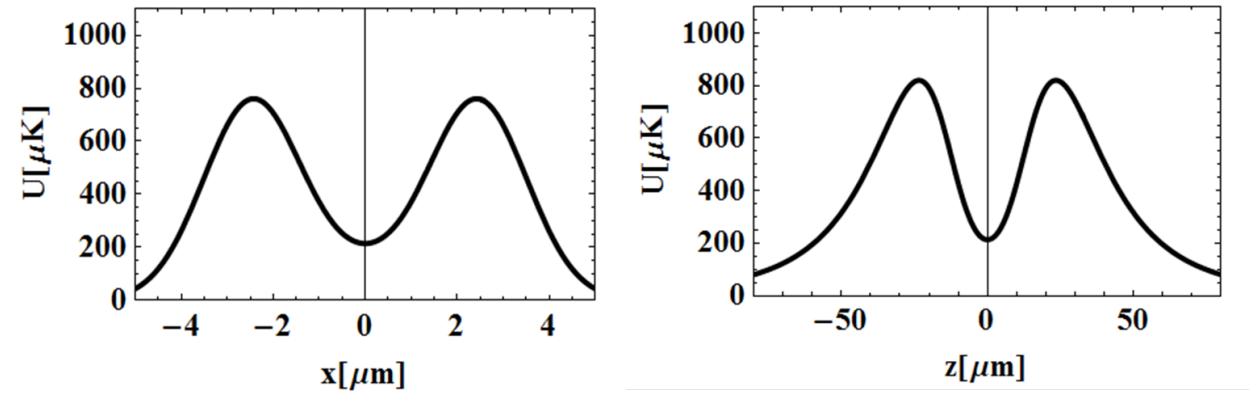

Figure 5.6: (Color online) Optical trapping potential produced at the bottle beam locations of the 2x1 array in the radial (x,y) and axial (z) directions. Using 750 mW of $\lambda = 780$ nm laser power, a trapping barrier of depth 547 μK is created in the x,y radial direction and a trap depth of 578 μK is created in the z, or axial direction. The trapping frequencies for this trap geometry are 8.35 kHz in the radial direction and 2.58 kHz in the axial direction.

Finally, to demonstrate the BoB array was capable trapping atoms, the array was overlapped with the center of a 3D MOT for 500 ms. After loading the array from a background MOT, polarization gradient cooling was performed on the atoms for 5 ms and then all MOT beams were extinguished for an additional 25 ms to allow un-trapped atoms to fall away. Fluorescence imaging (as described in section 4.5.3) was then performed on any trapped atoms by shining a three-dimensional optical molasses detuned -25 MHz from resonance. Repump light was also used to sustain the continuous fluorescence of each trapped atom. Each fluorescence image was taken with an Andor iXon EMCCD with an EM gain of 200, vertical pixel shift speed of 0.5 μs, and a horizontal pixel readout rate of 5 MHz. Results of the fluorescence imaging are shown in figure 5.7. Each trapping image shows the sum of 10 individual fluorescence imaging results of atoms confined in the two BoB traps. By improving the resolution of the florescence imaging system, the separation of the two BoB traps was observed to be 4.5 μm, which is slightly less than the expected separation of 4.95 μm that was observed from the imaged intensity profile in figure 5.5[3] .

5.3 Steering the Optical Conveyor Belt

To steer the optical conveyor belt, we modify the dynamic 1D lattice setup shown in figure 4.12 by placing two additional 4.2 mm x 4.2 mm aperture, 80 MHz acousto-optic modulators (AOMs) along the beam paths of both counter-propagating 1D lattice beams (figure 5.8). The AOMs, labeled the x-AOM and y-AOM for each beam path, execute angular deflections θ_x and θ_y of each lattice beam in the respective $\hat{x}$ and $\hat{y}$ directions by diffracting[4] each laser into the ± 1 order. An optical relay system shown in figure 5.9 was designed to precisely map the angular deflections θ_x and θ_y from the x-AOMs and y-AOMs into lateral displacements δx and δy at the

[3] It is important to mention that these results do not demonstrate that only a *single* atom is present in the BoB trap but rather that the array of BoBs *can* trap atoms. At this point in the IARPA MQCO experiment, things started become very rushed due to funding coming to an end. This data was taken in April 2016 and the entire project funding was scheduled to end in July 2016. As a result, I decided to move very quickly. The data showed that our array was capable of trapping atoms, whether it was one or more. Knowing that we had to still incorporate the optical conveyor belt, I decided to immediately sprint to that milestone.

[4] Because the beam steering system requires each lattice beam to be diffracted via an AOM, power loss starts to really play a factor. Thus, painstaking care was taken to optimize the AOM diffraction efficiency such that 90% of the beam power was diffracted into the +1 order.

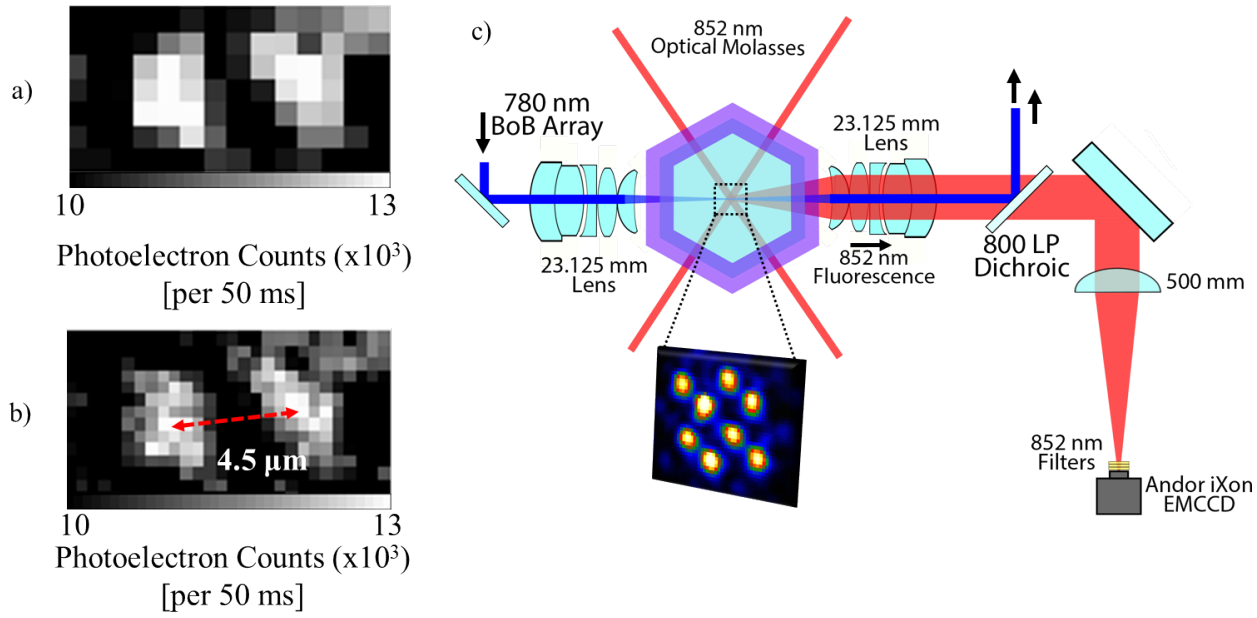

Figure 5.7: (Color online) Demonstration of atom trapping in the 2x1 array of BoB traps. The fluorescence images in a) and b) show a sum of 10 individual images. The schematic for fluorescence imaging the array is shown in c). By changing the final imaging lens from $f = 500$ mm to $f = 1000$ mm, the resolution was doubled which is the difference between images a) and b).

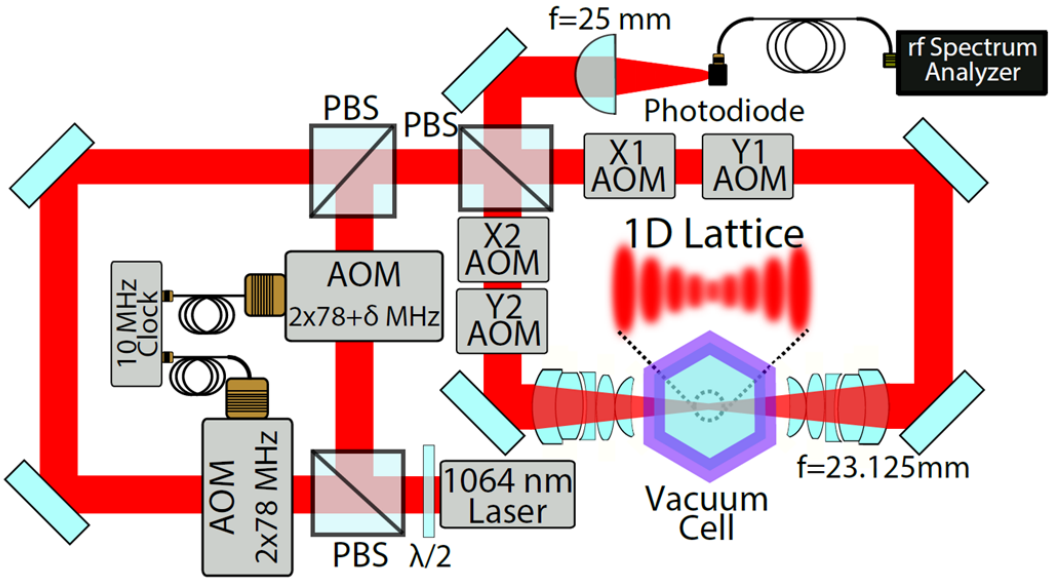

Figure 5.8: (Color online) The optical conveyor belt setup is modified by adding two additional AOMs along the beam paths of 1D lattice lasers in order to execute angular deflections of the beams along the x and y dimensions. As in the optical conveyor belt for the crossed vortex BoB setup (section 4.4.4) lattice beam overlap is monitored by measuring their relative beat frequencies with an RF spectrum analyzer.

focus of the 0.4 NA, $f = 23.125$ mm lens. For each lattice beam, the relay system (shown in figure 5.9) works by imaging the center of the x-AOM crystal onto the center of the y-AOM crystal using a 1:1 telescope. The "center" of the AOM crystal refers to the distance half-way through the crystal *and* the center of the face of the crystal. Next, a second 1:1 telescope images the center of the y-AOM crystal onto the center of the first lens of a 5x enlarging telescope. Each 1:1 telescope also serves to help minimize any beam walk-off, as each beam is imaged onto the center of the next subsequent optical element. The 5x telescope enlarges the lattice beam to 1 cm in diameter before being focused onto the plane of the BoB array with the 0.4 NA, $f = 23.125$ mm lens (figure 4.6) to a $1/e$ beam waist of approximately 1.7 μm. The reduced beam waist of the optical conveyor belt (as compared to the original setup in section 4.4.1) is to demonstrate atom delivery to single BoB traps in the GBA without overlapping adjacent BoB sites that are separated by 4.8 μm. With the smaller beam waist of the conveyor belt beams, we only need to use $P = 500$ mW of total power in the beams to still obtain the same trapping depths $U_0 = -1.88$ mK (equation 4.5) and axial trapping frequency $\Omega_z = 2\pi \times 454$ kHz (equation 4.6) as in section 4.4. However, the radial trapping frequency (equation 4.7) has increased to $\Omega_{\text{rad}} = 2\pi \times 75$ kHz.

As a result of this relay system, by driving the beam deflecting AOMs, we can laterally displace each 1D lattice beam by δx and δy at a resolution 1.06 μm/MHz. Since we can control the drivers to a resolution of $\delta\nu = \pm 0.1$ MHz, the beam steering setup can laterally displace the optical conveyor belt by some distance at a resolution of 0.1 μm. It is important to note that with this setup, in order for both lattice beams to remain overlapped after repositioning, the x-AOM drivers are set to the same driving frequencies but opposite sign (that is x-AOM1=$+\delta\nu_x$ and x-AOM2=$-\delta\nu_x$) while the y-AOM drivers are set to the same frequency (y-AOM1=y-AOM2=$\delta\nu_y$) in the steerable conveyor belt setup[5] . Moreover, while each AOM is driven with an independent RF driver, they are all phase locked to the same 10 MHz clock reference signal in order to minimize phase jitter of the lattice beams.

[5] This can cause a non-zero mutual detuning $\delta \neq 0$ between the transport beams, thus giving it an unwanted velocity. To correct this error, one must simply adjust the detuning δ in the original frequency chirping AOMs from figure 4.12

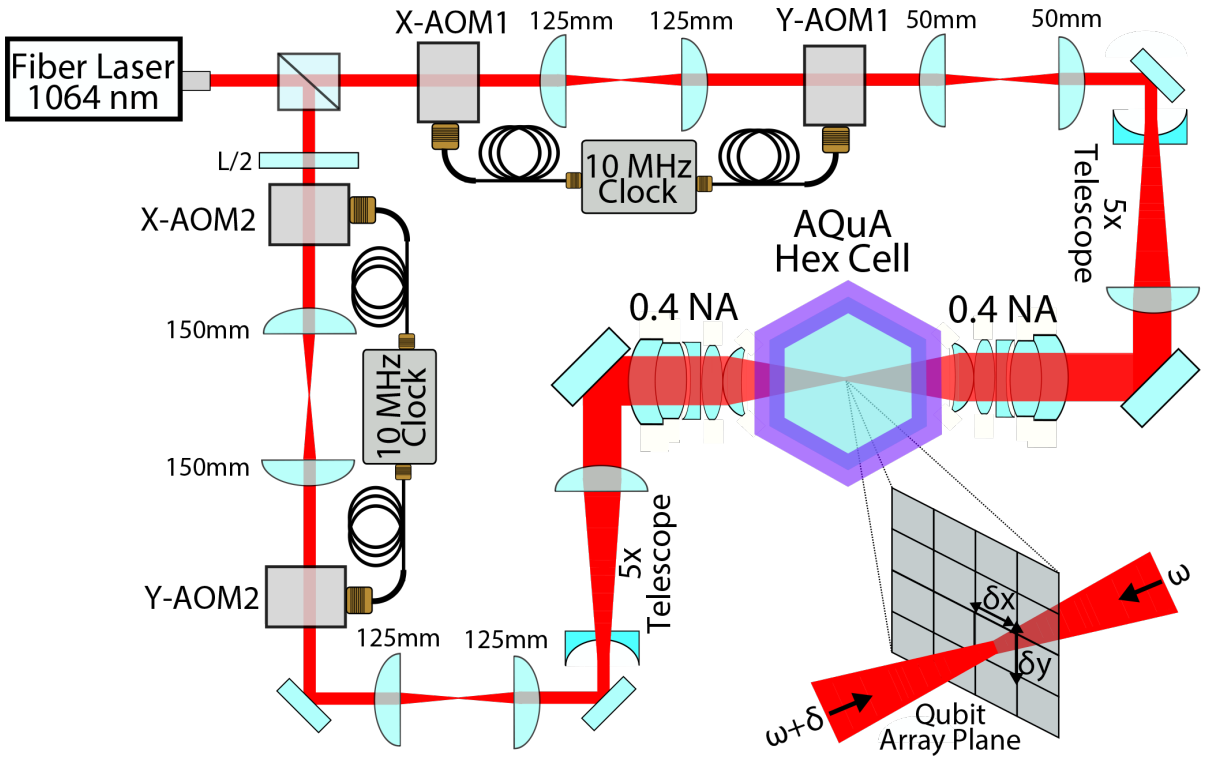

Figure 5.9: (Color online) Schematic of the beam steering system for the optical conveyor belt. The 1064 nm beams are split into two beam paths. Each beam passes through an x-AOM, which alters the angle of the beam in the x dimension. A 1:1 telescope relay images the center of the x-AOM on the center of the y-AOM. This y-AOM changes the beam angle in the y dimension. A second 1:1 telescope relays the center of the y-AOM onto the center of a 5x telescope, which magnifies the beam to 1 cm in diameter. The beam is then focused with a 0.4 NA custom lens onto the qubit array in the AQuA Hex cell. At the qubit array plane, the x and y positions of the beams can be laterally translated by δx and δy by varying the x and y angular deflections of the AOMs.

5.3.1 Single BoB Site Addressing

To demonstrate the single BoB site addressing capabilities with the steerable optical conveyor belt, the focused BoB array was imaged onto an Andor iXon EMCCD (figure 5.10a) using the same[6] imaging system used in figure 5.7. On this image, light from the focused optical conveyor belt can also be seen. By only changing the driving frequencies of the lattice deflecting x-AOMs and y-AOMs, the focus of the optical conveyor belt is repositioned such that it overlaps the center of either of the two BoB traps in the GBA (figure 5.10b, figure 5.10c, figure 5.10d). The beam deflecting AOM driving frequencies can be adjusted electronically within approximately 10 microseconds, allowing for very fast optical conveyor belt reposition times.

[6] Although it must be slightly modified as the optical conveyor belt is not drawn on this figure (simply note that both counter-propagating $\lambda = 1064$ nm beams spatially overlaps the 780 nm BoB array beams). After passing through the Hex cell, the 1064 nm and 780 nm beams are separated by simply placing 1000 nm low pass dichroic mirror directly after the $f = 23.125$ mm lens. However, 0.1% of the optical conveyor belt light still passes through the dichroic mirror and is then focused onto the Andor iXon EMCCD with an $f = 500$ mm lens. This forms a 23.125:500 confocal microscope that images the focus of the array-conveyor belt combination.

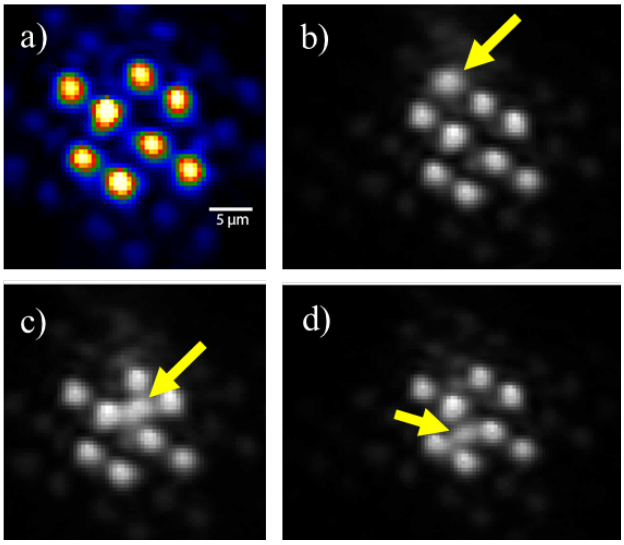

Figure 5.10: (Color online) Demonstration that the beam steering system is capable of addressing both BoB trapping sites in the GBA. These images were taken by only changing the 1064 nm beam deflecting x-AOM and y-AOM driving frequencies with no manual realignment of any beams. a) Focused GBA located inside the Hex cell. b) The focus of the optical conveyor belt spatially overlaps the focus of the GBA. The yellow arrow points to light from the focused conveyor belt. Using the lattice deflected x-AOMs and y-AOMs, the optical conveyor belt is repositioned to overlap the first BoB trap, shown in image c), and the second BoB trap, shown in image d).

5.3.2 Atom Transport and Delivery Sequence with Steerable Conveyor Belt

The sequence of delivering atoms to either of the array BoB traps begins by first choosing a BoB trap to deliver atoms to. With the spatial coordinates of both BoB traps known, the driving frequencies of the beam deflecting AOMs was set to the proper value such that the focus of the optical conveyor belt is repositioned to overlap the center of the target BoB trap. Specifically, in this setup shown in figure 5.9:

- Setting the x-AOMs to $\pm$79.83 MHz and setting both y-AOMs to +79.69 MHz positions the focus of the optical conveyor belt at the center of BoB-1 (figure 5.10c)
- Setting the x-AOMs to $\pm$84.45 MHz and setting both y-AOMs to +79.69 MHz repositions the conveyor belt to overlap BoB-2 (figure 5.10d).

After the optical conveyor belt is repositioned, the degree of overlap for the lattice beams is always verified by using the same method described in section 4.4.4, where an RF spectrum analyzer measures the amplitude of the relative beat note between the both lattice beams. The procedure for transporting atoms from the 3D MOT to the programmed BoB trap follows the sequence described in section 4.6.1 and figure 4.24, although (as described in section 5.3.2.3) a different frequency chirp is applied to the lattice beams and, as described next, a considerably smaller number of atoms is loaded into the conveyor belt.

5.3.2.1 Loading the Optical Conveyor Belt With a Small Atom Number

Once a BoB destination is chosen, a 3D MOT is loaded into the AQuA Hex cell for 1 second using the methods described in section 4.3.2. During the final 530 ms of MOT loading, the 1064 nm transport beams are un-shuttered allowing the optical conveyor belt to overlap the MOT where 5 atoms on average[7] are loaded into the optical conveyor belt. After loading the conveyor belt, the

[7] Compared to the atom transport experiments in section 4.5.3, considerably fewer atoms (by about a factor of 10^3) are loaded into the optical conveyor belt. This is explained by the appearance of the collisional blockade effect due to reducing the lattice beam waists from 35 μm (as in section 4.5.3) to $w_0 = 1.7$ μm [149]. The collisional blockade, combined with any light assisted collisions from the cooling light prevents more than a single atom occupying in each potential well of the 1D lattice potential [149].

MOT was extinguished by shuttering the 852 nm cooling and repump beams as well as turning off the 3D MOT magnetic fields. The conveyor belt was held in place for 20 ms to allow the remaining untrapped atoms to fall away due to gravity.

5.3.2.2 Measuring Conveyor Belt Occupancy

The occupancy of the conveyor belt was measured by illuminating it with a 3D optical molasses by turning on the 3D MOT lasers and detuning them -30 MHz. Repump light is also turned on. Additionally, shim coils are used to eliminate any residual magnetic fields. As a result, the 3D molasses light induces atom fluorescence from any atoms loaded into the optical conveyor belt. The 852 nm scattered fluorescence light is collimated with one of the 0.4 NA, $f = 23.125$ mm lenses used to focus the conveyor belt and separated from the 1064 nm trapping light with a 900 nm short pass dichroic mirror (figure 5.11a). Using an $f = 500$ mm achromatic lens, the fluorescence light is then focused onto an Andor iXon EMCCD with single photon sensitivity where photon counting is performed over a 10 ms time interval. The overall imaging system features a magnification of 21.6 and results in a 0.740 μm/pixel ratio for the EMCCD. A set of three 852 nm laser line filters are used to eliminate any stray 1064 nm lattice light. A histogram showing the photon counting results of 500 individual loading sequences is shown in figure 5.11b and was fitted to a compound binomial-Poisson function:

$$f(x) = A\sum_{k=0}^{n}(1-p)^{n-k}\binom{n}{k}\frac{\langle N\rangle^k e^{-\langle N\rangle}}{k!}\frac{1}{\sqrt{2\pi\left(n_{bg}+kn_1\right)}}\exp\left[-\frac{\left(n-\left(n_{bg}+kn_1\right)\right)^2}{2\left(n_{bg}+kn_1\right)}\right]. \quad (5.11)$$

Physically, the appearance of this compound probability distribution is due to the combination of

- The random, discrete number of atoms loading into the optical conveyor belt
- The Poissonian spread of observed photon counts from each of the loaded atoms.

The fitting result is $p = 0.5$, $N = 5$, $n = 10$, $n_{bg} = 120$, and $n_1 = 120$. The appearance of multiple peaks in the photon counting histogram (as compared to 2 peaks in figure 4.22) is due to loading more than one atom in the conveyor belt. From the photon counting statistics the most probable loading number is 5 atoms (figure 5.11b).

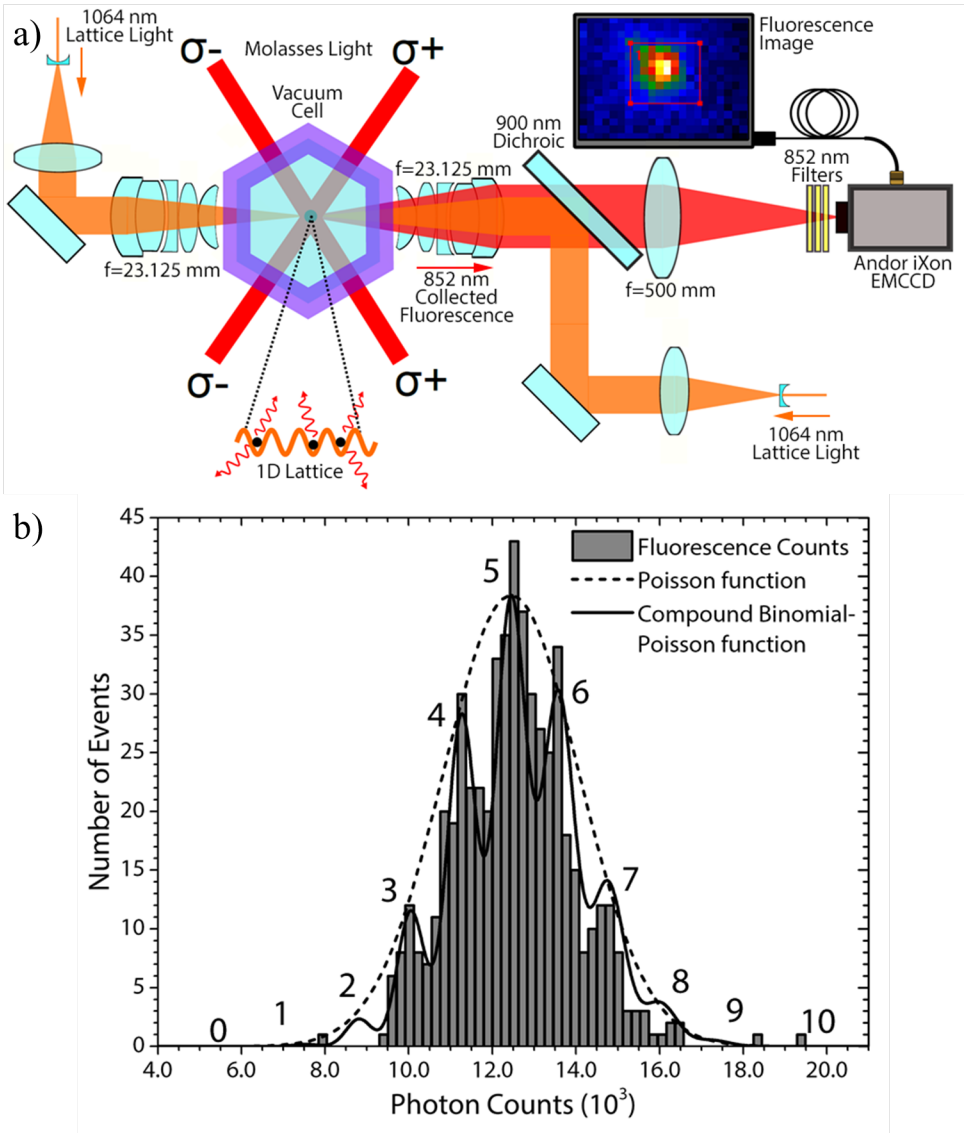

Figure 5.11: (Color online) a) Setup for fluorescence imaging of the 1D optical lattice. An optical molasses is applied to atoms trapped in the 1D lattice and a fraction of the induced fluorescence is collected with the 0.4 NA custom lens and focused onto an Andor iXon EMCCD. b) Histogram of photon counting data recorded during fluorescence imaging of the 1D lattice. The data shows multiple Poisson distributions that emerge due to different amounts of atoms loaded in the 1D lattice. Each number N shows the Poisson distribution corresponding to loading N atoms in the lattice. The distribution is fitted to a compound binomial-quasi Poisson function, which accounts for the random and discrete atom loading along with the sub-Poissonian spread of observed photon counts. The statistics show that the most probable loading number is 5 atoms.

5.3.2.3 Transporting Small Atom Number to BoB Site

Unlike the crossed vortex BoB trap loading (section 4.6), the BoB traps formed by the GBA are *never* turned off during the atom transport sequence. Turning off the GBA in order to reload a new atom to an empty BoB trap would ruin any previously loaded traps and ongoing quantum computations would also be ruined. Because the GBA and this optical conveyor belt are focused through the same 0.4 NA, $f = 23.125$ mm lens, the conveyor belt will pierce atoms through the weaker, axial confining potential of the array BoBs. During this process, atoms confined to the conveyor belt will not be expelled, as the axial trapping frequency of the conveyor belt, $\Omega_z = 2\pi\times450$ kHz is considerably greater than the axial potential of the array BoB trap $\Omega_z = 2\pi \times 2.58$ kHz.

To transport the small number of loaded atoms to the desired array BoB trap, one lattice beam is linearly frequency chirped by $\delta = 20$ kHz over 5 ms. Because the frequency chirping AOMs (figure 5.8) are in the double pass configuration, this causes a total lattice beam detuning of 40 kHz, With 40 kHz detuning, the optical conveyor belt accelerates to a maximum velocity of 21 mm/s. After this frequency chirp, the lattice beam is linearly chirped down -40 kHz over 5 ms to bring the conveyor belt to a halt. The entire procedure transports the atoms a total distance of approximately 100 μm in 10 ms[8] Additionally, the adiabatic criterion for accelerating the optical conveyor belt (equation 4.17) is satisfied, as we are still chirping the moving lattice at a much lower rate than the square of the lattice axial oscillation frequency. That is $\Omega_z^2 >> d\Delta\omega/dt$, where $\Omega_z^2 \approx 10^{12}\text{s}^{-2}$ and $d\Delta\omega/dt \approx 10^7\text{s}^{-2}$. Fluorescence imaging, as described in section 5.3.2.2, is performed for 10 ms to observe atoms transported into either BoB trap (figure 5.12).

Note that this only shows atom transport to each array BoB trap and does not demonstrate *reloading* the empty traps. The next experimental plans were to optimize the atom transport sequence in order to load a single atom deterministically into either array BoB trap using the steerable conveyor belt (similar to section 4.6.1). Unfortunately, at this point in the atom transport and reloading project, funding was discontinued and the experiment reached its premature ending.

[8] This 100 μm transport distance is considerably smaller than the 1.1 mm transport distance in section 4.6. This is due to the steerable optical conveyor belt having a focused beam waist of $w_0 = 1.7$ μm, giving it a Rayleigh range approximately 225 times smaller than the optical conveyor belt in section 4.6.

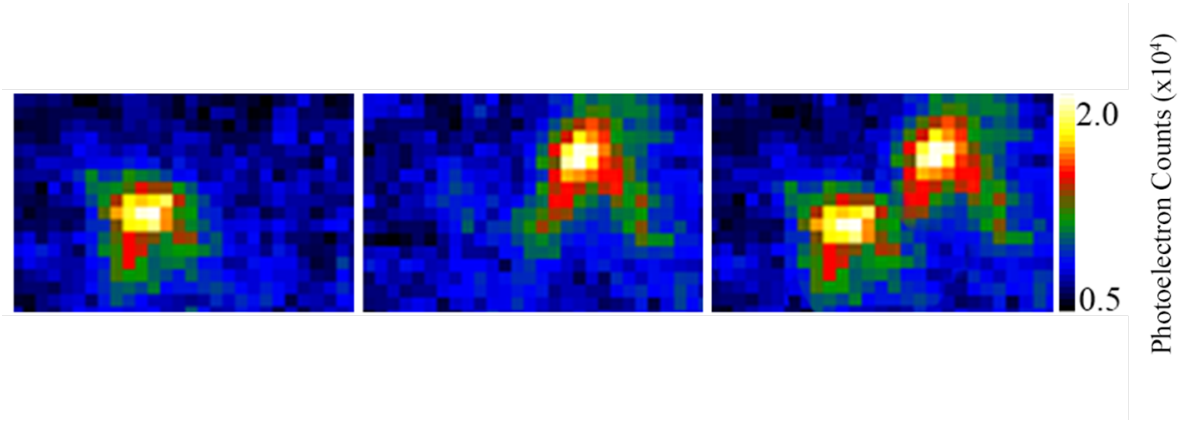

Figure 5.12: (Color online) Fluorescence images, all showing the same area of interest, of approximately 5 atoms after being transported 100 μm from a 3D MOT to an empty array BoB trap using the optical conveyor belt. Images a) and b) shows atoms transported to BoB2 and BoB1, respectively. Image c) is a combination of a) and b) to show their spatial separation of 5 μm.

Chapter 6

Conclusion to Part II

6.1 Summary

Part II of this dissertation has investigated individual atom delivery into optical bottle beam traps using an optical conveyor belt. In chapter 4, we describe a system for loading a single atom from a reservoir into a blue-detuned crossed vortex bottle beam trap using a dynamic 1D lattice. The lattice beams are frequency chirped using acousto-optic modulators, which causes the lattice to move along its axial direction and behave like an optical conveyor belt. A stationary lattice is initially loaded with approximately 6000 atoms from a reservoir, and the conveyor belt transports them 1.1 mm from the reservoir to a bottle beam trap, where a single atom is loaded into the bottle beam trap 13.1% of the time.

In chapter 5, we showed how this atom transport and reloading system can be scaled-up to deterministically transport approximately 5 atoms on average to an arbitrary site of an *array* of BoB traps. Accordingly, the atom transport system is "steerable" in that it could transport atoms to one BoB site and then be repositioned in order to deliver an atom to another array site. The beam steering of the optical conveyor belt was accomplished by using an additional pair of acousto-optic modulators for each of the 1D lattice beams making up the conveyor belt in order to reposition the optical conveyor belt to permit loading of any BoB array site at an arbitrary location [146, 147]. Modifications could be made to the single atom loading apparatus to reload an arbitrarily large array of BoB traps, such as figure 1.1. Unfortunately, funding for the IARPA AQuA-49 project ended and the reloading of an array of BoB traps was not completed. However,

with the results described in chapters 4 and 5, there are still interesting future experiments that could be performed to improve and extend this research.

6.2 Future Work and Experiments

6.2.1 Route to Continuous Atom Reloading: Vertical *then* Horizontal Transport

Demands for maintaining a satisfactory vacuum environment for trapped qubits and qubit gate operations suggest that the 3D MOT which supplies the source of cold atoms for atom reloading be located in a separate vacuum chamber positioned adjacent to the cell that houses the BoB array. This also permits the 3D MOT to be on continuously, as the MOT footprint will not disturb any previously trapped atoms. Subsequently, one practical atom reloading sequence would transport atoms vertically from a 3D MOT, using what is called a Moving Molasses MOT (figure 6.1b), to a position in the Hex cell that is off-axis from the BoB array (figure 6.2).

By making a 6-Beam MOT[1] with 3 pairs of counter-propagating cooling beams in a 2D magnetic field, we propel the entire MOT vertically, in what is called a Moving Molasses MOT [150], by mutually detuning the vertically oriented MOT beams by $\delta\omega$ (figure 6.1a). Similar to the physics behind the optical conveyor belt, this detuning creates a reference frame where where both pairs of cooling beams are Doppler shifted to the same frequency. This frame moves vertically (as an atom fountain) with velocity $v = 2\sqrt{2}\lambda\delta\omega$. A 12 W, 1064 nm dipole trapping beam helps to guide the atoms upwards. Once the atoms reach a maximum height in the Hex cell, they will be trapped in a crossed dipole trap which serves as a "secondary cold atom reservoir." The atoms from this secondary reservoir could then be *horizontally* transported to a BoB site using the methods described in chapters 4 and 5 of this dissertation. Using this transport scheme, while considerably more difficult, will not only maintain a better vacuum in the Hex cell, but would solve isolation issues by keeping the cold atom reservoir from disrupting any concurrently operating qubit gates taking place in the array, which allows for a *continuous* atom reloading.

[1] For more information on this Moving Molasses MOT and a complete diagram of the system, please refer to the PhD thesis of Kai Hudek.

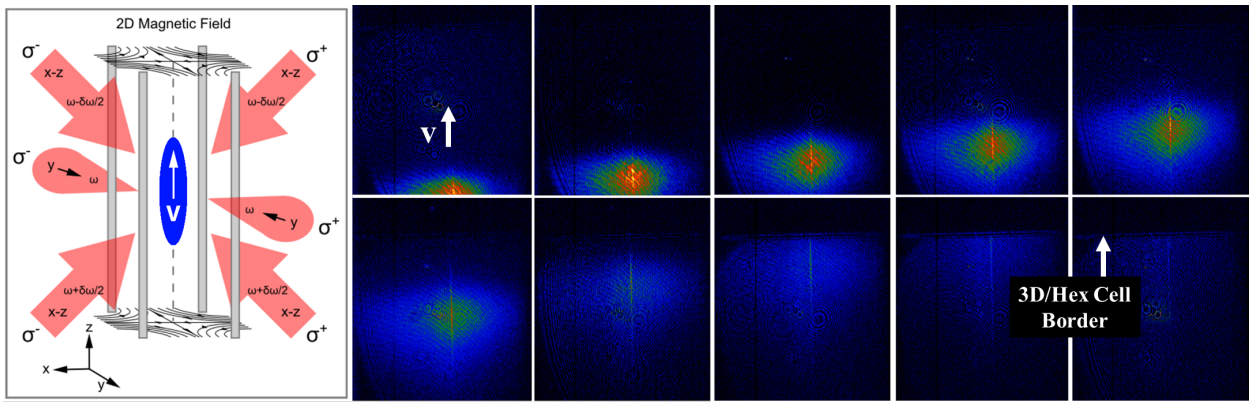

a) b)

Figure 6.1: a) MM MOT setup in the lower 3D MOT Chamber that can propel atoms up into the Hex Cell. Diagram taken from the PhD thesis of Kai Hudek [3]. b) Sequence of 10^5 atoms traveling vertically from the 3D MOT chamber into the Hex cell chamber. A 12W, 1064 nm dipole trapping beam helps guide the atoms upwards. Once the atoms reach a maximum height in the Hex cell, they will be trapped in a crossed dipole trap which serves as a "secondary cold atom reservoir."

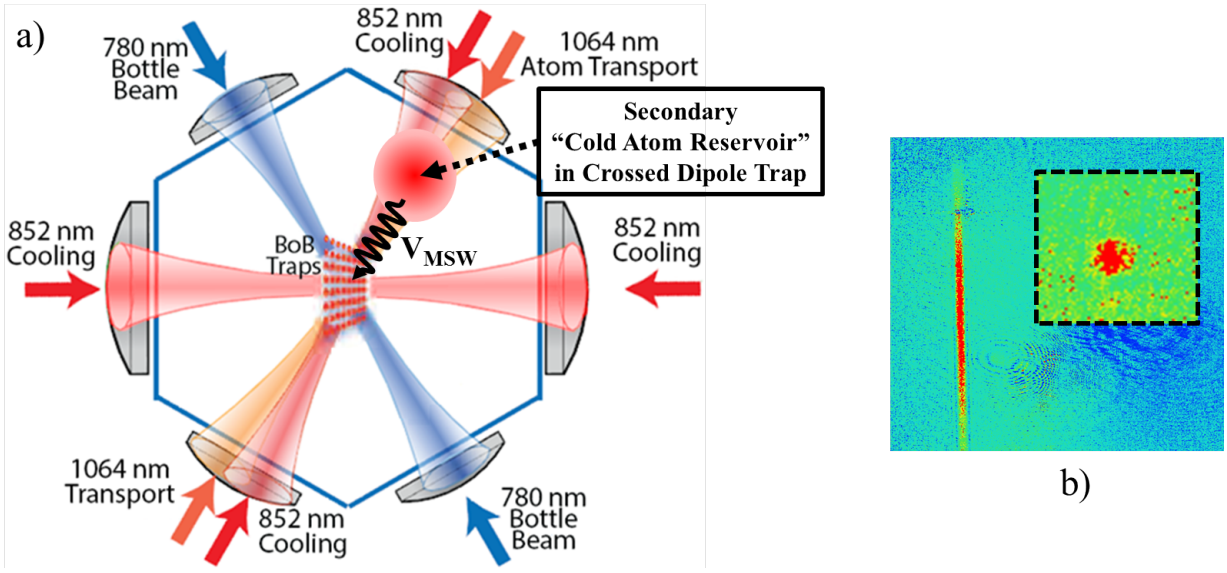

Figure 6.2: a) Diagram showing the location of the "secondary cold atom reservoir" in relation to the Hex cell lasers and the BoBs. Atoms confined to this reservoir can be transported and loaded into a BoB using the methods from chapter 4 and 5 of this dissertation. b) Atoms from the MM MOT that have traveled vertically into the uppermost chamber above the 3D chamber and have reached their highest trajectory. The inset shows a small crossed dipole trap as a result of intersecting this vertically traveling MOT with a horizontal dipole trap.

6.2.2 Using the Optical Conveyor Belt to Address a 2x3 BoB Array

The range of the steerable optical conveyor belt can be increased to address six BoB traps rather than just two. Such demonstration would show a fully capable atom reloading system for a qubit array without disturbing neighboring, previously loaded BoB traps. The optical system for creating the larger Gaussian beam array with 6 bottle beam trapping sites is shown in figure 6.3a and is just an extension of the GBA setup in section 5.2.2 and figure 5.2. A 2x2 array of identical Gaussian beams is created by a Holo/Or MS-248-X-Y-A diffractive beam splitter. The 100:35 telescope images the arrays in between two calcites. The first calcite replicates the 2x2 array into an array of 8 identical Gaussian beams separated by 353 μm, while the second calcite duplicates the 8 beams into a full 16 beam array with each beam separated by 250 μm. In order to have equal spacing of each array site, the fast axis of each of the calcites is rotated by 45 degrees with respect to each other. After passing through both calcites, the 2x3 array of Gaussian beams is demagnified by a 200:60 telescope to give each beam a waist of 34m and beam separation of 74 μm. The array is then demagnified one final time with a 500:23.125 telescope to image the array through the Hex cell. At the focus of the 0.4 NA, $f = 23.125$ mm lens, each beam has a separation of $d = 4.67$ μm and each beam waist is $w = 2.22$ μm, giving an aspect ratio of $d/w = 2.10$ (figure 6.4a). The steerable conveyor belt system in chapter 5 could then be used to address all 6 BoB traps (figure 6.4b).

6.2.3 Outlook

The work in part II of this dissertation demonstrates single atom reloading on a small scale, but does not demonstrate loading in a manner that leaves neighboring BoB sites undisturbed. Moreover, the atom reloading process is inherently stochastic and thus does not provide a 100% reliable reloading system for every reloading attempt. Since the publication of the small scale reloading system [32], methods to reload arrays of up to 50 atoms within 400 ms have been demonstrated [151][152]. As neutral atom qubit arrays begin to grow to larger sizes of up to 100 sites [1]

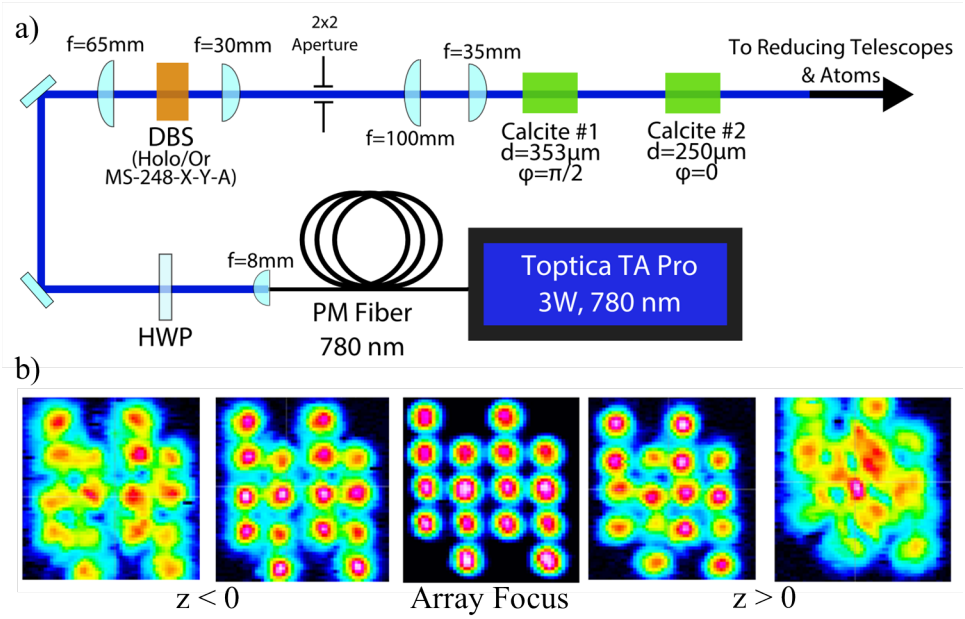

Figure 6.3: a) Optical setup to increase the BoB array from two traps to a 2x3 array of BoB traps. b) Intensity image of the 2x3 array as one sweeps through the focus of the array.

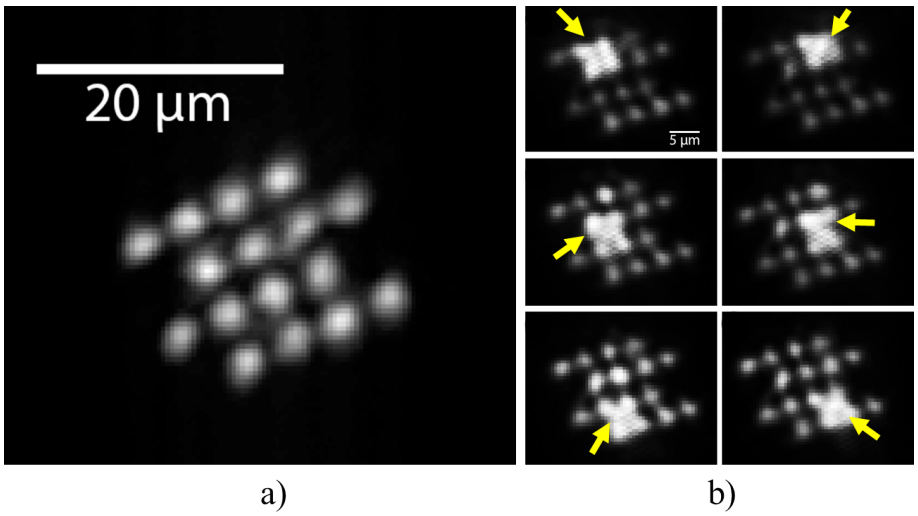

Figure 6.4: a) Image of the 2x3 BoB trapping array at the focus of the 0.4 NA, $f = 23.125$ mm lens. The optical configuration creates 6 BoB traps separated by $d = 4.67$ μm. b) Demonstration of the beam steering system addressing all 6 BoB traps in the array. The yellow arrow points to the optical conveyor belt light.

or even 3D array geometries [16], one conclusion remains perfectly clear: the process of reloading atoms due to finite trapping lifetimes presents a serious challenge to continuously operating neutral atom quantum computers. The atom transport and reloading system is but one cog in the neutral atom quantum computer (figure 6.5). Just like the rest of the quantum computing architectures, atom reloading must be sufficiently solved in order for neutral atoms to become a viable approach for quantum computation.

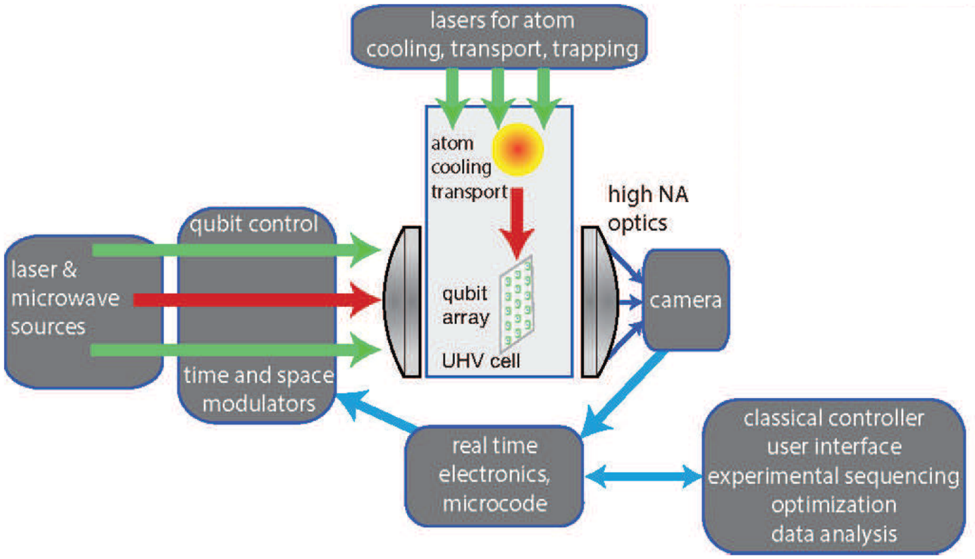

Figure 6.5: Chart taken from reference [1] conveying that single atom transport and reloading is but one element of a successfully operating neutral atom quantum computer.

Chapter 7

Part III: An Ultracold Gain Mechanism for a Matterwave Transistor Oscillator

Part III of this dissertation involves a drastically different theory and ongoing experiment in the field of atomtronics that introduces a new gain mechanism for a matterwave transistor oscillator. We start with a well-established, *semiclassical* description and experiment [33][5][34] of an atomtronic transistor and model the system with a purely quantum mechanical formalism. The quantum model predicts dynamics differently from the semi-classical results only when the atoms flowing through the transistor oscillator have sufficiently low enough temperatures such that the motional state of a dipole oscillating BEC, placed in the transistor itself, couples atom transitions between high lying transistor energy eigenstates. In this regime, the transistor oscillator displays interesting physics that was not observed in the semiclassical theory or experiments, namely the existence of a matterwave gain mechanism.

The remaining sections of this dissertation are organized as follows: Chapter 7 first gives a brief overview of atomtronics in relation to this work (section 7.1) and motivates the matterwave transistor oscillator (section 7.2). We then present the quantum model (sections 7.3 and 7.4) of the matterwave transistor oscillator and formally derive the gain mechanism whose physics resembles the Rabi model of a two-level atom interacting with a photon field (section 7.5). We then show the manifestation of matterwave gain in the model by comparing a matterwave current flowing through the transistor with and without the gain mechanism (section 7.6). Chapter 8 then presents the ongoing work to demonstrate the matterwave gain mechanism. Chapter 9 concludes.

7.1 Introduction to Atomtronics

Atomtronics [35][36] is an emerging field of ultracold atomic physics that focuses on quantum circuits that operate as atom analogues to electrical circuits, where an atom current takes the place of an electron current and the chemical potential takes the place of a voltage. In their design, atomtronic circuits are drastically different from their electronic circuit counterparts, as they involve manipulating ensembles of ultracold atoms to flow through a variety of potential energy landscapes, such as

- Optical potentials produced from laser beams (in particular, the experiments in [37][38])
- Harmonic magnetic potentials created with atom chips (as demonstrated in references [39][40][41][42][43])
- A hybrid combination of optical and magnetic potentials, such as the transistor potential used throughout chapters 7 and 8 of this dissertation.

At the heart of all atomtronic circuits is a Bose-Einstein condensate (BEC) [44], which supplies a source of coherent, ultracold atoms that are controlled to flow throughout a network of quantum potentials. Some recently demonstrated atomtronic circuits of note include BECs flowing throughout double-well [33] and triple-well potentials [5], as well as BECs flowing through 1D optical lattices [45][46][47] and optical ring lattices [48][49][50]. Irrespective of the circuit potential geometry, the objective of atomtronics remains the same: manipulate a current of ultracold atoms in some tailored potential in order to study fundamental physics or to create purely quantum mechanical technologies [51].

Accompanied with such high aspirations of atomtronics comes a difficult, innate challenge ingrained in the field: such ultracold atom circuits are inherently a many-bodied, open quantum system, since atoms and BECs interact and dissipate as they flow throughout the circuit from some source to a sink or drain. While this immensely complicates the theoretical description of atomtronic circuits, complete descriptions are usually simplified by invoking various approximations, such as

- Neglecting dissipation and treating the atomtronic circuit as a closed system (as demonstrated in references [52][53][54][55])
- Reducing the many-bodied system from a very large number to a three or four-body problem
- Ignoring the BEC mean-field interaction effects (as described in reference [34]).

The transistor oscillator model described in this dissertation uses all three of the above bulleted approximations and justifies the validity of each when applied to this transistor oscillator model in sections 7.4.1, 7.4.3, and 7.5.2, respectively.

Despite the the necessity of using approximations *just* to solve for *something*, atomtronics has made unwavering progress in ultracold atom technologies such as realizing quantum simulators [56][57][58][59], improving precision measurements [60][61], creating an atomtronic analogue to a SQUID (called an AQUID, or atomtronic quantum interference device [62][63]), and realizing the first-ever atom battery [33]. Moreover, if used in conjunction with well-established matterwave interferometry experiments, atomtronics can help enhance inertial sensing and gravimetry sensitivities by up to 10 orders of magnitude as compared to their light wave interferometry counterparts [64]. Finally, atomtronics can conceive new types of quantum technologies by combining various atomtronic circuit elements into an integrated ultracold atom circuit. One such integrated ultracold circuit, which is the subject of part III of this dissertation, is a matterwave transistor oscillator.

7.2 Background and Motivation for an Atomtronic Transistor Oscillator

7.2.1 Analogue to Electronic Transistors

Fundamental to many technological developments since its demonstration by Bardeen, Shockley, and Brattain at Bell Labs in 1948, the transistor is a three-terminal semiconductor electronic device that uses an applied voltage or current on one terminal to amplify or switch electrical signals on another terminal [65]. An *atomtronic* transistor would behave similarly to its semiconductor counterpart by switching or amplifying atom, or matterwave, currents rather than electrical currents. Moreover, in place of three electrical terminals (commonly known as the source, gate and

drain terminals) found on semiconductor transistors, an atomtronic transistor features three quantum potential energy wells that are capable of confining ultracold atoms, as shown in one of the original atomtronic transistor design concepts in figure 7.1. In similar form and function to the semiconductor transistor, these three potential energy wells, which are labeled the source-well, gate-well, and the drain-well, together behave as an atomtronic transistor source (to source an ultracold atom ensemble to flow through the system) a gate (confining an additional ultracold ensemble to provide a gain mechanism), and a drain (which functions as the output port of the transistor).

Most importantly, for such source-gate-drain system to be called an atomtronic transistor, it *must* display a gain mechanism for a matterwave or atom current. The overall concept of an atom current gain mechanism in an atomtronic transistor is shown in figure 7.1. As matterwaves flow from source, to gate, to drain via tunneling between each potential energy well, the gain mechanism emerges due to a change in the gate-well chemical potential (as a result of an ultracold atom population building up in gate-well) resulting in an increase of tunneling probability to flow through the gate-well and into the drain-well. This manifests itself in an increase of the atom flux Φ, or atoms per unit time, flowing through the potential [35].

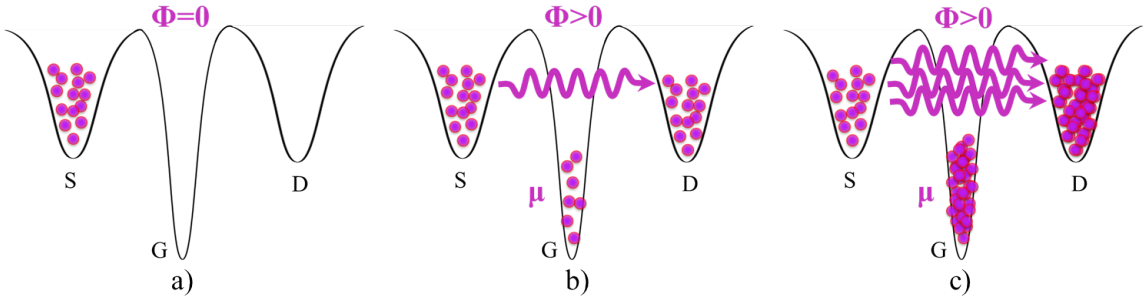

Figure 7.1: Concept of atomtronic transistor gain mechansim: a) With no atoms in the gate, no atom current flows from source (S) to gate (G) to drain (D), giving an atom flux $\Phi = 0$. b) As the gate occupancy increases, so does the gate-well chemical potential and a flux of atoms ($\Phi > 0$) flows into the drain. c) As the gate occupancy increases, so does the magnitude of the atom current and flux continues to increase ($\Phi >> 0$).

7.2.2 Extending the Semiclassical Descriptions of an Atomtronic Transitor

Before introducing our quantum model, we note that it begins with the setup and results of references [33][5][34], which investigates transistor-like behavior of ultracold atoms flowing through networks of quantum potential energy wells in a *semiclassical* formalism by creating matterwave analogues of Kirchoff's current and voltage laws for atoms flowing across a double Gaussian barrier potential. Compared to the quantum model, the semiclassical picture is defined as the set of experimental conditions where the thermal energy of the atoms flowing through the transistor potential is much *larger* than the energy level spacing of the transistor gate-well. In the semiclassical model summarized in figure 7.2, atom currents are driven by collisions and their flow is described using classical Boltzmann statistics [34]. Atoms that have enough thermal energy to traverse the Gaussian barriers flow into the drain and establish an atom current I_{SD}. A non-intuitive result of the semiclassical model is that given an initially empty gate-well, an atom population quickly grows in the gate and rapidly condenses into a Bose-Einstein condensate. Not only was this remarkable effect experimentally observed [153], but the BEC steady state population was also shown experimentally to influence the atom current I_{SD} flowing from source to drain [34], which (as described in section 7.2.1) is characteristic of a gain mechanism.

For the remainder of this chapter, we start with the results of the semiclassical model and examine the transistor behavior and gain mechanism in a purely quantum description. As described in subsequent sections of chapter 7, there are major differences between the semiclassical and quantum transistor models. Namely, in the quantum model:

- The thermal energy of the source-well atom ensemble is comparable (ideally equal) to the gate-well energy level spacing
- Atoms flowing through the transistor potential are described as matterwaves.
- The gate-well condensate is treated as a coherent state.
- The flow of atoms through the transistor is a result of resonant tunneling from the source-

well, *through the gate-well*, and into the drain-well (as opposed to the collisions primarily driving the semiclassical atom current).

- When the atom current reaches low enough energies, a new interaction, not observed in the semiclassical model or experiment, arises in the gate-well between the gate-well BEC and the atom current.

This new interaction, which arises due to the motional state of an oscillating gate-well BEC coupling high lying gate-well energy eigenstates, is similar to the Rabi model interaction between two-level atoms and a photon field. The interaction serves to increase the atom current by ultimately amplifying the matterwave probability amplitude in the transistor drain-well. This introduces an additional gain mechanism that *only* appears when the atom current is at sufficiently low enough temperatures for the BEC coupling (described above) to occur. We now describe this quantum model and principle of operation of our matterwave transistor oscillator.

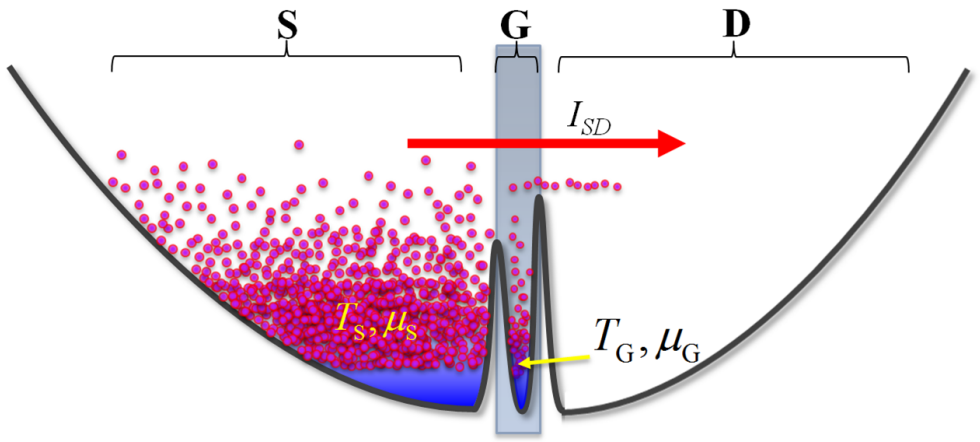

Figure 7.2: Summary of the semiclassical atomtronic transistor: 1D potential energy diagram of the triple-well transistor potential where an source-well ensemble of atoms at a chemical potential μ_S and temperature T_S flow with current I_{SD} into the drain well by classically traversing the barriers separating the centrally located gate from the source and drain. As the current flows, some atoms rapidly form a BEC in the gate well with a well-defined, steady state chemical potential μ_G and T_G. Previous experimental work shows the occupancy of this BEC can increase or decrease the current flowing from to source to drain, which provides an atom current gain mechanism.

7.3 Matterwave Transistor Oscillator Principle of Operation

Following references [33][5][34], our matterwave transistor is constructed by overlapping a harmonic, magnetic potential with two repulsive Gaussian barriers. This setup forms three potential energy wells which are labeled the source well, gate well, and drain well (figure 7.3a). Because the barriers separate the source-well from the gate-well and the gate-well from the drain-well, they are fittingly labeled the "source-gate" (SG) and "gate-drain" (GD) barriers.

Given a thermal atom ensemble originating in the source-well, a flux Φ of atoms per unit time flows through the transistor potential and into the drain-well by resonantly tunneling [154][155][156] through the transistor gate-well. Our model operates with the assumption that *only* the phenomenon of tunneling facilitates the flow of atoms throughout the transistor potential and does not allow atoms to classically traverse the SG or GD barriers. Thus, the atoms are hereafter described as matterwaves. With this definition, we arrive at the first principle of our matterwave transistor model:

- Only the source matterwaves satisfying the resonant tunneling boundary conditions of the gate-well will successfully flow with flux Φ into the drain-well (figure 7.3b).

This means that the incident source matterwaves *must* match gate-well boundary conditions (i.e. a gate-well energy eigenstate) to experience transmission into the drain. Otherwise the matterwave will be reflected off of the GD barrier with probability unity. It should be noted that the physics of a matterwave current flowing through our transistor via resonant tunneling is synonymous to the resonance phenomena observed in already well-understood systems, such as resonant tunneling diodes [157][158][159][160], optical Fabry-Perot resonators [161][162][163][164] and coupled transmission line resonators. Additionally, numerous references have examined matterwaves resonantly tunneling through double barrier potentials [165][166][167][168]. All of these examples of transmission phenomena given here, as well as our transistor model, share them same fundamental characteristic: only the incident waves matching boundary conditions of a resonator in the system experience transmission while all other fields are reflected.

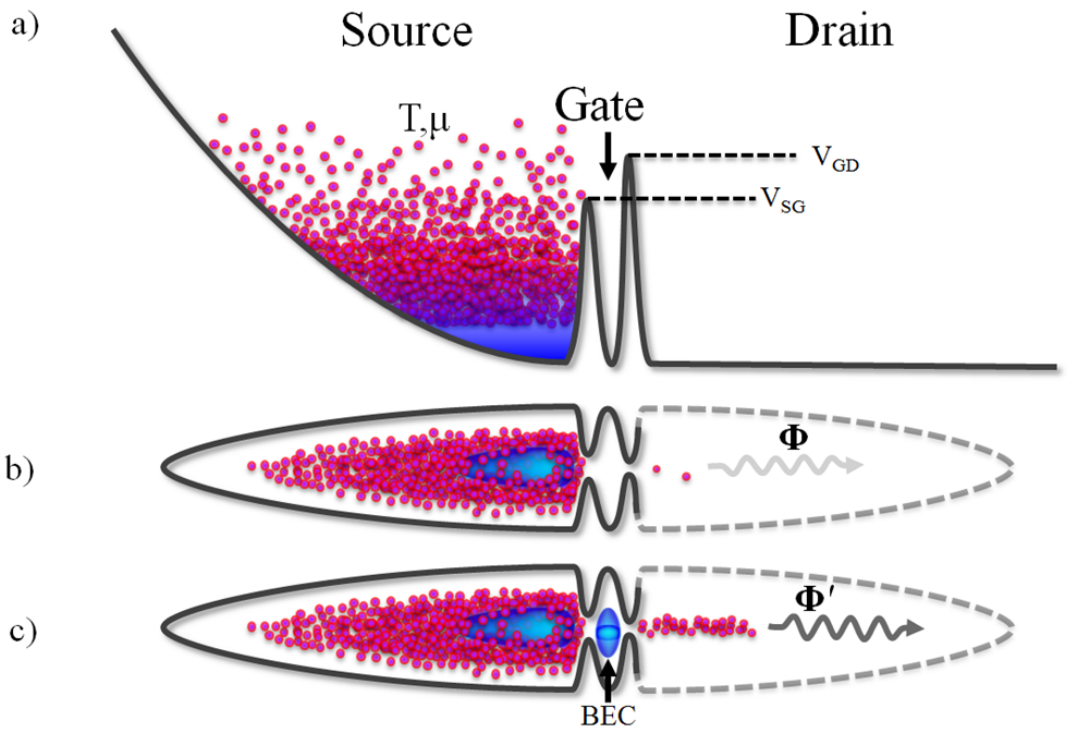

Figure 7.3: Setup and principle of operation of the matterwave transistor oscillator. a) A 1D potential energy diagram of the triple well matterwave transistor potential where an ensemble of atoms, at chemical potential μ and temperature T, occupies the source-well. The source-well and drain-well are separated by the gate-well, which is created with two repulsive Gaussian barriers called the Source-Gate (SG) and Gate-Drain (GD) barriers, which have potential energy heights V_{SG} and V_{GD}, respectively. Images b) and c) convey the principle of operation of the transistor, showing that a greater matterwave flux Φ' flows into the drain-well when a dipole oscillating BEC occupies the gate-well, compared to the matterwave flux Φ when a BEC is absent from the gate-well.

This leads to the second principle of our matterwave transistor model:

- By placing a dipole oscillating BEC in the gate-well, the matterwave current flowing into the drain-well with flux Φ' is amplified due to the BEC broadening the resonant tunneling boundary conditions (figure 7.3c).

The mechanism responsible for this increase of matterwave current is the emergence of an atom-BEC interaction that occurs only when the motional state of a gate-well BEC couples high lying gate-well energy eigenstates. An interesting consequence is the atom-BEC interaction allows matterwaves that do not *initially* match a resonance condition of the gate-well to absorb energy from or deposit energy into the interaction, allowing off-resonant matterwaves to shift their energy and satisfy the resonant boundary conditions of the gate-well. The now-resonant matterwaves are then permitted to resonate and build up inside the gate-well followed by subsequent flow out into the drain. Combining principles 1 and 2 gives the basis of our matterwave transistor model: When a dipole oscillating BEC occupies the transistor gate well, the matterwave current flowing into the drain with flux Φ' is greater than the flux Φ when the BEC is absent. This characteristic shows the presence of a gain mechanism, where gain $\mathcal{G}$ is defined as

$$\mathcal{G} = \Phi'/\Phi > 1. \tag{7.1}$$

The remainder of this chapter proceeds as follows: In section 7.4, we introduce the source, gate, and drain-well formalism in the quantum theory as well as present a reduced representation of the gate-well that is necessary to formulate a solvable Hamiltonian. Section 7.5 derives the many-bodied Hamiltonian for our transistor and explicitly shows the emergence of a gain mechanism when atom temperatures are sufficiently cold and an oscillating BEC is present in the gate-well. Section 7.6 directly shows that the gain mechanism amplifies an atom current flowing through the transistor by comparing the flux of matterwaves flowing from source-well to drain-well when the gain mechanism is absent to when it is present. Thus, we now introduce the formalities of the quantum model.

7.4 Modeling Matterwave Transmission Through 1D Transistor Potential

7.4.1 Source, Gate, and Drain Well Setup and Formalism

We begin the model by simplifying the problem by considering the flow of matterwaves through the transistor potential in one dimension only. In this 1D system, both the source and drain wells are treated as constant, flat potentials $V_S(x)$ and $V_D(x)$ (figure 7.4a) with

$$V_S(x) = V_D(x) = 0 \tag{7.2}$$

where matterwaves are described for free particles and the source and drain wavefunctions, $\Psi_S(x,t)$ and $\Psi_D(x,t)$, are given as plane wave solutions

$$\begin{aligned} \Psi_S(x,t) &= A_S e^{\pm i(k_S x - \omega_S t)} \\ \Psi_D(x,t) &= A_D e^{\pm i(k_D x - \omega_D t)} \end{aligned} \tag{7.3}$$

where wavenumber $k_i = \sqrt{2mE_i}/\hbar$ for kinetic energy E_i (where $i = S, D$ for source and drain) and mass m. The centrally located gate-well is separated from the source-well and drain-well by the SG and GD repulsive Gaussian barriers featuring equal $1/e$ waists of $w_0 = 2$ μm and asymmetric heights[1] of $V_{SG}/\hbar = 30$ kHz and $V_{GD}/\hbar = 33$ kHz. The asymmetry in the barrier heights is chosen such that the ratio $\upsilon = (V_{SG} - V_{GD})/T_s$, called the "feedback parameter" of the transistor oscillator [34], is equal to $\upsilon = 1$. As derived in reference [34], when barrier heights V_{SG}, V_{GD} and source-well ensemble temperature T_s give a feedback parameter $\upsilon = 1$, there will be an optimal balance of particle and energy currents flowing into and out of the gate-well to yield a stable atom ensemble in the gate well with high enough phase-space density to condense[2] in steady state. Thus, the barrier height asymmetry in the model allows for a steady-state BEC to collect in the gate-well as source atoms flow through the gate and into the drain-well.

By separating the SG and GD barriers by a distance $d = 4.85$ μm, the gate-well becomes a *slightly* anharmonic, asymmetric oscillator potential capable of confining ultracold atoms. An

[1] We shall assume throughout the rest of this dissertation that potential energy is expressed in frequency units.

[2] This remarkable behavior is equivalent to a resistor with *negative* resistance since the source atoms at temperature T_s that enter the gate and condense into a BEC are cooled to a lower temperature. If one were to flip the barrier heights so that $V_{SG} = 33$ kHz and $V_{GD} = 30$ kHz, the atom current would actually heat up upon entering the gate and no BEC would form. This latter case is equivalent to a resistor with *positive* resistance.

important result (that is critical to the emergence of gain in the model) of the anharmonicity[3] is that it establishes a degeneracy amongst transitions between the gate-well ground and first excited states and the highest lying pair of bound energy eigenstates (figure 7.4b). Additionally, this degeneracy (with difference ΔE) is unique to *this* particular pair of transitions and will not exist between any other pairs of states. By varying the $1/e$ widths w_0 and separation d of the SG and GD barriers, the degeneracy between the lowest lying and highest lying energy eigenstates can be transferred between various pairs of eigenstates or even removed entirely (figure 7.5 and 7.6).

Finally, despite the slight anharmonicity of the gate-well, we approximate the gate-well wavefuctions $\psi_n(x,t)$ as solutions to the quantum harmonic oscillator with

$$\psi_n(x) = \frac{1}{\sqrt{2^n n!}} \left(\frac{m\omega}{\pi\hbar}\right)^{1/4} H_n\left(\sqrt{\frac{m\omega}{\hbar}}x\right) e^{-m\omega x^2/2\hbar} \tag{7.4}$$

where n corresponds to the nth energy eigenstate of the gate well and $H_n(x)$ is the nth Hermite polynomial. With the gate-well eigenfunctions assumed to be harmonic oscillator solutions, as well as noting the gate-well potential used in this model features 24 bound energy eigenstates (figure 7.9b), the degeneracy described above exists between gate-well energy eigenstates $\psi_0(x,t)$ and $\psi_1(x,t)$ with $\psi_{22}(x,t)$ and $\psi_{23}(x,t)$.

7.4.2 Coupling Gate Well Energy Eigenstates With a Dipole Oscillating BEC

With the degeneracy between lowest and highest lying pairs of eigenstates present, we can write that

$$E_1 - E_0 = E_{23} - E_{22} = \hbar\omega_p \tag{7.5}$$

where each E_n is the energy eigenvalue for the ψ_n gate well eigenstate and ω_p is the fundamental oscillation frequency of the gate well potential defined as $E_0 = \hbar\omega_p/2$. As a consequence of this degeneracy (equation 7.5), given a gate-well BEC occupying ψ_0 with an excited portion occupying ψ_1 and undergoing dipole oscillation at frequency ω_p, the BEC will couple the highest lying pair

[3] The anharmonicity of the gate-well potential can also be observed in the non-linear increase of the gate-well energy eigenvalues. As shown in figure 7.9b, the gate-well energy eigenvalues do not increase linearly but rather follow a (very slight) s-curve function.

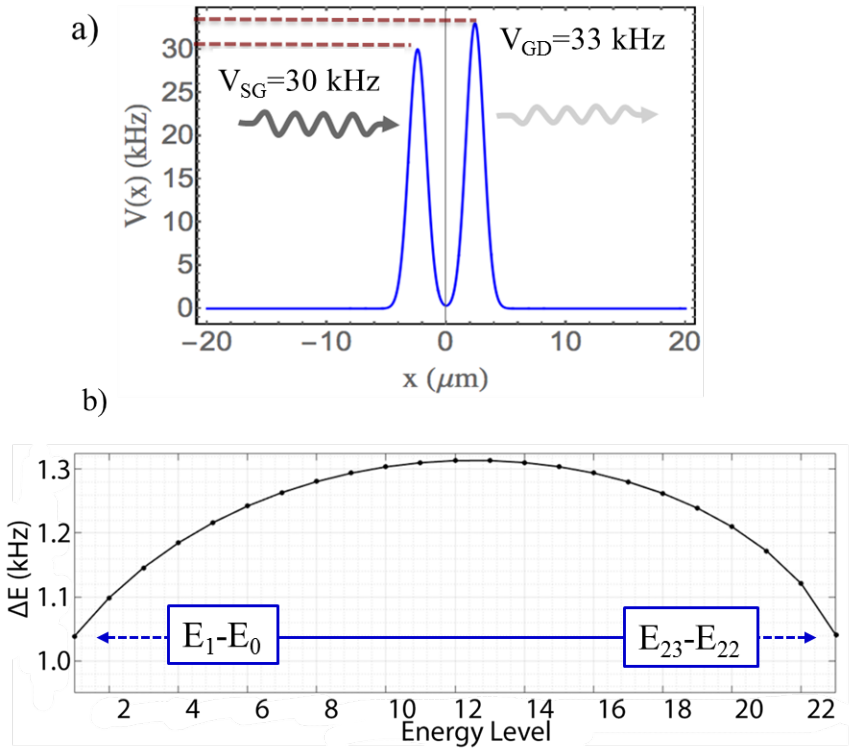

Figure 7.4: Setup and principle of operation of the matterwave transistor: a) Plot showing the source-gate (SG) and gate-drain (GD) barriers at potential energy heights $V_{SG} = 30$ kHz and $V_{GD} = 33$ kHz, respectively. The barriers separate the transistor into the three source, gate, and drain-well regions. In this model, the source and drain-wells are treated as flat potentials $V_S(x) = V_D(x) = 0$ and the gate-well is a slightly anharmonic oscillator. b) Plot showing the difference in energy ΔE between sequential energy eigenstates of the transistor gate-well. The horizontal axis lists the n^{th} gate-well energy level and the vertical axis is the corresponding energy difference $\Delta E = E_n - E_{n-1}$. For example, the left-most data point shows the energy difference between the first excited state and the ground state: $E_1 - E_0$. The next data point shows the energy difference $E_2 - E_1$, and so on. From this plot, it is clear that for our model with barrier parameters $V_{SG} = 30$ kHz, $V_{GD} = 33$ kHz, $w_0 = 2$ μm and $d = 4.85$ μm, a degeneracy exists between the ground and first excited state of the gate-well and the highest lying pair of gate-well energy eigenstates. That is, $E_1 - E_0 = E_{23} - E_{22}$.

of energy eigenstates, ψ_{22} and ψ_{23}. Therefore, as atoms occupying ψ_{22} and ψ_{23} collide with the oscillating BEC, stimulated emission and absorption of phonons with energy $\hbar\omega_p$ results in continuous Rabi flopping between the upper two energy eigenstates. It is from this continuous atom-BEC interaction (as a result of the BEC coupling the highest lying pair of states) that leads to a gain mechanism in the transistor oscillator model. The presence and effects of such gain mechanism emerges directly from the gate-well many-bodied Hamiltonian (section 7.5).

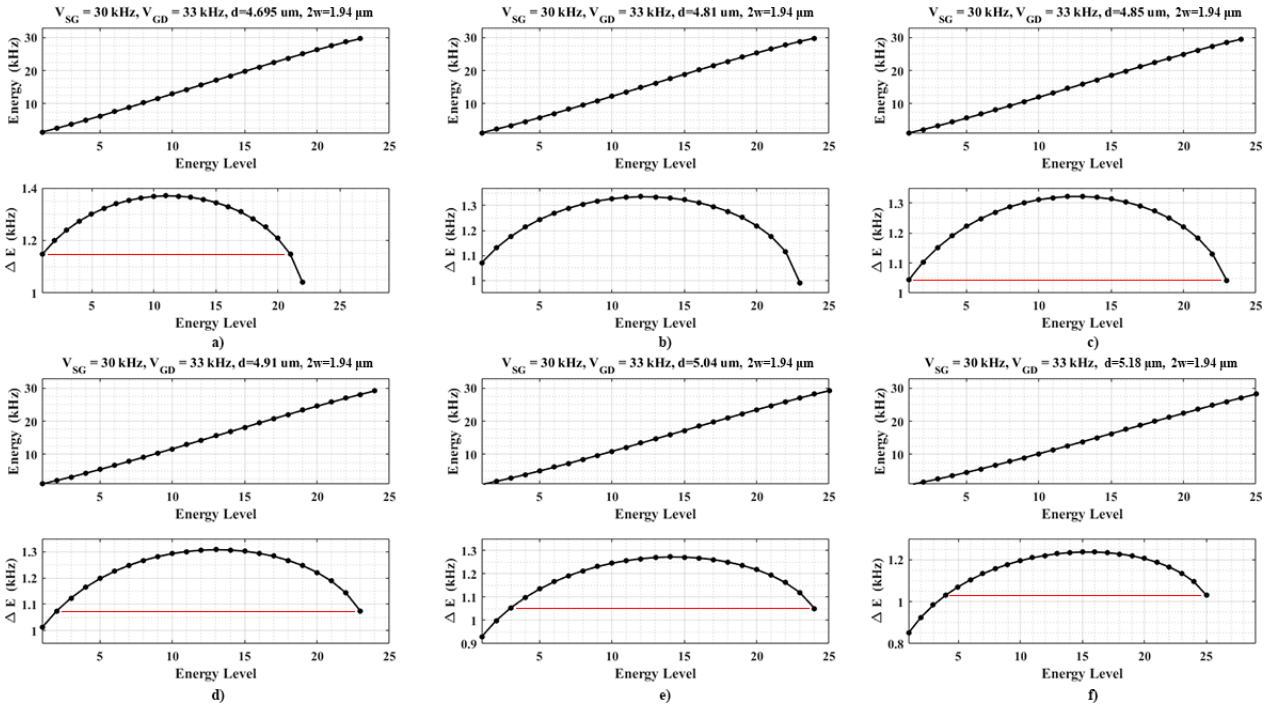

Figure 7.5: Plots showing the energy value of each gate-well eigenstate as well as the energy difference ΔE between adjacent energy eigenstates for various SG and GD barrier separations for the gate-well potential when $V_{SG} = 30$ kHz, $V_{GD} = 33$ kHz, and barrier widths are held constant. The solid red line indicates two pairs of adjacent eigenstates with the same ΔE value. Thus, altering the barrier separation d can change what transitions are degenerate with each other.

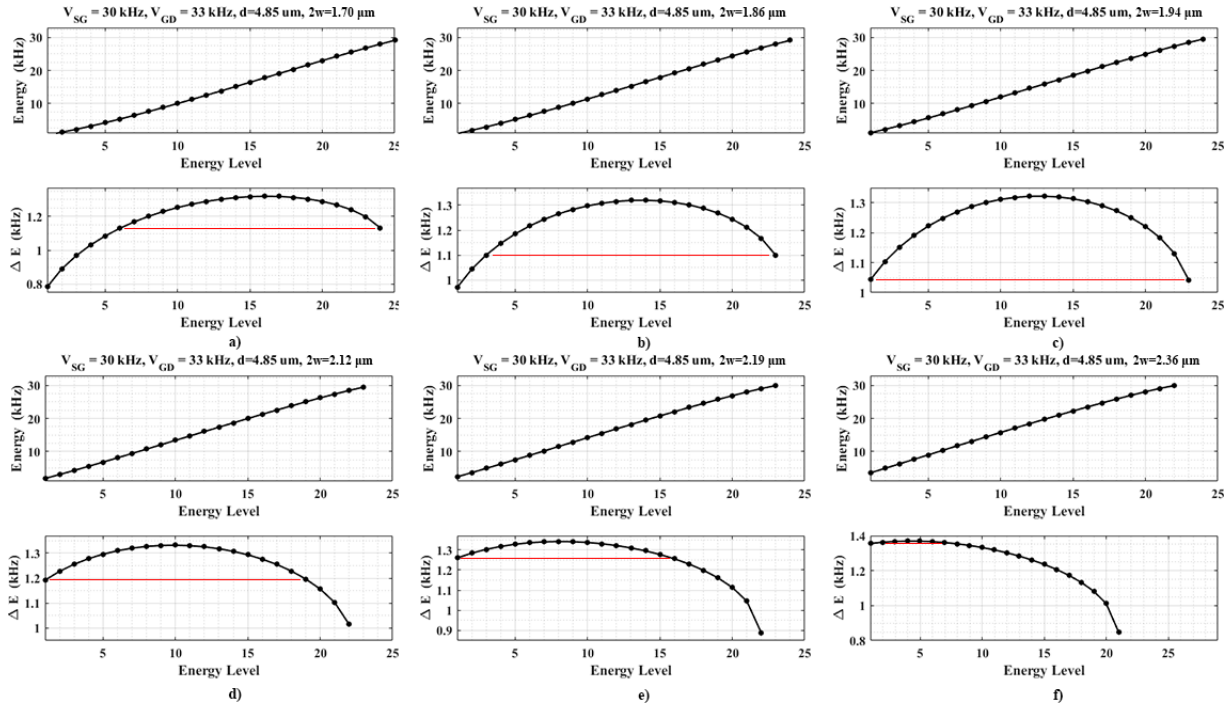

Figure 7.6: Plots showing the energy value of each gate-well eigenstate as well as the energy difference ΔE between adjacent energy eigenstates for various SG and GD barrier widths for the gate-well potential when $V_{SG} = 30$ kHz, $V_{GD} = 33$ kHz, and barrier separation is held constant. The solid red line indicates two pairs of adjacent eigenstates with the same ΔE value. Thus, altering the barrier separation d can change what transitions are degenerate with each other.

7.4.3 Reduced Representation of the Quantized Gate Well

Prior to formulating the gate-well many-bodied Hamiltonian that includes the atom-BEC interaction, our model simplifies the quantized energy structure of the gate-well by ignoring[4] any intermediate energy eigenstates located in-between the lowest and highest lying pairs of states. That is, the model only considers states ψ_0, ψ_1, ψ_{22} and ψ_{23}. Using this approximation, we reduce the gate well from 24 states to a four-level system and relabel the aforementioned four meaningful energy eigenstates to $|0\rangle$, $|1\rangle$, $|2\rangle$ and $|3\rangle$, where the first two states ($|0\rangle$ and $|1\rangle$) are the ground and first excited states and the latter two states ($|2\rangle$ and $|3\rangle$) pertain to the highest lying pair of bound energy eigenstates in the gate well (figure 7.7). The respective corresponding energy eigenvalues are E_0, E_1, E_2 and E_3, where

$$E_1 - E_0 = E_3 - E_2 = \hbar\omega_p. \tag{7.6}$$

In this reduced representation, as atoms transition between upper states $|2\rangle$ and $|3\rangle$ by colliding with the BEC, the excited condensate occupying $|1\rangle$ consequently gains (or loses) a phonon of energy $\hbar\omega_p$ by absorbing (or depositing) a quanta of energy $\hbar\omega_p$ from (or into) $|0\rangle$. Our reduced gate well picture is completely analogous to the Rabi model for two-level atoms interacting with a quantized electromagnetic field [169]. Where the Rabi model features transitions between excited and ground electronic states $|e\rangle \leftrightarrow |g\rangle$ by absorbing (and emitting) photons from an oscillating electric field, our gate model features similar transitions between upper harmonic oscillator states $|2\rangle \leftrightarrow |3\rangle$ by absorbing (and emitting) phonons from an oscillating BEC.

Finally, it is important to comment about the validity of reducing the gate-well down from 24 states to a four-level system. We may neglect the intermediate eigenstates of the gate-well since omitting such states will not change the final results of this model. Regardless of how many energy eigenstates make up the transistor oscillator gate-well, the model only requires a dipole oscillating BEC in the ground and first excited states to couple the highest lying pair of bound eigenstates and no other states. Whether the gate well has 24 states, 100 states, or 4 states, as long as *this*

[4] We make this assertion our model because as shown in sections 7.4.1 and 7.4.2. the dipole oscillating BEC couples *only* the highest lying pair of energy eigenstates and is decoupled from any other transition.

constraint is fulfilled, the gate-well many-bodied Hamiltonian, as well as the results of the model, will remain unchanged. In this regard, the reduced gate-well Hamiltonian is presented.

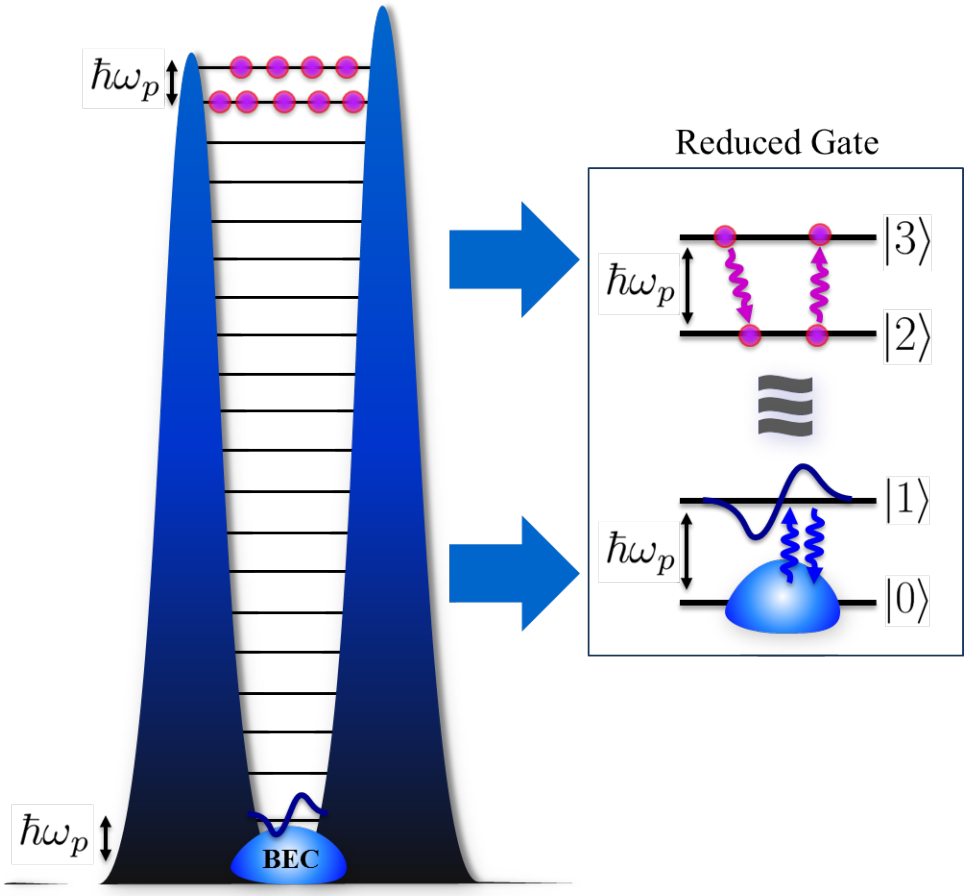

Figure 7.7: Diagram showing the reduced representation of the transistor gate well where the system has been reduced from a 24 state to a 4 state system. Stimulated emission and absorption (purple arrows) between $|2\rangle$ or $|3\rangle$ occurs due to phonon exchange from atom-BEC interactions with the dipole oscillating BEC (blue arrows)

7.5 Reduced Gate Well Many-Bodied Hamiltonian

To explicitly show the emergence of a transistor oscillator gain mechanism in this model, the many-bodied Hamiltonian of the reduced gate-well confining a BEC undergoing dipole oscillation with frequency ω_p must be formulated. Treating the reduced gate-well shown in figure 7.7 as a closed system with four energy eigenstates $|0\rangle$, $|1\rangle$, $|2\rangle$, and $|3\rangle$, the many-bodied Hamiltonian takes the form[5]

$$H = \sum_{il=0}^{3} \langle i| \hbar\omega_i |l\rangle \, a_i^\dagger a_l + \frac{g}{2} \sum_{i,j,k,l=0}^{3} \langle ij| V |kl\rangle \, a_i^\dagger a_j^\dagger a_k a_l. \tag{7.7}$$

where $\hbar\omega_i$ is the single particle energy of gate well eigenstate $|i\rangle$ and where $a_i^\dagger$ and a_i are the eigenstate's corresponding creation and annihilation operators. Since this model uses harmonic oscillator eigenfunctions, the operators are defined in the number state basis as

$$\begin{aligned} a_i |N_i\rangle &= \sqrt{N_i}\, |N_i - 1\rangle \\ a_i^\dagger |N_i\rangle &= \sqrt{N_i + 1}\, |N_i + 1\rangle \\ \left[a_i, a_i^\dagger\right] &= 1 \\ \left[a_i, a_j^\dagger\right] &= 0. \end{aligned} \tag{7.8}$$

The factor g in equation 7.7, which is derived in section 2.6.2 (equation 2.41), is the interaction energy between two low energy, long wavelength atoms with equal masses m, given as

$$g = \frac{4\pi\hbar^2}{m} a \tag{7.9}$$

where a is the s-wave scattering length of the colliding atoms. Finally, the inner product $\langle ij| V |kl\rangle$ is the overlap integral over four harmonic oscillator eigenfunctions (equation 7.4)

$$\langle ij| V |kl\rangle = V_{ijkl} = \int \psi_i(x)\psi_j^*(x)\psi_k(x)\psi_l^*(x)dx \tag{7.10}$$

giving the relative amplitude of a transition $a_i^\dagger a_j^\dagger a_k a_l$ between the normalized reduced gate well eigenstates $|i\rangle$, $|j\rangle$, $|k\rangle$, and $|l\rangle$ [170]. Using the definitions in equations 7.8, 7.9, and 7.10, the first summation of equation 7.7 physically represents all energy contributions from individual gate atoms

[5] The factor of 1/2 in equation 7.7 prevents double counting of atom-BEC interactions.

occupying eigenstates $|i\rangle, |j\rangle, |k\rangle$, and $|l\rangle$, while the second summation is energy contributions from atom-BEC collisions that result in transitions $a_i^\dagger a_j^\dagger a_k a_l$ between gate-well eigenstates.

7.5.1 Single-Particle Contributions

Since the gate-well eigenstates are orthogonal, expanding the single-particle contributions to equation 7.7 (which we will label H_0) yields

$$H_0 = \sum_{il}^{3} \langle i| \hbar\omega_i |l\rangle a_i^\dagger a_l = \sum_{il}^{3} \hbar\omega_i a_i^\dagger a_l \delta_{ij} = \hbar\omega_0 a_0^\dagger a_0 + \hbar\omega_1 a_1^\dagger a_1 + \hbar\omega_2 a_2^\dagger a_2 + \hbar\omega_3 a_3^\dagger a_3 \tag{7.11}$$

where δ_{ij} is the Kronecker delta. The model treats the BEC occupying state $|0\rangle$ of the gate-well as a macroscopic occupation of the gate-well ground state and accordingly uses the Bogoliubov approximation[6] to state

$$a_0 \approx \sqrt{N_0} \tag{7.12}$$

where N_0 is the number of atoms in the ground state BEC [172][173]. Using this approximation, equation 7.11 can be expressed as

$$H_0 = \hbar\omega_0 N_0 + \hbar\omega_1 a_1^\dagger a_1 + \hbar\omega_2 a_2^\dagger a_2 + \hbar\omega_3 a_3^\dagger a_3. \tag{7.13}$$

7.5.2 Atom-BEC Collision Contributions

From equation 7.7, the summation for energy contributions due to atom-BEC collisions, given as

$$H = \frac{g}{2} \sum_{i,j,k,l=0}^{3} \langle ij| V |kl\rangle a_i^\dagger a_j^\dagger a_k a_l. \tag{7.14}$$

is considerably larger than the summation for single particle energies (equation 7.11) and contains 256 terms when evaluated exactly. Thankfully, some helpful approximations can eliminate all but four of the terms *without* altering the results of the model. Justification for excluding certain collective sets of terms in the summation in equation 7.14 is provided as follows:

[6] Equation 7.8 shows the ground state annihilation and creation operators are $a_0 |N_0\rangle = \sqrt{N_0} |N_0 - 1\rangle$ and $a_0^\dagger |N_0\rangle = \sqrt{N_0 + 1} |N_0 + 1\rangle$. However, if the BEC is contains a large number of atoms, then $N_0 \approx N_0 - 1$ and we can reasonably approximate $a_0 |N_0\rangle \approx \sqrt{N_0} |N_0\rangle$. Therefore, the result of this Bogoliubov approximation is to replace the ground state operators a_0 and $a_0^\dagger$ with the real $\sqrt{N_0}$ [171].

- Mean-field energy shifts are neglected. That is, terms in the summation containing factors of $a_i^\dagger a_i^\dagger a_i a_i$ or $a_i^\dagger a_i^\dagger a_k a_l$ such as $a_0^\dagger a_0^\dagger a_0 a_0$, $a_0^\dagger a_0^\dagger a_k a_l$, or $a_1^\dagger a_1^\dagger a_k a_l$ are excluded from the model. Since mean-field shifts increase all gate-well energy levels *equally*, the shifts do not change the overall eigenstate layout of the gate-well and, more importantly, preserve the coupling between the highest pair of bound eigenstates via the oscillating condensate. Whether the mean-field energy shifts are included or not, the physics of the model remains unchanged. Accordingly, the model ignores the mean-field terms in equation 7.14.

- Nonsensical transitions with the form $a_i^\dagger a_i^\dagger a_i a_j$ are neglected from the model. These represent meaningless transitions that are either unphysical such as $a_3^\dagger a_3^\dagger a_3 a_0$ or transitions that leave the system unchanged, such as $a_3^\dagger a_3 a_3 a_2^\dagger$ or $a_1^\dagger a_1 a_1 a_0^\dagger$.

- The rotating wave approximation is used to eliminate the terms $a_0^\dagger a_1^\dagger a_2 a_3$ and $a_0 a_1 a_2^\dagger a_3^\dagger$. These contributions in equation 7.14 oscillate rapidly compared to the other terms and thus average approximately to zero.

- The Bogoliubov approximation (equation 7.12) is once again used since the number of atoms occupying the ground state BEC is considered to be large.

Using the first two bullet points in the above described set of approximations, the Hamiltonian for atom-BEC collisions, which is now labeled the interaction Hamiltonian H_{int}, is reduced to

$$\begin{aligned} H_{int} &= \frac{g}{2}\sum_{ijkl}^{3} \langle ij|\, V\, |kl\rangle\, a_i^\dagger a_j^\dagger a_k a_l \\ &= \frac{1}{2}V\Big[a_0^\dagger a_1^\dagger a_2 a_3 + a_0^\dagger a_1^\dagger a_3 a_2 + a_1^\dagger a_0^\dagger a_2 a_3 + a_1^\dagger a_0^\dagger a_3 a_2 \\ &\qquad + a_0^\dagger a_2^\dagger a_1 a_3 + a_0^\dagger a_2^\dagger a_3 a_1 + a_2^\dagger a_0^\dagger a_1 a_3 + a_2^\dagger a_0^\dagger a_3 a_1 \\ &\qquad + a_0^\dagger a_3^\dagger a_2 a_1 + a_0^\dagger a_3^\dagger a_1 a_2 + a_3^\dagger a_0^\dagger a_1 a_2 + a_3^\dagger a_0^\dagger a_2 a_1 \\ &\qquad + a_1^\dagger a_2^\dagger a_3 a_0 + a_1^\dagger a_2^\dagger a_0 a_3 + a_2^\dagger a_1^\dagger a_3 a_0 + a_2^\dagger a_1^\dagger a_0 a_3 \\ &\qquad + a_1^\dagger a_3^\dagger a_0 a_2 + a_1^\dagger a_3^\dagger a_2 a_0 + a_3^\dagger a_1^\dagger a_2 a_0 + a_3^\dagger a_1^\dagger a_0 a_2 \\ &\qquad + a_2^\dagger a_3^\dagger a_0 a_1 + a_2^\dagger a_3^\dagger a_1 a_0 + a_3^\dagger a_2^\dagger a_0 a_1 + a_3^\dagger a_2^\dagger a_1 a_0\Big]. \end{aligned} \tag{7.15}$$

Using the commutation relations for creation and annihilation operators $[a_i^\dagger, a_j^\dagger] = [a_i, a_j] = 0$ and $[a_i, a_j^\dagger] = \delta_{ij}$, equation 7.15 is further reduced to only six unique terms and is expressed as

$$\begin{aligned} H_{int} &= \frac{g}{2}\sum_{ijkl}^{3} \langle ij|\, V\, |kl\rangle\, a_i^\dagger a_j^\dagger a_k a_l \\ &= V\left[a_0^\dagger a_1^\dagger a_2 a_3 + a_0^\dagger a_1 a_2^\dagger a_3 + a_0^\dagger a_1 a_3^\dagger a_2 + a_1^\dagger a_0 a_2^\dagger a_3 + a_1^\dagger a_0 a_3^\dagger a_2 + a_0 a_1 a_2^\dagger a_3^\dagger\right]. \end{aligned} \tag{7.16}$$

Finally, using the third and fourth bullet point in the list of approximations, the rotating wave and Bogoliubov approximations reduce the interaction Hamiltonian to its most condensed form in the harmonic oscillator basis:

$$\begin{aligned} H_{int} &= \frac{g}{2}\sum_{ijkl}^{3} \langle ij|\, V\, |kl\rangle\, a_i^\dagger a_j^\dagger a_k a_l \\ &= gV\sqrt{N_0}\left(a_1\left[a_2^\dagger a_3 + a_3^\dagger a_2\right] + a_1^\dagger\left[a_2^\dagger a_3 + a_3^\dagger a_2\right]\right) \\ &= gV\sqrt{N_0}\left(a_1 + a_1^\dagger\right)\left(a_2^\dagger a_3 + a_3^\dagger a_2\right). \end{aligned} \tag{7.17}$$

7.5.3 Expressing Gate-Well Hamiltonian in the Basis of Normal Modes and Normal Mode Basis Definitions

The Hamiltonians H_0 (equation 7.13) and H_{int} (equation 7.17) for single-particle and atom-BEC contributions to the gate well many-bodied Hamiltonian are expressed in the harmonic oscillator (or number) basis. Considering that the dipole oscillating BEC couples upper states $|2\rangle$ and $|3\rangle$, the reduced gate-well (shown in figure 7.7) is a *coupled* harmonic oscillator and it proves to be much more illuminating to express the many-bodied Hamiltonian in a basis where the symmetric and antisymmetric normal modes of the reduced gate-well are the energy eigenstates. This new basis, which for the remainder of this dissertation is labeled as the *normal mode basis*, has orthogonal basis states

$$|+\rangle = \frac{1}{\sqrt{2}}\left(|2\rangle + |3\rangle\right) \tag{7.18a}$$

$$|-\rangle = \frac{i}{\sqrt{2}}\left(|2\rangle - |3\rangle\right) \tag{7.18b}$$

where $|+\rangle$ and $|-\rangle$ are the symmetric and antisymmetric normal modes[7] , respectively. Additionally, in the normal mode basis, the oscillating, excited portion of the gate-well condensate that occupies $|1\rangle$ is described as a coherent state $|\alpha\rangle$ with magnitude $|\alpha|$.

When using matrix notation, the symmetric and antisymmetric modes given in equations 7.18a and 7.18b are defined as

$$|+\rangle = \begin{pmatrix} 1 \\ 0 \end{pmatrix}, |-\rangle = \begin{pmatrix} 0 \\ 1 \end{pmatrix}. \tag{7.19}$$

To convert H_0 (equation 7.13) and H_{int} (equation 7.17) into the normal mode basis, the following symmetric and antisymmetric operator transformations are introduced:

$$a_+ \equiv \frac{1}{\sqrt{2}}(a_3 + a_2) \tag{7.20a}$$

$$a_- \equiv \frac{i}{\sqrt{2}}(a_3 - a_2) \tag{7.20b}$$

$$a \equiv a_1. \tag{7.20c}$$

Applying the operator transformations 7.20a, 7.20b, and 7.20c to equation 7.13 outputs

$$\begin{aligned} H_0 &= \sum_{il}^{3} \langle i| \hbar\omega_i |l\rangle a_i^\dagger a_l \\ &= \hbar\omega_0 N_0 + \hbar\omega_1 a^\dagger a + \frac{\hbar\omega_2}{2}(a_+^\dagger - ia_-^\dagger)(a_+ + ia_-) + \frac{\hbar\omega_3}{2}(a_+^\dagger + ia_-^\dagger)(a_+ - ia_-) \end{aligned} \tag{7.21}$$

and applying the operator transforms to equation 7.17 produces

$$\begin{aligned} H_{int} &= \frac{g}{2}\sum_{ijkl}^{3} \langle ij| V |kl\rangle a_i^\dagger a_j^\dagger a_k a_l \\ &= gV\sqrt{N_0}\left\{a[a_+^\dagger a_+ - a_-^\dagger a_-] + a^\dagger[a_+^\dagger a_+ - a_-^\dagger a_-]\right\} \\ &= gV\sqrt{N_0}\left\{(a + a^\dagger)(a_+^\dagger a_+ - a_-^\dagger a_-)\right\}. \end{aligned} \tag{7.22}$$

Combining equations 7.21 and 7.22 gives the many-bodied Hamiltonian for the reduced gate-well

[7] Realize that the normal mode basis, with eigenstates $|+\rangle$ and $|-\rangle$, is simply a 2D vector space rotated $\Theta = \pi/4$ from the original $|2\rangle$ and $|3\rangle$ basis states.

in the normal mode basis:

$$\begin{aligned} H &= H_0 + H_{int} \\ &= \hbar\omega_0 N_0 + \hbar\omega_1 a^\dagger a + \frac{\hbar\omega_2}{2}(a_+^\dagger - ia_-^\dagger)\,(a_+ + ia_-) + \frac{\hbar\omega_3}{2}(a_+^\dagger + ia_-^\dagger)\,(a_+ - ia_-) \\ &+ gV\sqrt{N_0}\left\{(a + a^\dagger)(a_+^\dagger a_+ - a_-^\dagger a_-)\right\}. \end{aligned} \tag{7.23}$$

Equation 7.23 can be simplified further by using the following identities:

$$a_+^\dagger a_+ = |+\rangle\langle+| \tag{7.24a}$$

$$a_-^\dagger a_- = |-\rangle\langle-| \tag{7.24b}$$

$$(a_+^\dagger \pm ia_+^\dagger)\,(a_+ \mp ia_-) = \mathbf{1} \pm \sigma_2 \tag{7.24c}$$

$$(a + a^\dagger)(a_+^\dagger a_+ - a_-^\dagger a_-) = (a + a^\dagger)\sigma_3 \tag{7.24d}$$

where $\mathbf{1}$ is the identity matrix, σ_2 is the Pauli y-matrix, and σ_3 is the Pauli z-matrix defined as

$$\mathbf{1} = \begin{pmatrix} 1 & 0 \\ 0 & 1 \end{pmatrix}, \sigma_2 = \begin{pmatrix} 0 & -i \\ i & 0 \end{pmatrix}, \sigma_3 = \begin{pmatrix} 1 & 0 \\ 0 & -1 \end{pmatrix}. \tag{7.25}$$

Plugging equations 7.24a-7.24d into equation 7.23 and simplifying gives the many-bodied Hamiltonian for the reduced gate-well in the normal mode basis as

$$\begin{aligned} H &= H_0 + H_{int} \\ &= \hbar\omega_0 N_0 + \hbar\omega_1 a^\dagger a + \frac{\hbar}{2}(\omega_2 + \omega_3)\mathbf{1} - \frac{\hbar}{2}(\omega_3 - \omega_2)\sigma_2 + gV\sqrt{N_0}(a + a^\dagger)\sigma_3. \end{aligned} \tag{7.26}$$

Treating[8] matterwaves occupying the reduced, coupled gate-well as a linear combination of normal modes

$$\Psi_G(x) = \frac{1}{\sqrt{2}}\left[A_+ |+\rangle + A_- |-\rangle\right] \tag{7.27}$$

where $A_\pm$ are the probability amplitudes for the $|\pm\rangle$ modes, there exists matterwave interference between the constituent (and simultaneously occupying) $|+\rangle$ and $|-\rangle$ modes. As a result, the total wavefunction in the gate-well has a beat note that oscillates with a relative phase[9] ϕ_ζ (see figure

[8] The assumption can be made because the normal modes $|+\rangle$ and $|-\rangle$ are orthogonal and complete.

[9] This phase described here is a *relative* phase defined with respect to some reference in the gate well, such as the ground state BEC occupying $|0\rangle$. An example of the superposition of gate well normal modes, as well as the relative phase ϕ_ζ, is shown in figure 7.8.

7.8 for a depiction of ϕ_ζ). Therefore, the amplitude of the atom-BEC interaction Hamiltonian, $gV\sqrt{N_0}$, gains a phase dependence and can be expressed as a complex valued function ζ as

$$\zeta = gV\sqrt{N_0}e^{i\phi_\zeta}. \tag{7.28}$$

Using equation 7.28 in equation 7.26, the entire gate-well many-bodied Hamiltonian can be expressed in the normal mode basis as a sum of a free space term H_0, a condensate term H_c, and the atom-BEC interaction term H_{int} as

$$\begin{aligned} H_G &= H_0 + H_c + H_{int} \\ &= \underbrace{\hbar\overline{\omega} - \frac{1}{2}\hbar\omega_p\sigma_2}_{\text{free space}} + \underbrace{\hbar\omega_0 N_0 + \hbar\omega_p a^\dagger a}_{\text{condensate}} + \underbrace{(\zeta^* a + \zeta a^\dagger)\sigma_3}_{\text{interaction}} \end{aligned} \tag{7.29}$$

where $\overline{\omega} = (\omega_2 + \omega_3)/2$ and $\omega_p = \omega_3 - \omega_2$ is the phonon frequency.

Other than a change of basis and the fixed condensate energy, equation 7.29 is identical to the Rabi Hamiltonian[10] for a two-level atom interacting with an electromagnetic field. Where the Rabi Hamiltonian has electronic states interacting with photons, the gate-well Hamiltonian H_G involves *center-of-mass states* (meaning the symmetric and antisymmetric normal modes) interacting with *phonons*.

7.5.4 Eigenstates and Eigenvalues of the Interaction Hamiltonian

As shown in equation 7.29, the atom-BEC interaction Hamiltonian expressed in the normal mode basis is

$$H_{int} = (\zeta^* a + \zeta a^\dagger)\sigma_3. \tag{7.30}$$

Eigenstates of the interaction Hamiltonian are $|\alpha, \pm\rangle = |\alpha\rangle \otimes |\pm\rangle$ where $|\alpha\rangle$ is a coherent state with magnitude $|\alpha|$, and $|\pm\rangle$ are the symmetric and antisymmetric normal modes of the gate-well. The

[10] Similar to the Rabi Hamiltonian, in the gate-well *free space* Hamiltonian component H_0 derived in equation 7.29, the σ_2 term represents spontaneous emission:

$$H_{se} = \frac{\hbar}{2}(\omega_3 - \omega_2)\sigma_2$$

and couples states of opposite symmetric or anti-symmetric parity.

corresponding eigenvalues E_{int} of the interaction Hamiltonian are

$$\begin{aligned} E_{int} = \langle \alpha, \pm | \, H_{int} \, | \alpha, \pm \rangle &= \pm \left(\zeta^* \alpha + \zeta \alpha^* \right) \\ &= \pm 2 |\zeta| |\alpha| \cos \left(\phi_\zeta - \phi_\alpha \right) \\ &= \pm 2 |\zeta \alpha| \cos \varphi \end{aligned} \tag{7.31}$$

where φ is the relative phase difference between ϕ_ζ, the phase of the matterwave interference of the gate-well normal modes, and ϕ_α, the phase of the gate-well dipole oscillating BEC. Therefore, the physical interpretation of $\varphi = \phi_\zeta - \phi_\alpha$ is that it represents the phase of a *difference of phases*. The oscillating condensate and matterwave interference are shown relative to each other in figure 7.8 in order to conceptualize the phases ϕ_ζ, ϕ_α, and φ. It immediately follows from the domain of equation 7.31 that the eigenvalues of the interaction Hamiltonian take on a range of values depending on the relative phase φ:

$$-2|\zeta\alpha| \leq E_{int} \leq +2|\zeta\alpha|. \tag{7.32}$$

The interaction energy eigenvalue in equation 7.31 can be written in a more complete form by taking the expressions for g (equation 2.41) and V (equation 7.10) and plugging them into the expression for ζ (equation 7.28), giving

$$\zeta = \sqrt{N_0} \left(\frac{4\pi\hbar^2}{m} \frac{a}{\upsilon} \right) e^{i\phi} \int_{-\infty}^{\infty} \psi_0^*(x) \psi_1(x) \psi_2^*(x) \psi_3(x) dx. \tag{7.33}$$

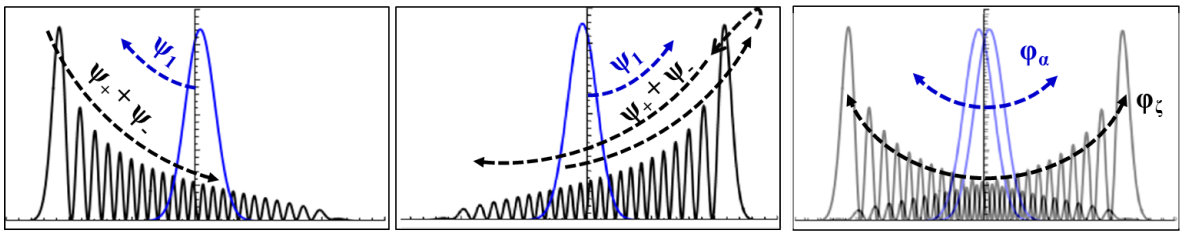

Figure 7.8: Plots showing a time lapse of the matterwave superposition of normal modes $\psi_+ + \psi_-$ occupying states ψ_2 and ψ_3 and oscillating with a phase ϕ_ζ as well as the excited condensate occupying state ψ_1 and oscillating with a phase ϕ_α. The phase φ used for determining the eigenvalue of the interaction Hamiltonian is the difference of these phases, given as $\varphi = \phi_\zeta - \phi_\alpha$.

Additionally, since the dipole oscillating BEC occupying $|1\rangle$ is described as a coherent state $|\alpha\rangle$, we use the definition of the coherent state magnitude to write

$$|\alpha| = \sqrt{N_1}. \tag{7.34}$$

Taking the results of equation 7.33 and 7.34 and inserting them into equation 7.31 yields a complete expression for the eigenvalue of the interaction Hamiltonian H_{int} in the normal mode basis:

$$\begin{aligned} \langle \alpha, \pm | \, H_{int} \, | \alpha, \pm \rangle &= \pm 2 |\zeta \alpha| \cos\varphi \\ &= \pm 2\sqrt{N_0 N_1} \left(\frac{4\pi\hbar^2}{m} \frac{a}{v} \right) \left(\int_{-\infty}^{\infty} \psi_0^*(x) \psi_1(x) \psi_2^*(x) \psi_3(x) dx \right) \cos\varphi. \end{aligned} \tag{7.35}$$

With the eigenvalue of the interaction Hamiltonian fully defined in the normal mode basis, the following section of this dissertation demonstrates how the interaction Hamiltonian (equation 7.30) acts as a gain mechanism.

7.6 Matterwave Current Flow From Source to Gate to Drain

The gain mechanism of the matterwave transistor oscillator is understood by comparing the flow of a matterwave current resonantly tunneling from the source-well, through the gate-well, and into the drain-well in two different cases:

- When no dipole oscillating BEC occupies the transistor gate-well; that is when the gate-well is "empty" and $H_{int} = 0$
- When a dipole oscillating BEC occupies the gate-well and couples high lying gate-well eigenstates; that is when $H_{int} \neq 0$.

In this section, we show that a greater flux of source-well matterwaves flow via resonant tunneling through the gate-well and into the drain-well when a dipole oscillating BEC occupies the gate (when $H_{int} \neq 0$) as opposed to when the gate has no such BEC (when $H_{int} = 0$). As a result, a greater matterwave probability amplitude exists in the transistor drain-well when the interaction potential H_{int} is present compared to when it is missing from the system, thus establishing the interaction potential H_{int} as a matterwave gain mechanism.

7.6.1 Empty Gate-Well with No BEC Present

Consider the triple-well transistor potential with no oscillating BEC present in the gate-well (which is labeled as an "empty gate"). As a source-well matterwave flows through the gate-well, it's probability amplitude in the drain-well is a function of the transmission coefficients of the gate-well. Such transmission coefficients are calculated for our specific gate-well potential (figure 7.4) by utilizing a numerical technique called the general impedance method [174][175][176][177][178][179], which cleverly formulates an equivalence between matterwaves tunneling through the gate-well (whose solutions are governed by the 1D time-independent Schrodinger equation) and electromagnetic waves propagating through transmission line junctions (whose solutions are governed by transmission-line theory from classical electrodynamics). Relying on the philosophy that "similar problems have similar solutions", the general impedance method is capable of calculating transmission coefficients for arbitrary potential barriers in quantum systems, making it useful for determining transmission properties of the asymmetric, double Gaussian gate-well for the atomtronic transistor. The actual calculation of applying the general impedance method to our gate-well potential to solve for the transmission coefficients is covered in the Master's thesis of Ava Ashby [180].

Examination of the transmission spectrum (figure 7.9) reveals that sharp resonances in the gate-well tunneling probability occur when the energy of incident source-well matterwave coincides with an energy eigenstate of the gate-well[11] . Using the reduced gate-well nomenclature, when incident source-well matterwaves match a gate-well resonance boundary condition by having energy E_2 or E_3, the matterwaves couple into the gate-well and resonate in the gate-well, followed by subsequent tunneling into the drain-well with probability $\tau_2 \approx 10^{-4}$ or $\tau_3 \approx 10^{-4}$, respectively. Slight deviations from these transmission resonances (by having an energy E just off-resonance from E_2 or E_3) results in a substantial decrease in matterwave probability amplitudes in the drain-well. Consequently, for the case of no BEC in the gate well: the resulting observable effect is that an appreciable atom flux Φ flows into the drain-well *only* when source-well atoms are initially

[11] As mentioned in section 7.3, this transmission behavior is synonymous with Fabry-Perot resonators, resonant tunneling diodes, and other systems that feature maximum transition when incident fields match resonance boundary conditions.

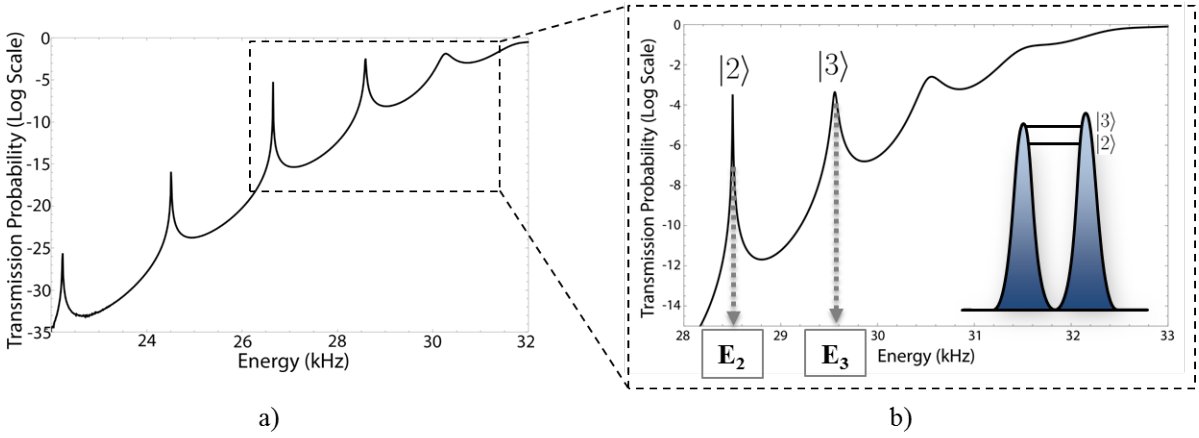

Figure 7.9: a) Transmission probability of the transistor gate-well as a function of incident matterwave energy when no BEC occupies the gate-well, as calculated by the general impedance method. Resonances in transmission occur when incident matterwaves have energy coinciding with a gate-well energy eigenstate. b) This inset shows the transmission resonances near energies coinciding with the highest lying pair bound energy eigenstates (which correspond to reduced gate-well energy eigenstates $|2\rangle$ and $|3\rangle$). If incident matterwaves have a slightly different energy, the probability of transmission through the gate-well and into the drain-well decreases significantly and can be reduced by more than 10 orders of magnitude. Essentially, transmission through the "empty" gate-well occurs only when incident matterwaves have energy coinciding with a gate-well eigenstate. Thus, in the reduced gate-well, incident matterwaves *must* have energy equal to E_2 or E_3 for transmission into the drain-well to occur. Otherwise, the matterwaves are reflected.

prepared to match a gate-well eigenstate.

7.6.2 Effect of Interaction Potential on Matterwave Current and Gain

We now examine matterwave current flow from source to drain when a dipole oscillating BEC occupies the gate-well and couples upper states $|2\rangle$ and $|3\rangle$. With the presence of the BEC, the atom-BEC interaction Hamiltonian H_{int} (equation 7.30) must be included in the gate-well many-bodied Hamiltonian. As we will now show, by including H_{int}, the matterwave current (an atom flux) flowing from source to drain *increases*. To understand why the current is increased, consider a single matterwave $\psi_s(x,t)$ with frequency ω_s originating in the source-well and whose energy *does not* coincide with a gate-well eigenstate; that is $\omega_s \neq \omega_2 \neq \omega_3$. Using the definitions from section 7.4.1, the model treats the source-well matterwaves as plane wave solutions (equation 7.3). We also operate in the normal mode basis and additionally, treat the source-well matterwave as a linear combination of the gate-well symmetric $\psi_{s+}(x,t)$ and antisymmetric $\psi_{s-}(x,t)$ normal modes:

$$\psi_s(x,t) = A_+\psi_{s+}(x,t) + A_-\psi_{s-}(x,t) \tag{7.36}$$

with amplitudes A_+ and A_- (and s denotes a source-well quantity). Using the definitions for the symmetric and anti-symmetric modes (equation 7.18a and 7.18b) produces expressions for $\psi_{s+}(x,t)$ and $\psi_{s-}(x,t)$ as

$$\begin{aligned}
\psi_{s+}(x,t) &= \frac{1}{\sqrt{2}}\left[\psi_{s3}(x,t) + \psi_{s2}(x,t)\right] \\
&= A_{s+}(x,t)e^{i(k_s x - \omega_s t)}\cos\left(\frac{\omega_p}{2}t + \varphi\right) \qquad (7.37a) \\
\psi_{s-}(x,t) &= \frac{1}{\sqrt{2}}\left[\psi_{s3}(x,t) - \psi_{s2}(x,t)\right] \\
&= A_{s-}(x,t)e^{i(k_s x - \omega_s t)}\sin\left(\frac{\omega_p}{2}t + \varphi\right) \qquad (7.37b)
\end{aligned}$$

with wavenumber k_s and frequency ω_s. Since the symmetric (equation 7.37a) and antisymmetric (equation 7.37b) components of $\psi_s(x,t)$ are sinusoids that are offset by $\pi/2$ radians, they are characterized as the in-phase and quadrature components of the source-well matterwave, respectively.

Using the above source-well matterwave definitions, when $\psi_s(x,t)$ (equation 7.3) penetrates the SG barrier and enters the gate-well, the atom-BEC interaction, described by H_{int}, occurs. In order for the incoming wave $\psi_s(x,t)$ to simultaneously match the gate-well boundary conditions *and* conserve energy, the wave must deposit energy into, or absorb energy from the atom-BEC interaction energy. The energy shift ΔE imparted by the atom-BEC interaction was calculated in equation 7.31 as $\Delta E = \pm 2|\zeta\alpha|\cos\varphi$ where the sign of the energy shift is positive for the symmetric component $\psi_{s+}(x,t)$ and negative for the antisymmetric component $\psi_{s-}(x,t)$. It immediately follows that for an initially off-resonant matterwave $\psi_s(x,t)$ with frequency ω_s to match a gate-well eigenstate with frequency ω_g *and* satisfy gate-well resonance boundary conditions, the atom-BEC interaction must change the incoming wave energy by $\Delta E = \hbar\omega_s - \hbar\omega_g$. Using equation 7.31, this energy shift defines an in-phase[12] condition

$$\varphi = -\cos\left(\frac{\omega_g - \omega_s}{2|\zeta\alpha|}\right) \tag{7.38}$$

whereby if satisfied, the in-phase, symmetric component $\psi_{s+}(x,t)$ (equation 7.37a) is shifted onto a gate-well eigenstate and couples into the gate-well, while the quadrature, antisymmetric component $\psi_{s-}(x,t)$ (equation 7.37b) is completely reflected since $\psi_{s-}(x,t)$ is shifted even further from the gate-well resonance.

The domain of equation 7.38 reveals that the range of source-well matterwave frequencies ω_s that may be shifted onto a gate-well resonance with frequency ω_g via the atom-BEC interaction is given by

$$\omega_g - 2\left(\frac{|\zeta\alpha|}{\hbar}\right) \leq \omega_s \leq \omega_g + 2\left(\frac{|\zeta\alpha|}{\hbar}\right) \tag{7.39}$$

which indicates the interaction Hamiltonian *broadens* the gate-well resonant tunneling bandwidths

[12] One could, without changing the model results, define instead a *quadrature* condition of

$$\varphi = -\cos\left(\frac{\omega_g - \omega_s}{2|\zeta\alpha|} + \frac{\pi}{2}\right) = \sin\left(\frac{\omega_g - \omega_s}{2|\zeta\alpha|}\right)$$

whereby if satisfied, the *antisymmetric* component $\psi_{s-}(x,t)$ couples into the gate with the in-phase, symmetric component being reflected.

Λ from the very narrow peaks shown in figure 7.9a to the wider bands

$$\Lambda_2 = \omega_2 \pm 2\left(\frac{|\zeta\alpha|}{\hbar}\right) \tag{7.40a}$$

$$\Lambda_3 = \omega_3 \pm 2\left(\frac{|\zeta\alpha|}{\hbar}\right) \tag{7.40b}$$

where subscripts 2 and 3 correspond to the resonant frequencies ω_2 or ω_3 of gate-well eigenstates $|2\rangle$ and $|3\rangle$, respectively. The result of equations 7.40a and 7.40b are shown pictorially in (figure 7.10). From these equations, it is immediately apparent that the resonant tunneling bandwidth is controlled by the magnitude $|\zeta\alpha|$, which is an experimentally tunableparameter in the sense that the larger the gate-well condensate, the greater the magnitude of $|\alpha|$, and hence a larger interaction potential H_{int}, which results in broader resonant tunneling bandwidths Λ_2 and Λ_3.

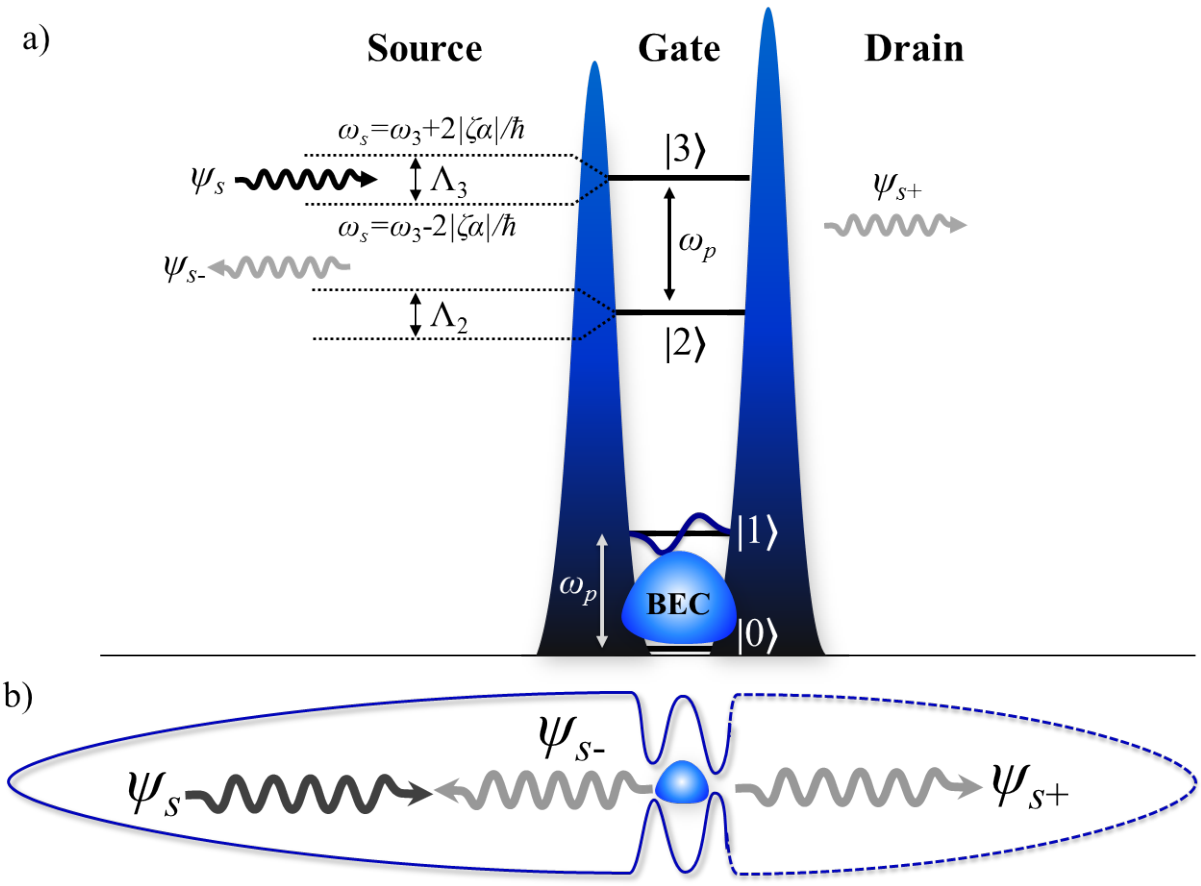

Figure 7.10: a) Diagram showing how the presence of a dipole oscillating BEC in the transistor gate-well that specifically couples the highest lying pair of bound gate-well energy eigenstates broadens the gate-well resonant tunneling bandwidths by introducing the interaction Hamiltonian, H_{int} (equation 7.30). The resonant tunneling bandwidths are broadened from a very narrow transmission resonance (as shown in figure 7.9), to a wider band Λ_2 and Λ_3 (given in equation 7.40a and equation 7.40b). b) As a result of the interaction Hamiltonian, in the example given in section 7.6.2, as a source-well matterwave ψ_s, initially off-resonance from a gate-well eigenstate, enters the gate-well, the interaction Hamiltonian permits the atom to exchange energy with the dipole oscillating BEC in order to match gate-well resonant boundary conditions while conserving energy. Consequently, the symmetric mode ψ_{s+} couples into the gate-well with subsequent flow into the drain while the antisymmetric mode ψ_{s-} is reflected with probability unity. The net effect is the interaction potential has permitted a matterwave to resonantly tunnel through the gate-well and into the drain with *considerably* greater probability than if the interaction potential was missing.

7.6.3 Gain Mechanism

By comparing the analysis of section 7.6.2 (which treats matterwave transition *with* the gate-well BEC) and section 7.6.1 (which examines transmission *without* the gate-well BEC) we arrive at the matterwave gain mechanism of our transistor oscillator: compared to when no BEC is present in the gate-well, the atom-BEC interaction H_{int} increases the range of matterwaves that may couple into the gate-well with subsequent resonant tunneling out to the drain-well. The gain mechanism thus amplifies the matterwave probability density in the drain-well, which results in the observable effect of intensifying the atom flux tunneling into the drain-well when a gate well BEC is present compared to when it is absent.

7.6.4 Characterizing the Matterwave Gain Mechanism

The equations derived in section 7.5.3 communicate a significant result of the model: Since each of the symmetric and antisymmetric components $\psi_+(x,t)$ and $\psi_-(x,t)$ constitute fractions $|A_+|^2$ and $|A_-|^2$ of the *total* wavefunction $\psi_s(x,t)$, we thus find that given a gate-well, dipole oscillating BEC described by $|\alpha\rangle$ with magnitude $|\alpha|^2$ that couples gate-well eigenstates $|2\rangle$ and $|3\rangle$, if a source-well matterwave with frequency ω_s is within either frequency bands Λ_2 or Λ_3, then the symmetric component $\psi_{s+}(x,t)$ is transmitted through the gate-well $100 \times |A_+|^2$ percent of the time with probability τ_2 or τ_3, respectively. The remaining fraction is reflected with certainty.

The physics in the transistor oscillator model draws very similar comparisons to the cold atom micromaser [181][182], where a slow, excited-state atom approaching a microwave cavity will be randomly reflected from or transmitted through with 50% probability. This behavior occurs due to a coherent interaction between a quantized field of microwave photons and two-level atoms, which creates a potential barrier that reflects one component of the atom wavefunction with certainty and transmits the other component with probability close to unity. In the micromaser case, since each of the components constitutes half of the wavefunction, about half of the atoms are transmitted through the maser cavity with the other half reflected. The atomtronic transistor oscillator is

analogous, except that it additionally demands resonant tunneling for transmission.

Finally, as an example to characterize the gain mechanism, the general impedance method is used to numerically calculate the gate-well transmission spectrum when a dipole oscillating BEC (described as a coherent state $|\alpha\rangle$) with $N_0 = 20,000$ atoms occupies the ground state $|0\rangle$ and $N_1 = |\alpha|^2 = 5$ atoms occupies the first excited state $|1\rangle$ of the gate-well. The transmission spectrum for *this specific* case is shown in figure 7.11a and is compared to the transmission spectrum for the exact same gate well, but *without* a BEC present. With the dipole oscillating BEC coupling upper states $|2\rangle$ and $|3\rangle$, the atom-BEC interaction potential described by H_{int} (equation 7.30) broadens the resonant transmission peaks by $\Lambda_2 = \Lambda_3 = 150$ Hz (equations 7.40a,b). To approximate the gain of the transistor oscillator in *this* example, the ratio of matterwave transmission curves when the BEC is present to when the BEC is absent is plotted in figure 7.11b. The gain plot shows that with the dipole oscillating BEC coupling upper states $|2\rangle$ and $|3\rangle$, matterwaves have their transmission probabilities increased by the interaction potential from as low as $\tau_0 \approx 10^{-12}$ (in the empty-gate well case) to $\tau \approx 10^{-3}$ (when the gate-well dipole oscillating BEC is present), which subsequently increases matterwave current flowing from source to drain, giving a gain $\mathcal{G} > 1$ (equation 7.1).

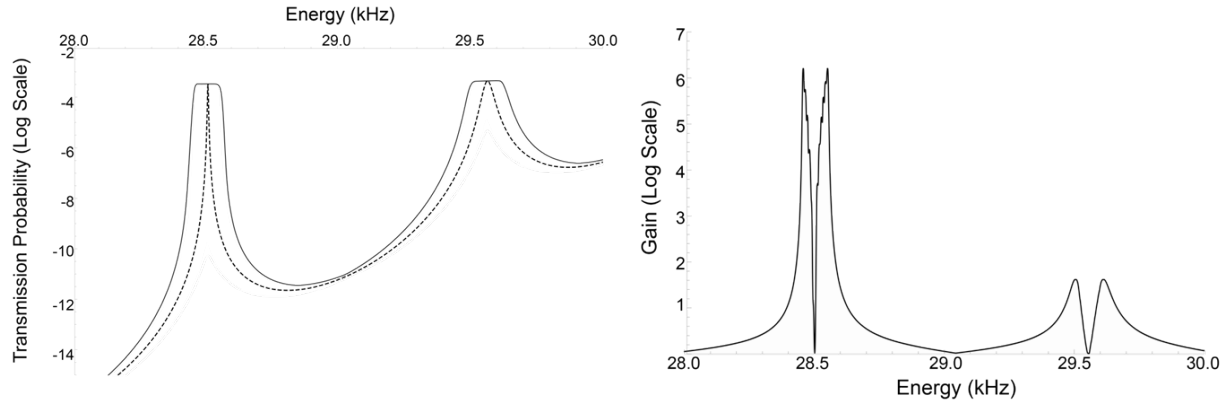

Figure 7.11: a) Plot showing the gate-well resonant tunneling transmission probability for the case, described above, without the dipole oscillating BEC and interaction potential (dashed line) and when a dipole oscillating BEC occupies the gate-well with $H_{int} \neq 0$ (solid line). b) Ratio of matterwave resonant tunneling transmission curves when the BEC is present to when the BEC is absent. This quantifies that gain for this given example.

Chapter 8

Experimental Observations to Verify Transistor Gain Mechanism

This chapter presents the current experimental progress to observe the gain mechanism of the matterwave transistor oscillator. In section 8.1, we describe the experimental criteria that must be satisfied in order to observe effects of the interaction Hamiltonian (equation 7.30) and subsequent matterwave gain of the transistor oscillator. In section 8.2, we give an overview of the experimental apparatus as well as the procedure for preparing a source-well atom ensemble at a temperature low enough for the predicted transistor behavior to occur. Section 8.3 provides a detailed description of experimentally forming the proper transistor oscillator triple-well potential that was introduced in section 7.4.1. Section 8.4 details the matterwave transistor oscillator experiments aimed at observing the dynamics of an ultracold atom current flowing through the transistor. *In-situ* absorption images showing the flow of an ultracold atom current through the transistor are presented. Section 8.5 provides a discussion of the results that verifies some of the principles predicted by the model, namely the existence of a coherent matterwave gain mechanism.

8.1 Criteria for Observing Matterwave Transistor Gain Mechanism

Following the transistor oscillator model derived in chapter 7, there exist several criteria that must be satisfied in order to experimentally demonstrate the matterwave gain mechanism. First, for a gate-well BEC to couple the highest lying gate-well energy eigenstates, we must prepare the source-well atom ensemble at a temperature comparable (and ideally equal) to the gate-well energy level spacing (corresponding to $E_3 - E_2$ in the reduced gate-well in figure 7.7). In the

theory presented in chapter 7, the model triple well potential has sequential energy levels spaced by approximately 1 kHz, which corresponds to a temperature of $T_s \approx 50$ nK. Thus, when sourcing the atom current, the source-well ensemble thermal energy *must* be as close as possible to $T_s = 50$ nK.

Second, for the gain mechanism (equation 7.30) to be present in the transistor, we need to arrange the gate-well potential to sustain a steady-state BEC as atom current flows from source, to gate, to drain. As shown in section 7.4.1, the optimal balance of particle and energy flow that leads to a high enough phase-space density to maintain a stead-state gate-well BEC occurs when the "feedback parameter" $\upsilon = 1.1$, where recall υ is defined as

$$\upsilon = \frac{(V_{GD} - V_{SG})}{T_s} \tag{8.1}$$

where T_s is the temperature of the source-well ensemble. As described above, we restrict the value of $kT_s = 1$ kHz. It follows from equation 8.1 that the difference in SG and GD barrier heights must be 1.1 in order to maintain an optimal steady-state BEC in the gate-well. Consequently, we constrain[1] the SG and GD barrier heights at V_{SG} =30 kHz and V_{GD} =31 kHz.

Third, we need the atoms to be prepared in the source-well at an energy near the the highest lying pair of gate-well eigenstates (to within eigenvalue of the interaction Hamiltonian given by equation 7.31). Otherwise, the atoms will first, never tunnel[2] into the gate-well to begin with meaning atom currents never leave the souce-well, and second, none of the atoms will ever couple to either of the highest gate-well eigenstates, making the gate-well many-bodied Hamiltonian (equation 7.29) not applicable. As described above, for this experiment the source-well ensemble thermal energy is *constrained* at $T_s = 50$ nK, meaning source-well atoms are considerably below these energy values, and will never flow through the transistor. Physically, a loaded source-well functions as an atomtronic battery, making this particular scenario equivalent to sourcing an electrical circuit with a "poorly charged" battery. Since the stored energy in the source-well is characterized by the

[1] This moderate deviation from the *model* barrier heights (shown in figure 7.4) will not change the ΔE sequential energy level spacing of the gate-well (and hence will not change the constraint on T_s) as $\Delta E \approx 1$kHz remains true.

[2] This is because, in energy, the atoms are at the wide base of the SG barrier, where the tunneling probability is essentially non-existent.

ensemble thermal energy and its chemical potential, we must raise the source-well chemical potential μ_s from 0 (as in the model in figure 7.4) to $\mu_s \approx 27$ kHz such that the ensemble with thermal energy of 1 kHz has energy very near to the highest gate-well eigenstates.

Finally, with all of the above described criteria satisfied, we must verify the presence of a matterwave gain mechanism. The remainder of this chapter details the experiment and results aiming to verify the matterwave transistor oscillator model presented in chapter 7.

8.2 Production of a 50 nK Atom Ensemble

A finite temperature ^{87}Rb Bose-Einstein condensate of approximately 7×10^3 atoms at a temperature of 50 nK serves as the atom ensemble used to source the transistor oscillator system. The BEC is formed using an atom chip in the Atomtronics Double MOT UHV cell outlined in sections 3.2 and 3.3, as well as figure 3.5. The setup and procedure for making such a 50 nK atom ensemble is described in the following sections.

8.2.1 Laser System and Layout

A summary of all laser cooling, repump, optical pumping, and probe transitions are shown in figure 8.1 and the specific 780 nm laser setups used to produce a BEC is shown in figure 8.2. Note that all rubidium transitions described in this section refer to the D2 line. With respect to the cooling, repump, and optical pumping setups, each features a JILA made[3] master external cavity diode laser (ECDL) that is used to injection lock a slave laser.

The 780 nm cooling master ECDL is locked to the ^{85}Rb $|F = 3\rangle \rightarrow |F' = 2\rangle / |F' = 4\rangle$ crossover transition by picking off a small amount of light from the output of the ECDL using Doppler free saturated absorption spectroscopy. An additional 5 mW of cooling light is picked off from the main ECDL output to be used as a frequency reference which is stabilized using a phase locked loop [4]. Using a frequency offset locking setup, the light is blue-shifted 1.2 GHz such that

[3] The ECDL master lasers were designed by Scott Papp, built in the JILA electronics shop, and are detailed in his PhD thesis [183]. Additionally, each of the JILA made lasers are powered by JILA made current drivers. While a stark contrast to the commercially manufactured lasers systems used in the Cs experiments in chapter 4, they still work masterfully over 15 years later.

the laser is red-detuned by 2Γ from the ^{87}Rb $|F = 2\rangle \rightarrow |F' = 3\rangle$ cooling transition. Additionally, 40 mW of cooling light is used to seed a Toptica BoosTA tapered amplifier, which then outputs 1000 mW of 780 nm laser light. Using a polarizing beam splitter, the TA output is split into two paths, where 500 mW of 2D MOT cooling light and 70 mW of 3D MOT cooling light are coupled with 50 % efficiency into their individual polarization maintaining fibers and sent to the experimental apparatus.

For repumping light, a 780 nm repump master ECDL is locked to the ^{87}Rb $|F = 1\rangle \rightarrow |F' = 1\rangle / |F' = 2\rangle$ crossover transition by picking off a small amount of light from the output of the ECDL and using Doppler free saturated absorption spectroscopy. Approximately 1 mW of repump light is picked off from the main beam line and used to seed a repump slave laser. The output of both the master and slave lasers are each sent through a AOM driven at 87 MHz to blue-shift the beams onto resonance with the ^{87}Rb $|F = 1\rangle \rightarrow |F' = 2\rangle$ transition. Each beam is then coupled into a polarization maintaining fiber, where the master light is sent to the 2D MOT and the slave light is sent to the 3D MOT. With the described configuration, the master repump setup provides 1 mW of 3D repump light and the slave provides 12 mW of 2D repump light.

The final 780 nm laser system used for producing a BEC is the optical pumping and probe setup. The pump-probe master ECDL laser is locked to the ^{87}Rb $|F = 2\rangle \rightarrow |F' = 2\rangle / |F' = 3\rangle$ crossover transition by picking off a small amount of the main ECDL light and using Doppler free saturated absorption spectroscopy. The main beam line is then split into two paths using a polarizing beam splitter, with one beam used for optical pumping and the other for a resonant probe beam. With respect to the optical pumping light, an AOM red-shifts the beam by 121 MHz such that the pump light is blue-detuned 2Γ from the ^{87}Rb $|F = 2\rangle \rightarrow |F' = 2\rangle$ transition. Moreover, the probe light is blue-shifted by 133.5 MHz onto resonance with the $|F = 2\rangle \rightarrow |F' = 3\rangle$ cooling transition. After passing through their respective AOMs, a total of 3 mW of optical pumping light and 3 mW of resonant probe light are each coupled into their own polarization maintaining fiber, where the light is then sent to the experimental apparatus. Using the above described laser system, we can now create a BEC using the atom chip located at the top of the atomtronics UHV cell.

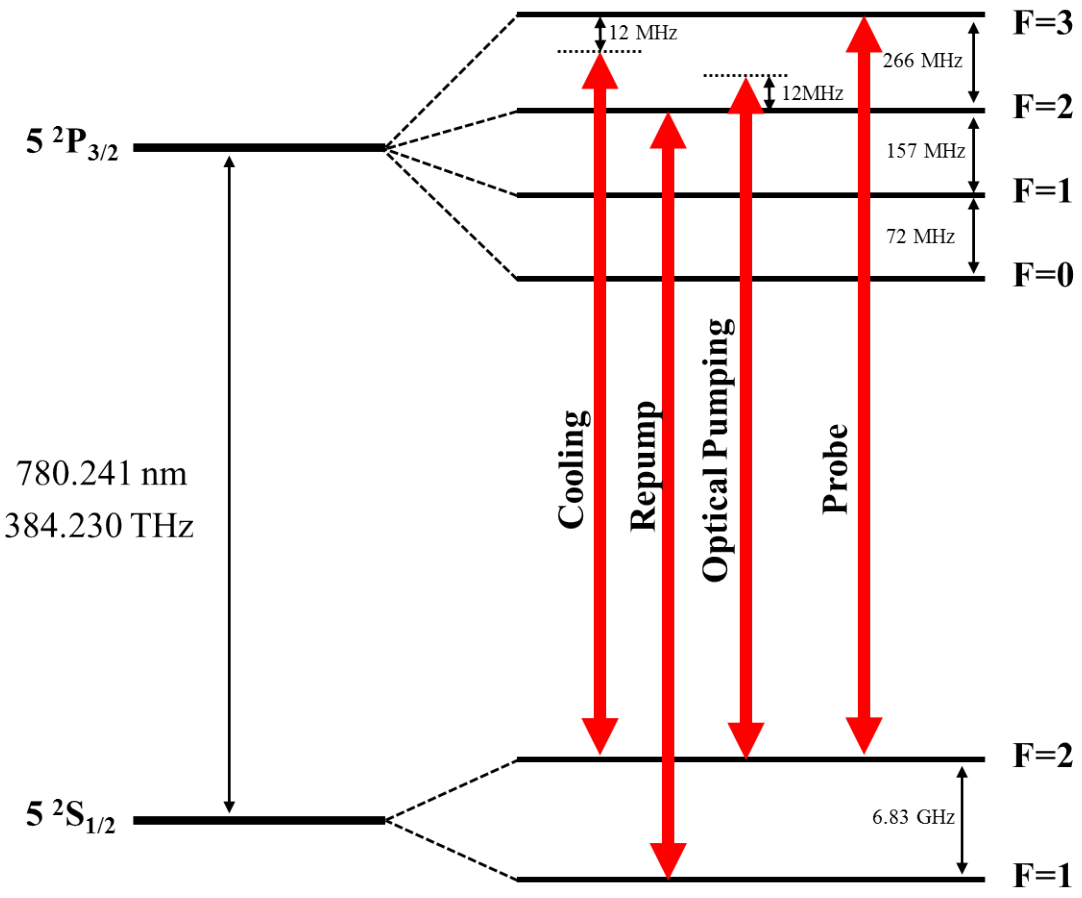

Figure 8.1: Transitions for the 780 nm cooling, repump, optical pumping, and probe lasers.

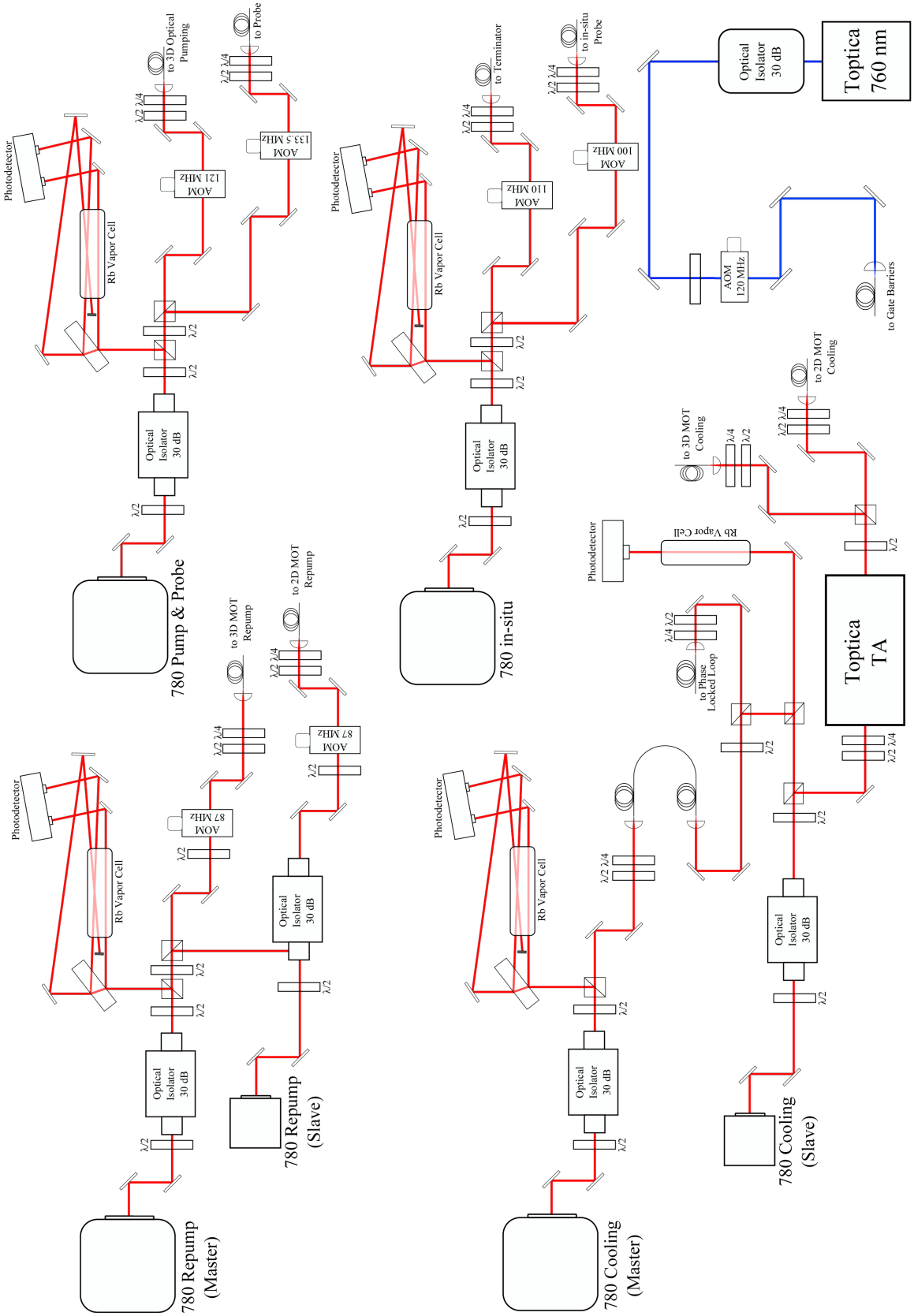

Figure 8.2: Complete laser setup for the atomtronics transistor oscillator experiment.

8.2.2 Loading Cold Atoms into the Atom Chip Trap

The production of a BEC in the Atomtronics Double MOT UHV cell follows similarly to the method developed by Evan Salim in [4] and begins by generating a 3D MOT of ^{87}Rb inside the 3D chamber of the UHV cell (figure 3.5). The 3D MOT is created by retroreflecting three pairs of 10 mW, 780 nm cooling laser beams with orthogonal σ_+/σ_- circular polarization and a beam waist of $w_0 = 5$ mm. The MOT beams are spatially overlapped with 3D repump light and all three pairs of lasers intersect at an angle of 90° with respect to each other approximately 15 mm below the bottom surface of the atom chip (figure 8.3a,b). This configuration provides 3D cooling along the orthogonal $\hat{x}$, $\hat{y}$, and $\hat{z}$ directions. Anti-Helmholtz coils oriented around the 3D chamber (figure 8.3b) provide a position dependent 8 G/cm magnetic field gradient necessary for creating the 3D MOT. Similar to the Cs MOT described in section 4.3.1, atoms are sourced into the 3D MOT from a 2D+ MOT formed in the adjacent 2D MOT vacuum chamber located below the 3D chamber (figure 3.5). During BEC production, a typical 3D MOT contains approximately 10^9 atoms and is loaded within 40 seconds.

After loading the 3D MOT, the 2D MOT lasers are shuttered and the 3D MOT is compressed into a CMOT by ramping the anti-Helmholtz field gradient up an additional 10 G/cm while simultaneously detuning the cooling lasers by an additional 40 MHz and attenuating the 3D repump to 50 μW of optical power. Typically, the CMOT stage lasts 15 ms and the MOT atom temperature after compression is approximately $T \approx 130$ to 160 μK. After CMOT, sub-Doppler cooling is performed. The MOT anti-Helmoltz coils are switched off while x-bias, y-bias, and z-bias coils are turned on in order to eliminate any stray magnetic fields at the location of the atoms such that a PGC stage can properly be performed. After eliminating stray magnetic fields at the atoms, we red-detune the 3D cooling lasers an additional 105 MHz for 3 ms, which cools the atoms to temperatures of approximately $T \approx 20$ μK. After PGC, all cooling light is extinguished while optical pumping light illuminates the atoms for 800 μs to pump as many atoms as possible to the $|F = 2, m_F = 2\rangle$ Zeeman magnetic sublevel. As shown in equations 2.18 and 2.19, since $m_F > 0$,

this permits the optically pumped atoms to be trapped in a minimum of a spatially varying magnetic field. At the conclusion of the optical pumping stage, all lasers are extinguished and no more laser cooling stages are applied.

8.2.3 Transferring pre-Cooled Atoms to the Atom Chip

Given that the atoms are prepared in the $|F = 2, m_F = 2\rangle$ Zeeman sublevel, if we linearly ramp current through the 3D MOT coils in the *Helmholtz* configuration over a span of 35 ms, the optically pumped atoms are then captured in a magnetic quadrupole field with a 60 G/cm field gradient. To vertically transport the atoms from the location of the 3D MOT up to the atom chip, current is linearly run through a pair of magnetic transport coils, also in the Helmholtz configuration (figure 8.3c), to produce a transport field gradient of 110 G/cm while the quadrupole field is linearly ramped to zero over the same time period. This operation vertically shifts the zero point of the quadrupole field that the atoms are trapped in. As long as the movement is done adiabatically, the atoms remain trapped in the magnetic quadrupole field as it is transported vertically. Upon reaching the height of the atom chip, the transported atoms are transferred into a single-guide wire Ioffe-Pritchard trap produced on the atom chip (described in section 3.3.1).

To transfer atoms into this chip trap, the transport field is first compressed over a time span of 65 ms such that the magnetic quadrupole field gradient matches the (anticipated) chip trap gradients. After such compression, the chip guide-wire and H-wire currents, as well as the y-bias current are linearly ramped on over a span of 10 ms and a magnetic potential, as shown in section 3.3.1, is formed. Approximately 20×10^6 atoms at a temperature of 17 to 20 μK remain in the Ioffe-Pritchard trap after this transfer sequence and are located approximately 150 μm below the bottom surface of the atom chip.

8.2.4 Reaching Bose-Einstein Condensation with Forced RF Evaporation

To condense the atoms into a BEC, a forced RF evaporation (section 2.5.1) stage is applied to the trapped atom ensemble to further cool the atoms below the BEC critical temperature (equation

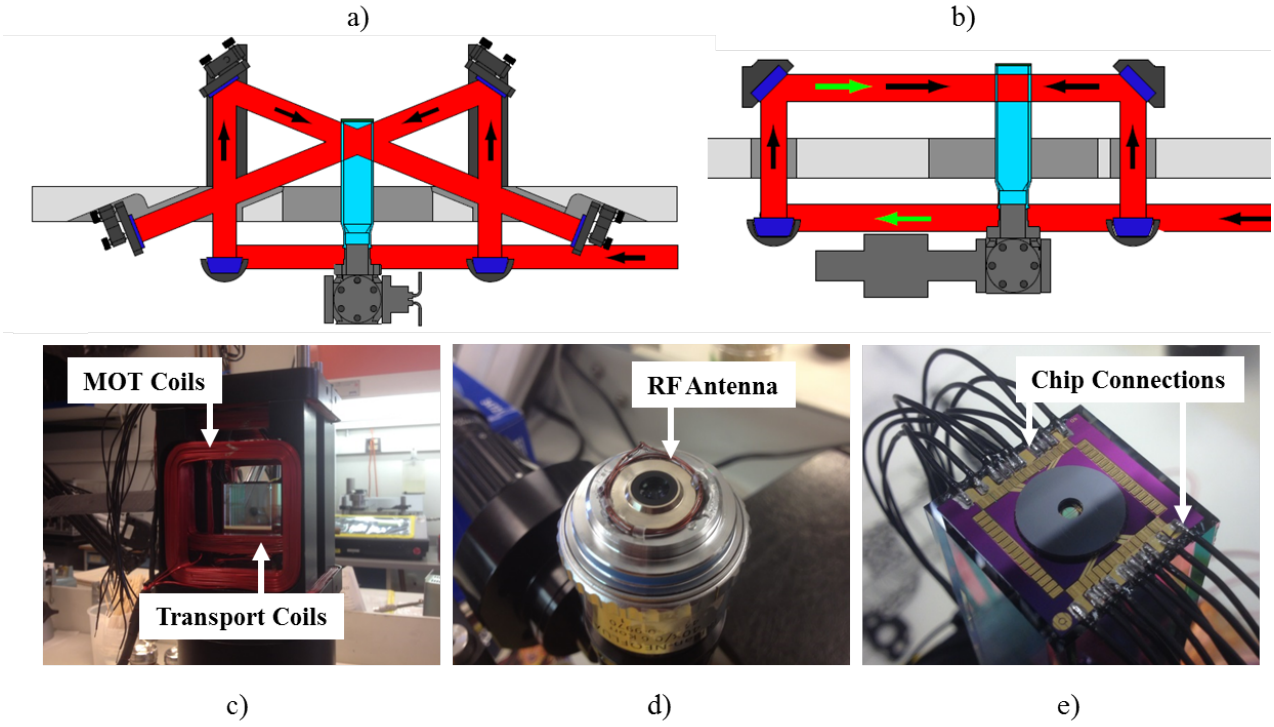

Figure 8.3: Diagram a) and b) show the orientation of the 3D MOT lasers with respect to the atomtronics vacuum cell. In a) the pair of vertically oriented MOT beams intersecting in an X shape 15 mm below the bottom surface of the atom chip. In b) the third set of MOT beams oriented normal to the X shape beams. Note that the top and bottom diagrams are rotated 90 degrees with respect to each other. This diagram is taken from the thesis of Evan Salim in reference [4], as it was his design that is still being used today. Image c) shows the orientation of the MOT coils and magnetic transport coils with respect to the 3D MOT chamber. Not visible in this image are the y-bias and z-bias coils. d) Image of the RF antenna that is located approximately 3 mm above the top layer of the atom chip. e) Imaging showing Cooner wire bonded to individual conductive pads of the atom chip using a conductive epoxy.

2.29) necessary for condensation to occur. In order to perform efficient RF evaporation, the chip magnetic trap is compressed along the radial and longitudinal directions in 500 ms in order to increase the atom collision and re-thermalization rate during the evaporative cooling stage. Using an RF antenna located 3 mm above the top surface of the atom chip (figure 8.3c), RF radiation with a frequency of $\nu_{\mathrm{RF}} = 40$ MHz is illuminated onto the atoms. The RF frequency is then linearly swept from $\nu_{\mathrm{RF}} = 40$ MHz to 26 MHz in 150 ms, which expels the absolute warmest atoms from the chip trap. Afterwards, the RF frequency is swept over a span of 1800 ms from

$$\nu_{\mathrm{RF}} = 26 \text{ MHz} \rightarrow 11 \text{ MHz} \rightarrow 6.5 \text{ MHz} \rightarrow 4.8 \text{ MHz} \rightarrow 2.62 \text{ MHz} \tag{8.2}$$

where the final RF value is approximately 100-200 kHz above the trap bottom, leaving on the coldest of the cold atoms remaining in the magnetic trap.

After the above described RF evaporation sequence, a Bose-Einstein condensate of about 7×10^3 atoms is produced in the chip guide-wire trap. As explained in section 3.3.1, this BEC is produced *under* the chip guide wire and thus blocks optical access to the condensate. To move the BEC out from under the wire and align it with the center of the atom chip window (as shown in figure 3.6b), we slowly ramp a current of equal magnitude but opposite direction through the second chip guide-wire (as detailed in section 3.3.2) in 80 ms. This adiabatically deforms the single guide-wire magnetic trap into the split guide-wire magnetic trap located 150 μm below the center of the atom chip window. At this final location, a Bose-Einstein condensate of 7×10^3 is confined to a cigar shaped magnetic potential with trapping frequencies along the $\hat{x}$, $\hat{y}$, and $\hat{z}$ directions of

$$\omega(x, y, z) = 2\pi \times (67, 1500, 1500) \text{ Hz}. \tag{8.3}$$

Absorption images showing the momentum distribution of the atoms (figure 8.4) taken at final RF evaporation frequencies of 2.68 MHz, 2.66 MHz, and 2.62 MHz show the appearance of an inverted parabola profile, which (as derived in equation 2.39) is characteristic of atoms that have undergone a phase transition to a Bose-Einstein condensate. The atom density profile of the condensate shown in 8.4 was fitted to a binomial distribution, which is the sum of a Gaussian distribution

(representing the thermal atoms in the ensemble) and an inverted parabola (for the condensed atoms in the ensemble). The final temperature of the condensate was measured by performing time-of-flight imaging on the expansion of the Gaussian tails of the BEC density profile. Using a final RF evaporation frequency of 2.62 MHz, the BEC temperature was measured at approximately $T = 50$ nK.

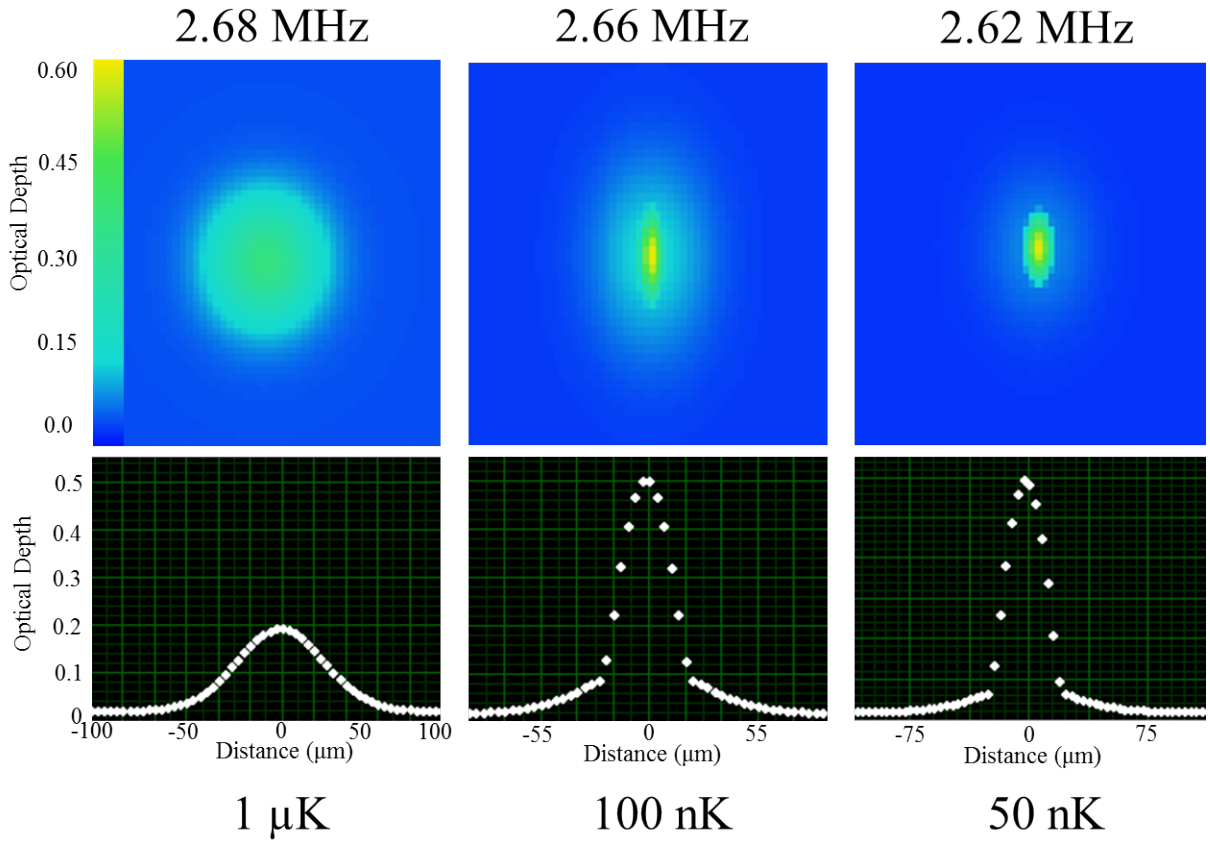

Figure 8.4: Time-of-flight absorption images showing the momentum distribution of the atomic cloud after a 22 ms TOF. From left to right the images show the atom cloud momentum just before the condensate, at the appearance of the condensate, and at nearly a pure condensate.The transition to a BEC occurs during the forced RF evaporation stage for RF frequencies of approximately 2.66 MHz. At this stage, the condensate temperature was measured to be $T = 50$ nK. The appearance of an inverted parabola profile shown in the central and right image is characteristic of the onset of a BEC as derived in equation 2.46 and shown in figure 2.8.

8.3 Forming the Transistor Oscillator Model Triple-Well Potential

The triple-well transistor oscillator potential (figure 7.3) is formed by overlapping a harmonic magnetic potential with two repulsive Gaussian barriers. Here, we detail the creation of both elements. First, the harmonic magnetic potential is the same cigar shaped Ioffe-Pritchard trap with radial and longitudinal trapping frequencies of $\omega_{\rm rad} = 2\pi \times 67$ Hz and $\omega_{\rm rad} = 2\pi \times 1600$ Hz, respectively that confines the 50 nK BEC formed in section 8.2.3. The magnetic potential is located approximately 150 μm below the bottom surface of the atom chip window. Next, the repulsive source-gate (SG) and gate-drain (GD) barriers are formed by focusing two blue-detuned, 760 nm Gaussian laser beams with equal beam waists of $w_0 = 2.0$ μm and a separation of $d = 4.8$ μm onto the center of this harmonic magnetic potential.

8.3.1 Projecting SG and GD Barriers onto the Magnetic Potential

The 760 nm laser setup for producing the SG and GD barriers is shown in figure 8.2 and the schematic for projecting them onto the magnetic potential is shown in figures 8.5a and 8.5b. A total of 35 mW of 760 nm laser light enters the barrier projection system from a polarization maintaining, single mode fiber and is collimated to a beam waist of $w = 4$ mm with an f=15mm aspherical lens. The 760 nm light then propagates into an IntraAction Corp DTD-6010RH29 2D acousto-optic deflector[4] (AOD), which can dynamically control the shape and positions of the SG and GD barriers. To generate the longitudinal (or $\hat{x}$) position of the barriers, two RF tones, one for each barrier, drive the AOD and diffracts each beam into its +1 order along the $\hat{x}$ direction. The RF tone for the GD barrier is generated by a VCO while the tone for the SG barrier is produced by a Lecroy ArbStudio Arbitrary Waveform Generator (AWG). Because the RF driving voltages are easily adjustable, this scheme provides a mechanism to dynamically change the longitudinal positions of the SG and GD barriers during the experiment (which, as shown in section 8.4, is an absolute necessity for the experiment). The radial (or $\hat{y}$) position of the both SG and GD barriers

[4] The 0 order beams are blocked leaving only the +1, +1 diffracted order beams for the experiment.

is generated by using a second channel of the AWG to continuously raster the SG and GD barriers back-and-forth in the $\hat{y}$ direction at a frequency of 20 kHz.

Using an Infinity Probe TS-160 objective in conjunction with a Zeiss LD Plan Neofluar 0.6 NA, 40x magnification microscope objective, the optical barrier potential is projected onto the harmonic magnetic potential (figure 8.5b). Note that the barriers are focused *through* the 2mm wide, 0.420 μm thick atom chip window (as shown in figure 3.6b). The Zeiss objective features an adjustable correction collar to eliminate aberration introduced when the light focuses through the 0.42 μm thick window. Additionally, because the 20 kHz raster frequency of the barriers in the radial direction is considerably faster than the 1.6 kHz radial trapping frequencies of the magnetic potential, atoms confined in the magnetic potential encounter the constant *time-averaged* optical intensity of the laser beams in the $\hat{y}$ direction. Thus, the above description produces two barriers with optical intensity profiles that are Gaussian beams (with width $w = 2$ μm) in the longitudinal direction and a "top hat" potential (with length 8 μm) in the radial direction (figure 8.5c). By overlapping an atom ensemble in the magnetic potential, the SG and GD barriers can section off the potential into the source-well, the gate-well, and the drain-well (figure 8.5d).

This barrier projection system also doubles as an imaging system to observe the flow of ultracold atoms through the triple-well transistor potential. To observe atoms in the transistor potential, *in-situ* absorption imaging is performed (as opposed to time-of-flight imaging) while the atoms are still confined to the triple well potential. A probe beam resonant with the ^{87}Rb D2 $|F = 2\rangle \rightarrow |F' = 3\rangle$ transition is propagated vertically through the vacuum cell (entering through the base of the 2D MOT chamber and exiting though the atom chip window, see figure 8.5b) where it intersects ultracold atoms trapped in the hybrid magnetic and optical transistor potential. Positioned 3 mm above the outside surface of the atom chip, the same Zeiss 0.6 NA microscope objective that focuses the barriers is used to collect and collimate the absorption image signal. An Infinity PhotoOptical KC Lens then focuses the probe light onto an Andor iXon EMCCD for imaging (figure 8.6). An absorption image of approximately 20,000 ultracold atoms trapped in the triple-well transistor potential is shown in figure 8.5d.

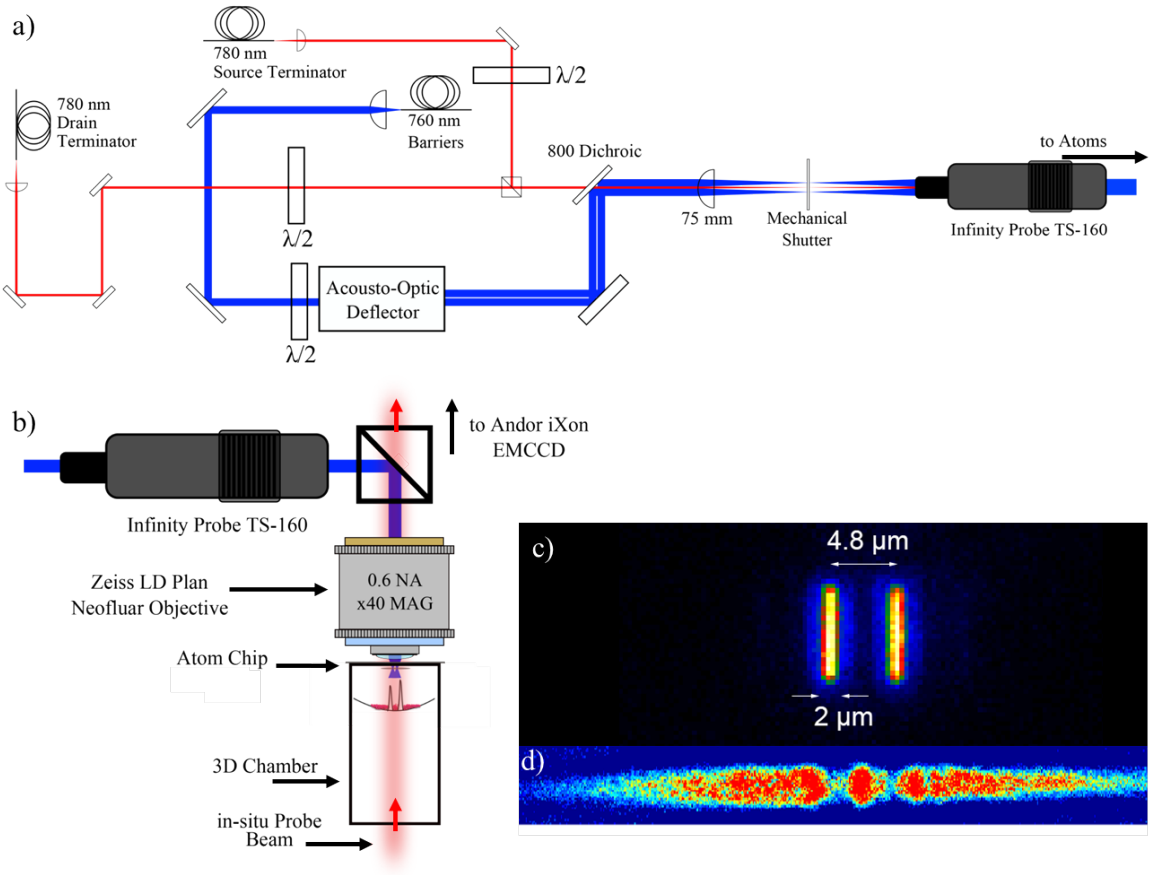

Figure 8.5: a) Optical setup for producing dynamically controllable SG and GD barriers. b) Setup to project the SG and GD barriers through atom chip window and onto the harmonic magnetic potential. The same lens that focuses the barriers also serves to for *in-situ* absorption imaging of atoms. c) Optical intensity image of the focused SG and GD barriers with beam waists of $w_0 = 2$ μm and a separation of $d = 4.8$ μm. d) An *in-situ* absorption image taken through the atom chip window showing ultracold atoms trapped in the triple-well transistor potential.

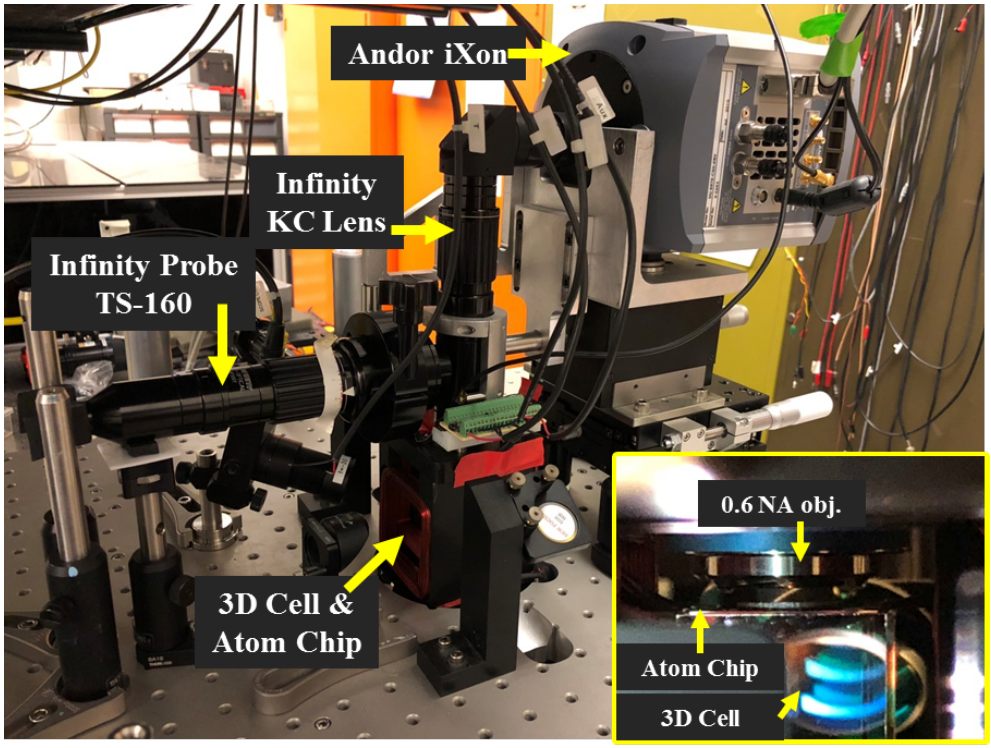

Figure 8.6: Image showing the experimental setup of the SG and GD barrier projection system as well as the *in-situ* imaging system relative to the 3D MOT cell and the atom chip. The inset shows the 0.6 NA Zeiss objective located approximately 3 mm above the top surface of the atom chip.

8.4 Matterwave Transistor Oscillator Experiments: Flow of an Ultracold Atom Current Through Transistor Oscillator Potential

Experiments to observe transistor behavior begin with following the procedure of section 8.2 and loading a Bose-Einstein condensate of approximately 7×10^3 atoms with a temperature of $T = 50$ nK (figure 8.4) into a harmonic magnetic potential located 150 μm below the center of the atom chip window (figure 8.7a).

8.4.1 Loading Ultracold Atoms into the Source-Well

Ultracold atoms are then loaded into the transistor source-well by turning on the SG barrier and adiabatically sweeping it from the right-most longitudinal boundary of the harmonic magnetic potential to near the center of the magnetic potential in 40 ms (figure 8.7b). As the SG barrier is swept across the magnetic potential, the barrier height is set at $V_{SG} = 100$ kHz, which is considerably higher than the corresponding temperature of the trapped atoms ($T = 50$ nK $\approx$1 kHz) and as a result, nearly all of the atoms are compressed into the transistor source well by the repulsive SG barrier (figure 8.7b). Any atoms that happen to remain in the adjacent drain well are quickly removed by optically pumping them to the $|m_F = -2\rangle$ anti-trapping state by illuminating a laser beam, called the drain terminator, that is locked to the ^{87}Rb $|F = 2\rangle \rightarrow |F' = 2\rangle$ transition. The drain terminator, which is a 10^{-13} W, 780 nm beam focused to a waist of 16 μm, is projected onto the center of the transistor drain-well using the same optical projection system for the SG and GD barriers (section 8.3) and can remove all drain-well atoms within 5 ms without disturbing any atoms confined to the source or gate well. After clearing any residual atoms not swept into the source-well, the SG barrier height is ramped down to its desired height of $V_{SG} = 30$ kHz while simultaneously, the GD barrier is ramped on to a height of $V_{GD} = 31$ kHz and is displaced from the SG barrier by a distance $d = 4.8$ μm. After this sequence, the matterwave transistor is prepared in a state shown in figure 8.7c.

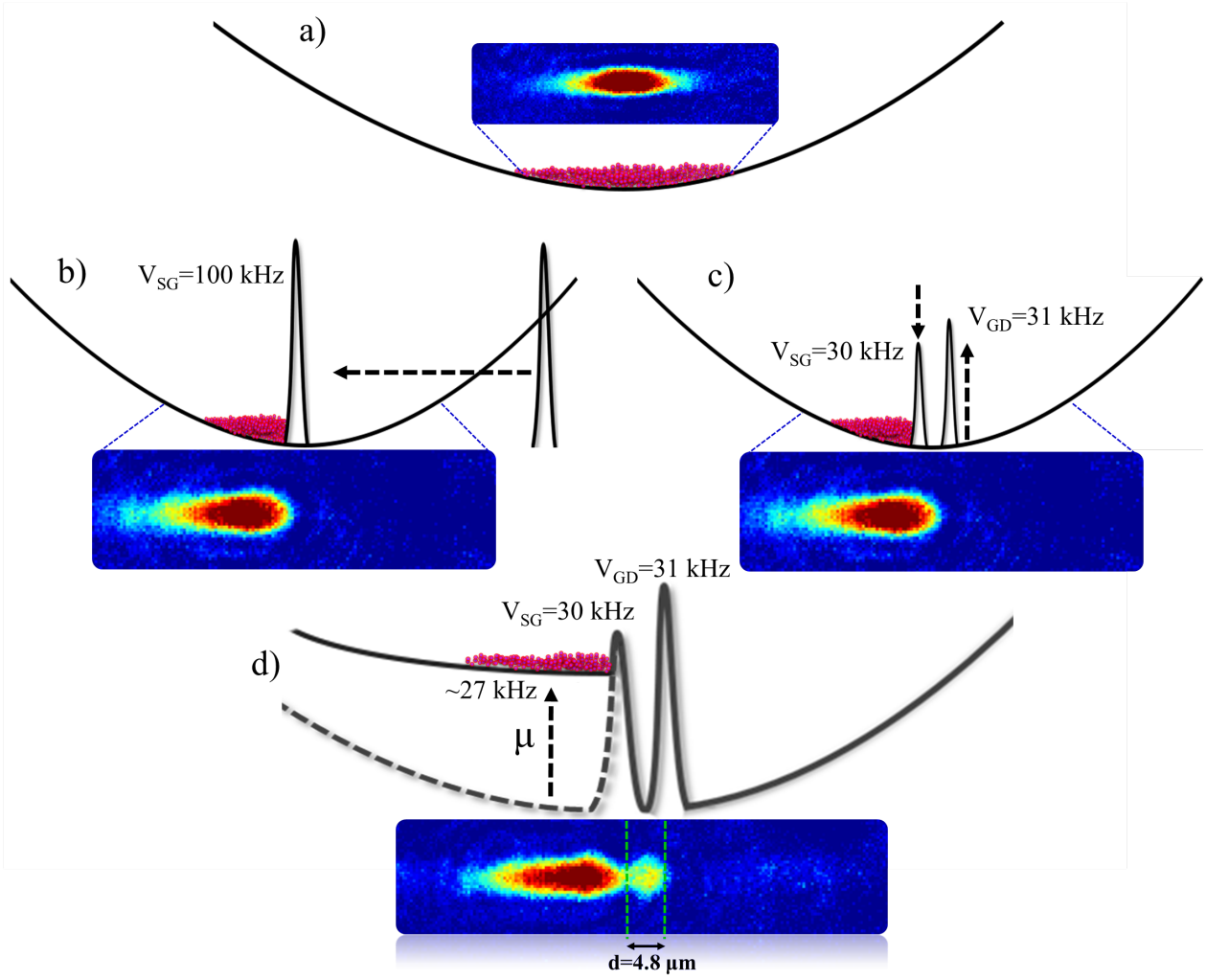

Figure 8.7: The following are *in-situ* absorption images of ultracold atoms at various stages of preparing the source-well ensemble. a) A Bose-Einstein condensate with approximately 6,000 atoms at a temperature of 50 nK loaded into the harmonic magnetic potential. b) By sweeping the SG barrier from the longitudinal edge of the magnetic potential, nearly all atoms are confined into the transistor source-well. c) The SG barrier is lowered to its desired height of 30 kHz and the GD barrier is raised to 31 kHz. d) Source-well atom ensemble after raising the source-well chemical potential (described in the upcoming section 8.4.2). By allowing source-well atoms to flow into the gate-well, we can directly measure the size of the gate-well to verify the SG and GD barriers are separated by $d = 4.8$ μm.

8.4.2 Powering the Source-Well Ensemble to Commence Atom Currents

With their current energy of approximately 1 kHz, the source-well atom ensemble will not flow through the transistor-oscillator potential. The energy of the atoms places the source-well ensemble at the base of the SG barrier (figure 8.7c) making subsequent flow into the gate and drain-wells highly unlikely. In this condition, the source-well in the atomtronic transistor is equivalent to an electronic battery with insufficient energy to power an electrical circuit. To raise the energy of the source-well atom ensemble to high enough energies such that an atom current flows, the source-well chemical potential is raised from 0 to approximately $\mu_S \approx 27$ kHz (figure 8.7d).

This is accomplished by rapidly sweeping the SG barrier back-and-forth at a frequency of 19 kHz, extending over a majority of the source well, while ramping up the optical power of laser beam forming the SG barrier. Specifically, an AWG is used to ramp the driving voltage of the AOD that controls the longitudinal position of the SG barrier. The sweeping sequence begins by holding the SG barrier at its initial position (as shown in figure 8.7b) for 4 μs. Then the AOD driving voltage is ramped up by 1 V over the span of 24 μs. This serves to sweep the SG barrier from its initial position to the left-most attainable longitudinal position such that the barrier sweeps over as much length of the source-well as possible. The AOD voltage is then ramped down over 22 μs, bringing the SG barrier back to its starting point, where the sweeping sequence is repeated for the remainder of the experiment. Note that the longer the barrier is held at its starting point, the higher the SG barrier will be.

The total sweeping frequency of the SG barrier is 19 kHz, which is considerably larger than both the 1.6 kHz and 125 Hz radial and longitudinal trapping frequencies of the transistor source-well potential. As a result, by continuously repeating this waveform, the atoms experience the time averaged intensity of the sweeping optical field, which is shown in figure 8.8b. As the SG barrier is swept back-and-forth, the optical power of the laser beam forming the SG barrier is linearly ramped from its initial value of 1.7 mW to 2.5 mW over a span 10 ms. This process serves to raise the bottom of the source-well potential from 0 to 27 kHz and places the source-well ensemble at a

much higher chemical potential of $\mu_s = 27$ kHz (figure 8.8). Finally, by supplying 2.5 mW and 0.8 mW of optical power to the laser beams that form the SG and GD barriers respectively, the final time averaged optical intensity of the barriers still maintains a gate-well with SG and GD barrier heights of $V_{SG} = 30$ kHz and $V_{GD} = 31$ kHz in addition to the raised source-well with chemical potential $\mu_s \approx 27$ kHz (figure 8.8c). The source-well is now prepared in a state shown in figure 8.7c where an ultracold atom current may flow into the transistor gate-well and subsequently into the drain.

Time-of-flight imaging performed on the atom ensemble in the raised source-well shows that the atom temperature has increased to approximately 78 nK and the ensemble is no longer condensed into a BEC. The heating is attributed to technical noise from position fluctuations of the

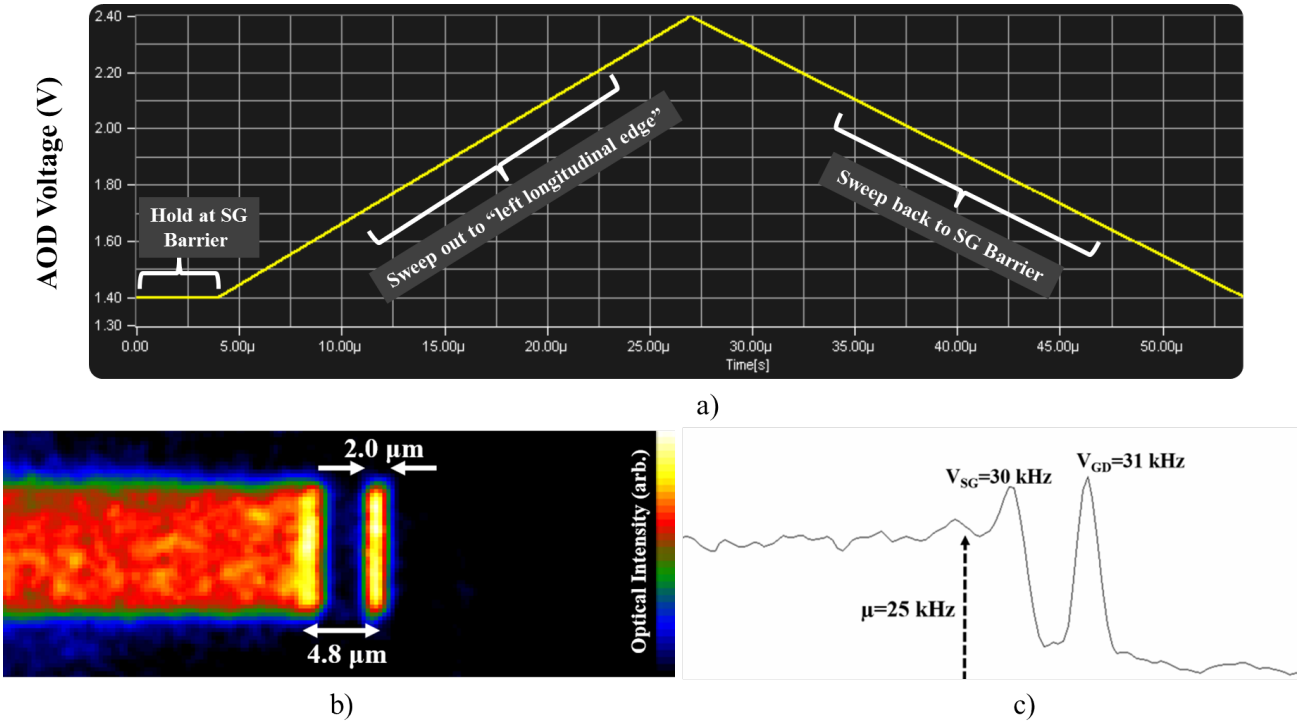

Figure 8.8: a) Voltage driving the AOD that controls the $\hat{x}$ (or longitudinal) position of the SG barrier as a function of time. By using this sweeping function for the SG barrier, the time averaged optical potential for the SG barrier is shown in b). Image b) is an intensity image of the SG and GD barriers after the above sweeping function. This serves to raise the source-well chemical potential with the corresponding transistor potential shown in c).

magnetic potential due to current noise of 35 nA/$\sqrt{\text{Hz}}$ in the current drivers that supply the atom chip currents I_x and 120 nA/$\sqrt{\text{Hz}}$ in the current drivers that form the z-bias field β_z were measured in reference [153] to account for a 1 nK/ms heating rate. We did not observe any measurable heating from sweeping the SG barrier back and forth.

8.4.3 Atom Current Flow Through the Transistor Oscillator

With an ultracold atom ensemble prepared in the raised source-well, the flow of an atom current through the transistor oscillator is observed by probing the system *in-situ*. Each run of the experiment begins with the raised source-well loaded with approximately $N = 7 \times 10^3$ atoms at a temperature of approximately $T_s = 78$ nK and a chemical potential of $\mu_s = 27$ kHz. The atom current begins to flow at time $t = 0$, which is defined as the time when the source-well chemical potential is raised to $\mu_s = 27$ kHz and the SG and GD barriers are set to their desired heights of $V_{SG} = 30$ kHz and $V_{GD} = 31$ kHz.

The transistor oscillator system is allowed to evolve[5] for some time Δt, during which an atom current flows throughout the transistor potential landscape. After an ultracold atom current flows for some time Δt, the occupancy of the source, gate, and drain wells of the transistor oscillator is observed by performing *in-situ* absorption imaging. Figure 8.9 shows a series of absorption images demonstrating the flow of an atom current from source-well, through the gate-well, and into the drain-well at various flow times. In figure 8.9, the first image shows the source-well atom ensemble at a chemical potential of $\mu_s = 27$ kHz and temperature of $T = 78$ nK immediately before the start of an atom current at $t = 0$. Within 10 ms, a very large population of atoms becomes trapped in the gate-well. However, it takes approximately another 5 ms for the current flow into the drain-well and collect at the drain classical turning point. Over the next 7.5 ms, the atom current flowing into the drain-well steadily increases, with a corresponding decrease in the gate-well occupation.

[5] As explained in great detail in reference [153], as the system evolves, the drain-well is constantly illuminated with the drain terminator beam (section 8.4.1) to remove any atoms that flow into the drain-well. The terminator ultimately prevents the transistor oscillator system from reaching an equilibrium. Note however, that the terminator beam is extinguished approximately 6 ms prior to taking an absorption image in order to take an instantaneous snapshot of the atom current accumulating in the drain-well. The 6 ms corresponds to approximately $1/4\nu_x$ where ν_x is the longitudinal trapping frequency of the harmonic magnetic potential.

At $\Delta t = 22.5$ ms, the atom flux flowing into the drain-well reaches a maximum, and subsequently starts to decay, decreasing over the next 6.5 ms until the current stops flowing into the drain-well. After a flow time of $\Delta t = 30$ ms, no atom current was observed to flow into the drain-well.

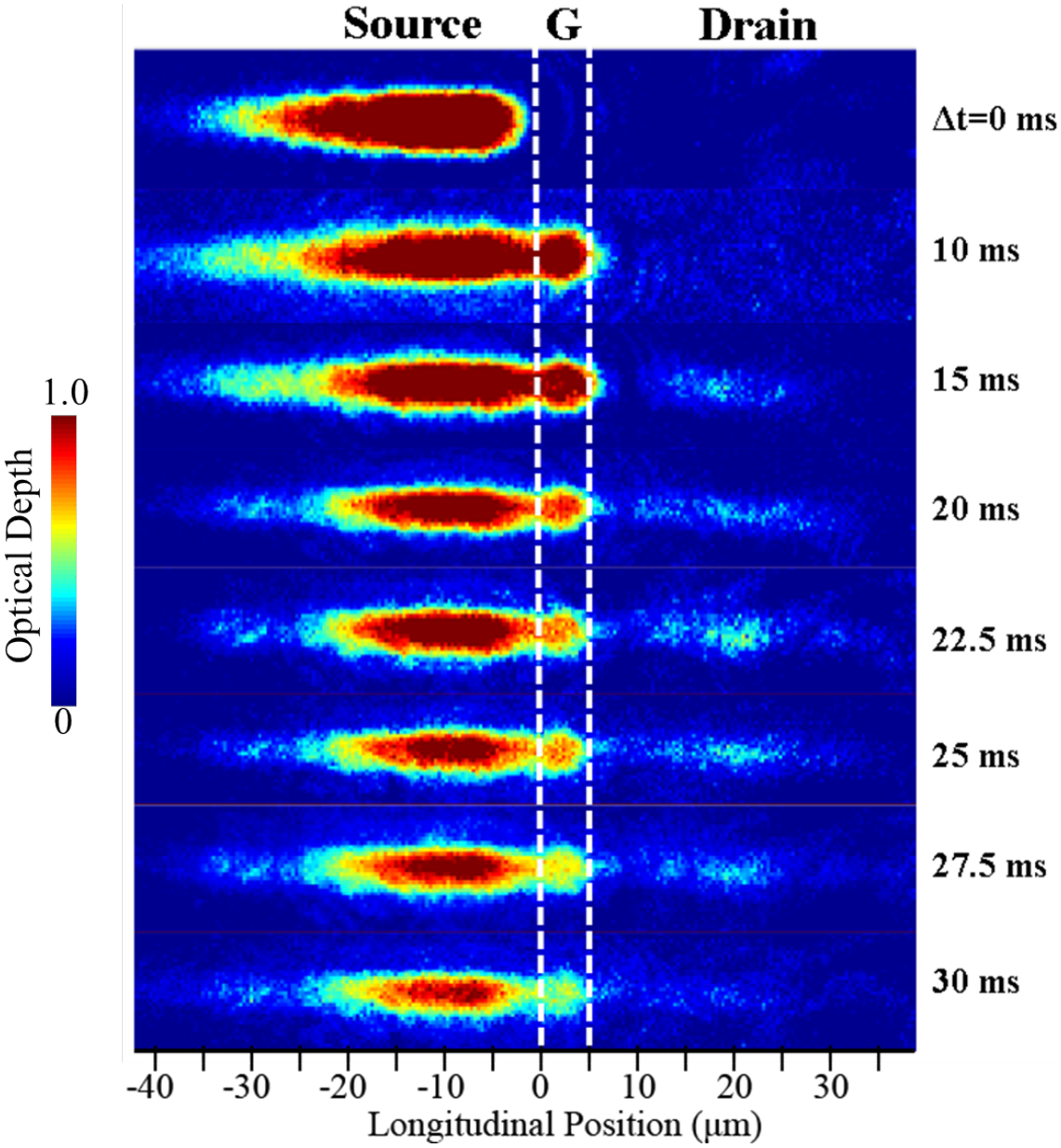

Figure 8.9: *in-situ* absorption images of the transistor oscillator at various flow times as an atom current flows from the source-well, through the gate-well and into the drain-well. The spatial locations of the SG and GD barriers are indicated with the dashed lines.

Time-of-flight measurements show that during the first 10 ms of the atom current flow time, the source-well ensemble temperature increases from 78 nK to approximately 109 nK. However, once the current begins to flow into the drain-well, the source-well ensemble continuously cools (figure 8.10). This is consistent with the semi-classical atomtronic transistor experiments [5][34] and shows that as the atom current flows into the gate and drain wells, it carries away energy from the source-well. This source-well heating and cooling behavior should be expected since the *in-situ* absorption images show that an atom current isn't flowing during the first 10 ms, so we shouldn't expect any flow of energy out of the source well. Once current begins to flow into the gate and drain wells we see a noticeable drop in source-well temperature.

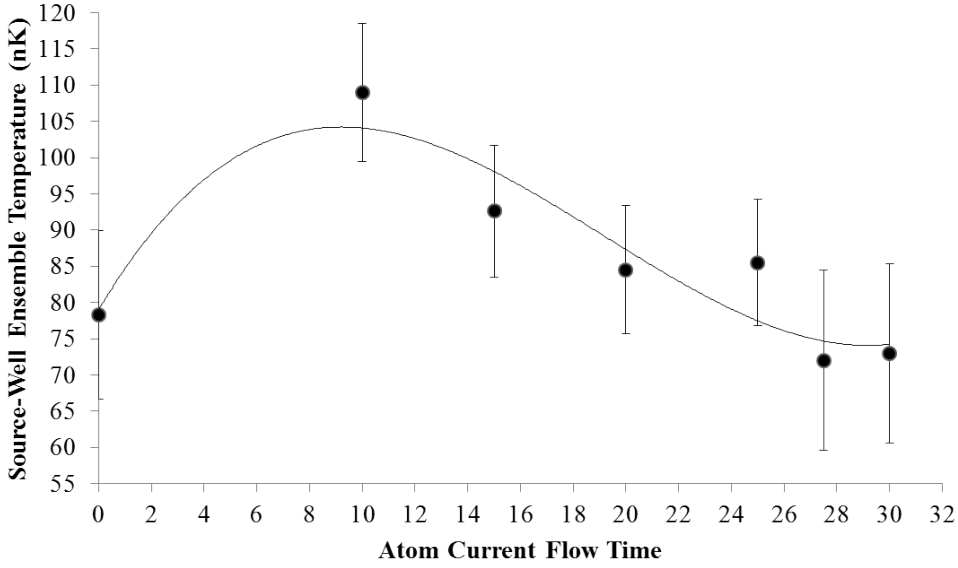

Figure 8.10: Plot showing the temperature T_s of the source-well atom ensemble as a function of atom current flow time. The source-well ensemble temperature in each data point was measured using time-of-flight imaging after each subsequent current flow time. Error bars are propagated from the standard error of the mean for T_s.

8.4.4 Using a Colder Source-Well

The ultracold atom current flowing through the transistor oscillator in figure 8.9 begins at a temperature of $T = 78$ nK, but is not condensed into a BEC. At the cost of a smaller source-well atom number, we performing a more intense RF evaporation stage when preparing the source-well ensemble, by using a higher intensity of RF radiation. With the more intense RF evaporation, the atom ensemble in the *raised* source-well is at a cooler temperature of $T \approx 54$ nK compared to section 8.4.3. More importantly, the ensemble remains condensed in a BEC. We then repeated the methods of section 8.4.3 to observe the atom current flow when the source-well ensemble is a BEC. As in the previous section, the flow of an atom current through the transistor oscillator is observed by probing the system *in-situ* and is shown in figure 8.11a. Additionally, time-of-flight (TOF) absorption images of the source-well ensemble following a 22 ms TOF show the presence of a source-well condensate at times immediately before the flow of atom currents ($t = 0$, figure 8.11b) and after an atom current flow time of 25 ms (figure 8.11c).

8.5 Discussion of Results: Verifying Transistor Gain and Coherence

Verifying the existence of a coherent gain mechanism in the atomtronic transistor oscillator can be accomplished by examining *in-situ* absorption images of ultracold atom currents flowing through the transistor triple-well potential, such as the images shown in figures 8.9 and 8.11. We now confirm the transistor model formulated in chapter 7 by explicitly showing the presence of a matterwave gain mechanism. We directly observe an increase in the spread of the energy of the drain-well atom flux as the source-well temperature is reduced (and coupling strength to the gate-well subsequently increases). This behavior is consistent with the presence of the matterwave gain mechanism that was derived in chapter 7 and further described in sections 7.6.2 and 7.6.3. Finally, we conclude this chapter by further verifying the transistor model by showing experimental evidence suggesting coherence between the matterwaves flowing into the drain-well and accordingly establishes the interaction potential (equation 7.30) as a coherent gain mechanism.

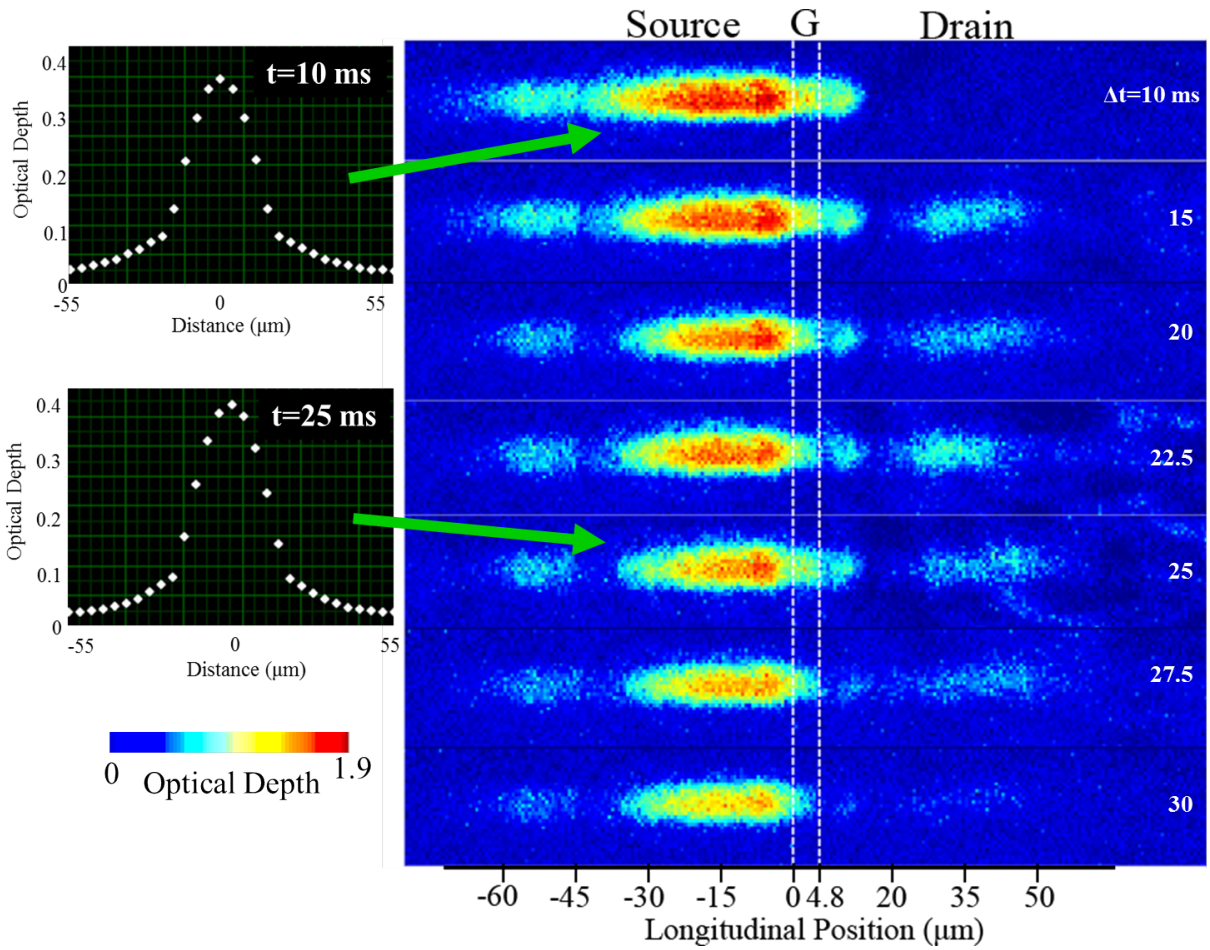

Figure 8.11: *in-situ* absorption images of the transistor oscillator at various flow times as an atom current flows from the source-well, through the gate-well and into the drain-well. The spatial locations of the SG and GD barriers are indicated with the dashed lines. Insets show the longitudinal density profiles of the source-well ensemble immediately before the flow of an atom current (at $\Delta t = 10$) and after an atom current flow time of 25 ms. Both images show that the source-well ensemble is a BEC as the system begins to evolve and remains a BEC as current flows though the gate-well and into the drain.

8.5.1 Observation of Transistor Gain Mechanism

Before discussing the atom current results that lead to conclusions showing the presence of a matterwave gain mechanism in our transistor oscillator, it is important to first establish what the *in-situ* absorption images convey about the energy of a flux of matterwaves flowing into the drain well. When examining *in-situ* absorption images of a matterwave current flowing though the transistor, it is important to note that the longitudinal position of the atom flux flowing into the drain-well is indicative of drain-well ensemble's energy. That is, the greater total energy the drain-well atoms have, the farther the longitudinal distance they will flow into the drain-well until reaching their turning point in the potential (figure 8.12). It then follows that the longitudinal *width* of the drain-well ensemble is a measurement of the distribution, or *spread*, of the energy of the drain-well flux. For example, if every single atom entering the drain-well had the same energy, then every single atom would travel to the *same* longitudinal turning point in the drain-well. However (as in our atom currents shown in sections 8.4.3 and 8.4.4), if the drain-well current contains atoms with a spread of energy ΔE, then there will be a corresponding spread of the drain-well ensemble's absorption image that is centered at the location of the longitudinal turning point corresponding to the average energy in the drain-well flux. (figure 8.12).

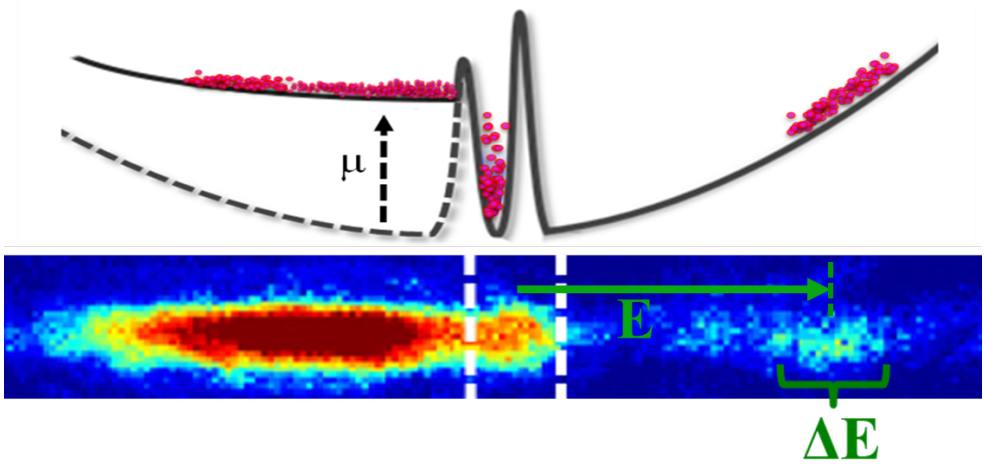

Figure 8.12: Plot conveying how one observes the spread of energy ΔE of the drain-well flux. The longitudinal position of the flux of atoms in the drain-well is indicative of their energy and the longitudinal spread of the atoms is an indication of the spread ΔE of the atom flux energy.

Depending on whether the prepared[6] source-well atom ensemble was a purely thermal ensemble with temperature $T = 78$ nK (similar to the methods described in section 8.4.3), or a condensate with temperature $T = 54$ nK (as in section 8.4.4), we observed different spreads of energy ΔE in the drain-well current (see figure 8.13). Specifically, the drain-well flux sourced with the colder, $T = 54$ nK source-well ensemble, contains a *broader* spread of energy as compared to drain-well flux sourced with the warmer $T = 78$ nK source-well ensemble. This important result, shown in figure 8.13a, indicates that the gate-well coupling strength for a matterwave current has a dependence on the source-well ensemble temperature. The correspondence between the increased spread in matterwave energy flowing into the drain-well as the gate-well coupling strength increases agrees with the quantum, many-body model of the transistor presented in chapter 7 and thus suggests the presence of a matterwave gain mechanism in the gate-well. This behavior was also observed for an atom current flowing through a modified triple-well potential with parameters $V_{SG} = 15$ kHz, $V_{GD} = 16$ kHz, and source chemical potential $\mu = 12$ with the results shown in figure 8.13b.

By comparing all of the drain-well ensembles in figure 8.13, it is clear that the drain-well atom flux sourced with the $T = 57$ nK ensemble covers a wider longitudinal range in position space than the drain-well atom flux sourced with the $T = 78$ nK ensemble. This result demonstrates that the source-well atoms that *couple into the gate-well*, with subsequent flow into the drain, for the 57 nK case contains a broader range of energy, as compared to the 78 nK case. Not only do these results agree with the gain mechanism of the model derived in chapter 7, but the results also demonstrate a canonically conjugate relationship between the total position space wavefunction $\Psi(x)$ and momentum space wavefunction $\Phi(p)$ in the transistor gate-well. As we now explain, this conjugate relationship is also consistent with the existence of a matterwave gain mechanism in the gate well and cannot be explained using the semi-classical models from [33][5][34], but rather can only be interpreted by describing the flow of the atom currents with a quantum mechanical, matterwave interference, description.

[6] Recall from section 8.4.2, the atom current is flowing though the triple-well transistor potential with SG and GD barrier heights of $V_{SG} = 30$ kHz and $V_{GD} = 31$ kHz and with a source-well chemical potential $\mu = 25$ kHz (figure 8.8).

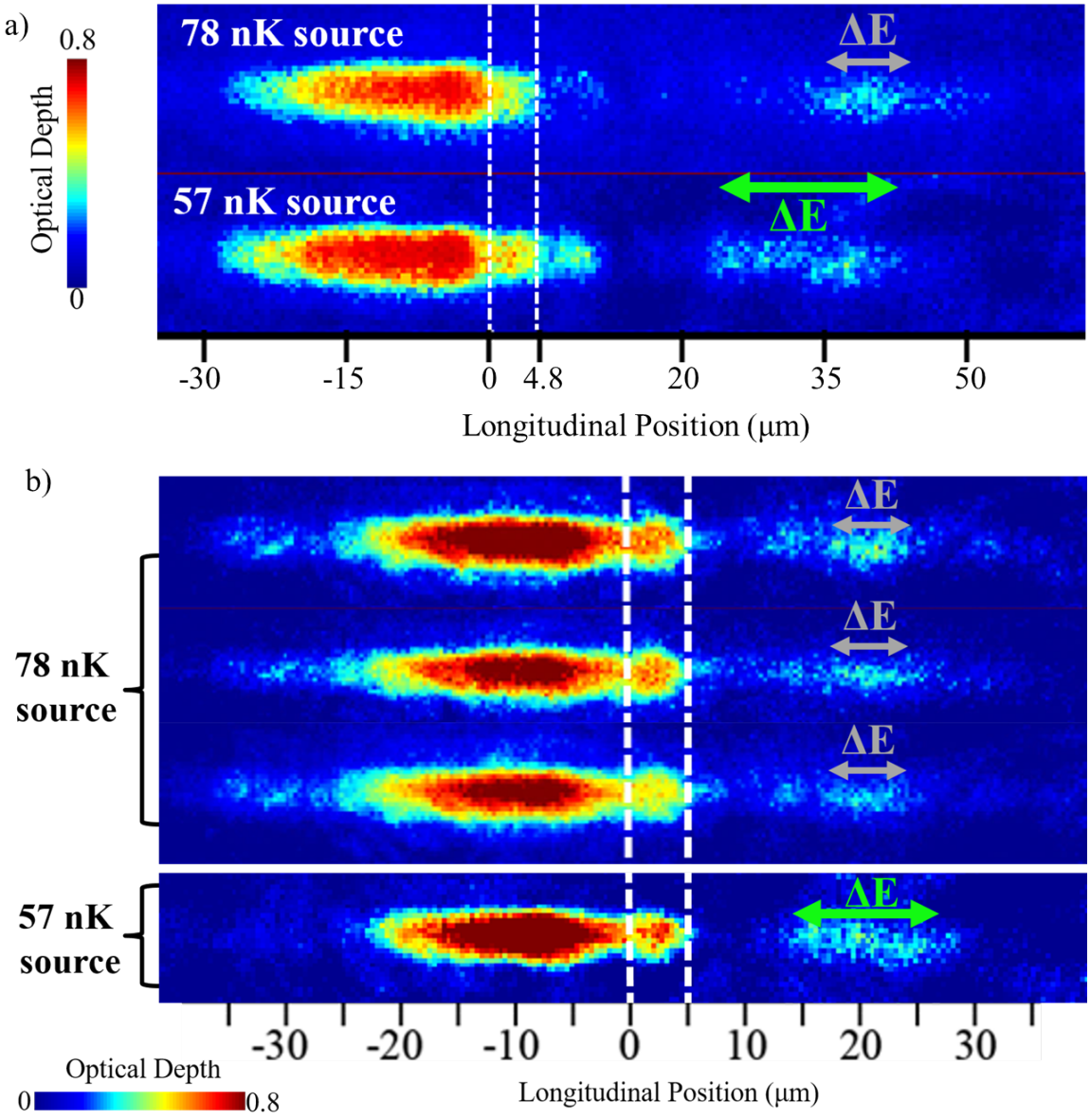

Figure 8.13: a) *in-situ* absorption images showing the flow of ultracold atoms through the transistor potential with $V_{SG} = 30$ kHz, $V_{GD} = 31$ kHz, and source well chemical potential $\mu = 25$ kHz after 25 ms of flow time. The images show a comparison of the atom current for cases of a 78 nK and 57 nK source-well ensemble. From the images, it is immediately apparent that a wider range of matterwave energy flows into the drain-well when the current is sourced with the 57 nK BEC, rather than 78 nK thermal source. This important result indicates that gate-well coupling strength for a matterwave current increases as the source-well ensemble temperature approaches the 50 nK energy spacing of the eigenstates of the gate-well (as explained in section 8.1). The correspondence between the increased spread in matterwave energy flowing into the drain-well as gate-well coupling strength increases suggests the presence of a matterwave gain mechanism. b) *in-situ* absorption images showing the flow of ultracold atoms through the transistor potential with $V_{SG} = 15$ kHz, $V_{GD} = 16$ kHz, and source well chemical potential $\mu = 12$ kHz. In the 78 nK images, the atom current has flowed for 22.5 ms, 25 ms, and 27.5 ms respectively (from top to bottom). The 57 nK image shows the atom current after 25 ms of flow time. Similar to figure a), we still observe a wider range of matterwave energy flows into the drain-well when the current is sourced with the 57 nK BEC, rather than 78 nK thermal source.

8.5.2 Additional Evidence of Gain Mechanism: Observing Canonically Conjugate Relationship Between Gate-well Position and Momentum Wavefunctions

While the model formulated in chapter 7 is derived considering a single matterwave flowing through the transistor potential, the experimental results shown in sections 8.4.3, 8.4.4, and 8.5.1 are for a source-well containing an *ensemble* of many atoms. Thus, we aim to describe the observed matterwave current dynamics by considering a superposition of many source-well matterwaves, spanning a range of energies, just as in the above experiments. As described in section 7.6.2, the gain mechanism permits *only* the symmetric (or antisymmetric) mode ψ_+ (or ψ_-) to couple into the gate-well with the mode of opposite parity, which in this case is the antisymmetric (or symmetric) mode ψ_- (or ψ_-), always reflected. By summing[7] all of the symmetric modes ψ_+ (or antisymmetric modes ψ_-) that couple into the gate-well over a broad range of initial energies, the resulting envelope of the matterwave superposition (figure 8.14a) gives a sinc function:

$$\Psi(x) = \mathrm{sinc}(x). \tag{8.4}$$

Because position and momentum space wavefunctions are conjugates of each other, we can immediately surmise the total momentum space wavefunction $\Phi(p)$ that couples into the gate-well (figure 8.14b) by performing the Fourier transform of equation 8.4. That is, the envelope of the total momentum space wavefunction $\Phi(p)$ coupling into the gate-well is a "box" function

$$\Phi(p) = \begin{cases} 0 & p \leq p_{min} \\ \mathcal{P} & p_{min} \leq p \leq p_{max} \\ 0 & p \geq p_{max} \end{cases} \tag{8.5}$$

where $\mathcal{P}$ is constant and the width of $\Phi(p)$ is equal to the range of momenta $\Delta p = p_{max} - p_{min}$ of the matterwaves that couple into the gate-well. Because $\Psi(x)$ and $\Phi(p)$ are canonically conjugate parameters, as the gate-well coupling increases, the $\Psi(x) = \mathrm{sinc}(x)$ position wavefunction becomes

[7] In this summation, we assume that all symmetric modes contribute with *equal* amplitudes. Note that a symmetric modes ψ_+ with different initial energies will have a different phase ϕ_ξ relative to each other in order to remain coupled into the gate-well. This occurs because the phase condition (equation 7.38), unique to each matterwave energy must *always* remain satisfied for each symmetric mode ψ_+ to couple to the gate-well, otherwise the wave would have been reflected. Thus the superposition in the gate-well is a summation of symmetric modes ψ_+ with different phases.

tighter while the width of the $\Phi(p)$ box momentum wavefunction becomes *wider*. Therefore, due to the gain mechanism, as more source-well atoms couple into the gate-well, the momentum spread of the resulting superposition *increases*. As the gate-well superposition subsequently flows into the drain-well, the observed atom flux will be distributed over a wider longitudinal position in the drain-well, since the matterwave flux contains a wider distribution of momentum (and hence energy).

This exact behavior was observed[8] in our experiments: as the temperature of the source-well ensemble becomes closer to the desired $T = 50$ nK (where coupling is max), we observe an increase in the spread of energy (and hence momentum) in the drain-well flux (figure 8.13). As described in section 8.5.1, this indicates that coupling to the gate-well *increases* as the source-well ensemble temperature decreases from 78 nK to 54 nK, which is consistent with the existence of the matterwave gain mechanism derived in chapter 7. Our observations in figure 8.13 would *not occur*

[8] The absorption images, such as those shown in figures 8.9 and 8.11, are also measurements of the atom current probability amplitudes at all longitudinal positions of the transistor oscillator.

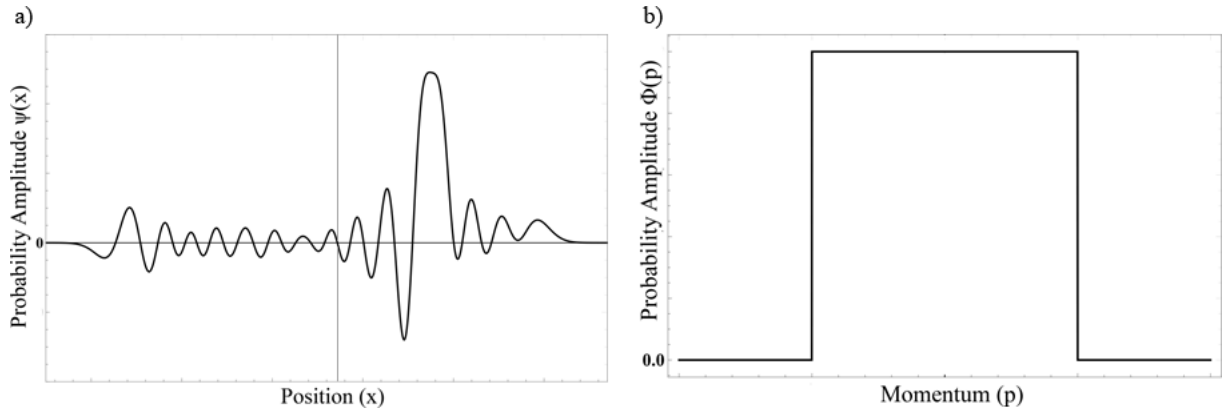

Figure 8.14: a) Envelope of the total position space wavefunction, $\Psi(x)$, of the gate-well, formed by summing symmetric modes ψ_+ over a broad range of initial energies that couple into the gate-well. b) Envelope of the corresponding momentum space wavefunction, $\Phi(p)$. Because momentum and position are canonically conjugate variables, by taking the Fourier transform of the gate-well position space wavefunction $\Psi(x)$, we immediately arrive at the gate-well momentum space wavefunction $\Phi(p)$. This result shows the effects of the gain mechanism: as more atoms couple into the gate-well, the corresponding momentum spread in $\Phi(p)$ also increases. This is directly observed in figure 8.13, as the spread in momenta (and energy) of the drain-well flux increases as source-well temperature decreases and gate-well coupling increases.

without this gain mechanism, as there cannot be matterwaves possessing a continuous *spread* of energy that couple into the gate-well without it (shown in figure 7.10). Consequently, if there were no gain-mechanism, one would not observe an increase in matterwave momentum (and energy) flowing into the drain-well as source-well temperature decreases.

With the presence of a matterwave gain mechanism experimentally verified, we conclude this chapter by describing how the ultracold atom current results shown in sections 8.4.3, 8.4.4, 8.5.1, and 8.5.2 suggest that the matterwave gain mechanism is also coherent.

8.5.3 Coherence in the Matterwave Gain Mechanism

The model presented in chapter 7 suggests that coherence exists between matterwaves coupling into the gate-well and flowing into the drain-well. This coherence occurs due to the following:

- In order for source-well matterwaves to couple into the gate-well and flow into the drain, each matterwave *must* satisfy gate-well resonant boundary conditions.
- The gain mechanism (i.e. the interaction potential given in equation 7.30) transmits *only one* gate-well normal mode: either the symmetric ψ_+ or antisymmetric ψ_- mode. The mode of opposite parity is always reflected.
- For matterwaves ψ_+ (or ψ_-) to match gate-well boundary conditions and couple to the gate-well, the precise phase condition (equation 7.38) *must always* be satisfied, otherwise the wave is reflected from the gate.
- Axiomatically, the relative phase difference between each normal mode ψ_+ (or ψ_-) that couples into the gate-well cannot change and remains constant (if it does change then the mode will not couple to the gate, is reflected, and is not part of the gate-well superposition).

Therefore, the superposition that couples into the gate-well features a sum of purely symmetric (or antisymmetric) modes ψ_+ (or ψ_-) whose phases relative to each other do not change; giving rise to coherence between each matterwave in the gate-well superposition.

Furthermore, the results of the matterwave current from sections 8.4.3 and 8.4.4 show evidence suggesting the coherence between matterwaves is preserved as the superposition flows into the drain-well. Shown in figure 8.15a, *in-situ* absorption images demonstrate that a drain-well atom flux *only* appears at the longitudinal turning point[9] of the drain-well. Nearly the entire remaining regions of the drain-well contain no atom current. This result is attributed to:

- Destructive interference occurring within the matterwave superposition at longitudinal positions between the gate-drain barrier and the drain-well turning point.
- The matterwaves of different frequencies in the drain-well interfering constructively at the drain-well turning point to form a localized atom flux.

The results seen in the drain-well current (summarized in figure 8.15) and behaviors described in the above bullet ponts suggests that coherence exists between the drain-well matterwaves.

We can verify that coherence is in fact imparted by the gain mechanism by intentionally making the matterwave current *incoherent* by removing the gate-drain barrier from the triple-well transistor potential (thus only having the source-well and drain-well). Removal of the gate-well eliminates the matterwave gain mechanism. In this case, the matterwave superposition flowing into the drain-well contains many matterwaves with different phases that are not fixed, and thus the current is incoherent. *In-situ* absorption images of the atom current in this regime shows atoms appearing in all locations throughout the entire drain-well (figure 8.15b) and shows that destructive interference is not taking place without the presence of the matterwave gain mechanism, verifying that the atom current here is *incoherent*. Additionally, previous semi-classical transistor experiments described in references [153] examine a considerably warmer atom current at temperature $T = 850$ nK flowing through the gate-well. In this case, even with the inclusion of the gate-well, no matterwave interference effects are observed in the drain-well and a very large population of atoms is found at all longitudinal locations in the drain. This is attributed to the current being

[9] Although a small population of atoms appears in between the GD barrier and the drain well at Δt=20 ms in figure 8.9.

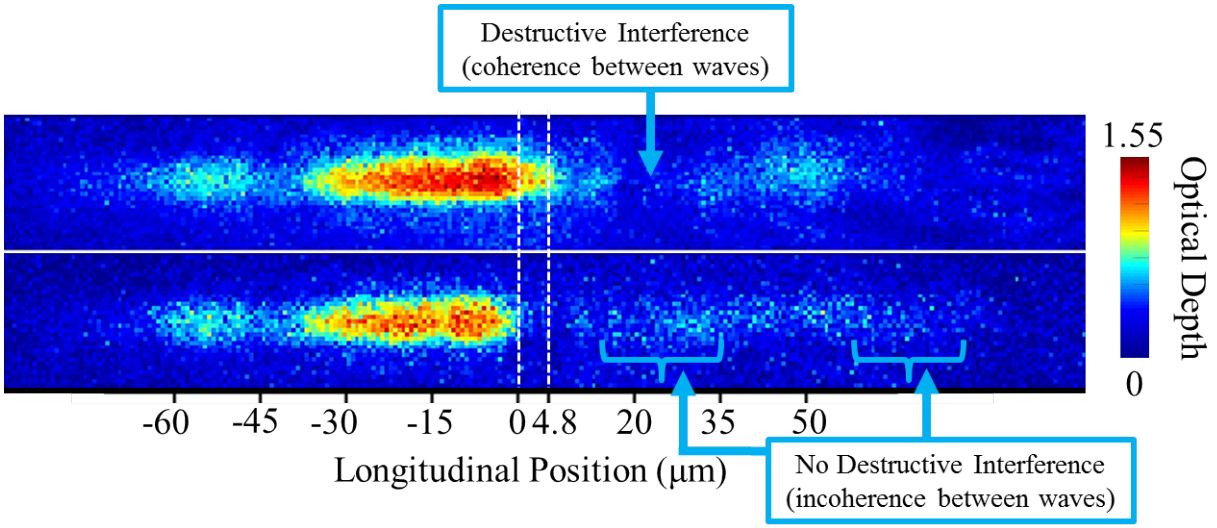

Figure 8.15: *in-situ* absorption images after 20 ms of flow time showing the observed difference of a drain-well matterwave current of coherent and incoherent matterwaves. The white dashed lines show the locations of the SG and GD barriers. Top: With the gate-well and the gain mechanism present, a drain-well atom flux *only* appears at the longitudinal turning point of the drain-well, with no drain-well atoms located at longitudinal positions from the GD barrier to the turning point. This is attributed to destructive interference occurs within the matterwave superposition at longitudinal positions between the GD barrier and the drain-well turning point. Moreover, the matterwaves of different frequencies interfere constructively at the drain-well turning point to form a localized atom flux. This behavior suggests that coherence exists between drain-well matterwaves. We can test that the interference effects are due to the gain mechanism by removing it entirely. Bottom: The gate-well is removed, which elimates the gain mechanism. With a now incoherent matterwave current, no such interferences occur and atoms appear at all longitudinal locations of the drain-well. From this set of experiments, we conclude that the interaction potential (equation 7.30) establishes a coherent gain mechanism in the atomtronic transistor.

far too hot[10] for the gain mechanism to take place. Thus, the matterwaves in this case are also incoherent. We conclude that coherence between matterwaves in the drain-well occurs only when the gate-well is present and the atom current is cold enough for the gain mechanism (equation 7.30) to materialize. Finally, the empirical observation of the canonically conjugate relationship between the envelopes of the gate-well position space wavefunction $\Psi(x)$ and the drain-well momentum space wavefunction $\Phi(p)$ is also suggestive that the matterwaves flowing into the drain-well have coherence. Without coherence, this canonically conjugate relationship would not be observed in the transistor oscillator results.

From the set of experiments described in this chapter (summarized in figure 8.13 and figure 8.15), we conclude that the interaction potential (equation 7.30) establishes a coherent gain mechanism in the atomtronic transistor.

[10] Recall from section 8.1 that for the matterwave gain mechanism to be relevant, the atom current must have a temperature on the order of the spacing between adjacent gate-well eigenstates, which for this experiment is approximately 50 nK.

Chapter 9

Conclusion to Part III

9.1 Summary

In part III of this dissertation, I described a theory and experiment in the field of atomtronics that displays an ultracold gain mechanism for a matterwave transistor oscillator. The theory presented in chapter 7 starts with a well-established semi-classical model of an atomtronic transistor but models the system with a purely quantum mechanical formalism. The quantum model predicts dynamics different from the semi-classical results only when the atoms flowing through the transistor oscillator have sufficiently low enough temperatures such that the motional state of a dipole oscillating BEC, placed in the transistor itself, couples atom transitions between high lying transistor energy eigenstates. In this ultracold temperature regime, interesting physics that were not observed in the semi-classical theory or experiments occurs, specifically the manifestation of a coherent gain mechanism that broadens the range of energy (and by extension, momenta) of a matterwave current flowing from the source-well, through the gate-well, and into the drain-well.

In chapter 8, I reported on the current experiment aimed at verifying the quantum transistor oscillator model presented in chapter 7. In this experiment, an ultracold atom ensemble is loaded into the source-well at a temperatures of 57 nK and 78 nK. By raising the chemical potential of the source-well, I showed that an atom current flows throughout the transistor by first collecting in the gate-well followed by flowing into the drain. Time-of-flight temperature measurements of the transistor source-well ensemble confirm that as an atomic current flows through the transistor, the current constantly carries energy away from the source-well ensemble, which provides continuous

cooling to the source-well atoms. Interestingly, our experimental results showed that a wider energy spread in the atom flux flowing into the drain-well is detected when the source-well ensemble contains a condensate at cooler temperature of $T = 57$ nK, compared to when the source-well ensemble is a purely thermal collection of atoms at a temperature of $T = 78$ nK. The correspondence between the increased spread in matterwave energy flowing into the drain-well as gate-well coupling strength increases (as source-well temperature approaches the 50 nK energy spacing between adjacent gate-well eigenstates) agrees with the quantum, many-body model of the transistor presented in chapter 7 and thus suggests the presence of a matterwave gain mechanism in the gate-well.

Additionally, this result confirms a canonically conjugate relationship between the spatial wavefunction of the gate-well and the momentum wavefunction of the drain-well, which suggests coherence in the transistor gain mechanism and the drain-well atom current. Evidence of a coherent drain-well atom current can also be observed in the complete absence of an atom flux at all positions in the drain-well with the exception of an atom flux located at the longitudinal turning point. We conclude that this observation is due to a superposition of coherent matterwaves where destructive interference occurs throughout the entire drain-well except at the longitudinal turning point, where the matterwave superposition constructively interferes. From the set of experiments described in chapter 8 (summarized in figure 8.13 and figure 8.15), we conclude that the interaction potential (equation 7.30) establishes a coherent gain mechanism in the atomtronic transistor.

The results given in chapter 8 help to verify principles of the quantum model derived in chapter 7. Our experiment suggests the presence of a coherent, matterwave gain mechanism in the transistor gate-well. However, further experimentation must be carried out in order to draw a complete conclusion. Specifically, the drain-well atom flux must be measured for many more initial conditions of the source-well. It will be interesting to observe the position-momentum conjugate relationship as the source-well ensemble is cooled to lower and lower temperatures. If the model presented in chapter 7 is correct, absorption images of the drain-well flux will show an atom ensemble that continuously broadens along the longitudinal direction until the atom current is so cold that it no longer couples to the gate-well. Additionally, there are still many more experiments that pique

my interest, with differing degrees of veracity[1] , to investigate the quantum model further and to verify some of it's very fine details.

9.2 Future Work and Experiments

Here, I briefly outline two interesting routes the experiments in chapter 8 could take in order to further verify more principles of our matterwave transistor oscillator model. I first describe measuring the differential gain of the transistor followed by a "possible" method for explicitly detecting the transmission of the gate-well normal modes ψ_+ or ψ_- (equations 7.37a and 7.37b) into the drain-well.

9.2.1 Measuring Differential Matterwave Gain

In order to measure the differential matterwave gain due to the atom-BEC interaction (equation 7.30) we must measure the *change* in atom flux flowing into the drain-well as a function of the *change* of occupancy of the gate-well BEC. If we are working in an experimental regime where a matterwave current *only* flows via tunneling through the SG and GD barriers, this measurement could provide a more robust method of quantifying matterwave gain, as it removes any impact of stray source-well atoms that may randomly enter the gate and drain-wells (as noise) by classically traversing the SG and GD barriers. This is because we would be measuring the changes in drain-well flux as a function of the change in gate-well occupancy, rather than strictly[2] measuring the drain-well flux as a function of gate-well atom number. This method would essentially "ignore" noise in the atom flux.

A challenge of measuring differential gain is changing the occupancy of the gate-well BEC without altering the gate-well potential. From the semiclassical models [5] and experiments [34],

[1] These experiments may be very hard to do. I am not suggesting they are even possible in the current iteration of this experiment, but rather they are brief overviews (or brainstormings, for a lack of a better term) of experiments I've been thinking about for some distant future iteration of the experiment.

[2] In this case, any stray atoms that enter each well by classically traversing each barrier will pollute the measurement with noise. If we instead measure *change* in atom flux flowing into the drain-well as a function of the *change* of occupancy of the gate-well BEC, we can get a measurement of the gain of the transistor that may be less influenced by noise from atoms that do not flow via tunneling.

the size of the gate-well BEC is controlled by the ratio of SG and GD barrier heights, V_{SG} and V_{GD}. While we can readily control the BEC occupancy by adjusting V_{SG} and V_{GD}, the *quantum* model shows (section 7.4.2, figures 7.5 and 7.6) that doing so changes the degeneracy (and subsequent coupling) between the dipole oscillating BEC and the highest lying pair of gate-well eigenstates. This degeneracy and coupling, being an essential precondition to matterwave gain, cannot be altered. This renders the methods developed in references [5] and [34] ineffective for increasing (and decreasing) the size of the gate-well BEC.

Instead, we can adjust the flux of source-well atoms that enter the gate-well by increasing or decreasing the source-well chemical potential, μ_s. Extending the semiclassical formalism from reference [5], an atom current flowing from the source-well to the gate-well I_{SG} is proportional to the fugacity factor

$$I_{SG} \propto \exp\left(\frac{\mu_s}{kTs}\right) \tag{9.1}$$

where k is the Boltzmann constant, T_s is the source-well temperature, and μ_s is the source-well chemical potential. Since the source-well chemical potential can be freely adjusted (section 8.4.2), the parameter μ_s becomes a tunable characteristic of the transistor *without* impacting the SG and GD barrier heights or the gate-well eigenstates. From this, we have an experimentally adjustable "knob" that we may be able to use to control the amount of atoms that enter the gate-well, allowing us to measure the transistor differential gain.

9.2.2 Observing Transmission of Gate-Well Normal Modes

Explicitly measuring the transmission of the gate-well symmetric or antisymmetric modes $\psi_+(x)$ and $\psi_-(x)$ (equations 7.37a and 7.37b) "may" be accomplished by performing a Hermite-Gaussian transform of the drain-well atom flux *in-situ* absorption images. A Hermite-Gaussian transform is a mathematical operation that would decompose the drain-well probability amplitude signal (which note is just the drain-well absorption image), such as in figure 8.9) which is a function of position, into the Hermite-Gaussian functions that make it up. That is, the Hermite-Gaussian transform could decompose a drain-well absorption image signal into the *harmonic oscillator* func-

tions (and thus gate-well modes) that make it up. To further investigate this idea, we define the Hermite-Gaussian transform: Given some Hermite function $H_m(x)$ of order m, the Hermite-Gaussian transform $\mathcal{H}\{H_m(x)\}$ is defined as

$$\mathcal{H}\{H_m(x)\} = \int_{-\infty}^{\infty} e^{-x^2} H_n(x) H_m(x) dx = \sqrt{\pi} 2^n n! \delta(n-m). \tag{9.2}$$

Realize that this operation is completely analogous to the Fourier transform which decomposes a function of *time* into the *frequencies* that make it up (figure 9.1). To give an example comparing the Fourier and Hermite-Gaussian transforms, consider some sine wave function, such as $f(x) = \sin(2x) + \sin(5x)$. The Fourier transform of $f(x)$ is expressed in the frequency basis and would feature delta functions $F(\omega) = \delta(\omega \pm 2) + \delta(\omega \pm 5)$ corresponding to the frequencies $\omega = 2$ and $\omega = 5$ present in the original function $f(x)$. Now, given some harmonic oscillator wavefunction, such as $\psi(x) = \psi_2(x) + \psi_5(x)$, the Hermite-Gaussian transform of $\psi(x)$ decomposes the function to the *harmonic oscillator* basis and would feature delta functions $\mathcal{H}(n) = \delta(n-2) + \delta(n-5)$ corresponding to the Hermite-Gaussian modes $n = 2$ and $n = 5$ present in $\psi(x)$.

Next, in the transistor-oscillator experiment in chapter 8, the observable signal (i.e. the drain-well *in-situ* absorption image) is comprised of the *square* of Hermite-Gaussian functions (since the absorption image really represents the matterwave probability amplitude squared). Thus, we cannot take the Hermite-Gaussian transform of the drain-well wavefunction, but rather we must take the transform of the square of the wavefunction.

The corresponding Hermite-Gaussian transform for this signal can be found by taking the definition of the Hermite-Gaussian transform (equation 9.2) and applying the convolution theorem to arrive at

$$\mathcal{H}\{H_m(x)H_l(x)\} = \mathcal{H}\{H_m(x)\} * \mathcal{H}\{H_l(x)\}. \tag{9.3}$$

It then follows that the Hermite-Gaussian transform of a *product* of Hermite-Gaussian functions is

$$\begin{aligned} \mathcal{H}\{H_m(x)H_l(x)\} &= \left(\sqrt{\pi}2^n n!\right)\left(\sqrt{\pi}2^l l!\right)[\delta(n-m) * \delta(n-l)] \\ &= \pi 2^{n+p} n! l! \,[\delta(n-m-l))] \end{aligned} \tag{9.4}$$

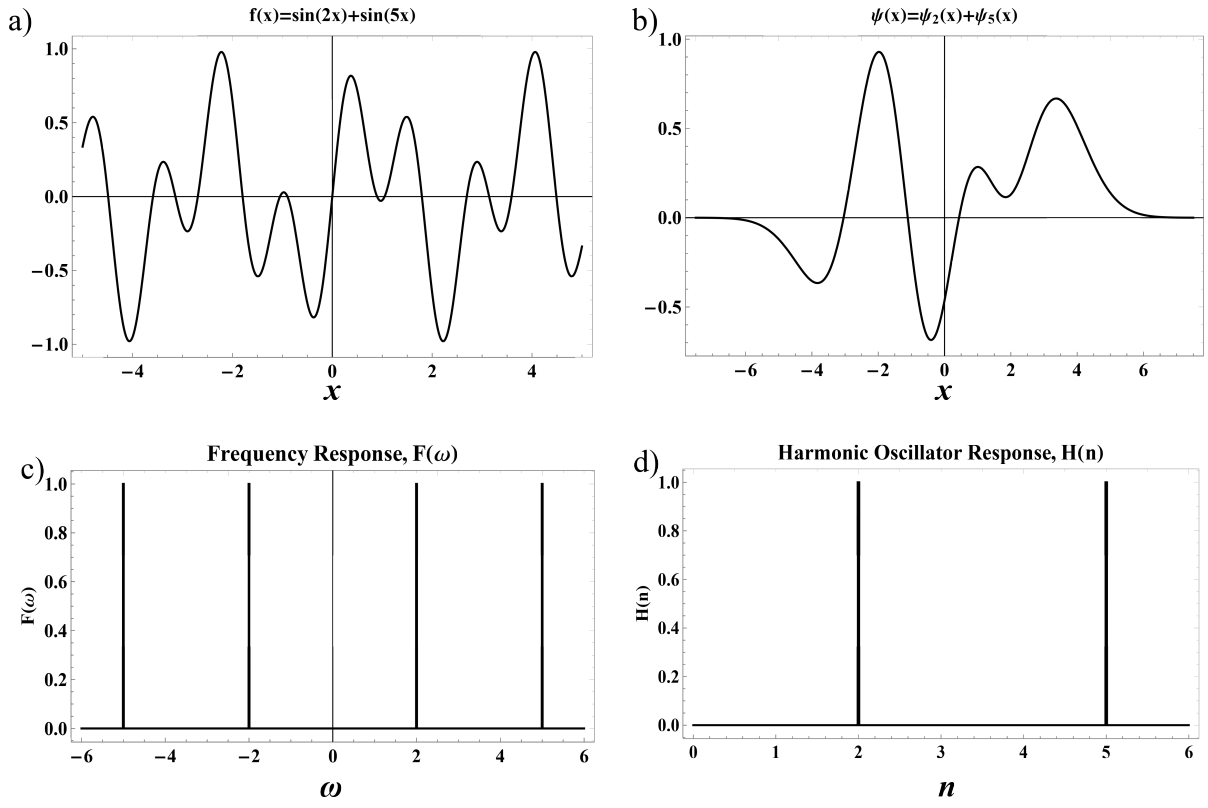

Figure 9.1: Plot a) is some function $f(x)$ composed of sine waves with various frequencies. The plot in c) is the Fourier transform showing what frequencies are present in $f(x)$. Plot b) is a function $\psi(x)$ that is comprised of a linear combination of harmonic oscillator functions (equation 7.4). The plot in d) is the Hermite-Gaussian transform of $\psi(x)$ which shows what harmonic modes are present in the function $\psi(x)$.

where the "$*$" operation denotes the convolution. We must now apply this formalism to our case in order to determine the expected Hermite-Gaussian transform of the drain-well signal. Given the symmetric mode that transmits into the drain-well is

$$\psi_+(x) = \frac{1}{\sqrt{2}}\left[\psi_{22}(x) + \psi_{23}(x)\right] \tag{9.5}$$

the *observable* signal will be

$$|\psi_+^*(x)\psi_+(x)| = \frac{1}{2}\left[|\psi_{22}(x)|^2 + |\psi_{23}(x)|^2 + 2|\psi_{22}(x)\psi_{23}(x)|\right]. \tag{9.6}$$

Applying equation 9.3 to take the Hermite-Gaussian transform of each product, we find the transform would be proportional to:

$$\begin{aligned}\mathcal{H}\left\{|\psi_+(x)|^2\right\} &= \frac{1}{2}\left[\mathcal{H}\left\{|\psi_{22}\psi_{22}(x)|\right\} + \mathcal{H}\left\{|\psi_{23}\psi_{23}(x)|\right\} + \mathcal{H}\left\{|\psi_{22}\psi_{23}(x)|\right\}\right] \\ &\propto \delta(n-44) + \delta(n-45) + \delta(n-46)\end{aligned} \tag{9.7}$$

Therefore, we find that the Hermite-Gaussian transform of the observed symmetric mode transmitted into the drain-well takes the form of three delta functions in the harmonic oscillator basis:

- one at twice the mode number corresponding to the highest lying gate-well eigenstate (corresponding to $|3\rangle$ in the reduced model)
- one at twice the the mode number corresponding to the second highest lying gate-well eigenstate (corresponding to $|2\rangle$ in the reduced model)
- one at the sum of both gate-well eigenstate modes making up the symmetric normal mode.

A plot showing this result of a Hermite-Gaussian transform applied to a hypothetical transmitted symmetric mode is shown in figure 9.2. This could be a useful tool to explicitly measure what mode has transmitted into the transistor gate-well, which also tells us what modes are having their probability amplified as a result the gate-well gain mechanism. As a generalized extension of equation 9.6 and 9.7, if the constructed gate-well potential has N bound energy eigenstates,

then the Hermite-Gaussian transform of the drain-well signal in the presence of the ultracold gain mechanism is

$$\mathcal{H}\left\{|\psi_+(x)|^2\right\} \propto \delta(n-(2N-2)) + \delta(n-(2N-1) + \delta(n-2N) \tag{9.8}$$

Finally, recall from equation 7.31 that the atom-BEC interaction responsible for transmitting symmetric (or antisymmetric) modes into the drain well has a phase dependence φ. Consequently, the phase of the transmitted symmetric mode that enters the drain-well may not be the same for each successive run of the experiment. This complicates the problem of averaging drain-well images (such as averaging *in-situ* absorption images to filter random noise) due to the symmetric mode having a different phase between shot-to-shot. Because the Hermite-Gaussian transform of the drain-well signal will produce the same result irrespective of the phase of the transmitted symmetric mode, one must perform many data runs of the experiment and average all of the Hermite-Gaussian transforms of the absorption images rather than the raw absorption image themselves in order to collect reliable data to verify the presence of a specific symmetric of antisymmetric normal mode flowing into the drain-well. Such a measurement will very difficult to make, however, if successful, would be truly fascinating.

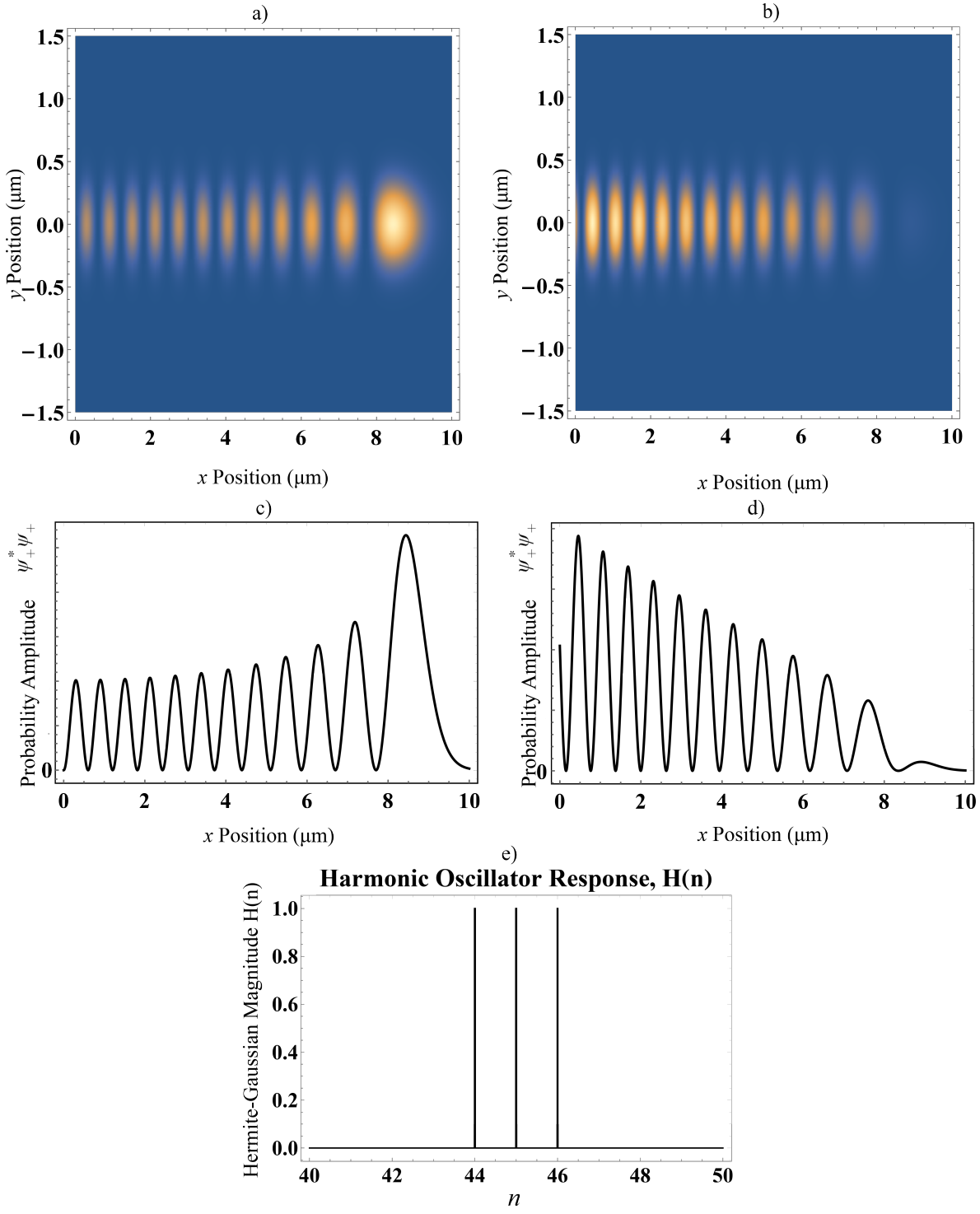

Figure 9.2: Images a) and b) show a 2D plot of $|\psi_+(x)|^2$ for the symmetric mode $\psi_+(x) = \frac{1}{\sqrt{2}}[\psi_{22}(x) + \psi_{23}(x)]$ (which realize corresponds to $\psi_+ = \frac{1}{\sqrt{2}}[\psi_2(x) + \psi_3(x)]$ in the reduced gate-well model, section 7.4.3) located in the transistor drain-well and with two different oscillation phases. Images c) and d) are the respective probability amplitudes $|\psi_+(x)|^2$. Finally, image e) is the Hermite-Gaussian transform of $|\psi_+(x)|^2$, showing that the transmitted symmetric mode is comprised of Harmonic oscillator modes $\psi_{22}(x)$ and $\psi_{23}(x)$, as described in equations 9.7 and 9.8.

9.3 Outlook: Integrated Atomtronic Transistors

The work in part III of this dissertation demonstrates results that suggest the existence of a coherent matterwave gain mechanism. If such an atom transistor is realized (and perfected), more complex, integrated atomtronic circuits with multiple transistors could theoretically be developed. This would permit atomtronic equivalences of logic gates. Theorists have recently proposed an atomtronic controlled NOT (CNOT) gate that would be implemented with two independently controlled atom transistors [184]. Since the CNOT gate is a "universal" gate, any other logic gate can be constructed from sets of CNOT gates. The realization of an atomtronic CNOT gate would be extremely influential in computing and eventually realizing an "atomtronic computer."

Finally, the work in this dissertation could act as another route for building a continuous, coherent matterwave source otherwise known as a "practical atom laser." While nothing in this dissertation addresses testing the coherent output (such as performing interferometry experiments), such tests could certainly be a future milestone that evolves from this work. Within the previous year, various experiments in AMO physics have provided excellent starting points for a continuous atom laser, such as continuously cooling a BEC such that it could (in theory) exist for long periods of time and provide a constant source of coherent atoms [185]. If achieved, the *continuous* coherent matterwaves could be used to source integrated matterwave circuits. These integrated circuits examine the physics of coherent matterwaves launched into waveguides where the matterwave current can switched, divided, and recombined as the matterwaves flow throughout the system [186]. It would undoubtedly be fascinating if the these circuits could be sourced with a continuous, coherent matterwave source rather than sourced with a "pulse" of coherent atoms. The results presented in part III of this dissertation can provide an additional method of realizing such a practical atom laser.

Bibliography

[1] M Saffman. Quantum computing with atomic qubits and rydberg interactions: progress and challenges. Journal of Physics B: Atomic, Molecular and Optical Physics, 49(20):202001, 2016.

[2] L. Isenhower, E. Urban, X. L. Zhang, A. T. Gill, T. Henage, T. A. Johnson, T. G. Walker, and M. Saffman. Demonstration of a neutral atom controlled-not quantum gate. Phys. Rev. Lett., 104:010503, Jan 2010.

[3] Kai Hudek. A Compact and Transportable Ultracold Matter System and Progress Towards a Continuously Operating Neutral Rydberg Atom Quantum Computer. PhD thesis, University of Colorado, Boulder, 2012.

[4] Evan Salim. Ultracold matter systems and atomtronics instrumentation. PhD thesis, JILA, University of Colorado, Boulder, 2011.

[5] Seth C Caliga, Cameron J E Straatsma, and Dana Z Anderson. Transport dynamics of ultracold atoms in a triple-well transistor-like potential. New Journal of Physics, 18(2):025010, 2016.

[6] Richard P. Feynman. *There's Plenty of Room at the Bottom*, APS Annual Meeting Lecture, Caltech, Dec 1959.

[7] C. Monroe, D. M. Meekhof, B. E. King, W. M. Itano, and D. J. Wineland. Demonstration of a fundamental quantum logic gate. Phys. Rev. Lett., 75:4714–4717, Dec 1995.

[8] R. Blatt and D. Wineland. Entangled states of trapped atomic ions. Nature, 453:1008, 2008.

[9] V.M. Schäfer, C.J. Ballance, K. Thirumalai, L.J. Stephenson, T.G. Ballance, A.M. Steane, and D.M. Lucas. Fast quantum logic gates with trapped-ion qubits. Nature, 555:75–78, 2017.

[10] J. Zhang, A. Kyprianidis, P. Becker, H. Kaplan, A.V. Gorshkov, Z.X. Gong, and C. Monroe. Observation of a many-body dynamical phase transistion with a 53-qubit quantum simulator. Nature, 551:601–604, 2017.

[11] L. DiCarlo, J.M. Chow, J.M. Gambetta, Lev S. Bishop, B. R. Johnson, D.I. Schuster, J. Majer, A. Blais, L. Frunzio, S.M. Girvin, and R.J. Schoelkopf. Demonstration of two-qubit algorithms with a superconducting quantum processor. Nature, 460:240–244, 2009.

[12] Jay M. Gambetta, Jerry M. Chow, and Matthias Steffen. Building logical qubits in a superconducting quantum computing system. npj Quantum Information, 3:2, 2017.

[13] Nicolai Friis, Alexey A. Melnikov, Gerhard Kirchmair, and Hans J. Briegel. Coherent controlization using superconducting qubits. Scientific Reports, 5, 2015.

[14] Alberto Politi, Jonathan C.F. Matthews, and Jeremy L. O'Brien. Shor's quantum factoring algorithm on a photonic chip. Science, 325.

[15] Stefanie Barz, Ivan Kassal, Martin Ringbauer, Yannick Ole Lipp, Borivoje Dakic, Alan Aspuru-Guzik, and Philip Walther. A two-qubit photonic quantum processor and its application to solving systems of linear equations. Scientific Reports, 4.

[16] David Weiss and Mark Saffman. Quantum computing with neutral atoms. Physics Today, 70.

[17] K. M. Maller, M. T. Lichtman, T. Xia, Y. Sun, M. J. Piotrowicz, A. W. Carr, L. Isenhower, and M. Saffman. Rydberg-blockade controlled-not gate and entanglement in a two-dimensional array of neutral-atom qubits. Phys. Rev. A, 92:022336, Aug 2015.

[18] Y.Y. Jau, A.M. Hankin, T. Keating, I.H. Deutsch, and G.W. Biedermann. Entangling atomic spins with a rudberg-dressed spin-flip blockade. Nature Physics, 12:71–74, 2016.

[19] P. Shor. Polynomial-time algorithms for prime factorization and discrete logarithms on a quantum computer. SIAM Journal on Computing, 26(5):1484–1509, 1997.

[20] A fast quantum mechanical algorithm for database search. Proc. 28th Annual ACM Symp. on Theory of Computing, STOC 96, page 212, 1996.

[21] Jan Benhelm, Gerhard Kirchmair, Christian F. Roos, and Rainer Blatt. Towards fault-tolerant quantum computing with trapped ions. Nature Physics, 4:463–466, 2008.

[22] T. P. Harty, D. T. C. Allcock, C. J. Ballance, L. Guidoni, H. A. Janacek, N. M. Linke, D. N. Stacey, and D. M. Lucas. High-fidelity preparation, gates, memory, and readout of a trapped-ion quantum bit. Phys. Rev. Lett., 113:220501, Nov 2014.

[23] C. J. Ballance, T. P. Harty, N. M. Linke, M. A. Sepiol, and D. M. Lucas. High-fidelity quantum logic gates using trapped-ion hyperfine qubits. Phys. Rev. Lett., 117:060504, Aug 2016.

[24] Jerry M. Chow, Jay M. Gambetta, A. D. Córcoles, Seth T. Merkel, John A. Smolin, Chad Rigetti, S. Poletto, George A. Keefe, Mary B. Rothwell, J. R. Rozen, Mark B. Ketchen, and M. Steffen. Universal quantum gate set approaching fault-tolerant thresholds with superconducting qubits. Phys. Rev. Lett., 109:060501, Aug 2012.

[25] R. Barends, J. Kelly, A. Megrant, A. Veitia, D. Sank, E. Jeffrey, T.C. White, J. Mutus, A.G. Fowler, B. Campbell, Y. Chen, Z. Chen, B. Chiaro, A. Dunsworth, C. Neill, P. O'Malley, P. Roushan, A. Vainsencher, J. Wenner, A.N. Korotkov, A.N. Cleland, and John M. Martinis. Superconducting quantum circuits at the surface code threshold for fault tolerance. Nature, 508:500–503, 2014.

[26] W. Hänsel, J. Reichel, P. Hommelhoff, and T. W. Hänsch. Magnetic conveyor belt for transporting and merging trapped atom clouds. Phys. Rev. Lett., 86:608–611, Jan 2001.

[27] A Aghajani-Talesh, M Falkenau, A Griesmaier, and T Pfau. A proposal for continuous loading of an optical dipole trap with magnetically guided ultra-cold atoms. Journal of Physics B: Atomic, Molecular and Optical Physics, 42(24):245302, 2009.

[28] Kevin M. Fortier, Soo Y. Kim, Michael J. Gibbons, Peyman Ahmadi, and Michael S. Chapman. Deterministic loading of individual atoms to a high-finesse optical cavity. Phys. Rev. Lett., 98:233601, Jun 2007.

[29] D. Schrader, S. Kuhr, W. Alt, M. Muller, V. Gomer, and D. Meschede. An optical conveyor belt for single neutral atoms. Appl. Phys. B: Lasers Opt, 73:819, 2001.

[30] Y. Miroshnychenko, D. Schrader, S. Kuhr, W. Alt, I. Dotsenko, M. Khudaverdyan, A. Rauschenbeutel, and D. Meschede. Continued imaging of the transport of a single neutral atom. Opt. Express, 11(25):3498–3502, Dec 2003.

[31] Stefan Schmid, Gregor Thalhammer, Klaus Winkler, Florian Lang, and Johannes Hecker Denschlag. Long distance transport of ultracold atoms using a 1d optical lattice. New Journal of Physics, 8(8):159, 2006.

[32] Brad A. Dinardo and Dana Z. Anderson. A technique for individual atom delivery into a crossed vortex bottle beam trap using a dynamic 1d optical lattice. Review of Scientific Instruments, 87(12):123108, 2016.

[33] Seth C Caliga, Cameron J E Straatsma, and Dana Z Anderson. Experimental demonstration of an atomtronic battery. New Journal of Physics, 19(1):013036, 2017.

[34] Seth C Caliga, Cameron J E Straatsma, Alex A Zozulya, and Dana Z Anderson. Principles of an atomtronic transistor. New Journal of Physics, 18(1):015012, 2016.

[35] B. T. Seaman, M. Krämer, D. Z. Anderson, and M. J. Holland. Atomtronics: Ultracold-atom analogs of electronic devices. Phys. Rev. A, 75:023615, Feb 2007.

[36] R. A. Pepino, J. Cooper, D. Z. Anderson, and M. J. Holland. Atomtronic circuits of diodes and transistors. Phys. Rev. Lett., 103:140405, Sep 2009.

[37] A Ruschhaupt, J G Muga, and M G Raizen. Improvement by laser quenching of an 'atom diode': a one-way barrier for ultra-cold atoms. Journal of Physics B: Atomic, Molecular and Optical Physics, 39(6):L133, 2006.

[38] Filip Krzysztof Auksztol. Tailored Optical Potentials for Atomtronic Devices. PhD thesis, Centre for Quantum Technologies, National University of Singapore, 2017.

[39] J. Reichel, W. Hänsel, and T. W. Hänsch. Atomic micromanipulation with magnetic surface traps. Phys. Rev. Lett., 83:3398–3401, Oct 1999.

[40] E A Hinds and I G Hughes. Magnetic atom optics: mirrors, guides, traps, and chips for atoms. Journal of Physics D: Applied Physics, 32(18):R119, 1999.

[41] Ron Folman, Peter Krger, Jrg Schmiedmayer, Johannes Denschlag, and Carsten Henkel. Microscopic atom optics: From wires to an atom chip. volume 48 of Advances In Atomic, Molecular, and Optical Physics, pages 263 – 356. Academic Press, 2002.

[42] József Fortágh and Claus Zimmermann. Magnetic microtraps for ultracold atoms. Rev. Mod. Phys., 79:235–289, Feb 2007.

[43] W. Hänsel, P. Hommelhoff, T.W. Hänsch, and J. Reichel. Bose-einstein condensation on a microelectric chip. Nature, 413(6855):498, 2000.

[44] M.H. Anderson, J.R. Ensher, M.R. Matthews, C.E. Wieman, and E.A. Cornell. Observation of bose-einstein condensation in a dilute atomic vapor. Science, 269(5221):198–201, 1995.

[45] Ronald A. Pepino. Open Quantum System Studies of Optical Lattices and Nonlinear Optical Cavities: A Comprehensive Development of Atomtronics. PhD thesis, JILA, University of Colorado, Boulder, 2011.

[46] C. Ryu, P. W. Blackburn, A. A. Blinova, and M. G. Boshier. Experimental realization of josephson junctions for an atom squid. Phys. Rev. Lett., 111:205301, Nov 2013.

[47] Ralf Labouvie, Bodhaditya Santra, Simon Heun, Sandro Wimberger, and Herwig Ott. Negative differential conductivity in an interacting quantum gas. Phys. Rev. Lett., 115:050601, Jul 2015.

[48] Stephen Eckel, Jeffrey G. Lee, Fred Jendrzejewski, Noel Murray, Charles W. Clark, Christopher J. Lobb, William D. Phillips, Mark Edwars, and Gretchen K. Campbell. Hysteresis in a quantized superfluid atomtronic circuit. Nature, 506:200–203, 2014.

[49] D Aghamalyan, N T Nguyen, F Auksztol, K S Gan, M Martinez Valado, P C Condylis, L-C Kwek, R Dumke, and L Amico. An atomtronic flux qubit: a ring lattice of boseeinstein condensates interrupted by three weak links. New Journal of Physics, 18(7):075013, 2016.

[50] Tobias Haug, Joel Tan, Mark Theng, Rainer Dumke, Leong-Chuan Kwek, and Luigi Amico. Readout of the atomtronic quantum interference device. Phys. Rev. A, 97:013633, Jan 2018.

[51] Luigi Amico, Gerhard Birkl, Malcolm Boshier, and Leong-Chuan Kwek. Focus on atomtronics-enabled quantum technologies. New Journal of Physics, 19(2):020201, 2017.

[52] R. Gati, M. Albiez, J. Fölling, B. Hemmerling, and M.K. Oberthaler. Realization of a single josephson junction for bose–einstein condensates. Applied Physics B, 82(2):207–210, Feb 2006.

[53] R Gati and M K Oberthaler. A bosonic josephson junction. Journal of Physics B: Atomic, Molecular and Optical Physics, 40(10):R61, 2007.

[54] M. Rab, J. H. Cole, N. G. Parker, A. D. Greentree, L. C. L. Hollenberg, and A. M. Martin. Spatial coherent transport of interacting dilute bose gases. Phys. Rev. A, 77:061602, Jun 2008.

[55] Stuart Moulder, Scott Beattie, Robert P. Smith, Naaman Tammuz, and Zoran Hadzibabic. Quantized supercurrent decay in an annular bose-einstein condensate. Phys. Rev. A, 86:013629, Jul 2012.

[56] Davit Aghamalyan, Marco Cominotti, Matteo Rizzi, Davide Rossini, Frank Hekking, Anna Minguzzi, Leong-Chuan Kwek, and Luigi Amico. Coherent superposition of current flows in an atomtronic quantum interference device. New Journal of Physics, 17(4):045023, 2015.

[57] Nuria Barbern, Daniel Dagnino, Miguel Angel Garca-March, Andrea Trombettoni, Josep Taron, and Maciej Lewenstein. Quantum simulation of conductivity plateaux and fractional quantum hall effect using ultracold atoms. New Journal of Physics, 17(12):125009, 2015.

[58] Geva Arwas and Doron Cohen. Chaos and two-level dynamics of the atomtronic quantum interference device. New Journal of Physics, 18(1):015007, 2016.

[59] T. A. Haase, D. H. White, D. J. Brown, I. Herrera, and M. D. Hoogerland. A versatile apparatus for two-dimensional atomtronic quantum simulation. Review of Scientific Instruments, 88(11):113102, 2017.

[60] A Kumar, N Anderson, W D Phillips, S Eckel, G K Campbell, and S Stringari. Minimally destructive, doppler measurement of a quantized flow in a ring-shaped boseeinstein condensate. New Journal of Physics, 18(2):025001, 2016.

[61] P Navez, S Pandey, H Mas, K Poulios, T Fernholz, and W von Klitzing. Matter-wave interferometers using taap rings. New Journal of Physics, 18(7):075014, 2016.

[62] Yi-Hsieh Wang, A Kumar, F Jendrzejewski, Ryan M Wilson, Mark Edwards, S Eckel, G K Campbell, and Charles W Clark. Resonant wavepackets and shock waves in an atomtronic squid. New Journal of Physics, 17(12):125012, 2015.

[63] Amy C Mathey and L Mathey. Realizing and optimizing an atomtronic squid. New Journal of Physics, 18(5):055016, 2016.

[64] Brynle Barrett, Rmy Geiger, Indranil Dutta, Matthieu Meunier, Benjamin Canuel, Alexandre Gauguet, Philippe Bouyer, and Arnaud Landragin. The sagnac effect: 20 years of development in matter-wave interferometry. Comptes Rendus Physique, 15(10):875 – 883, 2014. The Sagnac effect: 100 years later / L'effet Sagnac : 100 ans aprs.

[65] J. Bardeen and W. H. Brattain. The transistor, a semi-conductor triode. Phys. Rev., 74:230–231, Jul 1948.

[66] L. Mandel. Electric dipole interaction in quantum optics. Phys. Rev. A, 20:1590–1592, Oct 1979.

[67] David J Griffiths. Introduction to electrodynamics; 3rd ed. Pearson, Boston, MA, 1999.

[68] C. J. Pethick and H. Smith. BoseEinstein Condensation in Dilute Gases. Cambridge University Press, 2 edition, 2008.

[69] C. Cohen-Tannoudji, G. Grynberg, and J. Dupont-Roc. Atom-Photon Interactions: Basic Processes and Applications. Wiley, New York, 1992.

[70] David J Griffiths. Introduction to Quantum Mechanics; 2nd ed. Pearson, Boston, MA, 2005.

[71] Harold J. Metcalf and Peter van der Straten. Laser Cooling and Trapping. Springer-Verlag, New York, 1999.

[72] Rudolf Grimm, Matthias Weidemller, and Yurii B. Ovchinnikov. Optical dipole traps for neutral atoms. volume 42 of Advances In Atomic, Molecular, and Optical Physics, pages 95 – 170. Academic Press, 2000.

[73] Steven Chu, J. E. Bjorkholm, A. Ashkin, and A. Cable. Experimental observation of optically trapped atoms. Phys. Rev. Lett., 57:314–317, Jul 1986.

[74] Albert Einstein. On the Electrodynamics of Moving Bodies. Annalen der Physik, 17, 1905.

[75] T.W. Hansch and A.L. Schawlow. Cooling of gases by laser radiation. Optics Communications, 13(1):68 – 69, 1975.

[76] Steven Chu, L. Hollberg, J. E. Bjorkholm, Alex Cable, and A. Ashkin. Three-dimensional viscous confinement and cooling of atoms by resonance radiation pressure. Phys. Rev. Lett., 55:48–51, Jul 1985.

[77] A. Ashkin and J. P. Gordon. Stability of radiation-pressure particle traps: an optical earnshaw theorem. Opt. Lett., 8(10):511–513, Oct 1983.

[78] P. Zeeman. On the Influence of Magnetism on the Nature of the Light Emitted by a Substance. APJ, 5:332, May 1897.

[79] E. L. Raab, M. Prentiss, Alex Cable, Steven Chu, and D. E. Pritchard. Trapping of neutral sodium atoms with radiation pressure. Phys. Rev. Lett., 59:2631–2634, Dec 1987.

[80] Y. Castin, H. Wallis, and J. Dalibard. Limit of doppler cooling. J. Opt. Soc. Am. B, 6(11):2046–2057, Nov 1989.

[81] J. Dalibard and C. Cohen-Tannoudji. Laser cooling below the doppler limit by polarization gradients: simple theoretical models. J. Opt. Soc. Am. B, 6(11):2023–2045, Nov 1989.

[82] M. Walhout, J. Dalibard, S. L. Rolston, and W. D. Phillips. Optical molasses in a longitudinal magnetic field. J. Opt. Soc. Am. B, 9(11):1997–2007, Nov 1992.

[83] Shengwang Du. Atom-chip Bose-Einstein condensation in a portable vacuum cell. PhD thesis, JILA, University of Colorado, Boulder, 2005.

[84] Mark Kasevich and Steven Chu. Laser cooling below a photon recoil with three-level atoms. Phys. Rev. Lett., 69:1741–1744, Sep 1992.

[85] Shengwang Du, Matthew B. Squires, Yutaka Imai, Leslie Czaia, R. A. Saravanan, Victor Bright, Jakob Reichel, T. W. Hänsch, and Dana Z. Anderson. Atom-chip bose-einstein condensation in a portable vacuum cell. Phys. Rev. A, 70:053606, Nov 2004.

[86] László Erdős, Benjamin Schlein, and Horng-Tzer Yau. Rigorous derivation of the gross-pitaevskii equation. Phys. Rev. Lett., 98:040404, Jan 2007.

[87] Tim Langen. Non-equilibrium Dynamics of One-Dimensional Bose Gases, chapter 1, page 1–37. Number Springer Theses. Springer International Publishing, Cham, 2015.

[88] T. Gog, D. M. Casa, I. Kuzmenko, R. J. Krakora, and T. B. Bolin. Windowless transition between atmospheric pressure and high vacuum *via* differential pumping for synchrotron radiation applications. Journal of Synchrotron Radiation, 14(4):339–344, Jul 2007.

[89] T. B. Swanson, D. Asgeirsson, J. A. Behr, A. Gorelov, and D. Melconian. Efficient transfer in a double magneto-optical trap system. J. Opt. Soc. Am. B, 15(11):2641–2645, Nov 1998.

[90] V Greco, F Marchesini, and G Molesini. Optical contact and van der waals interactions: the role of the surface topography in determining the bonding strength of thick glass plates. Journal of Optics A: Pure and Applied Optics, 3(1):85, 2001.

[91] Jan Haisma and G.A.C.M. Spierings. Contact bonding, including direct-bonding in a historical and recent context of materials science and technology, physics and chemistry: Historical review in a broader scope and comparative outlook. Materials Science and Engineering: R: Reports, 37(1):1 – 60, 2002.

[92] Adriana Cozma Lapadatu and Henrik Jakobsen. Chapter 30 - anodic bonding. In Markku Tilli, , Teruaki Motooka, , Veli-Matti Airaksinen, , Sami Franssila, , Mervi Paulasto-Krckel, , and Veikko Lindroos, editors, Handbook of Silicon Based {MEMS} Materials and Technologies (Second Edition), Micro and Nano Technologies, pages 599 – 610. William Andrew Publishing, Boston, second edition edition, 2015.

[93] Zheng Cui. Anodic Bonding, pages 50–54. Springer US, Boston, MA, 2008.

[94] George Wallis and Daniel I. Pomerantz. Field assisted glassmetal sealing. Journal of Applied Physics, 40(10):3946–3949, 1969.

[95] M. K. Ivory, A. R. Ziltz, C. T. Fancher, A. J. Pyle, A. Sensharma, B. Chase, J. P. Field, A. Garcia, D. Jervis, and S. Aubin. Atom chip apparatus for experiments with ultracold rubidium and potassium gases. Review of Scientific Instruments, 85(4):043102, 2014.

[96] Reichel Jakob. Trapping and Manipulating Atoms on Chips, chapter 2, pages 33–60. Wiley-Blackwell, 2011.

[97] Mark Keil, Omer Amit, Shuyu Zhou, David Groswasser, Yonathan Japha, and Ron Folman. Fifteen years of cold matter on the atom chip: promise, realizations, and prospects. Journal of Modern Optics, 63(18):1840–1885, 2016.

[98] J. C. Maxwell. Li. on physical lines of force. The London, Edinburgh, and Dublin Philosophical Magazine and Journal of Science, 21(141):338–348, 1861.

[99] D. M. Brink and C. V. Sukumar. Majorana spin-flip transitions in a magnetic trap. Phys. Rev. A, 74:035401, Sep 2006.

[100] Ettore Majorana. Atomi orientati in campo magnetico variabile. Il Nuovo Cimento (1924-1942), 9(2):43–50, Feb 1932.

[101] M. Saffman, T. G. Walker, and K. Mølmer. Quantum information with rydberg atoms. Rev. Mod. Phys., 82:2313–2363, Aug 2010.

[102] S. Zhang, F. Robicheaux, and M. Saffman. Magic-wavelength optical traps for rydberg atoms. Phys. Rev. A, 84:043408, Oct 2011.

[103] T. Xia, M. Lichtman, K. Maller, A. W. Carr, M. J. Piotrowicz, L. Isenhower, and M. Saffman. Randomized benchmarking of single-qubit gates in a 2d array of neutral-atom qubits. Phys. Rev. Lett., 114:100503, Mar 2015.

[104] L. Isenhower, M. Saffman, and K. Mølmer. Multibit c k not quantum gates via rydberg blockade. Quantum Information Processing, 10(6):755–770, 2011.

[105] K. M. Maller, M. T. Lichtman, T. Xia, Y. Sun, M. J. Piotrowicz, A. W. Carr, L. Isenhower, and M. Saffman. Rydberg-blockade controlled-not gate and entanglement in a two-dimensional array of neutral-atom qubits. Phys. Rev. A, 92:022336, Aug 2015.

[106] Martin Lichtman. Coherent Operations, Entanglement, and Progress Toward Quantum Search in a Large 2D Array of Neutral Atom Qubits. PhD thesis, University of Wisconsin, Madison, 2015.

[107] Mark Saffman. Quantum computing with atomic qubits and rydberg interactions: Progress and challenges, 2016.

[108] Cristoforo Benvenuti. Extreme high vacuum technology for particle accelerators. In Particle Accelerator Conference, 2001. PAC 2001. Proceedings of the 2001, volume 1, pages 602–606. IEEE, 2001.

[109] Peng Xu, Xiaodong He, Jin Wang, and Mingsheng Zhan. Trapping a single atom in a blue detuned optical bottle beam trap. Opt. Lett., 35(13):2164–2166, Jul 2010.

[110] G. Li, S. Zhang, L. Isenhower, K. Maller, and M. Saffman. Crossed vortex bottle beam trap for single-atom qubits. Opt. Lett., 37(5):851–853, Mar 2012.

[111] M Khudaverdyan, W Alt, I Dotsenko, T Kampschulte, K Lenhard, A Rauschenbeutel, S Reick, K Schrner, A Widera, and D Meschede. Controlled insertion and retrieval of atoms coupled to a high-finesse optical resonator. New Journal of Physics, 10(7):073023, 2008.

[112] Kevin M. Fortier, Soo Y. Kim, Michael J. Gibbons, Peyman Ahmadi, and Michael S. Chapman. Deterministic loading of individual atoms to a high-finesse optical cavity. Phys. Rev. Lett., 98:233601, Jun 2007.

[113] J. A. Sauer, K. M. Fortier, M. S. Chang, C. D. Hamley, and M. S. Chapman. Cavity qed with optically transported atoms. Phys. Rev. A, 69:051804, May 2004.

[114] E. A. Donley, T. P. Heavner, F. Levi, M. O. Tataw, and S. R. Jefferts. Double-pass acousto-optic modulator system. Review of Scientific Instruments, 76(6):063112, 2005.

[115] M. Massari, G. Ruffato, M. Gintoli, F. Ricci, and F. Romanato. Fabrication and characterization of high-quality spiral phase plates for optical applications. Appl. Opt., 54(13):4077–4083, May 2015.

[116] A. Mawardi, S. Hild, A. Widera, and D. Meschede. Abcd-treatment of a propagating doughnut beam generated by a spiral phase plate. Opt. Express, 19(22):21205–21210, Oct 2011.

[117] A. Ashkin. Trapping of atoms by resonance radiation pressure. Phys. Rev. Lett., 40:729–732, Mar 1978.

[118] E. L. Raab, M. Prentiss, Alex Cable, Steven Chu, and D. E. Pritchard. Trapping of neutral sodium atoms with radiation pressure. Phys. Rev. Lett., 59:2631–2634, Dec 1987.

[119] A. Cable, M. Prentiss, and N. P. Bigelow. Observations of sodium atoms in a magnetic molasses trap loaded by a continuous uncooled source. Opt. Lett., 15(9):507–509, May 1990.

[120] C. Monroe, W. Swann, H. Robinson, and C. Wieman. Very cold trapped atoms in a vapor cell. Phys. Rev. Lett., 65:1571–1574, Sep 1990.

[121] K. Dieckmann, R. J. C. Spreeuw, M. Weidemüller, and J. T. M. Walraven. Two-dimensional magneto-optical trap as a source of slow atoms. Phys. Rev. A, 58:3891–3895, Nov 1998.

[122] T. Pyragius. Developing and building an absorption imaging system for Ultracold Atoms. ArXiv e-prints, September 2012.

[123] J. Dalibard and C. Cohen-Tannoudji. Laser cooling below the doppler limit by polarization gradients: simple theoretical models. J. Opt. Soc. Am. B, 6(11):2023–2045, Nov 1989.

[124] Paul D. Lett, Richard N. Watts, Christoph I. Westbrook, William D. Phillips, Phillip L. Gould, and Harold J. Metcalf. Observation of atoms laser cooled below the doppler limit. Phys. Rev. Lett., 61:169–172, Jul 1988.

[125] C. Salomon, J. Dalibard, W. D. Phillips, A. Clairon, and S. Guellati. Laser cooling of cesium atoms below 3 k. EPL (Europhysics Letters), 12(8):683, 1990.

[126] Dominik Schrader, Stefan Kuhr, Wolfgang Alt, Martin Müller, Victor Gomer, and Dieter Meschede. An optical conveyor belt for single neutral atoms. Applied Physics B, 73(8):819–824, 2001.

[127] S. Kuhr, W. Alt, D. Schrader, M. Mller, V. Gomer, and D. Meschede. Deterministic Delivery of a Single Atom. Science, 293:278, 2001.

[128] Wolfgang Alt, Dominik Schrader, Stefan Kuhr, Martin Müller, Victor Gomer, and Dieter Meschede. Single atoms in a standing-wave dipole trap. Phys. Rev. A, 67:033403, Mar 2003.

[129] Dieter Meschede and Arno Rauschenbeutel. Manipulating single atoms. volume 53 of Advances In Atomic, Molecular, and Optical Physics, pages 75 – 104. Academic Press, 2006.

[130] S. J. M. Kuppens, K. L. Corwin, K. W. Miller, T. E. Chupp, and C. E. Wieman. Loading an optical dipole trap. Phys. Rev. A, 62:013406, Jun 2000.

[131] Wolfgang Alt. Optical Control of Single Neutral Atoms. PhD thesis, University of Bonn, 2004.

[132] T. A. Savard, K. M. O'Hara, and J. E. Thomas. Laser-noise-induced heating in far-off resonance optical traps. Phys. Rev. A, 56:R1095–R1098, Aug 1997.

[133] M. E. Gehm, K. M. O'Hara, T. A. Savard, and J. E. Thomas. Dynamics of noise-induced heating in atom traps. Phys. Rev. A, 58:3914–3921, Nov 1998.

[134] M. J. Piotrowicz. Personal conversation, May 2014.

[135] Nir Davidson, Heun Jin Lee, Charles S. Adams, Mark Kasevich, and Steven Chu. Long atomic coherence times in an optical dipole trap. Phys. Rev. Lett., 74:1311–1314, Feb 1995.

[136] A. Fuhrmanek, R. Bourgain, Y. R. P. Sortais, and A. Browaeys. Light-assisted collisions between a few cold atoms in a microscopic dipole trap. Phys. Rev. A, 85:062708, Jun 2012.

[137] Tzahi Grünzweig, Matthew McGovern, Andrew J. Hilliard, and Mikkel F. Andersen. Using light-assisted collisions to consistently isolate individual atoms for quantum information processing. Quantum Information Processing, 10(6):925–940, 2011.

[138] J. Weiner. Cold and Ultracold Collisions in Quantum Microscopic and Mesoscopic Systems. Cambridge University Press, 2003.

[139] Siyuan Zhang. Trapping and Rydberg Excitation of a Single Atom Qubit in a Blue Detuned Bottle Beam. PhD thesis, University of Wisconsin, Madison, 2012.

[140] Wolfgang Wieser. An Optical Dipole Trap for Ultracold Bosons and Fermions. PhD thesis, Ludwig Maximilian University of Munich, 2006.

[141] Protsenko I Schlosser N, Reymond G and Grangier P. Sub-poissonian loading of single atoms in a microscopic dipole trap. Nature.

[142] S B Hill and J J McClelland. Atoms on demand: Fast, deterministic production of single cr atoms. Applied Physics Letters, 82(3128), 2003.

[143] Brian J. Lester, Niclas Luick, Adam M. Kaufman, Collin M. Reynolds, and Cindy A. Regal. Rapid production of uniformly filled arrays of neutral atoms. Phys. Rev. Lett., 115:073003, Aug 2015.

[144] Alicia V Carpentier, Yin H Fung, Pimonpan Sompet, Andrew J Hilliard, Thad G Walker, and Mikkel F Andersen. Preparation of a single atom in an optical microtrap. Laser Physics Letters, 10(12):125501, 2013.

[145] Y H Fung and M F Andersen. Efficient collisional blockade loading of a single atom into a tight microtrap. New Journal of Physics, 17(7):073011, 2015.

[146] Sangtaek Kim, Robert R. Mcleod, M. Saffman, and Kelvin H. Wagner. Doppler-free, multi-wavelength acousto-optic deflector for two-photon addressing arrays of rb atoms in a quantum information processor. Appl. Opt., 47(11):1816–1831, Apr 2008.

[147] Sangtaek Kim. Acousto-optic devices for optical signal processing and quantum computing. PhD thesis, University of Colorado, Boulder, 2008.

[148] M. J. Piotrowicz, M. Lichtman, K. Maller, G. Li, S. Zhang, L. Isenhower, and M. Saffman. Two-dimensional lattice of blue-detuned atom traps using a projected gaussian beam array. Phys. Rev. A, 88:013420, Jul 2013.

[149] N. Schlosser, G. Reymond, and P. Grangier. Collisional blockade in microscopic optical dipole traps. Phys. Rev. Lett., 89:023005, Jun 2002.

[150] K. Szymaniec, H. J. Davies, and C. S. Adams. An atomic fountain guided by a far-off resonance laser beam. EPL (Europhysics Letters), 45(4):450, 1999.

[151] Manuel Endres, Hannes Bernien, Alexander Keesling, Harry Levine, Eric R. Anschuetz, Alexandre Krajenbrink, Crystal Senko, Vladan Vuletic, Markus Greiner, and Mikhail D. Lukin. Atom-by-atom assembly of defect-free one-dimensional cold atom arrays. Science, 2016.

[152] Daniel Barredo, Sylvain de Léséleuc, Vincent Lienhard, Thierry Lahaye, and Antoine Browaeys. An atom-by-atom assembler of defect-free arbitrary 2d atomic arrays. Science, 2016.

[153] Seth Caliga. Experimental realization of atomtronic circuit elements in non-equilibrium ultracold atomic systems. PhD thesis, JILA, University of Colorado, Boulder, 2016.

[154] H. Yamamoto. Resonant tunneling condition and transmission coefficient in a symmetrical one-dimensional rectangular double-barrier system. Applied Physics A, 42(3):245–248, 1987.

[155] B. Ricco and M. Ya. Azbel. Physics of resonant tunneling. the one-dimensional double-barrier case. Phys. Rev. B, 29:1970–1981, Feb 1984.

[156] Avik Dutt and Sayan Kar. Smooth double barriers in quantum mechanics. American Journal of Physics, 78(12):1352–1360, 2010.

[157] R. Tsu and L. Esaki. Tunneling in a finite superlattice. Applied Physics Letters, 22(11):562–564, 1973.

[158] L. L. Chang, L. Esaki, and R. Tsu. Resonant tunneling in semiconductor double barriers. Applied Physics Letters, 24(12):593–595, 1974.

[159] Hiroshi Mizuta and Tomonori Tanoue. The Physics and Applications of Resonant Tunnelling Diodes (Cambridge Studies in Semiconductor Physics and Microelectronic Engineering). Cambridge University Press, New York, NY, USA, 2006.

[160] G. Keller, A. Tchegho, B. Mnstermann, W. Prost, F. J. Tegude, and M. Suhara. Triple barrier resonant tunneling diodes for microwave signal generation and detection. pages 228–231, Oct 2013.

[161] C. Fabry and A. Pérot. Théorie et applications d'une nouvelle méthode de spectroscopie intérferentielle. Ann. de Chim. et de Phys, 16, 1899.

[162] I-Hsing Tan, Gregory L. Snider, and Evelyn L. Hu. Fabry-perot analysis of resonant tunneling structures. Superlattices and Microstructures, 10(1):67 – 72, 1991.

[163] J. A. Kubby, Y. R. Wang, and W. J. Greene. Fabry-pérot transmission resonances in tunneling microscopy. Phys. Rev. B, 43:9346–9349, Apr 1991.

[164] The Fabry Perot Resonator. Springer New York, New York, NY, 2005.

[165] Jérémy Le Deunff, Amaury Mouchet, and Peter Schlagheck. Semiclassical description of resonance-assisted tunneling in one-dimensional integrable models. Phys. Rev. E, 88:042927, Oct 2013.

[166] Amaury Mouchet, Christopher Eltschka, and Peter Schlagheck. Influence of classical resonances on chaotic tunneling. Phys. Rev. E, 74:026211, Aug 2006.

[167] Tobias Paul, Klaus Richter, and Peter Schlagheck. Nonlinear resonant transport of bose-einstein condensates. Phys. Rev. Lett., 94:020404, Jan 2005.

[168] Olivier Brodier, Peter Schlagheck, and Denis Ullmo. Resonance-assisted tunneling. Annals of Physics, 300(1):88 – 136, 2002.

[169] E. T. Jaynes and F. W. Cummings. Proc. IEEE, 51:89, 1963.

[170] Tor Haugset and Hårek Haugerud. Exact diagonalization of the hamiltonian for trapped interacting bosons in lower dimensions. Phys. Rev. A, 57:3809–3817, May 1998.

[171] B. Kurucay. Second Quantization and Bogoliubov Approximation. eprint arXiv:quant-ph/0607201, July 2006.

[172] N Bogoliubov. On the theory of superfluidity. J. Phys, 11(1):23, 1947.

[173] Robert Seiringer. Bose gases, boseeinstein condensation, and the bogoliubov approximation. Journal of Mathematical Physics, 55(7):075209, 2014.

[174] A. N. Khondker, M. Rezwan Khan, and A. F. M. Anwar. Transmission line analogy of resonance tunneling phenomena: The generalized impedance concept. Journal of Applied Physics, 63(10):5191–5193, 1988.

[175] A. F. M. Anwar, A. N. Khondker, and M. Rezwan Khan. Calculation of the traversal time in resonant tunneling devices. Journal of Applied Physics, 65(7):2761–2765, 1989.

[176] S.M. Fazlul Kabir, M.R. Khan, and M.A. Alam. Application of quantum mechanical wave impedance in the solution of schrodinger's equation in quantum wells. Solid-State Electronics, 34(12):1466 – 1468, 1991.

[177] A. P. Stamp and G. C. McIntosh. A time dependent study of resonant tunneling through a double barrier. American Journal of Physics, 64(3):264–276, 1996.

[178] A. F. M. Anwar, A. N. Khondker, and M. Rezwan Khan. Calculation of the traversal time in resonant tunneling devices. Journal of Applied Physics, 65(7):2761–2765, 1989.

[179] S.M. Fazlul Kabir, M.R. Khan, and M.A. Alam. Application of quantum mechanical wave impedance in the solution of schrodinger's equation in quantum wells. Solid-State Electronics, 34(12):1466 – 1468, 1991.

[180] A. Ashby. PhD thesis, University of Colorado, Boulder, 2016.

[181] P. Meystre, G. Rempe, and H. Walther. Very-low-temperature behavior of a micromaser. Opt. Lett., 13(12):1078–1080, Dec 1988.

[182] B.-G. Englert, J. Schwinger, A. O. Barut, and M. O. Scully. Reflecting slow atoms from a micromaser field. EPL (Europhysics Letters), 14(1):25, 1991.

[183] Scott Papp. Experiments with a two-species Bose-Einstein condensate utilizing widely tunable interparticle interactions. PhD thesis, JILA, University of Colorado, Boulder, 2007.

[184] Miroslav Gajdacz, Tom Opatrn, and Kunal K. Das. An atomtronics transistor for quantum gates. Physics Letters A, 378(28):1919 – 1924, 2014.

[185] Shayne Bennetts, Chun-Chia Chen, Benjamin Pasquiou, and Florian Schreck. Steady-state magneto-optical trap with 100-fold improved phase-space density. Phys. Rev. Lett., 119:223202, Dec 2017.

[186] C Ryu and M G Boshier. Integrated coherent matter wave circuits. New Journal of Physics, 17(9):092002, 2015.

[187] Rainer Dumke, Zehuang Lu, John Close, Nick Robins, Antoine Weis, Manas Mukherjee, Gerhard Birkl, Christoph Hufnagel, L. Amico, Malcolm Boshier, K. Dieckmann, Wenhui Li, and Thomas. Killian. Roadmap on quantum optical systems. 2016.

[188] Luigi Amico, Gerhard Birkl, Malcolm Boshier, and Leong-Chuan Kwek. Focus on atomtronics-enabled quantum technologies. New Journal of Physics, 19(2):020201, 2017.

[189] Brad A. Dinardo and Dana Z. Anderson. A quantum thermodynamic model of a matterwave transistor oscillator. To be published.

[190] Carrie Weidner. Shaken Lattice Interferometry. PhD thesis, JILA, University of Colorado, Boulder, 2018.

[191] F.L. Pedrotti and L.S. Pedrotti. Introduction to Optics. Prentice Hall international editions. Prentice Hall, 1993.

[192] Thad G. Walker and M. Saffman. Consequences of zeeman degeneracy for the van der waals blockade between rydberg atoms. Phys. Rev. A, 77:032723, Mar 2008.

[193] M. Ebert, M. Kwon, T. G. Walker, and M. Saffman. Coherence and rydberg blockade of atomic ensemble qubits. Phys. Rev. Lett., 115:093601, Aug 2015.

[194] W Steckelmacher. A review of the molecular flow conductance for systems of tubes and components and the measurement of pumping speed. Vacuum, 16(11):561 – 584, 1966.

[195] J.M. Lafferty. Foundations of Vacuum Science and Technology. Wiley, 1998.

[196] David E. Pritchard. Cooling neutral atoms in a magnetic trap for precision spectroscopy. Phys. Rev. Lett., 51:1336–1339, Oct 1983.

[197] Dieter Meschede and Arno Rauschenbeutel. Manipulating single atoms. volume 53 of Advances In Atomic, Molecular, and Optical Physics, pages 75 – 104. Academic Press, 2006.

[198] E. A. Donley, T. P. Heavner, F. Levi, M. O. Tataw, and S. R. Jefferts. Double-pass acousto-optic modulator system. Review of Scientific Instruments, 76(6), 2005.

[199] Ashok Kumar, Pravin Vaity, Yedhu Krishna, and R.P. Singh. Engineering the size of dark core of an optical vortex. Optics and Lasers in Engineering, 48(3):276 – 281, 2010.

[200] S. C. Caliga, C. J. E. Straatsma, A. A. Zozulya, and D. Z. Anderson. New J. Phys., 18:015012, 2016.

[201] R. A. Pepino, J. Cooper, D. Meiser, D. Z. Anderson, and M. J. Holland. Phys. Rev. A, 82:013640, 2010.

[202] A. Micheli, A. J. Daley, D. Jaksch, and P. Zoller. Phys. Rev. Lett., 93:140408, 2004.

[203] James A. Stickney, Dana Z. Anderson, and Alex A. Zozulya. Transistorlike behavior of a bose-einstein condensate in a triple-well potential. Phys. Rev. A, 75:013608, Jan 2007.

[204] H. A. M. Leymann, A. Forester, and J. Wiersig. Phys. Rev. B, 89:085308, 2014.

[205] A. A. Zozulya and D. Z. Anderson. Phys. Rev. A, 88:043641, 2013.

[206] S. C. Caliga, C. J. E. Straatsma, and D. Z. Anderson. New J. Phys., 18:025010, 2016.

[207] J Rogel-Salazar, S Choi, G.H.C New, and K Burnett. Characterisation of the dynamical quantum state of a zero temperature boseeinstein condensate. Physics Letters A, 299(56):476 – 482, 2002.

[208] M. Gajdacz, T. Opatrný, and K. K. Das. Phys. Lett. A, 378:1919, 2014.

[209] J. A. Stickney, D. Z. Anderson, and A. A. Zozulya. Phys. Rev. A, 75:013608, 2007.

[210] R. A. Pepino, J. Cooper, D. Z. Anderson, and M. J. Holland. Phys. Rev. Lett., 103:140405, 2009.

[211] G. P. Agrawal. Nonlinear Fiber Optics. Academic Press, San Diego, CA, 3 edition, 2001.

[212] H.-P. Breuer and F. Petruccione. The Theory of Open Quantum Systems. Oxford University Press, 2002.

[213] S. C. Caliga. PhD thesis, University of Colorado, Boulder, 2016.

[214] I. Rabi. Phys. Rev., 51:652, 1937.

[215] I. Rabi. Phys. Rev., 49:324, 1936.

[216] John Weiner. Elementary Excitations in Ultracold Finite Systems. John Wiley and Sons, Inc., 2014.

[217] A. Griffin, T. Nikuni, and E. Zaremba. Bose-Condensed Gases at Finite Temperatures. Cambridge University Press, 2009.

[218] J. Dalibard. Collisional dynamics of ultra-cold atomic gases. IOS Press, 1999.

[219] Y. Castin. Bose-Einstein Condensates in Atomic Gases: Simple Theoretical Results. Springer Berlin Heidelberg, Berlin, Heidelberg, 2001.

[220] N. P. Proukakis and K. Burnett. Theory of bose-einstein condensation for trapped atoms. Philosophical Transactions: Mathematical, Physical and Engineering Sciences, 355(1733):2235–2245, 1997.

[221] Nick P Proukakis and Brian Jackson. Finite-temperature models of boseeinstein condensation. Journal of Physics B: Atomic, Molecular and Optical Physics, 41(20):203002, 2008.

[222] C.J. Pethick and H. Smith. Bose-Einstein Condensation in Dilute Gases. Cambridge University Press, 2002.

[223] A. E. Leanhardt, T. A. Pasquini, M. Saba, A. Schirotzek, Y. Shin, D. Kielpinski, D. E. Pritchard, and W. Ketterle. Cooling bose-einstein condensates below 500 picokelvin. Science, 301(5639):1513–1515, 2003.

[224] Patrick Medley, David M. Weld, Hirokazu Miyake, David E. Pritchard, and Wolfgang Ketterle. Spin gradient demagnetization cooling of ultracold atoms. Phys. Rev. Lett., 106:195301, May 2011.

[225] Juha Tuoriniemi. Physics at its coolest. Nat Phys, 12(1):11–14, Jan 2016. Commentary.

[226] Martin Zwierlein. Ultracold atoms: How hot is the coldest matter? Nat Phys, 11(9):706–707, Sep 2015. News and Views.

[227] Ryan Olf, Fang Fang, G. Edward Marti, Andrew MacRae, and Dan M. Stamper-Kurn. Thermometry and cooling of a bose gas to 0.02 times the condensation temperature. Nat Phys, 11(9):720–723, Sep 2015. Letter.

[228] Ryan Olf, Fang Fang, G. Edward Marti, Andrew MacRae, and Dan M. Stamper-Kurn. Thermometry and cooling of a bose gas to 0.02 times the condensation temperature. Nat Phys, 11(9):720–723, Sep 2015. Letter.

[229] T. van Zoest, N. Gaaloul, Y. Singh, H. Ahlers, W. Herr, S. T. Seidel, W. Ertmer, E. Rasel, M. Eckart, E. Kajari, S. Arnold, G. Nandi, W. P. Schleich, R. Walser, A. Vogel, K. Sengstock, K. Bongs, W. Lewoczko-Adamczyk, M. Schiemangk, T. Schuldt, A. Peters, T. Könemann, H. Müntinga, C. Lämmerzahl, H. Dittus, T. Steinmetz, T. W. Hänsch, and J. Reichel. Bose-einstein condensation in microgravity. Science, 328(5985):1540–1543, 2010.

[230] Marlan O. Scully, Georg M. Meyer, and Herbert Walther. Induced emission due to the quantized motion of ultracold atoms passing through a micromaser cavity. Phys. Rev. Lett., 76:4144–4147, May 1996.

[231] Georg M. Meyer, Marlan O. Scully, and Herbert Walther. Quantum theory of the mazer. i. general theory. Phys. Rev. A, 56:4142–4152, Nov 1997.

[232] Markus Löffler, Georg M. Meyer, Michael Schröder, Marlan O. Scully, and Herbert Walther. Quantum theory of the mazer. ii. extensions and experimental considerations. Phys. Rev. A, 56:4153–4163, Nov 1997.

[233] Fazal Badshah, Abdul Basit, Hamad Ali, and Guo-Qin Ge. Manipulating the tunneling of ultracold atoms through a mazer cavity via vacuum-multiparticle interactions. Laser Physics Letters, 14(2):025205, 2017.

[234] Carlton M. Caves and Bonny L. Schumaker. New formalism for two-photon quantum optics. i. quadrature phases and squeezed states. Phys. Rev. A, 31:3068–3092, May 1985.

[235] Seth Caliga. Experimental realization of atomtronic circuit elements in non-equilibrium ultracold atomic systems. PhD thesis, JILA, University of Colorado, Boulder, 2016.

[236] A. Derevianko, W. R. Johnson, M. S. Safronova, and J. F. Babb. High-precision calculations of dispersion coefficients, static dipole polarizabilities, and atom-wall interaction constants for alkali-metal atoms. Phys. Rev. Lett., 82:3589–3592, May 1999.

[237] Matt Squires. High repetition rate Bose-Einstein condensate production in a compact, transportable vacuum system. PhD thesis, JILA, University of Colorado, Boulder, 2008.